NASA Conference Publication 2081

13th Aerospace Mechanisms Symposium

Proceedings of a symposium held at
Lyndon B. Johnson Space Center
Houston, Texas
April 26-27, 1979

NASA

NASA Conference Publication 2081

13th Aerospace Mechanisms Symposium

Sponsored by
National Aeronautics and Space Administration
Lockheed Missiles and Space Company, Inc.
California Institute of Technology

NASA
National Aeronautics
and Space Administration

Scientific and Technical
Information Office

1979

ORGANIZING AND REVIEW COMMITTEE

The papers presented at the symposium were selected and reviewed by the Organizing Committee. Responsibility for content and technical accuracy lies with each respective author. The committee included the following members: Charles W. Coale, General Chairman, Lockheed Missiles and Space Company, Inc.; Ernest E. Sechler, Executive Co-Chairman, California Institute of Technology; Alfred L. Rinaldo, Operations Chairman, Lockheed Missiles and Space Company, Inc.; Aleck C. Bond, Host Chairman, NASA Lyndon B. Johnson Space Center; Paul W. Bomke, Kenneth C. Curry, and John D. Ferrera, NASA Jet Propulsion Laboratory; Mervin Briscoe, ESA European Space Research and Technology Center; Kenneth S. Bush and James H. Parks, NASA Langley Research Center; David F. Englebert and Angelo Giovannetti, NASA Ames Research Center; Allen J. Louviere, NASA Lyndon B. Johnson Space Center; Frank T. Martin and Bowden W. Ward, Jr., NASA Goddard Space Flight Center; and David F. Welch, California Institute of Technology.

PREFACE

The Thirteenth Aerospace Mechanisms Symposium held at the NASA Johnson Space Center, April 26 and 27, 1979, was sponsored jointly by the California Institute of Technology, Lockheed Missiles and Space Company, Inc., and the National Aeronautics and Space Administration. This series of symposia has filled a definite need in a highly important specialists' area not fully addressed and treated by technical symposia and conferences of existing technical societies. Through the years, the Aerospace Mechanisms Symposium has continued to grow in stature and prominence nationally and now enjoys a significant international flavor.

The Johnson Space Center was pleased to host this symposium since it offered a continuing opportunity for maintaining direct rapport and interaction with the technical community in the mechanisms area, which is so vitally important to our space-flight programs. Additionally, it provided for timely review and discussion of some of the more unique mechanisms and associated designs being employed on the Space Shuttle.

This document is a compilation of papers presented at the symposium, which were selected carefully for areas of current interest and applicability. It is a product which represents the work and efforts of many individuals. In this regard, I wish to thank the authors for the fine quality of papers, the Symposium Organizing Committee for the review and selection of papers and for developing the overall program, as well as the numerous other individuals who provided active support in the various facets of the symposium preparations. Additionally, I wish to acknowledge and thank Mr. Allen J. Louviere and Mr. Viljar Sova for their dedicated help and assistance and all the other members of the JSC Spacecraft Design Division who participated in the conduct of this symposium.

Aleck C. Bond
Host Chairman

CONTENTS

HYDRAZINE MONOPROPELLANT RECIPROCATING ENGINE DEVELOPMENT

James W. Akkerman
Lyndon B. Johnson Space Center

ABSTRACT

A hydrazine-fueled piston-type engine for providing 11.2 kW (15 hp) has been developed to satisfy the need for an efficient power supply in the range from 3.7 to 74.6 kW (5 to 100 hp) where existing non-air-breathing power supplies such as fuel cells or turbines are inappropriate. The engine was developed for an aircraft to fly to 21.3 km (70 000 ft) and above and cruise for extended periods. The NASA Hugh L. Dryden Flight Research Center developed a remotely piloted aircraft and the associated flight control techniques for this application. The engine is geared down internally (2:1) to accommodate a 1.8-m (6 ft) diameter propeller. An alternator is included to provide electrical power. The pusher-type engine is mounted onto the aft closure of the fuel tank, which also provides mounting for all other propulsion equipment.

About 20 hr of run time have demonstrated good efficiency and adequate life. One flight test to 6.1 km (20 000 ft) has been made using the engine with a small fixed-pitch four-bladed propeller. The test was successful in demonstrating operational characteristics and future potential.

BACKGROUND

Hydrazine (N_2H_4) is finding increasing acceptance as a non-air-breathing energy source for applications in which the complexity of using two reactants is prohibitive. Examples include many satellite rocket systems, aircraft emergency power units, undersea buoyancy systems, and as a primary energy source for the Space Shuttle flight control system. These applications have evolved because of the fundamental characteristics of high energy content and easy conversion of the liquid hydrazine, as a monopropellant, into hot gas at a temperature of approximately 1200 K (1700 deg F). However, very little work has been done on systems in the range of 7.5 to 37.3 kW (10 to 50 hp).

CONCEPT SELECTION

After the industry had been surveyed and several proposals had been considered, the "mini-sniffer" aircraft (fig. 1) was almost dropped as being beyond the scope of the available funding. The battery/motor approach for powering the mini-sniffer lacked high-energy capability and low-weight characteristics needed. The turbine machines lacked efficiency and the throttleability required. It seemed that some sort of hot-gas expander of the positive displacement type would fit the application and result in cost-effective

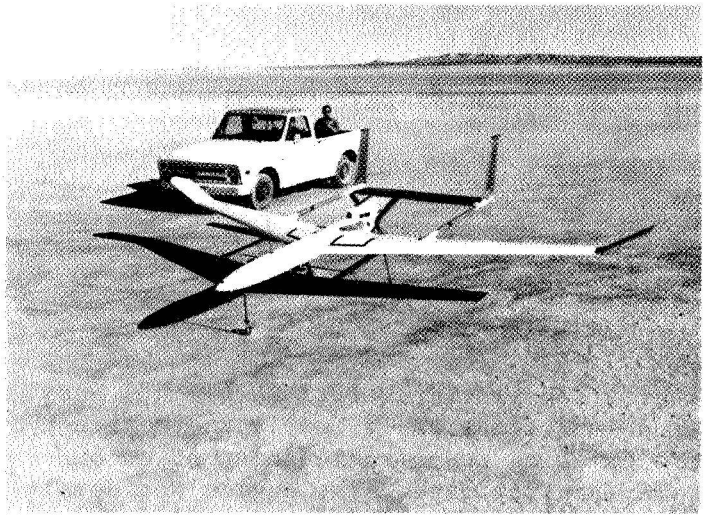

Figure 1.- The "Mini-Sniffer" aircraft.

system. Hydrazine was attractive as the fuel, because of its high energy content.

The basic objective of the mini-sniffer aircraft is to fly an 11.3-kg (25 lbm) air sampler unit to an altitude of 21.3 km (70 000 ft) or higher and maneuver it within a 370-km (200 n. mi.) range. Preliminary studies indicated that this objective could be accomplished with a vehicle having a wingspan of approximately 5.5 m (18 ft) and a takeoff weight of less than 90.7 kg (200 lbm). The climb power required was on the order of 11.2 kW (15 hp), the cruise power was approximately 2.2 kW (3 hp), and the fuel consumption was in the range of 1.01 kg/MJ (6 lbm/hp-h). (The theoretical minimum for hydrazine is approximately 0.59 kg/MJ (3.5 lbm/hp-h).) The configuration required a pusher propeller with a diameter of approximately 1.8 m (6 ft). A variable-pitch unit enabled the choice of a constant-speed engine.

DESIGN ANALYSIS

Power Level

An iteration of power level as a function of total propellant required was the first analysis performed. A high power level (22.4 kW (30 hp)) minimized the run time to reach altitude and, thereby, minimized fuel consumption. However, the large engine more than offset the hydrazine weight saving. Conversely, a smaller engine caused increased run time, which caused additional weight of hydrazine to be carried. The choice of 11.2 kW (15 hp) provided the minimum overall weight and was operationally consistent with ordinary airplanes; i.e., no vertical flight. An energy level of 26.85 MJ (10 hp-h) was established to fly the desired air-sampling mission.

Expansion Ratio

A second analysis was performed to determine the best choice of displacement for the engine. A large-displacement engine, operating at 11.2 kW (15 hp) output, could reduce the hydrazine required by increasing the expansion energy. Conversely, a small-displacement engine could minimize engine weight but would be less efficient in converting the hydrazine decomposition gases into shaft power. A trade study indicated that an intermediate size with an expansion ratio of approximately 5.5 to 1, using a total displacement of

approximately 131 cm^3 (8 in^3), was near optimum. This value provided a theoretical specific fuel consumption (SFC) of 0.73 kg/MJ (4.337 lbm/hp-h). Assuming a loss of 2% due to gas leakage, 7% due to heat leakage, 10% for mechanical loss, and 7% to run the fuel pump, the oil pump, and the alternator (72% overall efficiency), the SFC would be approximately 0.99 kg/MJ (5.85 lbm/hp-h). The total of engine and fuel weight varied about 50% between the extremes considered. However, for any normal operating pressure and efficiency, the trade was only affected by approximately 20%, or 9.1 kg (20 lbm), which made the final selection somewhat insensitive to displacement.

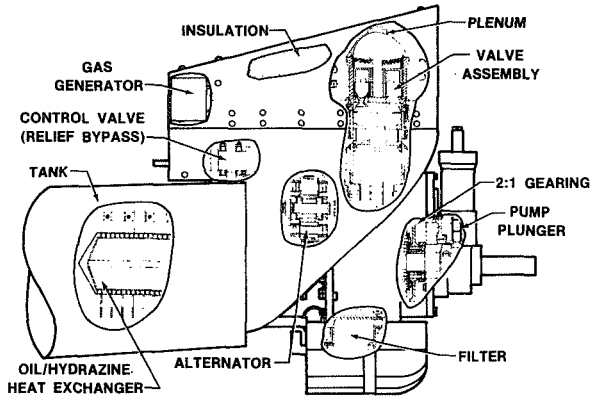

Figure 2.- Engine cross section.

SYSTEM DESCRIPTION

The description of the engine includes mechanical and electrical design, oil circuit design, and fuel circuit design.

Mechanical and Electrical Design

The mechanical arrangement is shown in its final form in figure 2. The assembly is mounted to the aft end of the aircraft fuselage by eight radial bolts and two tabs that attach the trailing edges of the wings. It weighs 17.3 kg (38.1 lbm) including the tank but excluding the propeller. The engine mechanism is conventional and uses elements typical of many small two-stroke engines of similar power output.

The alternator is mounted adjacent to the forward end of the crankshaft by a set of four fingers, which are a part of the crankcase. A clamp holds the fingers against the outside of the alternator stator to provide a friction-force retention. The magnesium crankcase also serves as a path for heat rejected from the alternator stator. Permanent magnets are used to provide the alternator flux field. Eight rare-earth magnets are mounted on the rotors on each end of the alternator and are rotated at engine speed with a coupling using dowel pins for the drive mechanism.

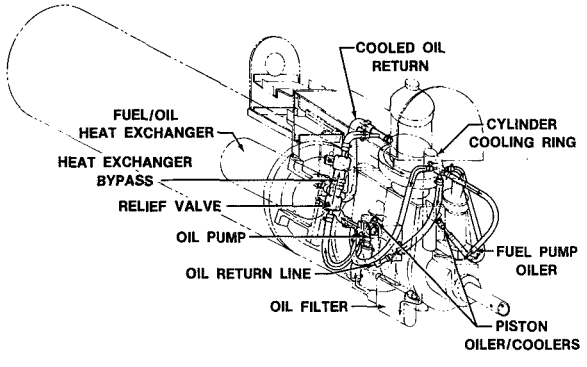

Figure 3.- Oil distribution system.

Oil Circuit Design

The oil circuit is shown isometrically in figure 3. It is designed for both lubricating and cooling and uses 5606 hydraulic fluid with a 3% by weight molybdenum disulfide additive. The system will operate satisfactorily with an oil quantity as low as 200 cm^3 or as high as 800 cm^3. The oil that is sprayed onto the underside of the piston for cooling also provides cylinder lubrication. The oil splashes through eight 0.102-cm

(0.040 in.) diameter holes in the piston wall just below the top ring. The holes are in line radially with the bridges between the exhaust ports in the cylinder. The holes in the piston also enable pressurization of the sealed crankcase and prevent cavitation of the oil pump in vacuum operation. Normal piston ring leakage goes into the crankcase during the top part of the piston travel, and oil flows out through the holes during the lower part of the piston travel. The lower ring spreads the oil on the upstroke and wipes the oil splashed on the lower cylinder back into the crankcase on the downstroke. The average crankcase pressure is approximately 13.8 kN/m^2 (2 psia) during vacuum operation.

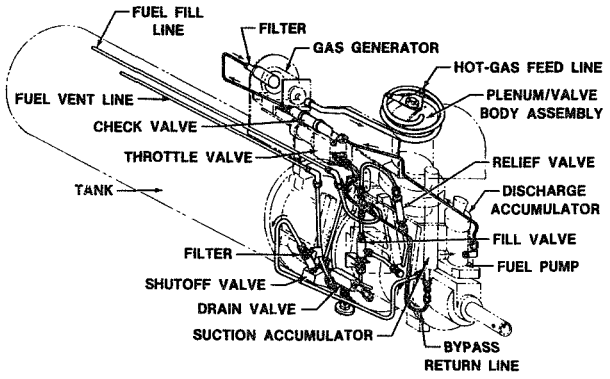

Figure 4.- Fuel piping system.

Fuel Circuit Design

The fuel circuit is shown in figure 4. The hydrazine is chemically unstable and requires special handling to avoid excessive pressure buildup due to decomposition and/or possible detonation, especially where the hydrazine is used as a heat-transfer fluid. The fuel transfers heat from the submerged lubricating oil heat exchanger to the surface of the tank.

The fuel system is fundamentally simple in that the hydrazine is pressurized with a plunger-type pump and the pressure is regulated with a controllable relief valve. The pressurized hydrazine is decomposed in a catalyst bed to generate hot gas to run the engine. However, the elements for safety, servicing, and draining add considerable complexity.

A suction accumulator supplies fuel to the pump intermittently on demand from the pump plunger; by this means, the flow from the tank is stabilized. A trap is built into the lower end of the suction accumulator to keep the gaseous bubble "spring" from passing into the pump. The proper bubble size is loaded as a part of the servicing. The system will not work with continuous negative gravity but will work with intermittent negative gravity.

The fuel pump uses a scotch yoke actuator mechanism and reed-type check valves. It pumps approximately 0.361 cm^3 (0.022 in^3) per revolution using a 0.953-cm (0.375 in.) bore. The reeds are fitted with a curved backstop to avoid overstressing. The steel plunger runs in a bronze bushing to provide proper alinement with the pumping cylinder. The plunger has a stainless steel cap which operates in a stainless steel cylinder with about 0.008-cm (0.003 in.) clearance. The bronze bushing fits close enough to the steel plunger to prevent contact between the stainless steel elements. An O-ring made of ethylene propylene rubber backed up by a tetrafluoroethylene insert acts as the plunger seal for the hydrazine. A second seal, below the stainless section, holds the oil in the pump case. A vent between the seals to the overboard relief valve prevents any leakage from either side from entering the other system.

A high-pressure accumulator is built into the pump body and connected to the discharge port. The piston-type accumulator has redundant O-ring seals and a nitrogen charge for a spring. A conventional charging-type check valve is used for charging the nitrogen, and a strain gage is mounted on the side of the accumulator for monitoring the nitrogen charge pressure.

The pressurized hydrazine flows through 0.318-cm (0.125 in.) tubing to the throttle valve, which is basically a relief valve with a controllable setting. At the idle position, the relief valve spring has enough tension to hold approximately 2068 kN/m^2 (300 psig). Any fluid in excess of the amount that will go through the engine at 2068 kN/m^2 (300 psig) is bypassed back to the suction accumulator through a 0.318-cm (0.125 in.) line. At full throttle, the throttle actuator compresses the relief valve spring by way of a push rod to hold approximately 5860 to 6205 kN/m^2 (850 to 900 psia) in the high-pressure section. To prevent oscillations in the spring/plunger mechanism of the throttle valve, a viscous damper is installed on the plunger. The damper is charged with oil (hydrazine-compatible polyalkaline glycol) with a viscosity of approximately 0.001 m^2/sec (225 Sus), providing a slow response to avoid engine speed oscillations.

A check valve is installed just downstream of the throttle valve in the liquid line to the gas generator to prevent backflow from the engine/gas generator into the fuel feed system. A 0.318-cm (0.125 in.) tube connects the feed system to the inlet of the gas generator through an inlet filter. The filter minimizes the possibility of catalyst from the gas generator entering the liquid feed system and causing decomposition and overpressures or detonations.

The gas generator is a catalyst type normally used on a small rocket engine. It was selected for its availability, not its design. The proper design for this application is a thermal-type gas generator having an almost unlimited life. The catalytic gas generator functioned satisfactorily, however, in converting the liquid hydrazine into hot gas as required.

The hot gas is piped across the engine-mounting interface through a 0.953-cm (0.375 in.) Hastelloy B (high nickel-chromium alloy) tube welded at each end. This tube circles twice around the hot-gas plenum on the engine to provide sufficient flexibility to minimize stress. The last loop of tubing is loosely restrained by a bracket joined to the plenum to minimize low-frequency, high-amplitude vibrations.

The plenum holds approximately 49 cm^3 (3 in^3) of hot gas, awaiting opening of the hot-gas valves. As the valves open, an additional 16-cm^3 (1 in^3) volume is provided in the cylinder, resulting in a rapid drop in plenum pressure to about three-fourths of the plenum charge pressure. After the valves close, the plenum repressurizes and the gas charge in the cylinder expands to push the piston to do work.

The hot-gas valves and associated hardware (fig. 5) are actuated open to approximately 0.064 cm (0.025 in.) by the piston as it reaches the top end of its stroke. To prohibit the valves from bouncing off the piston and lifting open more than they should, a cup-shaped foot seals a cavity between the valve and the piston. As the cylinder pressure rises, a clamping force develops. This pressure force holds the poppets against the piston as the piston goes

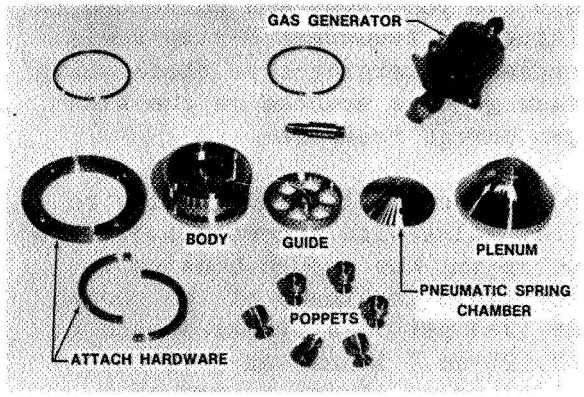

Figure 5.- Valves, plenum, and gas generator.

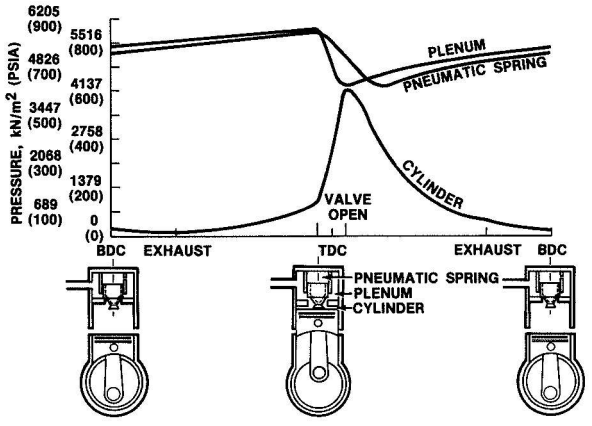

Figure 6.- Plenum pressure vs crank angle.

over top dead center (TDC). A pneumatic spring in the plenum helps hold the poppet against the piston and holds the valve closed as the piston pulls away from the poppet. The pneumatic spring is a small volume of gas trapped in a cavity behind the valve poppet and sealed by the valve guide as shown schematically in figure 6. The cavity is pressurized by the plenum and is sealed sufficiently by labyrinth-type seal glands to maintain the pneumatic spring pressure above plenum (and cylinder) pressure during the cylinder filling time, the closing part of the poppet motion, and for a period afterward. This pressure difference keeps the poppet from bouncing open after it seats. The piston velocity at the time of initial contact and during closing of the valve is low enough to avoid impact damage. The operation of the valves and the associated pressures are shown in figure 6.

Finally, the expended hot gas is vented to the atmosphere through eight exhaust ports at the lower end of the cylinder and ducted through a pair of short exhaust stacks - one out each side of the cowling. The fuel system also includes a tank drain valve, a fill tube, a vent tube, and an overboard relief valve.

TESTING

The testing is discussed in three parts: (1) component evaluation tests (pumps, valves), (2) engine evaluation, and (3) flight test.

Component Evaluation

The early tests were directed at establishing acceptable component performance and component configuration so that the integrated system design could proceed.

Fuel pump. Testing of the fuel pump resulted in several refinements. Early tests were performed with water. The results demonstrated the need for the accumulators and a controlled flexure of the reed valve. The pump will produce a discharge pressure of 6895 kN/m^2 (1000 psi) at the flow required for 11.2 kW (15 hp) output with a 13.8-kN/m^2 (2 psia) inlet pressure and

operation at 314.2 rad/sec (3000 rpm). The output pressure is steady within approximately 414 kN/m^2 (60 psi) using an orifice for flow control (simulation of the gas generator). In the approximately 20 hr of testing accumulated on the pump, the only problem was with particulate contamination under the reed valve. This contamination resulted in the addition of the filter at the outlet of the tank shutoff valve just upstream of the pump inlet. Momentary operation at pressures near 34 474 kN/m^2 (5000 psi) were observed without damage to the pump.

Hot-gas valving. Early tests of the hot-gas valves were done using a modified two-cycle engine. The results were very disappointing and indicated the existence of a very severe environment. Hammering was immediately evident even in tests using cold gas as a working fluid. It was apparent that the piston could potentially cause damage to the poppets during opening but not to the seat during closing, and the seats sustained the most damage. The valve was apparently being closed by the flowing gas, and the first design change was to reduce the opening lift to maintain enough pressure drop across the valves to force valve contact with the piston at all times. This modification severely reduced the power of the engine and increased the required feed pressure. At slow speeds, the pressure equalized anyway, still allowing the "float" situation and an uncontrolled gas-flow-induced closure of the valves.

The next modification was to make a suction cup on the stem of the valves such that, as the cylinder was pressurized, the pressure differential across the cup or valve "foot" would hold the valve onto the piston as outlined previously. This change gave tremendously improved life and performance, but the data relating gas pressure and output torque were still inconsistent and unpredictable. At this point, it was decided to instrument the cylinder pressure to see exactly what was happening. It became apparent that the valve poppet - once released from the hold of the suction cup - was bouncing off the seat very momentarily, admitting additional working fluid. The amount of extra fluid admitted was a function of speed and throttle setting.

Because the bouncing effect was not causing significant damage, there was a great temptation not to worry about it. The power could be adjusted with the throttle in any event. However, the bouncing could be expected to result in a somewhat reduced efficiency because the gas admitted late would not expand as much as planned. Because efficiency is very important for the application involved, a design change was considered.

Various concepts of antibounce mechanisms were evaluated analytically. Mechanical spring arangements considered lacked sufficient response to track the motion and could not apply an appropriate valve-closing force. Finally, the idea of a "pneumatic" spring evolved as outlined in the preceding design discussion. The pneumatic spring cavity "consumed" some of the plenum volume in an early version requiring extra feed pressure but produced repeatably good results. In the flight version, plenum volume was increased sufficiently to house the pneumatic spring and to feed the working chamber without excessive pressure drop.

The high efficiency achieved in tests of the flight engine evidences very little valve leakage. The most common problem with the valves was contamination of the seal area with particles from the gas generator. In

runs using a new gas generator, which produced few particles, the performance was near the theoretically expected levels.

Other tests. The alternator was tested extensively on the workbench. Several sets of stator windings were tested in an effort to achieve the rated 4-A current at as wide a speed range as possible. The only significant problem was with the pin drive, and the diameter of the pins was increased from 0.318 to 0.635 cm (0.125 to 0.25 in.).

The throttle valve was tested extensively in both water and methyl alcohol before it was committed to use with hydrazine. The throttle valve is probably the only part that functioned entirely satisfactorily as designed and fabricated the first time. It required only the appropriate shimming and adjustment. An improved version might be built with a steeper angle on the poppet seat or a longer spring to reduce the effect of flow variations on the pressure setting.

The oil pump tests were uneventful. However, the pump, a gear-type unit in an aluminum case, is prone to generation of particulate contamination and could be improved in that respect. Pump flow is 3.8 liters/min (1 gal/min) at 209.4 rad/sec (2000 rpm). It is about 85% efficient at 517-kN/m^2 (75 psi) discharge pressure. About 10% losses are due to leakage and about 5% to drag effects.

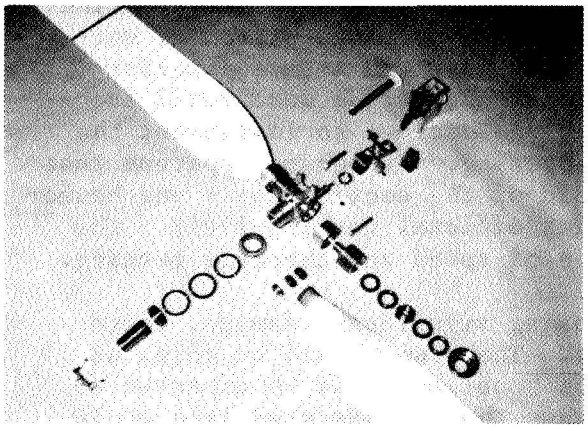

Figure 7.- Propeller assembly.

Performance testing of propellers and propellers in general was a problem in the program. The large, low-speed units required for this application require an extra degree of precision in manufacture to provide the same effective lift on both blades to avoid excessive vibration. The propeller being developed at the NASA Hugh L. Dryden Flight Research Center (DFRC) for ultimate use on the mini-sniffer is shown in figure 7. It is ground controllable in the same way as the throttle setting. Testing of this unit had not begun at the time of this writing.

Engine Assembly Tests

All the flight engine assembly testing was done on the stand arrangement shown in figure 8. Various loads were simulated by using different propellers. Most testing was done at sea level, with some high-altitude testing. Measurements were primarily of the slow-response type using the meters shown, except for the high-speed measurements of cylinder pressure and pump discharge pressure mentioned previously. The data were recorded on film in the form of meter readings.

The testing was done at the NASA Lyndon B. Johnson Space Center thermochemical test facility primarily by support contractor personnel. The

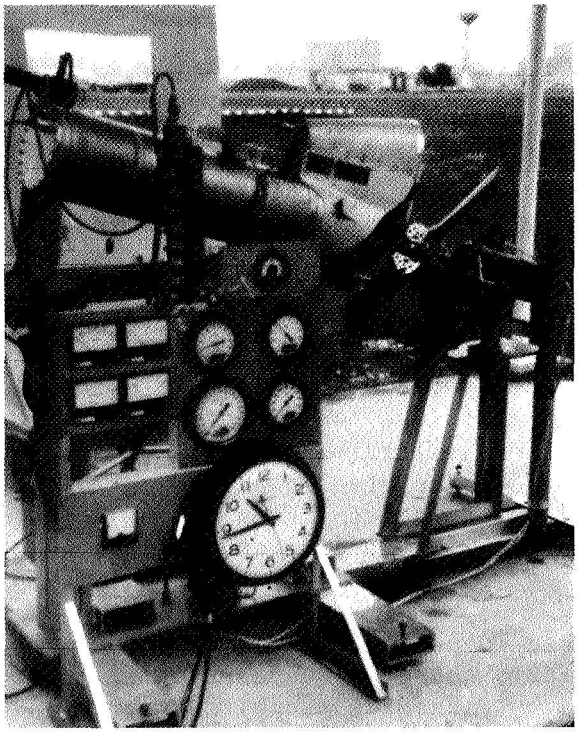

Figure 8.- Flight engine test stand.

secondary-priority nature of the work, behind Space Shuttle and other ongoing programs, and continuous redesign activities extended the testing over about 2 yr. The test stand was designed primarily to minimize interface with the facility data and control systems such that tests could be run on short notice whenever a schedule opening occurred. This configuration provided a very appropriate environment for experimental testing in which intermittent activity is caused by modifications and rework.

Only two controls were used: (1) the electric-motor-operated throttle and (2) a supplemental vent valve that positively vented the fuel pump discharge pressure back to the tank and simultaneously vented the fuel tank pressure.

The data for engine speed, feed pressure, and fuel level are shown in figure 9 for a 17-min, 638.79 $\pm$ 10.47-rad/sec (6100 $\pm$ 100 rpm) run (11.19 kW (15 hp)). It should be noted that the engine required approximately 1 min to heat the gas generator and the plenum. At about 60 sec, the throttle was

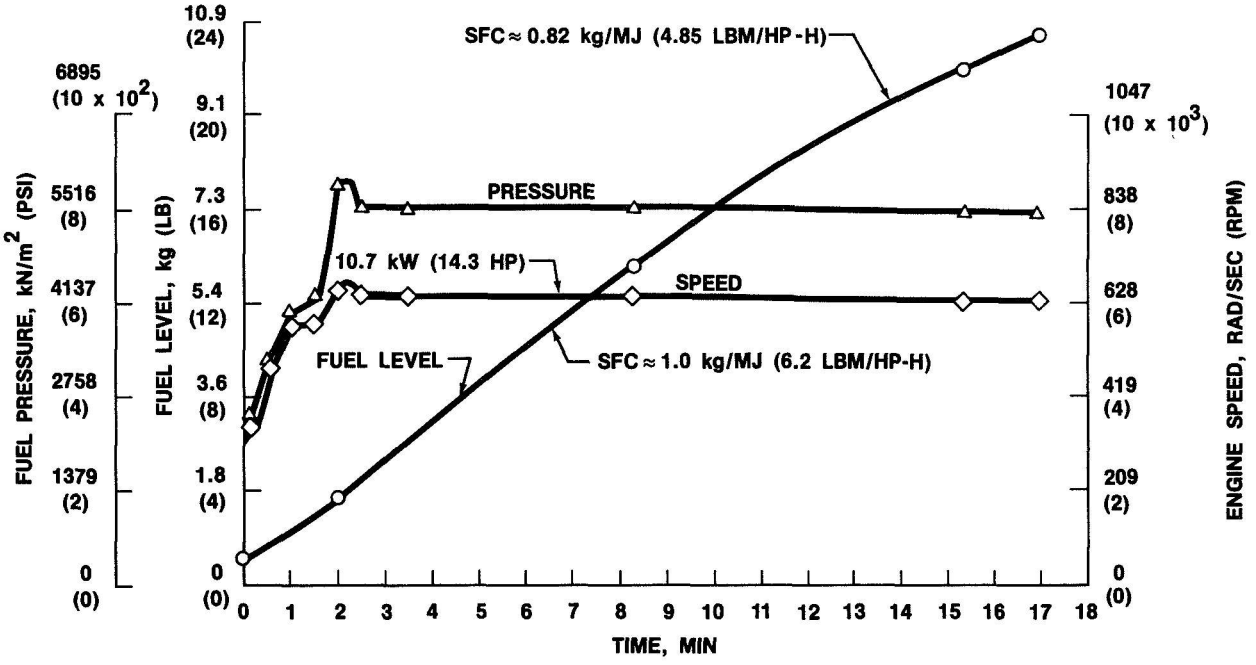

Figure 9.- Speed, pressure, and fuel level vs time for 17-min run at 628.32 rad/sec (6000 rpm) with small four-blade propeller.

advanced to full power, which resulted in slightly more than desired pressure at the 2-min point. The throttle was reduced slightly, and the power level stabilized approximately 150 sec into the run. The run was essentially steady for the duration and was terminated because of oil depletion. One significant aspect of this run, the improvement in efficiency as the run progressed, is apparently the result of steadily decreasing windage as the oil is lost and/or stabilization of the temperature of the hot-gas section occurs. The flight configuration was modified to include an oil baffle in the crankcase to reduce windage.

The heat leak through the Inconel piston cap is apparently minimal. No evidence of oil coking in the piston ring groove or on the bottom of the piston dome was observed, an indication that the operating temperature of the unit was less than 422 K (300 deg F). The stainless steel piston cap generally produced a straw color on the back side indicative of a temperature of approximately 589 to 700 K (600 to 800 deg F). The steel exhaust manifold showed no evidence of excessive heating, indicating that the flow of cooling air maintained a temperature below 533 K (500 deg F). It did get hot enough to coke oil, however.

Several interesting data points were taken in unusual circumstances, especially when the oil was lost and piston seizure caused a sudden stop. (Most oil losses were by way of broken lines caused by excessive propeller vibration.) Under this condition, liquid hydrazine is trapped between the check valve and the hot-gas generator. Typically, the shutdown would occur with the pressure at 5515.8 kN/m^2 (800 psi). In these cases, the pressure would slowly decrease to about 2758 kN/m^2 (400 psi) over a 30-min period. During this time, the only escape of gas is past the hot-gas valves and the piston rings. It is this condition that should provide the environment necessary to produce overpressurization of feed system hydrazine; however, it never occurred.

Apparently, the slow leakage past the valves and the piston was enough to vent the decomposition products as they were being generated by heat soak from the gas generator back into the feed tube. The feed tube into the gas generator is a comparatively heavy piece of aluminum into which the inlet filter is fastened. This element can apparently reject heat as rapidly as it soaks out of the gas generator to maintain a safe hydrazine temperature. The highest temperature measured at the gas generator inlet under these circumstances was about 366 K (200 deg F).

Another interesting occurrence documented some safety margin in the system. Excessive valve leakage caused ignition of the exhaust gases at a temperature of about 866 K (1100 deg F). Subsequently, several of the cloth and rubber oil lines just under the exhaust manifold ignited. The engine was shut down, but the fire continued and resulted in considerable heating of the hydrazine pump. Essentially all the combustible material in the engine cowl burned, but the hydrazine was not heated sufficiently to cause overpressurization. New oil lines were installed, the hot-gas valves were repaired, and the testing was continued.

On several occasions, hydrazine leaks occurred; however, no ignition resulted, even though the liquid and vapor were sprayed through the exhaust. This leakage also occurred in flight without incident. Of course, leaking

hot-gas valves (which dump 1200-K (1700 deg F) unexpanded gas out the exhaust) combined with a hydrazine leak would probably result in a fire, but that combination of problems never occurred.

One of the major problems in verifying the flight configuration was establishing the proper size holes in the piston to provide sufficient cylinder oiling without excessive loss of oil through the exhaust. The decision to fly a "demonstration" test using a fixed-pitch propeller complicated the situation because it demanded operation from about 419 rad/sec (4000 rpm) to 628 rad/sec (6000 rpm) during the climb. Holes that lubricated sufficiently at 419 rad/sec (4000 rpm) were insufficient at 628 rad/sec (6000 rpm). Conversely, holes that oiled sufficiently at 628 rad/sec (6000 rpm) passed oil excessively at 419 rad/sec (4000 rpm). A compromise could probably have been worked out; but, as the flight time approached, the only test catalyst bed available was shedding many particles, causing valve leakage, producing excessive heating, and shadowing the results. As a temporary solution for the one test flight, a special oiler was added having four separate injectors powered by a small electric motor. This system injected upper cylinder lubricant into the engine just downstream of the valves through small (0.033-cm (0.013 in.) i.d.) steel tubes. A final test run verified good performance, and the test injector was installed on the aircraft for lack of a new unit.

Flight Test

The new engine for the test flight passed all the checkout criteria with a good margin. Although a static test of the new engine before flight would have been desirable, the fact that the gas generator was seriously life limited together with the schedule and man-hour limitations prohibited a static test run.

The vehicle was checked out and serviced at DFRC the night before the flight. It was carried about 8 km (5 s. mi.) across the dry lake the morning of November 23, 1976. A final communication link checkout was made, the tank was pressurized to 413.69 kN/m^2 (60 psia), and the upper cylinder oiler was turned on. At about 9:30 a.m., the engine was started and the flight was begun. The same basic engine parameters were monitored in the ground telemetry van as were monitored in the development tests. Engine pressure and speed increased normally as the aircraft taxied for takeoff. The aircraft lifted off much the same as it had many times before using a chain-saw engine. About 20 sec into the climbout, however, the fuel feed pressure dropped suddenly and the power sagged; then, almost as suddenly, the power increased again. The first thought was that a bubble passed through the hydrazine pump.

The climbout continued, and a right turn was performed as planned. Within about 5 min into the flight, it became apparent from the climb rate that the power was a little less than expected but within the estimated tolerance. However, within 8 to 10 min, it appeared that the power level was out of tolerance on the low side.

About 25 min into the flight, the throttle was advanced in an effort to obtain more power, but this setting caused the power to decrease still further, even though the pressure increased properly. Since the pressure was

then dangerously high (near 6550 kN/m^2 (950 psi), the upper maximum allowable), the throttle was decreased slightly. The power increased appreciably. When the power increased, the climb began again but still at a less than desirable rate. At about 30 min into the flight, the fuel tank pressure was indicating near depletion of the fuel.

The slow climb proceeded to near 6.1 km (20 000 ft) at 34 min, when fuel feed pressure became slightly intermittent; the pressure dropped, the engine speed dropped, and the run was finished. The pilot, located in the base tower about 8 km (5 s. mi.) away, nosed the plane over, set the throttle to "off," and began the long glide down. About 30 min later, the vehicle landed on the dry lake near the takeoff point. The tank still had the same low pressure (about 13.8 kN/m^2 (2 psia)). The engine windmilled at about 189 to 209 rad/sec (1800 to 2000 rpm) all the way down because of the fixed-pitch propeller. The gas generator and all other components were at ambient temperature on landing.

The retrieval crew noticed almost immediately that the finish was removed from the propeller blades in an area about 15 cm (6 in.) from the hub. It was apparent that a strong solvent had rinsed the finish off. Approximately in line with the area, the hydrazine pump discharge fitting was found to be loose. There were no other indications of any problem with the engine at that time.

The craft was carried back to the checkout/servicing area and flushed with methanol; the loose fitting was verified as the source of a leak. The engine was disassembled to evaluate the condition of the hardware and to determine the cause of the low power and the inverted throttle response. No external leaks were found in the high-pressure hot-gas section, but one of the small oiler tubes was broken where it connected to the engine. Also, the valves and seats were somewhat brinelled. The piston and rings appeared normal and had no measurable dimensional change.

The liquid hydrazine leak could not account for the power reduction because it was small enough to be automatically correctable by the throttle valve. The momentary power sag during the takeoff had the characteristic timing of the throttle valve response. Also, because the pressure increased and was maintained during the flight, this leak was not the cause of the power sag. The valve damage observed (brinelling) was apparently the result of windmilling the engine with hot valves during the glide down (without the pneumatic springs operating). This problem will be eliminated with the new controllable-pitch propeller, stopping the engine after the run by going slightly past the feather point. The leak resulting from the fracture of the upper cylinder oiler tube (0.033 cm (0.013 in.) i.d.) was insufficiently large to be significant and very likely occurred on the way down since there was no evidence of any hot-gas leakage. There simply was no immediate explanation of the power reduction during the flight, or of the inverted throttle response.

The two possible explanations of the flight anomalies are fuel feed blockage and/or mechanical reduction of valve lift. The fuel system was verified to be open in the process of system flushing after flight. However, the new engine could possibly have readjusted itself mechanically during its first run to effectively reduce the valve lift. Actually, this self-adjustment

was expected, because it occurred to some extent on the test engine but not to the degree that apparently occurred during flight. The lift was set at 0.069 cm (0.027 in.) during assembly, 0.005 cm (0.002 in.) more than normal in the development engine. This adjustment was made to allow for "set" in the new three-piece crankshaft, run-in of the new bearings, and any other deflections which might affect the lift adversely. However, behavior of the flight engine in the final minutes of operation was similar to that of the development engine with low-valve-lift setting. With the valve lift near 0.030 cm (0.012 in.), higher pressure causes structural flexure and additional reduction in lift, which reduces both the flow area opened by the valves and the time for flow. Conversely, reduced pressure reduces structural deflection and thereby increases the area-time integral, which increases flow and power. The valves were deformed just enough by windmilling during descent to prohibit a good indication of whether valve-lift reduction actually happened, but it seems reasonable.

The flight test demonstrated the operational characteristics of a hydrazine-fueled non-air-breathing aircraft engine. The flight produced no complications or other unforeseen problems. With appropriate precautions, the system can be handled with little more time and effort than any other power system. Although the fluid is toxic, it requires a cumulative exposure to be seriously dangerous, barring excessive exposure. The most dramatic hazard is of course a fire, but the fluid - having relatively low vapor pressure - is not easily ignited. The possibility of detonation of the hydrazine is practically eliminated by proper design to keep the fuel cool (below about 366 K (200 deg F).

CONCLUSIONS

The valving concept has been demonstrated and is being patented, but the work required to optimize the performance of the valving concept for any specific application still must be done. The design for the best choice of seal perimeter, lift height, poppet length (for elastic deformation on contact with the piston), seal width, pneumatic spring volume, guide clearance and tolerances, and material choice for guide, seat, and poppet can only be established through analysis and considerable testing.

Any vapor or hot-gas expander-cycle machine can utilize the valving concept. A steam engine is a good example. The low-weight, simple, positive mechanism involved can make it a candidate for mobile applications. However, the valving concept may be limited to applications in which the engine always drives the load. In that case, the pneumatic springs are always pressurized and the valves will not float as they did during the downward glide in the flight test. However, if valve floating occurs at a sufficiently low speed and/or temperature, it may cause no problem. Also, depending upon the temperature and speed involved, a mechanical spring might be added to supplement the pneumatic spring for eliminating the floating operation. The most significant improvement for the concept might be the use of a thermal-type gas generator (one that does not shed particles into the engine). The technology is available, but the design details must be resolved and the hardware developed. A gas generator that mounts on the valve plenum, eliminating the hot-gas delivery tube, would also be a significant improvement. An appropriate

thermal-type gas generator could withstand the vibration environment of the engine, and its volume and weight could be combined with that of the plenum.

It appears that the most promising direction for optimizing the concept is to strive for higher pressure ratios across the engine (plenum to ambient); by this means, the theoretical work produced by the engine is maximized and the size required in the plenum and valving is minimized. The only offsetting effects are the leakage across the valves during the closed portion of the cycle and extra mechanical loading during opening. The results to date indicate, however, that these problems should not be serious, and pressures as high as 20 684 kN/m^2 (3000 psi) might be used.

Also, the use of very large bore to stroke ratios (2.0 or greater) should prove attractive because very large valves can be used and correspondingly smaller lifts. This technique enables an increase in engine speed with corresponding decrease in size and weight. It also enables building a stiffer engine mechanism so that higher pressures can be used. If the engine weight is reduced, the optimization of displacement and expansion ratio outlined in the design discussion is driven toward larger expansion ratios, which result in a more efficient overall design.

A mathematical model constructed to encompass all aspects of the engine operation and design will enable quick, easy optimization for any particular application. Testing of various designs as they evolve will refine the model. Hot-gas and vapor-cycle expanders using low-grade heat are finding increased applications because of the continued changes in the basic energy supply. This engine concept offers one additional design alternative for power system selection; its mechanical simplicity provides good economic viability.

DESIGN AND DEVELOPMENT OF A MOTION COMPENSATOR FOR THE RSRA MAIN ROTOR CONTROL

P. Jeffery*, R. Huber*

ABSTRACT

The RSRA, an experimental helicopter developed by Sikorsky Aircraft for NASA and the U. S. Army, is equipped with an active isolation system that allows the transmission to move relative to the fuselage. The purpose of the motion compensator is to prevent these motions from introducing unwanted signals to the main rotor control.

Review of motion compensator concepts indicates that most function only for limited motion. A new concept was developed that has six-degree-of-freedom capability. The mechanism was implemented on RSRA and its performance verified by ground and flight tests.

INTRODUCTION

The Rotor Systems Research Aircraft (RSRA) is an experimental helicopter intended for flight research on advanced rotor systems, designed and developed by Sikorsky Aircraft under the joint sponsorship of NASA and the U. S. Army. Two aircraft have been built. At present one aircraft is in compound configuration, equipped with a variable incidence wing, a moving stabilator and auxiliary thrust fan jet engines (Figure 1). This version will be used for high-speed research on highly loaded or partially unloaded rotors. The other aircraft is configured as a pure helicopter (Figure 2) and will be used for additional research on a variety of rotors. Both aircraft are presently flying with a baseline rotor system virtually identical to the Sikorsky S61 including bifilar vibration absorbers, and the vibrations transmitted to the fuselage are small in all flight regimes. However, it is anticipated that some of the rotor systems that may be mounted on the aircraft in the future will cause vibrations that cannot be alleviated by bifilar absorbers alone. Thus there are provisions for an isolation system that will allow the rotor and its transmission to move on springs relative to the fuselage, so preventing the transmittal of rotor induced vibrations to the fuselage.

The RSRA rotor control is conventional. Cyclic and collective blade pitch are controlled by pushrods attached to a swashplate whose vertical position and tilt about longitudinal and lateral axes are determined by the extension of three hydraulic servo actuators mounted on the transmission base. The signal to each servo actuator is a mechanical displacement transmitted from the cockpit by a set of rods and cranks. When the isolation system is operative, the transmission base is subject to transient and periodic motions relative to the fuselage. With no compensating device these motions would introduce unwanted signals to the servos and so cause collective and cyclic blade pitch changes. Apart from undesirable changes to the flight path, there are obvious possibilities for control coupled instabilities.

*Sikorsky Aircraft Division, United Technologies Corporation, Stratford, Conn.

THE ACTIVE ISOLATION SYSTEM

Various configurations of active isolation were under consideration in the early days of RSRA design. The purpose of the RSRA is to serve as a flying test bed for advanced rotor systems with different dynamic characteristics ranging from two-bladed teetering rotors to hingeless, bearingless, and fully articulated designs. For some applications it was known that extremely soft transmission supports would be required for acceptable isolation, while the total excursion of the transmission under steady loads must be restricted because of the limitations of interfacing systems - in particular engines, tail rotor drive, and controls. The soft restraints were thus provided by 'active isolators' consisting of servo-nulled hydro-pneumatic actuators with displacement feedback to recenter the transmission under steady flight loads while allowing oscillatory motion at the critical vibration frequencies. Other restraints consisted of very stiff pivoted links containing load cells. The number of independent soft restraints determines the number of degrees of freedom of the transmission relative to the fuselage.

During the course of development, a design evolved consisting of four active isolators (two independent) in the horizontal plane, a torque restraint linkage in the horizontal plane, and four load cell links with their axes focused to a point low down on the rotor axis (Figure 3). The active isolation system has been described by Kuczynski and Madden (Ref. 1). This system has two degrees of freedom - or three, when failure modes, e.g., fracture of the anti-torque linkage, are considered.

COMPENSATOR REQUIREMENTS

The preliminary design of the RSRA control system took place while the isolation system was undergoing many iterations. Many combinations and configurations of soft restraints and rigid links were investigated. The decision was made that the main rotor control would include compensating linkages with a full six-degree-of-freedom capability. Thus the isolation system design could proceed without any consideration of restraint imposed by control system requirements. Also, there would be no inhibition of development and reconfiguration of the isolation system at any future time.

The requirement for a control compensating linkage may be simply described. The input control signal is generated by the pilot commanding a displacement between his stick and the fuselage. The mechanical control system linkage transmits this signal to one of the hydraulic servo actuators that position the swashplate and are mounted on the transmission base. If an isolation system is incorporated, the transmission base can move relative to the fuselage. Thus a mechanical displacement relative to one body must be faithfully copied by a displacement relative to a second body, while remaining unaffected by relative motion between the bodies. In the most general case, the motions consist of translations along three mutually perpendicular axes and three rotations about these axes.

COMPENSATOR CONCEPTS

If the number of degrees of freedom are limited, then simple solutions are possible. For example, consider two bodies with relative translational freedom along one axis (Figure 4). A linkage consisting of a crank pivoted at each body and a long rod perpendicular to the axis is an effective approximate compensator, since small motions produce little disturbance to the signal in the rod. This simple idea was the subject of a patent in 1971 (Ref. 2). If the restraint between the two bodies is provided by parallel pivoted bars and the control rod is made parallel to the bar and equal in length, then a perfect compensator results.

If the bodies have translational freedom along all three axes but are restrained rotationally about at least one axis, then a solution is possible consisting of a torque tube, universally connected to the control linkage at each end and having a telescopic feature with a splined or scissors link connection. The control signal consists of rotation of the torque tube. This device, subject of a patent by Durno & Dean (Ref. 3), was used in the Sikorsky XH-59A ABC™ (Advancing Blade Concept) research helicopter, which had provisions for a passive isolation system while being restrained in roll by torque links (Figure 5).

A simple apparent solution to the problem of transmitting a displacement signal between two bodies with complete freedom of relative motion is to use a flexible push/pull cable operating within a flexible conduit. In fact, the best of these devices exhibits more friction and hysteresis than can be tolerated in a primary flight control.

COMPENSATOR DEVELOPMENT

Development of the RSRA motion compensator started with consideration of the problem of transmitting a mechanical control signal between two bodies having relative motion in a plane, i.e., translation along two axes and a rotation about a third axis perpendicular to these two. Thus a solution consists of a summing linkage containing two signal paths in parallel planes (Figure 6). One path transmits the control signal, the other a cancelling signal that removes the effect of the relative displacement between the two bodies. If body 2 is subjected to displacements d_x, d_y and rotation θ_z while a control input c_i is made the total displacement of the control output point is $d_x + c_i$. Hence the output signal $c_o = c_i$ and compensation is achieved. This relationship and the independence of the control output displacement on d_x and θ_z is true at the control signal mid-point and very nearly true for small displacements from the mid-point.

If the mechanism is implemented with self-aligning ball type connections, then this device provides compensation for the case where the two bodies also have translational freedom along the z axis and rotational freedom about the x axis (Figure 7). The control output is independent of the displacement d_z or rotation θ_x and is very nearly unaffected by a combination of these two motions. Rotation about the y axis is another matter. If the distance between the signal path planes is h, then a rotation θ_y will produce a false output signal $c_o = h \sin \theta_y$. It is evident that in order to achieve a full six-degree-of-freedom compensator, it is sufficient to let $h = 0$.

The implication of h = 0 is that the two signal paths occupy the same plane. The first development of this idea is shown in Figure 8. The summing beams are separated and connected by rods, and one beam has become shorter than the other to accommodate a bellcrank. Implementation of the idea to a mechanism designed to fit into the space available around the transmission base after the active isolators had been located led to even more complications (Figures 9, 10). Two linkages are installed at the right side of the transmission and one at the left. Local peculiarities of space and alignment imposed an individual approach at each location and there are no common parts anywhere in the linkages. Also a number of compromises had to be made away from the ideal geometry, each introducing another small error. At this time it was decided to make a new start.

The next development reverted to the basic simplicity of the original concept (Figure 11). In order to bring the signal paths into one plane, the summing linkage took the form of an open frame beam, with the other beam centered inside (Figure 12). Likewise, the two rods take the form of concentric tubular members. It was not possible to attach the outer (cancelling signal) rod to the transmission base at the same point that the inner (control signal) rod attaches to its output crank (Figure 13). This introduces an error, but it is extremely small if the rods are long compared to the attachment offset. For this reason, the rods were aligned horizontally and a bellcrank was needed at the output. The motion of the inner rod is limited by being stepped down 2:1 at the input end and stepped up 1:2 at the output bellcrank.

IMPLEMENTATION OF THE COMPENSATOR ON THE RSRA

Implementation of the motion compensators on the RSRA followed very closely the lines of this concept. A compromise forced by the limitations of space was the inversion of the summing linkage geometry.

The three linkages are similar in configuration and many common parts are used (Figure 14). A number of innovations were incorporated in the detail design of the summing linkages to make these units compact and prevent the possibility of fasteners slackening off and jamming the controls (Figure 15).

True compensation is achieved with the ideal linkage and for small control signal displacements about neutral. The compromises that had to be accepted introduced small errors. Also effective compensation was required over the whole range of control displacements. A criterion was set that the error in output should not exceed 2% full stroke at any control position while the transmission base was subject to motions in any direction up to the maximum stroke of the active isolator (±9 mm) taken in the worst combination of possible configurations. A geometric motion analysis was performed by computer program and performance within specification was determined.

The compensating linkage described was installed on both RSRA aircraft (Figures 16, 17). Only the second aircraft has been configured with the active isolation system operative, and tests of the compensator performance were conducted on this aircraft. The test consisted of setting a control input with a fixed stick in the cockpit and driving the transmission base to extremes of travel on the isolation system, while observing motion at the control output points. The results of these tests confirmed the predictions of analysis.

CONCLUSIONS

The RSRA has made many flights with the isolation system action and records indicate that the motion compensators have functioned to completely eliminate any measurable spurious control signals.

REFERENCES

1. Kuczynski, W. A., and Madden, J., The RSRA Active Isolation/Rotor Balance System, Paper No. 18, Fourth European Rotorcraft and Powered Lift Aircraft Forum, Stresa, Italy, September 1978.

2. Dueweke, J. E., U.S. Patent 3,563,499, Mechanism to Transfer Engine Torque and Control Motion Across Helicopter Rotor Vibration Isolator.

3. Durno, R. A., and Dean, J. C., U. S. Patent 3,908,399, Primary Flight Control With Isolated Gear Box.

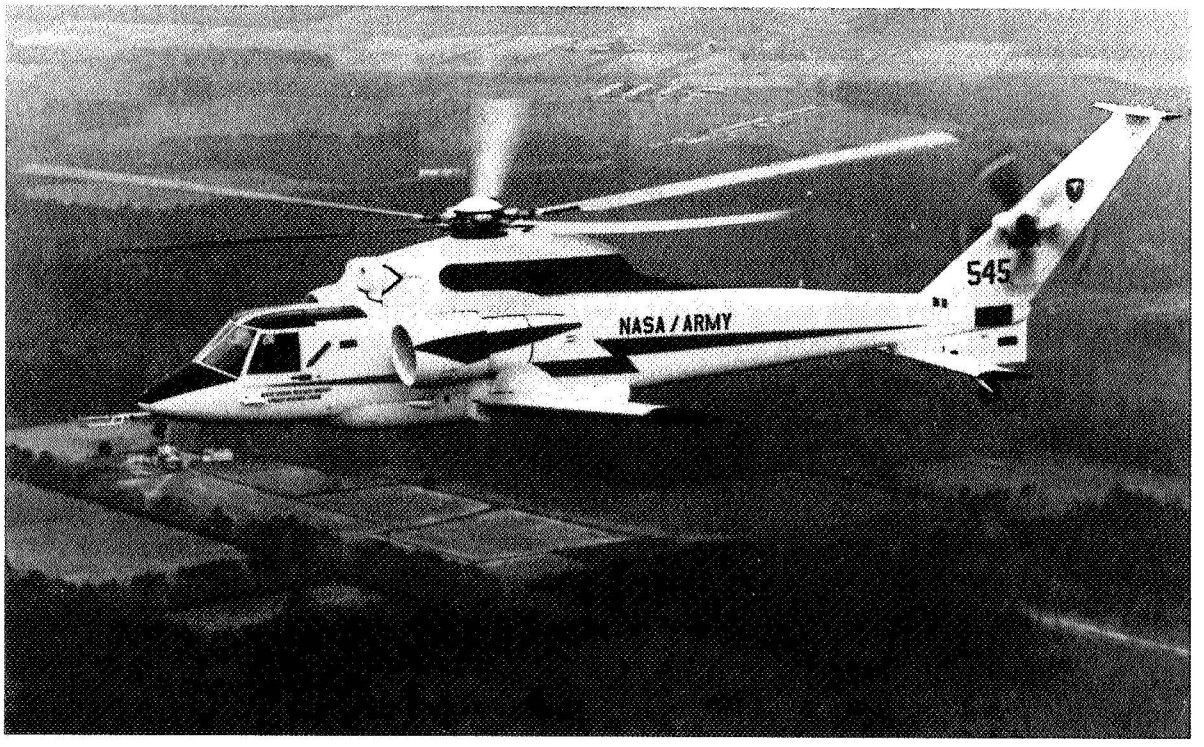

Figure 1 RSRA Compound Configuration

Figure 2 RSRA Helo Configuration

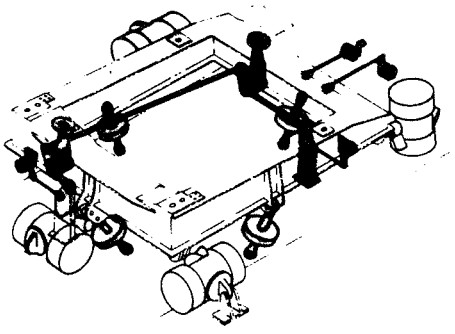

Figure 3 RSRA Transmission Active Isolation System

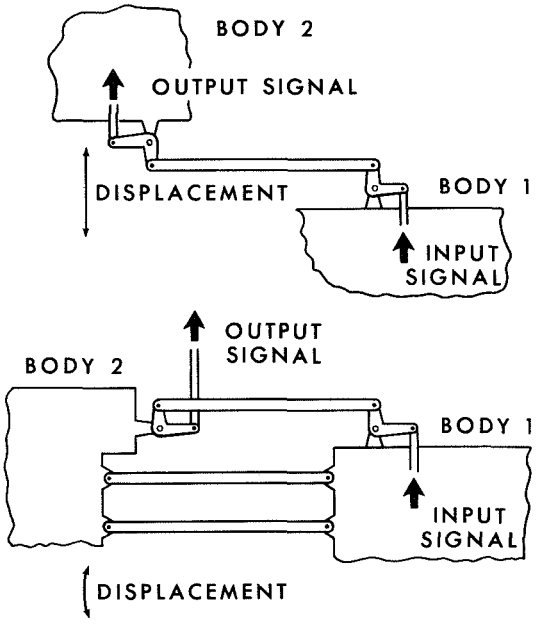

Figure 4 Compensator Concept - Linear Motion

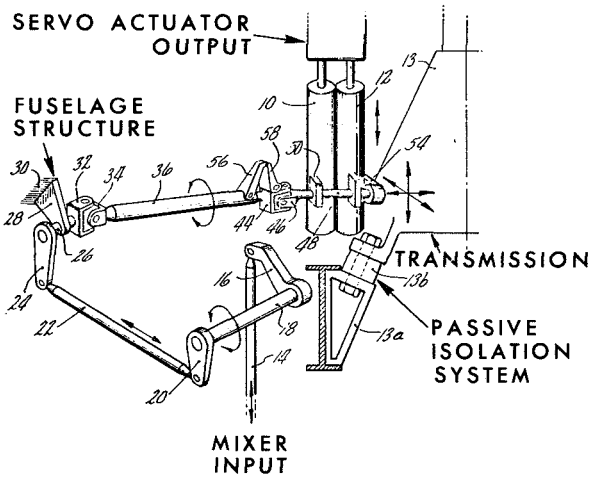

Figure 5 Controls Motion Compensator on Sikorsky ABC

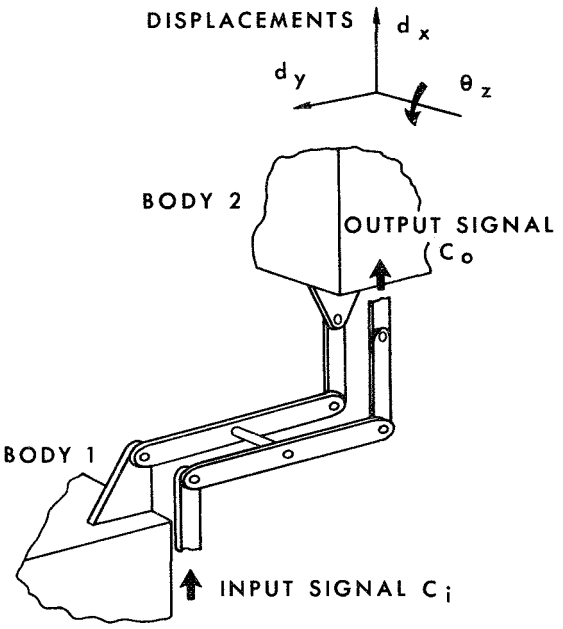

Figure 6 Compensator Concept - Plane Motions

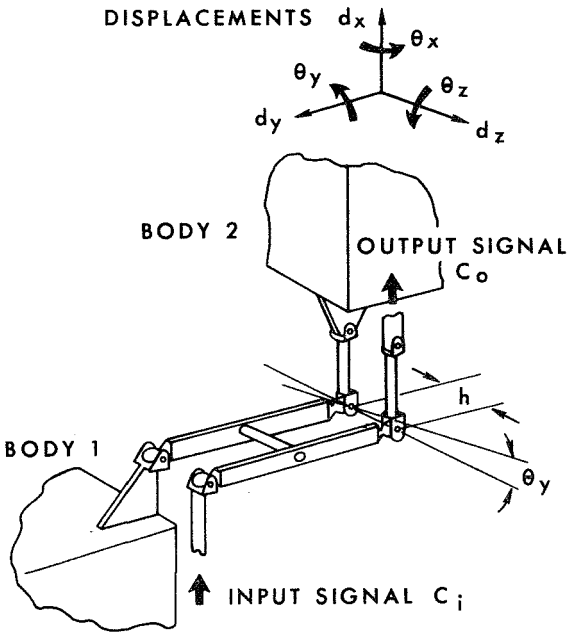

Figure 7 Compensator Concept - General Motions

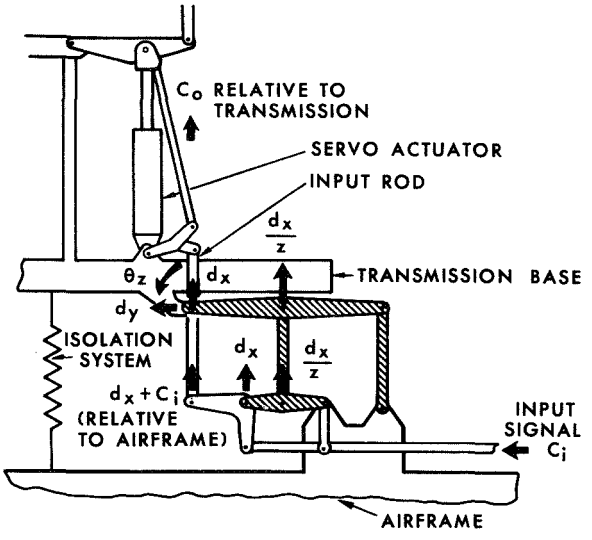

Figure 8 Compensator Concept Applied to RSRA

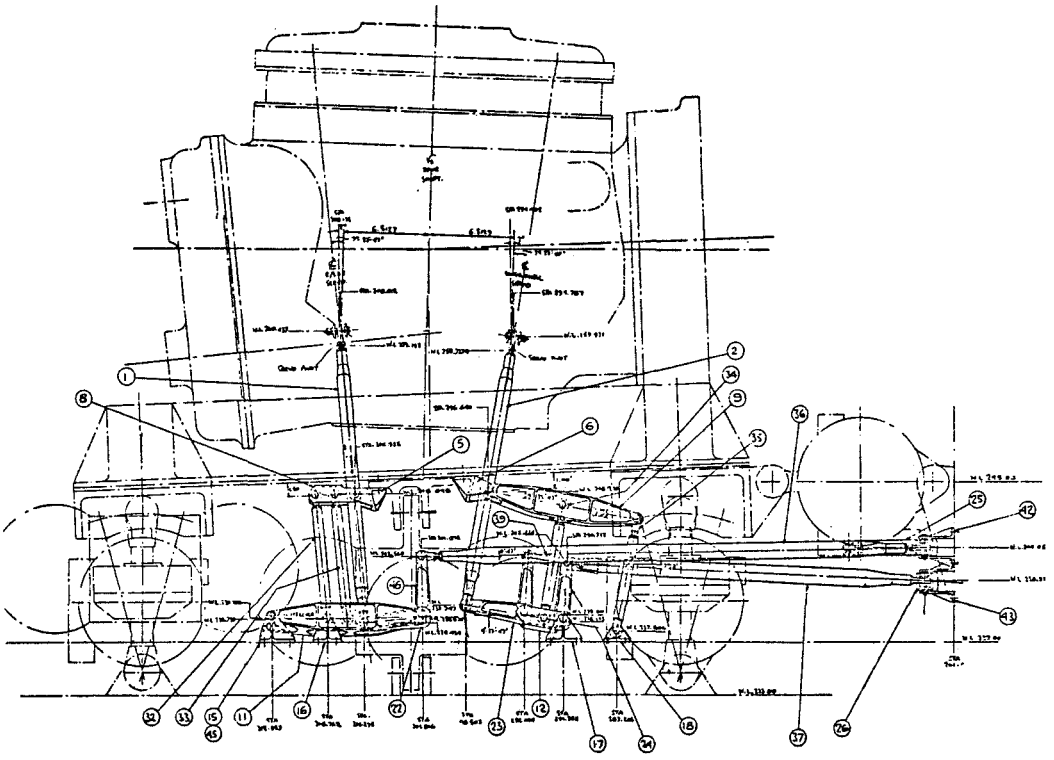

Figure 9 Preliminary Design for RSRA Motion Compensator - Right Side

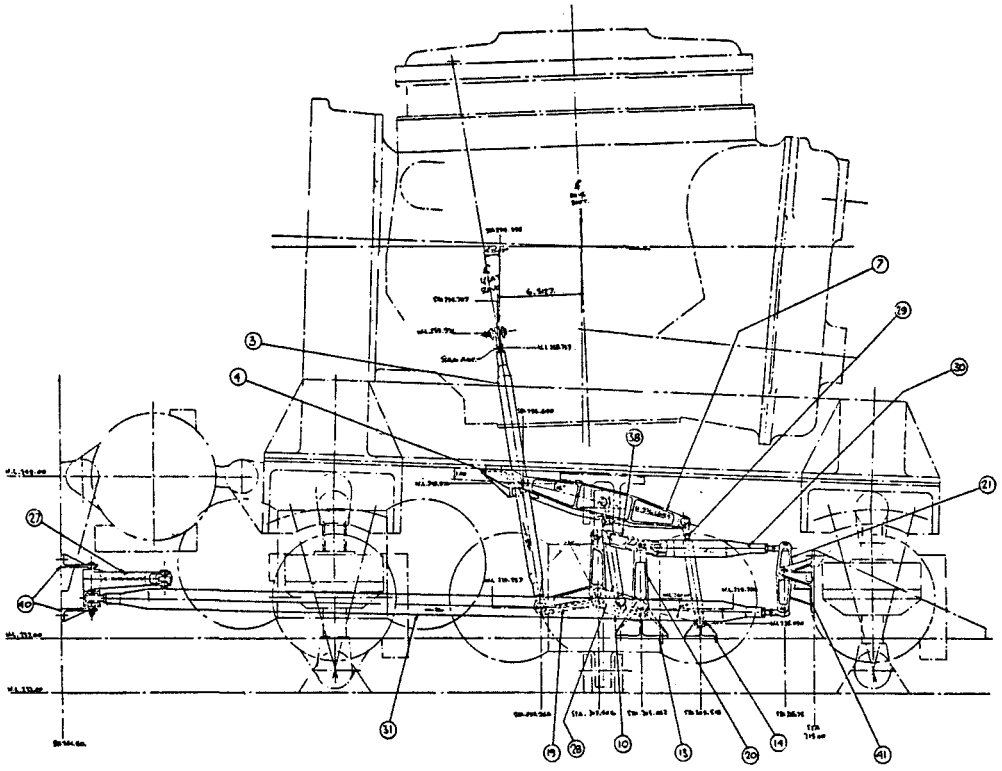

Figure 10 Preliminary Design for RSRA Motion Compensator - Left Side

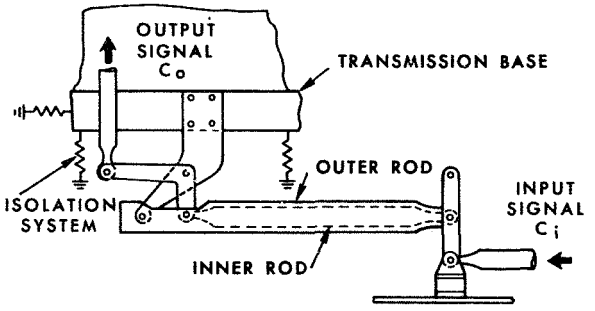

Figure 11 Revised Concept for RSRA Motion Compensator

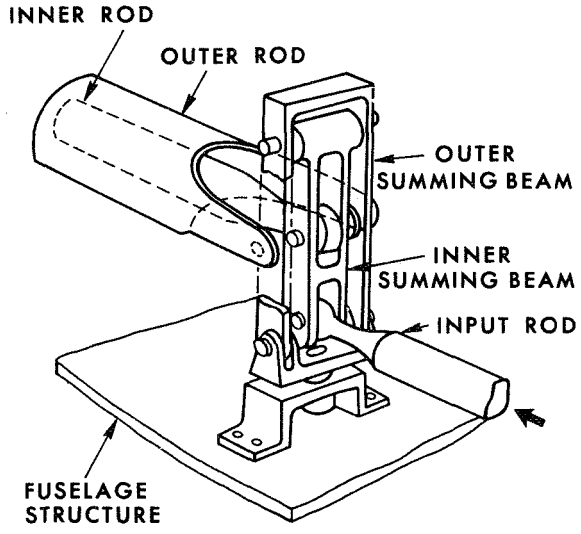

Figure 12 Revised Concept for RSRA Motion Compensator - Input and Summing Linkage

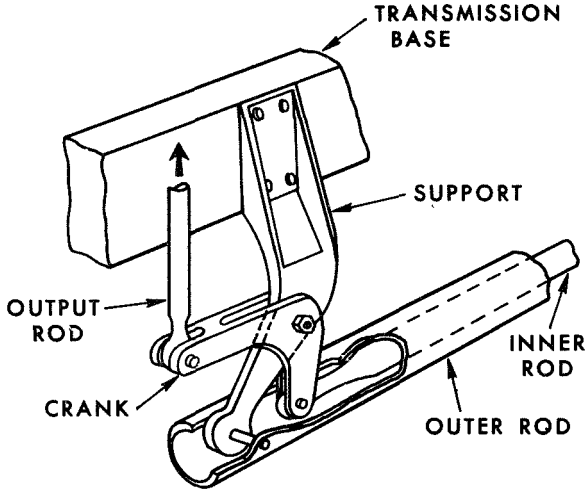

Figure 13 Revised Concept for RSRA Motion Compensator - Output Crank

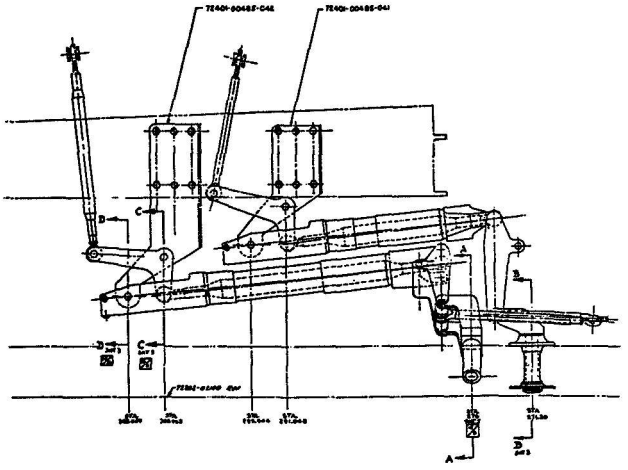

Figure 14 Final Design - RSRA Motion Compensator

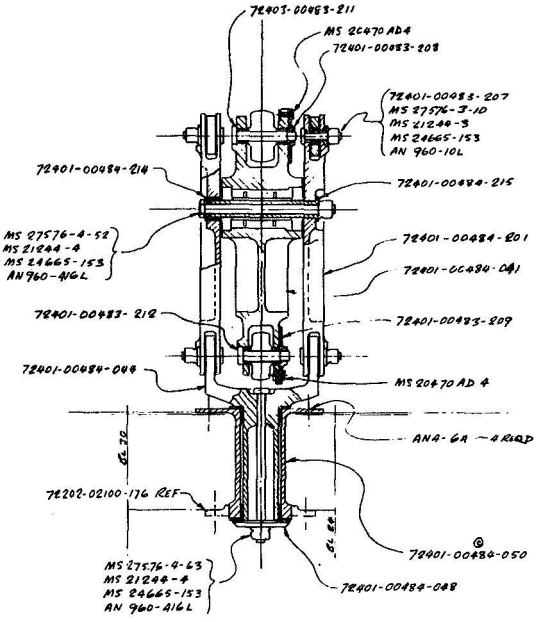

Figure 15 Final Design - RSRA Motion Compensator - Detail

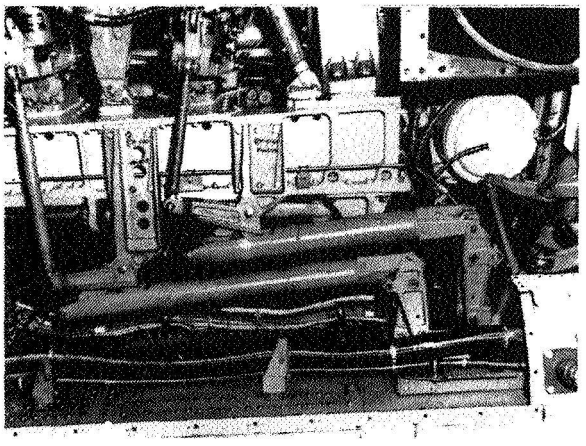

Figure 16 Motion Compensator Installation on RSRA

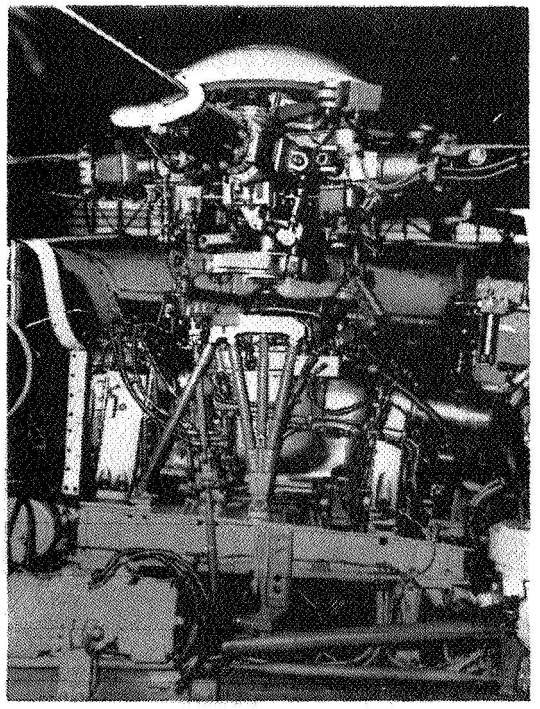

Figure 17 The RSRA Main Rotor and Transmission, Isolation System, and Flight Controls

A TWO AXIS POINTING SYSTEM FOR AN ORBITING ASTRONOMICAL INSTRUMENT

R F Turner - J G Firth

SRC Appleton Laboratory Astrophysics Research Division, Culham Laboratory, Abingdon, Oxon, OX14 3DB.

A B S T R A C T

The system described has been built for incorporation into a solar flare X-ray instrument due to be orbited as one of a number of instruments on the NASA Solar Maximum Mission (SMM) satellite in late 1979. It enables the instrument to be rotated about 2 mutually perpendicular axes in 5 arcsecond steps within a range of 7 arcminutes, thus giving the instrument the capability to map areas of the sun.

INTRODUCTION

The instrument for which the system was designed is a seven channel Flat Crystal Spectrometer (FCS) (Figure 1), and is the result of a collaboration between the Appleton Laboratory (Astrophysics Research Division, Culham) U.K., Mullard Space Science Laboratory U.K., and Lockheed Missiles and Space Corporation U.S.

Although the spacecraft has the capability to point at a flare region on the solar disc, the multiplicity of instruments on board implies that mapping requirements be met by individual raster systems. Spacecraft constraints in terms of mass and accommodation led us to choose a "flat pack" raster platform for this X-ray instrument. Similarly a constraint upon conduction transfer (virtually all heat generated or absorbed has to be radiated to the spacecraft wall) led to the selection of a low power raster system which could maintain its pointing in the unpowered mode.

It is anticipated that misalignment between instrument and spacecraft due to launch forces could be about 1 arcminute. The operating range of the system is designed to encompass any such misalignment.

Although originally conceived as a modular design, instrument and spacecraft needs (particularly the minimum natural frequency requirement of 45 Hz) caused the raster system to evolve into an integral part of the instrument.

Essentially the raster system consists of a two-axis flex pivot driven by a cam mechanism via an arm. For the purposes of description the system (Figure 2) can be broken down into five areas:

1) Two axis pivot
2) Raster drive
3) Position readout
4) Launch locks
5) Wiring

TWO AXIS PIVOT SYSTEM

The 5 arcsecond step requirement and the mass of the instrument led us to consider that the vibration environment could lead to problems of brinelling and torque noise with roller bearings, thus the frictionless flex pivot system was selected.

A compact two-axis gimbal platform 9 cm tall was designed around four standard 2.54 cm diameter electron beam welded flex pivots. The arrangement adopted is shown in figure 3. Each axis is formed by a pair of pivots with their inner sleeves clamped in a common yoke. The outer sleeves of the Z axis pair are clamped to the instrument base plate and the outer sleeves of the Y axis pair to the main instrument support structure.

Even though the raster system is latched down for launch it is estimated that the pivot will still carry some 30% of the load. These units can meet this demand and have an inbuilt flexibility which can tolerate structural movements during launch.

Flex pivots can be used up to some 7^{o} without significant centre axis shift so this application requiring only 0.5^{o} rotation is comfortably within the margin.

RASTER DRIVE

The drive part of the system is based upon two separate cam units (one for each axis) with an additional pair fitted for redundancy. These operate on roller followers, flexibly attached to the raster arm (figure 4).

The motors are 200 steps/rev. devices with 2 centre tapped windings driven in single phase mode so that powered and unpowered rotor positions coincide. They are of double ended shaft configuration and were specified with high detent torque to resist angular displacement in the unpowered state.

A cam is fitted to the forward end of each motor and an absolute 200 position/rev. shaft angle encoder to the other. The cam profile is such that 1 motor step will cause the instrument to move by 5 arcseconds. The drive circuitry contains a re-triggerable one-shot multivibrator which ensures that 60 milliseconds after the last clock pulse, power is removed from the motor.

In order to minimise power consumption all circuitry, with the exception of the motor power drivers, was built using CMOS. The power dissipation with no motors running is about 140 mW.

Mechanism

The drive principle is shown in Figure 5. Both drive units (Z and Y) are anchored to the base plate and are so arranged that each drive unit when operating utilises the other as a slide for the raster arm. The principle is that only one axis (Z for example) is active at a given instant. Of each drive unit, one stepping motor remains dormant while the other lifts a second order lever, pivoted at the contact with the dormant cam, to raise or lower the raster arm. The Y unit cam followers are required to ride over the cams but without deflecting the raster arm. This is achieved by opposing the cams so that as one follower rises the other falls, giving a zero net deflection at Y.

The cams are provided with sufficient lift so that should the first motor in any pair fail in the active range, then the other still has the capability to cover the operating region. The followers are kept in contact with the cams by spring force and the raster arm has a built-in adjustment capability to allow correction of tolerance build-up during assembly.

POSITION SENSING

Although the mode of control is step instruction from the on-board computer, three additional systems enable a check to be maintained on the memory accuracy. Together they provide a considerable capability for diagnosis of a system malfunction in orbit.

Shaft Angle Encoders

Each of the raster motors is equipped with a 200 position/rev. absolute encoder. The purpose of these is twofold:-

(a) To verify that the motor has in fact moved to the location commanded.

(b) To enable set up in orbit.

The assumption was made that the position of each cam cannot be determined with any certainty after the spacecraft is inserted into orbit. The possible permutations of the four cam positions could be unscrambled from the transducer and/or alignment sensor, given sufficient real time access to spacecraft and data. The far more realistic solution employing a shaft angle encoder on each cam has been utilised, the benefits of which have been noted when setting up even in the laboratory environment.

Position Transducers

Two strain gauge transducers are mounted across the raster platform flex pivots. They are arranged in such a manner that one measures angular movement between the instrument and the baseplate in the Y axis only, and the second detects similar shifts in the Z axis. The output from each

transducer is amplified and fed into an 8 bit Successive Approximation A to D convertor. The convertor output is in Natural Binary code, and the system gain is such that a single step of 5 arcsec causes a change of 1 in the output count.

Solar Sensor

The X-ray instrument is fitted with a solar sensor which can detect limb (edge of the solar disc) crossing to an accuracy of 5 arcseconds. With this information compared to the spacecraft solar pointing co-ordinates we can off-set the instrument to co-align with the spacecraft boresight.

LAUNCH LATCH

The purpose of the latching system is to carry the launch loads and to hold the raster followers clear of the cams. This area more than any other was the subject of on-going design evolution during instrument development. The original pin release system proved to be inadequate in the light of increased instrument mass and substantial finite element structural analysis of the instrument when subjected to the NASA environmental test requirements. The system shown in figure 6 was developed and meets the structural requirements.

The instrument is latched onto the baseplate by four clamps, each of which is held closed by a titanium tie bar. The latches are released by firing a pyrotechnic guillotine which cuts through the bar. The clamp arms are spring loaded so that when the bar is severed, they move apart. As a back-up a second guillotine is installed on each bar but this will not be fired unless the primary fails.

The latch mating surfaces are coated with a thin film of PTFE to reduce the possibility of binding.

WIRING

With light forces and precise positioning of the system, the need to carry some 200 wires across the raster interface can cause problems with harness stiffness and wind up during vibration.

The system evolved in figure 7 has proved most successful. All large bundles were split as shown. Several cables containing 3 or less wires were left intact but the effect of their stiffness was minimised by placing the thickest bundles nearest the pivot. The whole assembly was relaxed in the desired position by heating to $\sim 100^{\circ}C$.

The flat loop configuration attached at each end to the instrument and to the base plate has been shown to produce insignificant loads and has remained constant throughout environmental testing.

ACKNOWLEDGMENTS

The system described was designed and built with the assistance of our colleagues in the Engineering Group of the Astrophysics Research Division to whom full credit must be given.

Additionally we wish to acknowledge the role played by the consortium's three Principal Investigators, Dr. A. H. Gabriel, Dr. J. L. Culhane and Dr. L. W. Acton in setting the goals and providing constructive comment en route.

TABLE 1

SYSTEM CHARACTERISTICS

Mass of instrument (on raster platform)	100 kg
Raster pattern required	5 x 5 arcmin
Allowance for changes in spacecraft structure	2 x 2 arcmin
Designed scan size (with redundancy)	7 x 7 arcmin
Designed scan size (without redundancy)	28 x 28 arcmin
Single step size	5 arcsec
Accuracy (positioning)	1 step
Step rate (maximum)	32 steps/sec
Peak running power (at 32 steps/sec - fast reposition mode - 2.7 seconds max.).	6.5 watts
Data gathering mode (4 steps/sec)	0.78 watts

TABLE 2

COMPONENT SUMMARY

ITEM	MANUFACTURER	DESCRIPTION
Flex Pivot	Bendix, Utica, N.Y.	2.54 cm dia Electron beam welded.
Transducer	Kistler Morse, Seattle	Strain gauge type
Raster Motor	C. D. C., Los Angeles	Size 15 double ended 200 steps/rev. high detent
Shaft Angle Encoder	Moore Reed, Hungerford, U.K.	200 Step/rev. absolute, contacting
Guillotine	Holex, Holister, Cal.	Special version to cut titanium bar.

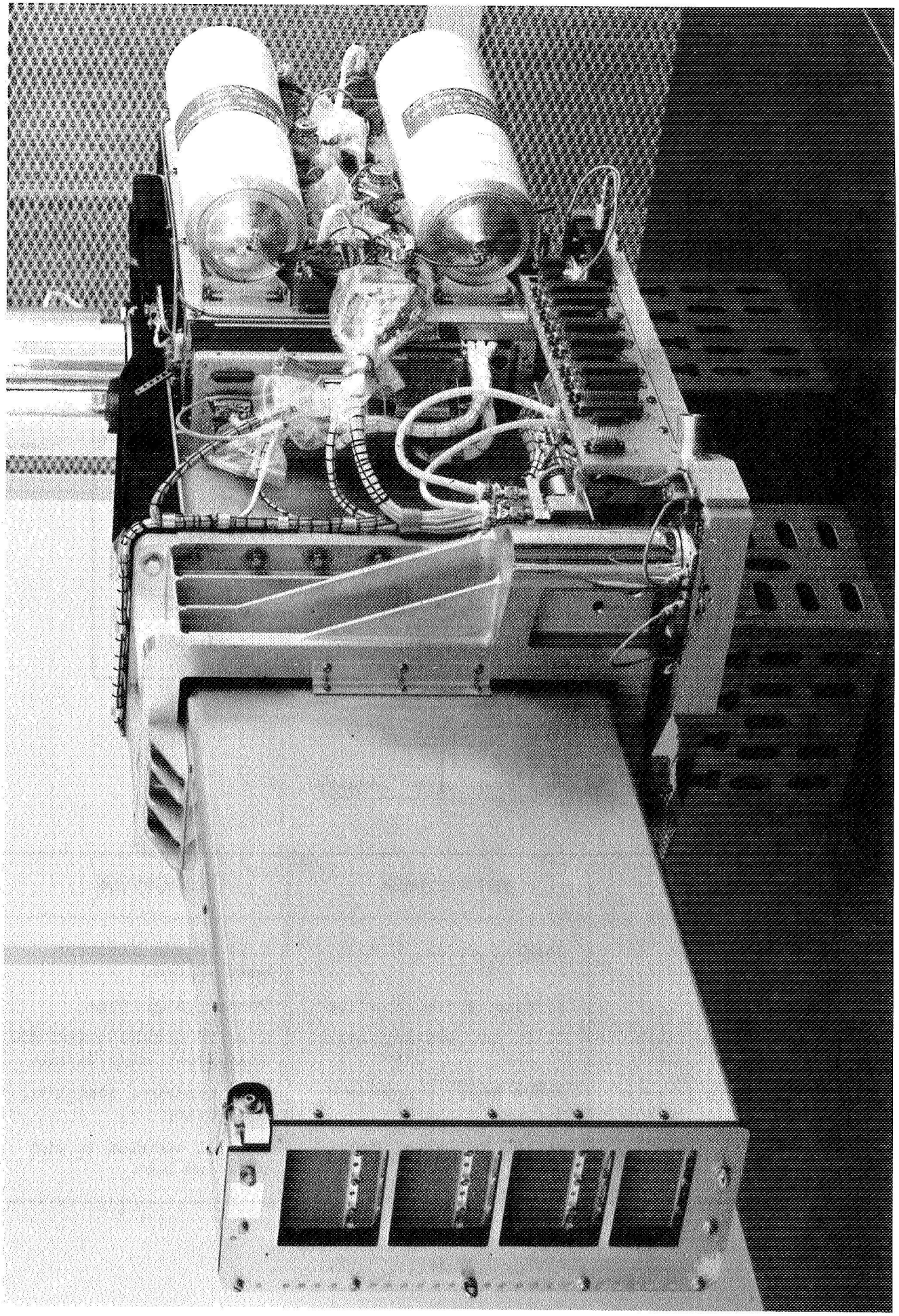

Fig. 1 FCS Instrument

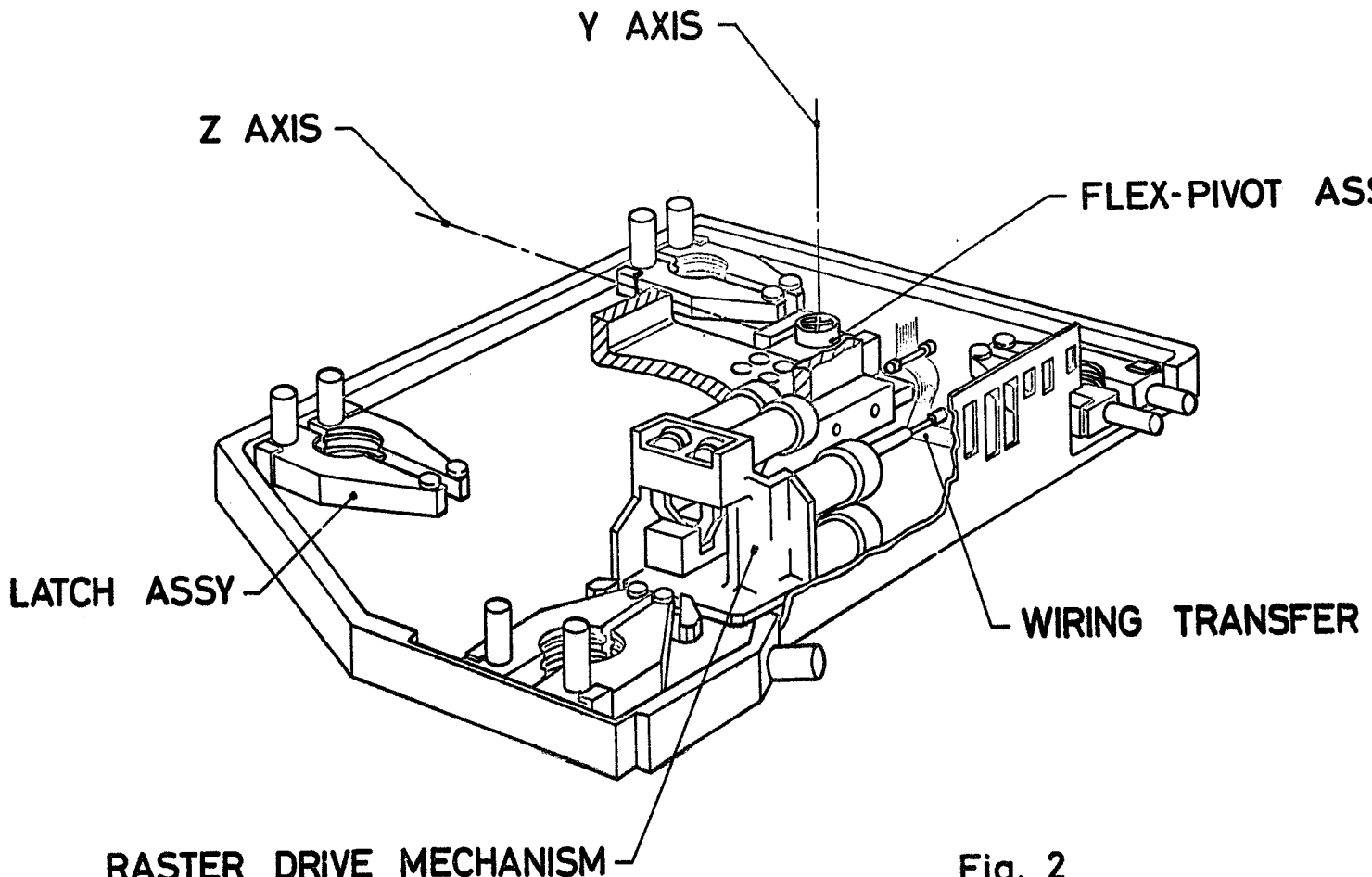

Fig. 2

Raster System

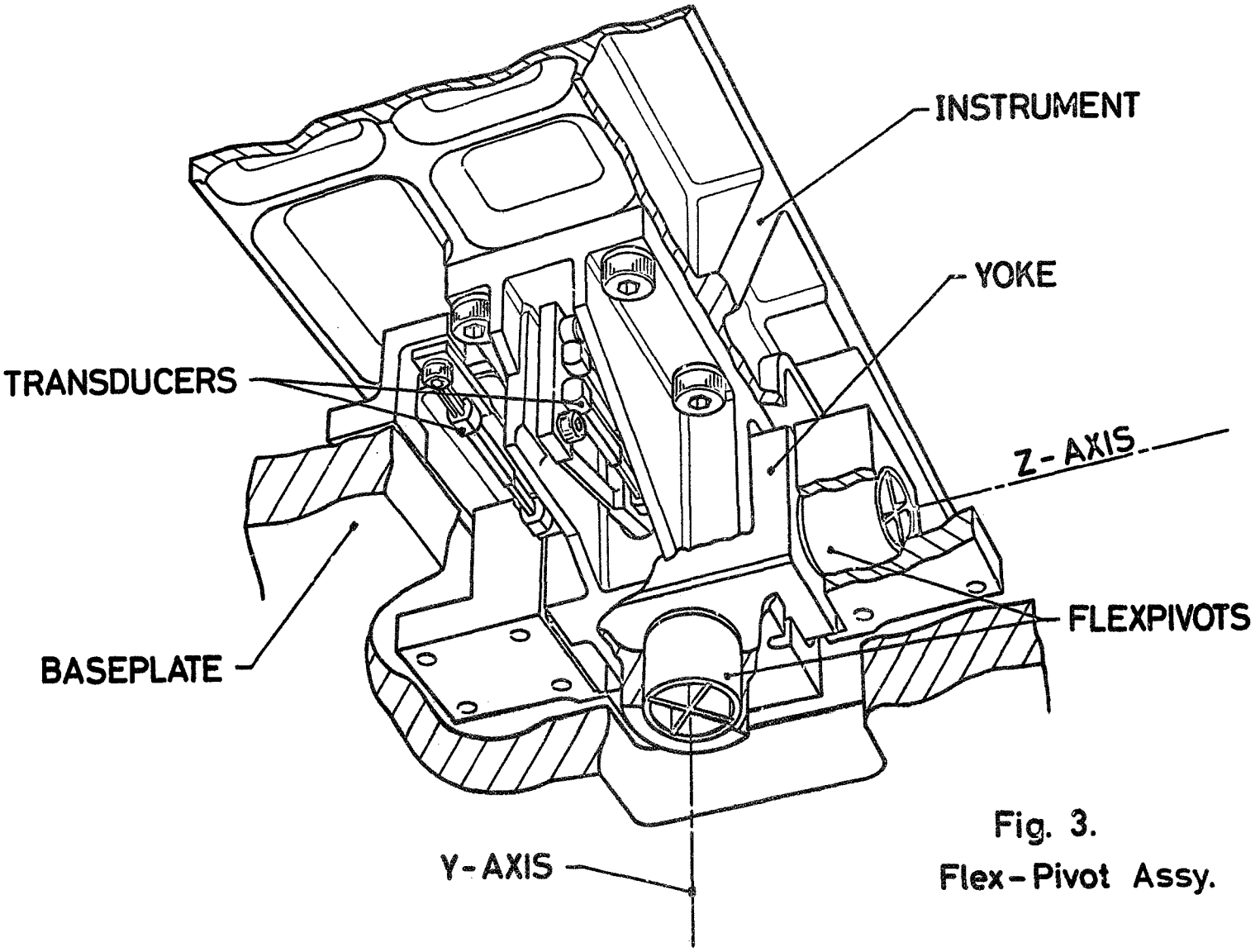

Fig. 3.
Flex-Pivot Assy.

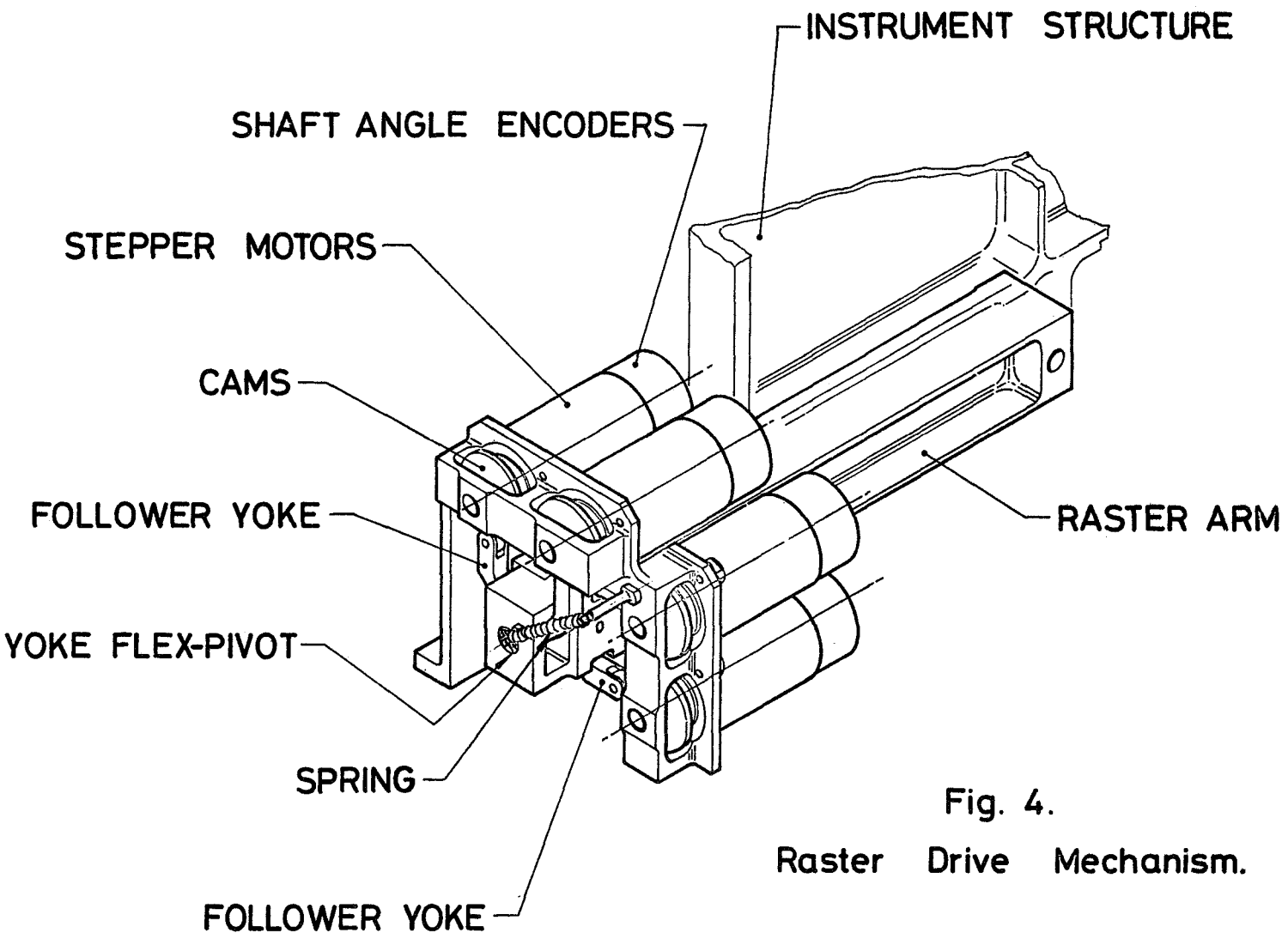

Fig. 4.

Raster Drive Mechanism.

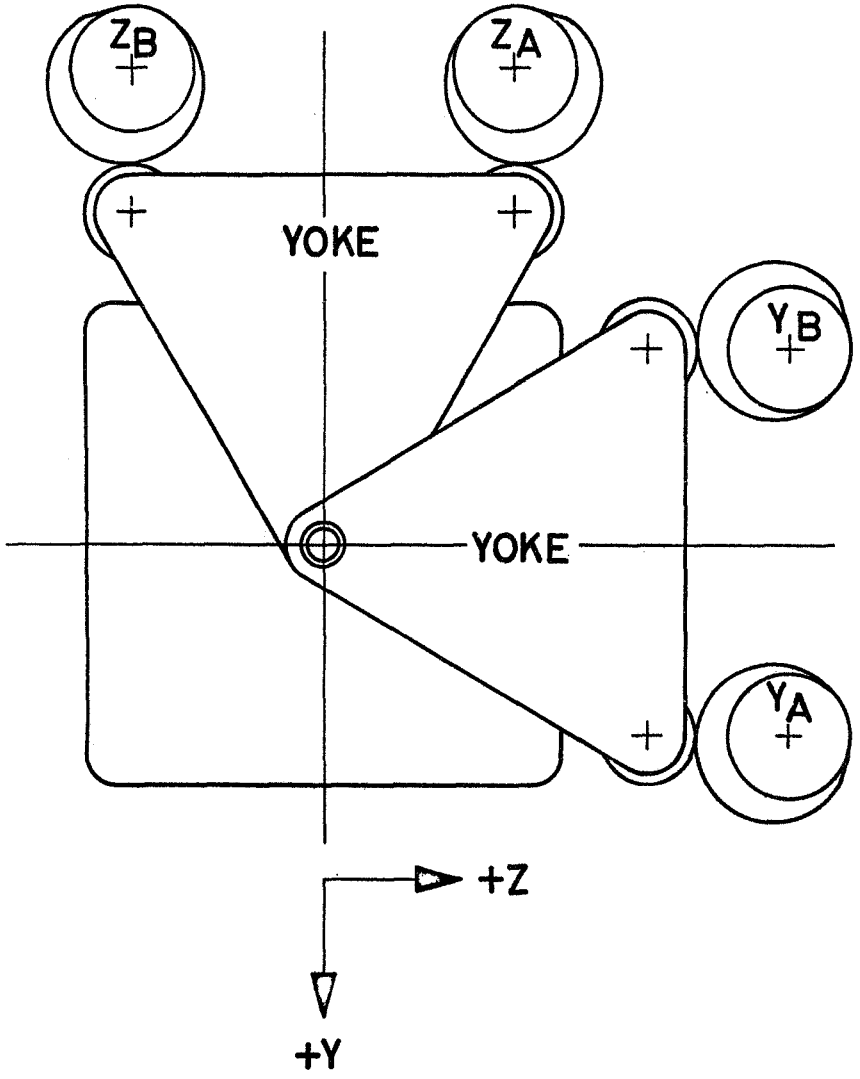

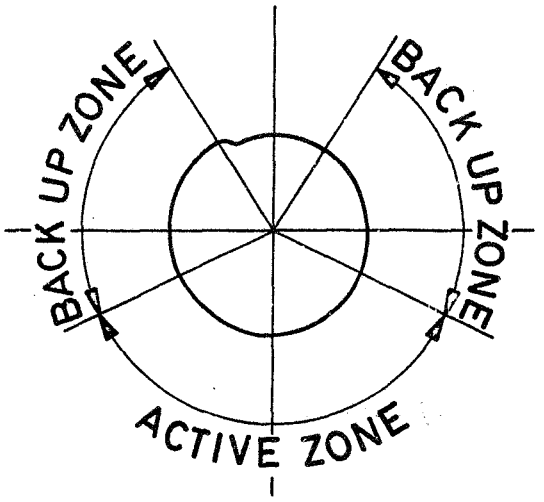

Cam Profile

Fig.5.

Principle of Raster Mechanism.

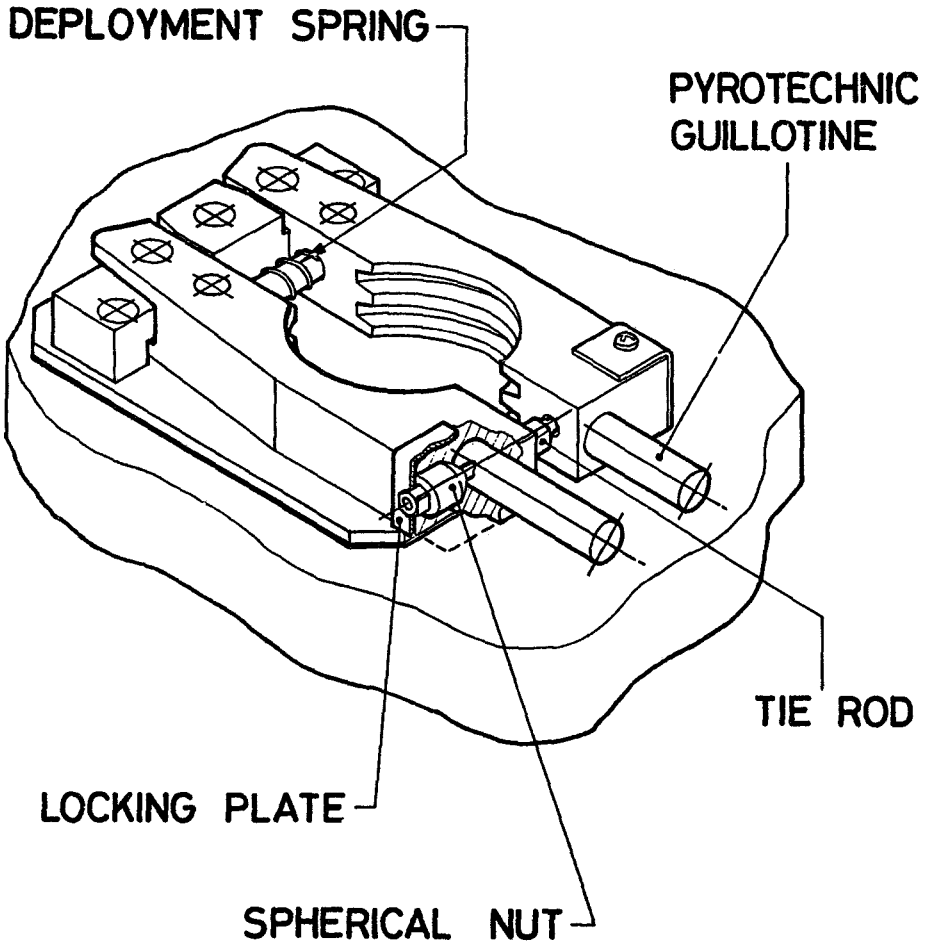

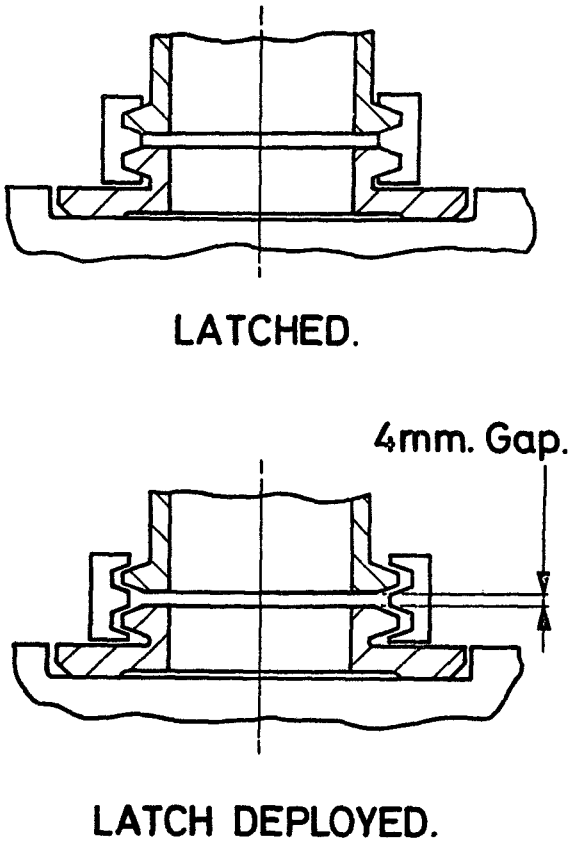

Fig. 6.
Launch Latch.

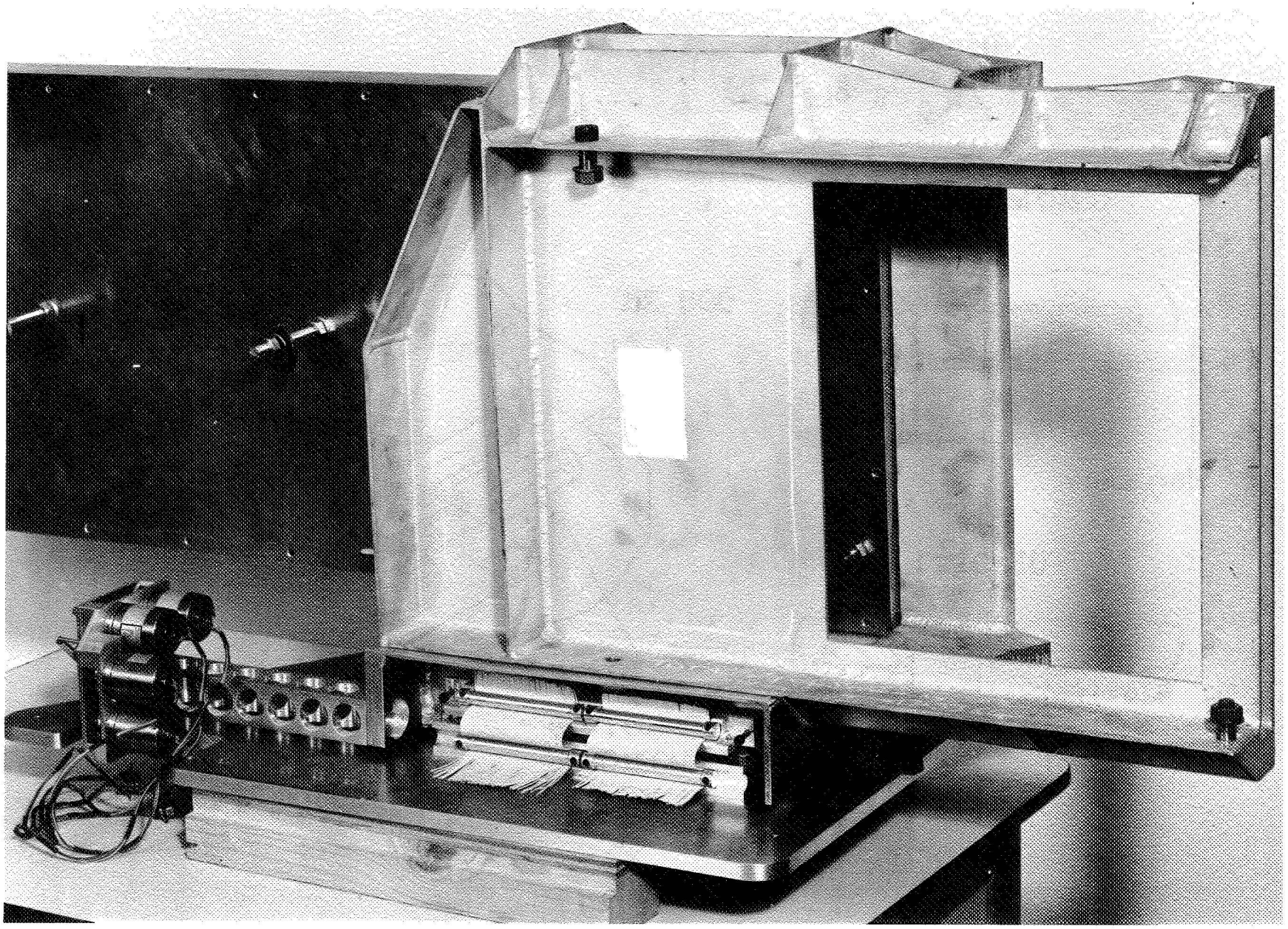

Fig. 7 Wiring Detail

DEVELOPMENT OF THE TRIDENT I AERODYNAMIC SPIKE MECHANISM

By Mark D. Waterman and B. J. Richter

Lockheed Missiles and Space Company

ABSTRACT

The Aerospike drag reduction mechanism was designed and developed for use on the Trident I submarine launched ballistic missile. This mechanism encounters a unique combination of environments necessitating unique design solutions to ensure satisfactory operation over its design life. This paper traces the development of the Aerospike emphasizing the unique and interesting problems encountered and their solutions.

INTRODUCTION

The Aerodynamic Spike (Aerospike) is a deployable drag reducing mechanism stowed within the nose fairing of the Trident I submarine launched ballistic missile. This mechanism maximizes missile performance within the limited envelope available by transforming the aerodynamic characteristics of a blunt, space efficient nose fairing into a more streamlined shape.

The Aerospike mechanism is comprised of three subsystems which perform three separate and distinct functions: The mechanical inertial initiator (I^2) discriminates the correct missile flight acceleration and initiates a gas generator; the gas generator provides the energy for deployment, and boom segments which once deployed and locked, establish a region of separated flow which provides the induced drag reduction. The Aerospike is required to be maintenance- and service-free over a ten year design life. Initiation and Deployment of the Aerospike occurs just after the missile is launched; after the missile leaves the atmosphere the Aerospike is jettisoned along with the nose fairing approximately 2 minutes after missile launch. The major components of the Aerospike are shown in Figure 1.

The Aerospike is now in production after a four year development program culminated by eighteen consecutive successful flight tests.

ACCELERATION SENSING

The first task of the Aerospike is to detect the correct flight acceleration profile and to ignite the gas generator at the proper time. An all-mechanical approach was selected for this function as the Aerospike is completely isolated from the missile electrical system due to its position in the nose fairing, which is subject to numerous installation cycles. The inertial initiator must also remain safe when subjected to a variety of transportation/handling environments of short term acceleration, vibration,

shock, and temperature/humidity extremes as well as the long term low level vibration encountered in the submarine launch tube. The inertial initiator must possess good aging characteristics as it is not tested or serviced once it is installed in the Aerospike; it must be flight ready over its 10 year design life.

The components of the inertial initiator are shown in Figure 2. A spring mass system senses missile acceleration and releases a timer once the correct acceleration level has been reached. Torque generated by a watch-like mainspring drives a timer escapement. After the correct time interval has been achieved, a spring-driven firing pin is released to ignite the gas generator. If the acceleration is removed before firing pin release, the unit will reset in less than one second. Figure 3 delineates the "must fire" regime of the inertial initiator; the inertial initiator will not fire when subjected to any acceleration outside of the "must fire" environment.

Correct operation of this mechanism is ensured by a series of in-process tests and a final acceptance test in which the "must fire" and "no fire" limit are checked. During development testing it was discovered that the unit would cease to operate properly after only three months of storage. The problem was traced to the lubrication system used and to the low design torque in the mainspring. Various design changes were incorporated to increase the torque margin of the I^2 so that the unit was much less susceptible to friction variations, and a change in the lubrication method was made.

The lubrication system originally used was a combination of the MIL-L-6085 oil for the linear and ball bearings, a dry film lubricant on the timer, and a combination of dry film lubricant and grease for the firing pin release mechanism. Examination of the aged units revealed that this system was unacceptable, mainly due to oil migration which made the unit susceptible to contamination and interaction of the oil and dry film lubricant. The dry film lubricant used in the timer also was a problem due to process variations and the extremely tight tolerances of the timer gears.

The aging problem was solved by reducing the amount of oil to a minimum by centrifuging the bearings, elimination of the grease on the firing pin release mechanism, and a change in the timer lubrication to a Lockheed Missiles & Space Co. (LMSC) developed process of applying dry moly disulfide powder to the part to be lubricated (Molykote Z). This method was chosen after testing showed it to be superior in terms of friction reduction, aging, and ability to withstand repetitive cycling (service life). Table 1 shows the results of the test. No inertial initiator timing anomalies have occurred in the two years after the new lubrication system was incorporated.

Table 1. Inertial initiator timer lubrication evaluation

Lubricant	Friction	Aging	Service Life
Dry Film			
o Everlube 620C	Low	Moderate	Moderate
o Electrofilm 77S	Low	Moderate	Good
No Lubrication	High	Good	Poor
Molykote Z	Low	Good	Good

DEPLOYMENT

The Aerospike is deployed shortly after the missile has reached a sustained acceleration and the deploying boom sections are subjected to a combination of aerodynamic loads, acceleration, and vibratory loadings; in addition to deploying under these flight loads, the Aerospike is ground tested on a centrifuge which imparts a large side load due to coriolis effects. Once deployed, the Aerospike must meet stringent dimensional and structural requirements.

Deployment is accomplished by internal pressures created by the solid propellant gas generator, which acts on the tube sections to overcome static and dynamic friction and external environments. The momentum and forces imparted by the gas force the joint/locking mechanism into the engaged position. Gas pressure initially builds up rapidly until a set of retention bolts fracture, releasing the tube sections. As the tube sections begin moving, the rapidly expanding volume within the Aerospike causes the pressure to decay; after the Aerospike is fully extended, the gas generator continues to build up pressure to ensure that all joints are in the locked position. Under large external loadings the deployment process is slowed sufficiently to require joint engagement due to internal pressure forces alone. Two related problems occurred during early deployment testing: Under ground test conditions the deployment was taking place too rapidly, causing joint structural damage and rebound, and the gas generator was extinguished by impact induced acoustic resonance. These two problems were solved by a complete redesign of the gas generator and modifications to the joint/locking mechanism.

The gas generator extinguishment problem was especially perplexing because the N-5 propellant is used throughout the industry (2.75 inch rocket) and was thought to be well characterized; additionally, the extinguishment phenomena was temperature related, occurring only at low ambient temperatures. The extinguishment problem was traced to acoustic resonances induced by the shocks produced by the joints impacting into place. This resonance caused pressure excursions outside the region of stable burning and extinguishments occurred. Although extinguishment occurred before final extension, the tube sections had sufficient momentum to complete the deployment. Two methods of solutions were pursued: The first was to alleviate the impact shocks through addition of an energy absorbing device in each joint, or to slow down the deployment by reducing gas generator flow rate. The second method was to mechanically break up the resonance in the gas generator through grain design and resonance rods.

Although a number of solutions could eliminate the extinguishment, complete elimination of the pressure fluctuations at joint impact could not be achieved and it was decided that the N-5 propellant was unsuited to this application. A low metalized propellant, Arcite 386 M with 2% aluminum for resonance suppression, was selected and the grain geometry was tailored to deploy the Aerospike more slowly thereby reducing the shock induced resonance as well as the related joint impact damage.

The second major problem was that the deployment was too rapid, causing damage to the joint/locking mechanism and rebound past the locking area. The most severe damage occurred at the innermost joint which is the last joint to impact and carries the greatest kinetic energy; internal gas pressure was insufficient to re-engage the lock mechanism on this joint which has the smallest cross sectional area for the gas to react against. The solution to this problem took three forms; the strength of the joint/locking

mechanism was increased to provide more resistance to impact damage and the locking finger strength was increased to reduce the chances of rebound. The deployment was slowed by decreasing the initial gas generator flow rate and reducing the strength of the retention bolts by 50%, and, finally, the propellant loading was increased by 70% to increase peak pressure to ensure pressure lockup.

Incorporation of the gas generator and the modifications have proven completely successful in solving the deployment problems. Aerospikes have since been tested under a large variety of conditions ranging from static ground tests to missile flight test without an anomaly. Figure 4 compares the two deployments and Table 2 gives a history of Aerospike deployments.

Table 2. Aerospike deployment

Test #	Deploy Time, ms	Peak Velocity in/sec	Peak Pressure psi	Joint Lock
1	75	-	240	No
2	82	-	175	No
3	92	960	177	No
4	138	560	470	Yes
5	118	695	500	Yes
6	135	540	575	Yes
7	136	550	550	Yes
8	137	-	500	Yes
9	123	-	500	Yes
10	120	-	-	Yes
11	138	-	-	Yes
12-18	-	-	-	Yes

Note: 1. Changes introduced at Test 4
2. Tests 12-18 were flight tests

STRUCTURAL

The Aerospike becomes a part of the missile structure after it has been deployed and locked and it is subjected to severe environments during powered missile flight. The primary requirement for the Aerospike is to maintain a first bending mode frequency of 25 Hz to assure overall missile stability. During its two minutes of operation, the Aerospike is subjected to a combination of aerodynamic heating loads that raise parts of the aerospike above 1000°F, compressive axial aerodynamic loads of up to 2300 pounds, and vibratory loads that results in tip accelerations of up to 60 G in the first lateral bending mode.

The Aerospike carries these loads through its joint/locking mechanism as shown in Figure 5. This mechanism, the primary determinant of natural frequency, carries the lateral bending loads through the two interference lands (this loading mechanism has been described in a previous paper, "Structural Evaluation of Deployable Aerodynamic Spike Booms," by B. J. Richter, 9th Aerospace Mechanisms Symposium), while the locking fingers provide the required axial strength. These fingers had to be redesigned after an early test revealed a design deficiency. The locking fingers were fastened to the tube section by pins; the early design had only one pin for every four lock fingers which allowed the fingers to rotate about the retaining pins and slip out of the lock groove. By doubling the number of pins, this rotation was minimized and the axial capability was doubled to about 16,000 pounds - more than five times the flight requirement. Other changes, detailed in Figure 5, also helped increase the axial capability and provided additional capability to withstand the deployment shock and subsequent rebound.

The Aerospike posed a challenge in testing the structural capability because each of the major environments — heat, vibration, and axial loads — affects the natural frequency and axial strength of the Aerospike, the prime determinants of Aerospike acceptability. A combined environments test was devised to apply simultaneously simulated flight loads to the Aerospike. A shaker is used to apply a simultaneous combination of sine and random vibration, radiant heat lamps provide simulated aerodynamic heating, and an air cylinder/cable arrangement applies the simulated aerodynamic compressive load. The Aerospike is subjected to vibration in both the axial and lateral directions, although not simultaneously. Figure 6 shows the results of a typical lateral combined environments test; natural frequency can be seen to decrease as both the vibration level is increased and the skin temperature increases. Data from wind tunnel tests and two instrumented flight tests have shown the combined environments test to be a reasonable simulation of flight environments and the Aerospike has been proven to have structural capability far exceeding its flight loadings due to being designed for natural frequency and heat loadings at the end of flight.

CONCLUDING REMARKS

The Aerospike has proven to be an extremely successful method of improving the range of the Trident I at minimum cost. The unique nature of the Aerospike highlighted the importance of overall system design in mechanisms of this type.

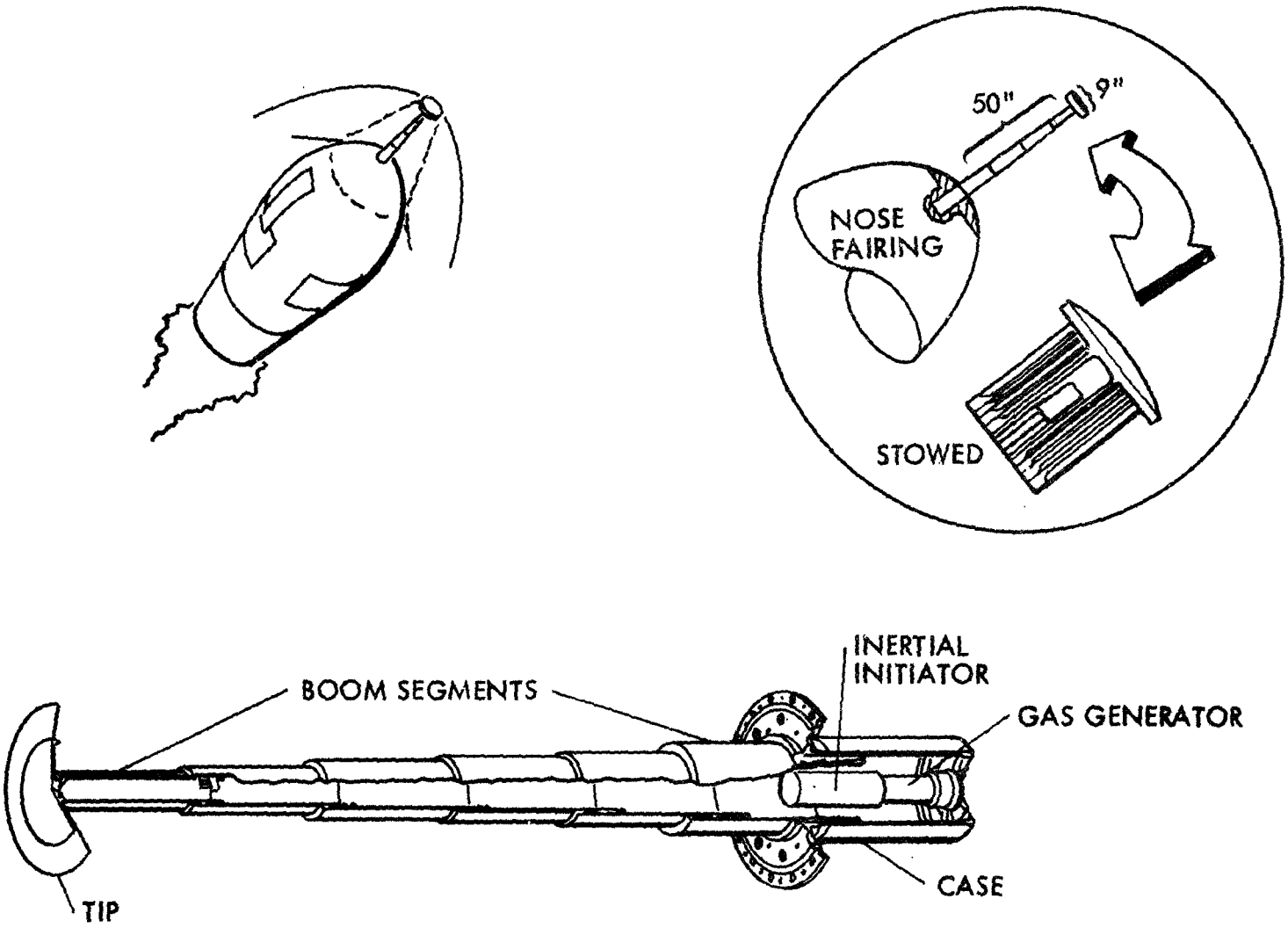

Figure 1 TRIDENT I Aerodynamic Spike

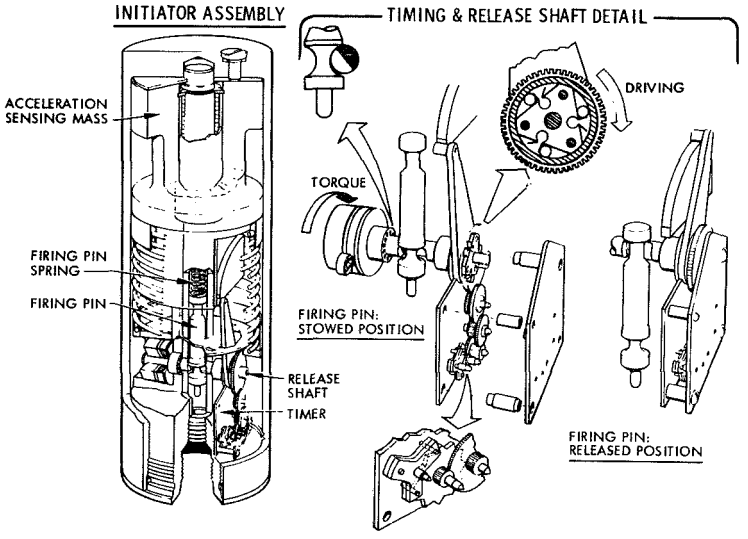

Figure 2 Aerospike Inertial Initiator

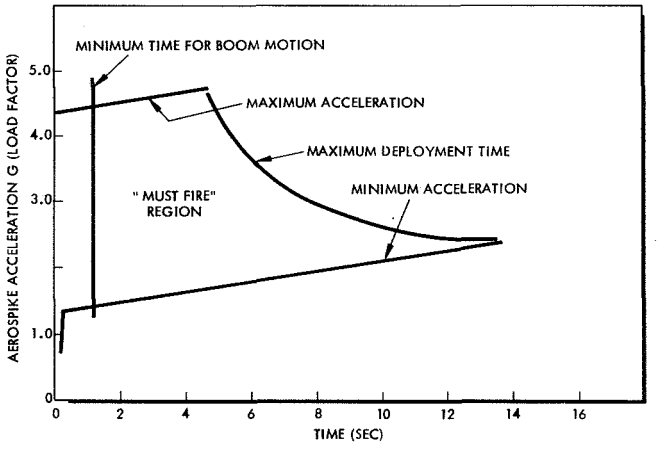

Figure 3 Aerospike Acceleration Initiation and Deployment Requirement

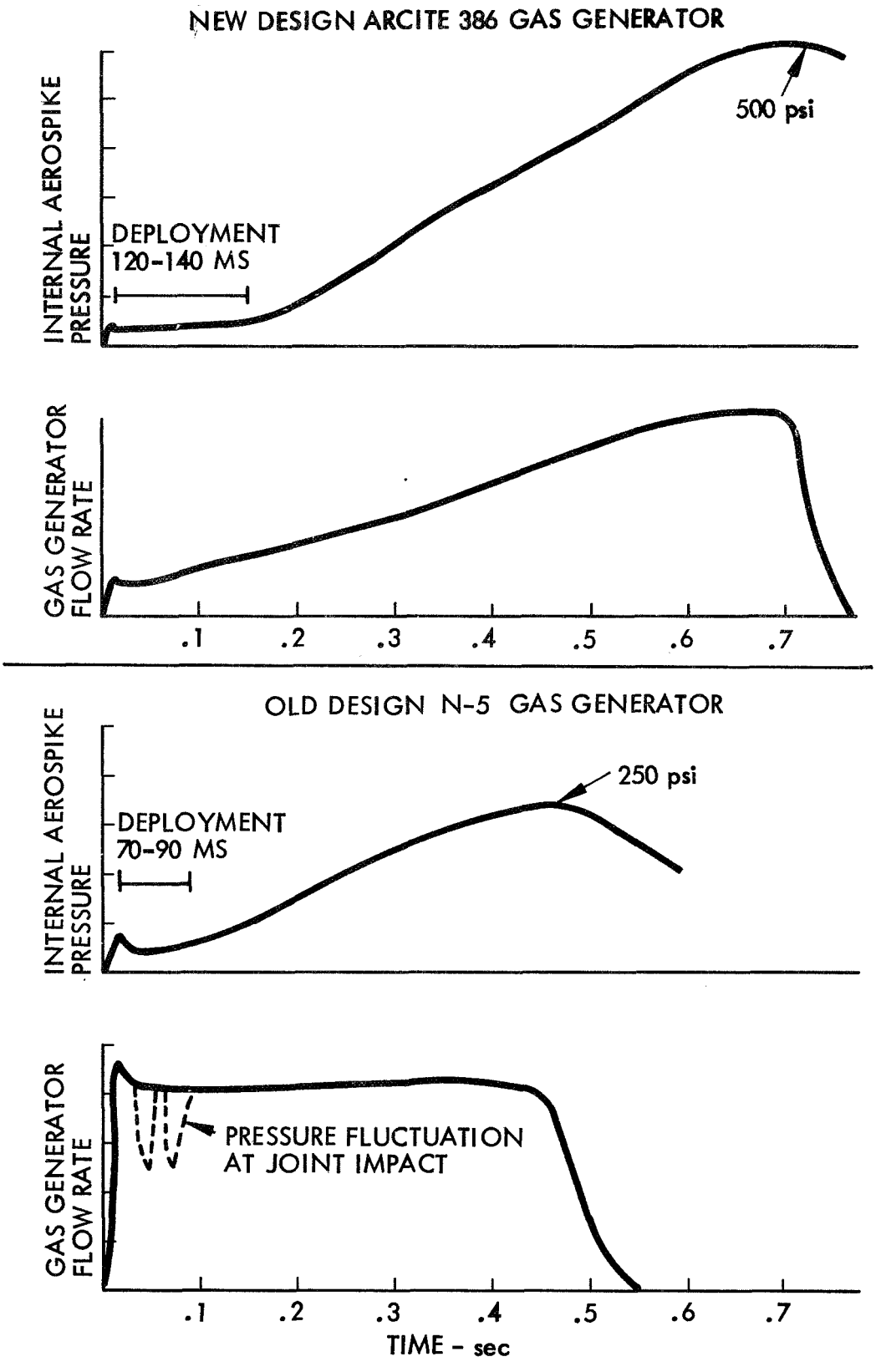

Figure 4 Aerospike Deployment

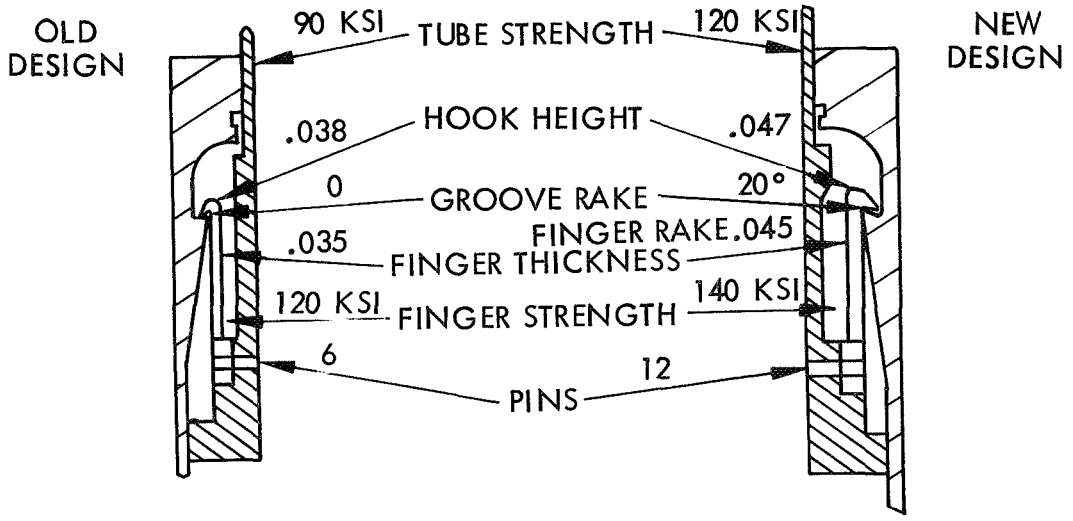

Joint/Lock Design Improvements

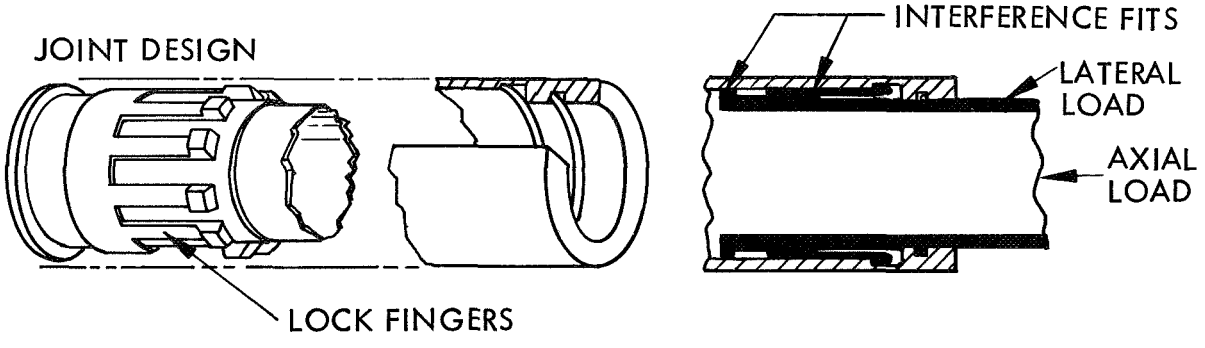

Figure 5 Joint/Lock Mechanism

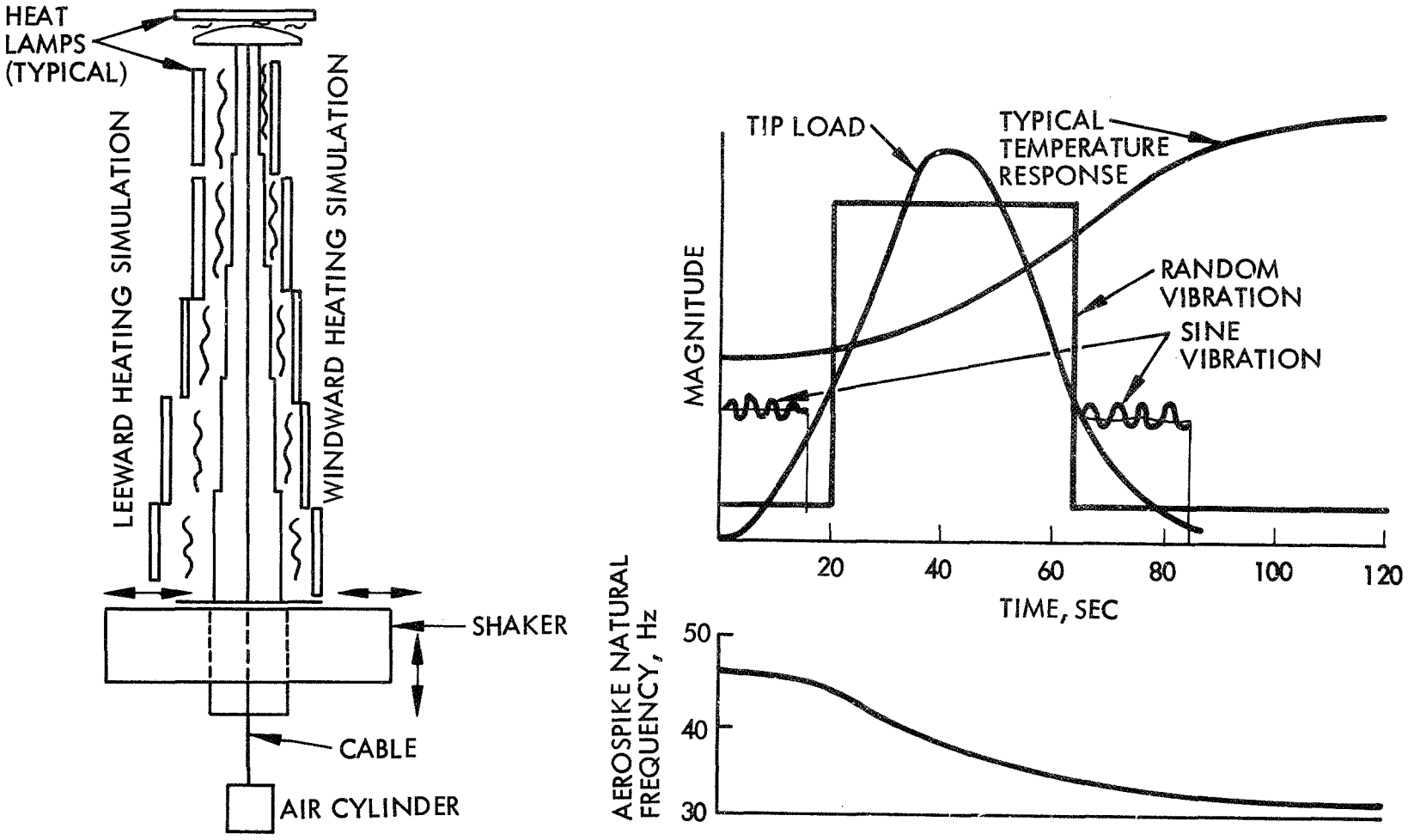

Figure 6 Aerospike Combined Environments Test

A TELESCOPIC JIB FOR CONTINUOUS ADJUSTMENT

By C. Ch. Etzler

Dornier System GmbH

ABSTRACT

For special space applications, e.g. for experiments distant from any orbital platforms or manipulators a new kind of jibs with extreme extension capacity has to be designed. Considering the requirements the telescopic principle is found to be the most promising. For the choice of the stiff structure, design criteria are evaluated. Special effort deals with the drive system. An electromechanical system can satisfy the requirements. First results of the development of such a drive are presented. The most significant features are: A telescopic assembly of tubes which can be mutually moved by a short spindle in the centre of the package. An elastically suspended screw is located at the bottom of each tube. For the jib extension these screws will be linked with the spindle. The control of their sequence and the adjustment of tubes in mutual end positions are performed by latches. A functional model proved the basic idea.

INTRODUCTION

There are fields of activities in space, where the application of extendable jibs is necessary. One field is signified by the requirement to perform experiments in a certain distance of the space shuttle and other orbital platforms. The physical reason is to be free of all kinds of disturbances caused by the platform. Distances between 30 and 50 meters are in discussion as being satisfactory. In other cases the establishment of special geometric positioning of experimental objects is desired. These targets have to be attained without introduction of intolerable inherent jib-dependent new disturbances, and within narrow tolerances for deviations. The other field refers to the construction of large structures in space. In this case the jib shall have the capacity of being the integral part of a manipulator which partly fulfills the task comparable to the function of a human arm amplified in range and force. The jib shall be easy to handle manually or automatically.

Up to now the extendable jibs are not constructed for general application and do not satisfy the whole requirements above circumferenced. This paper presents the characteristic items of a development we are persuaded to content an answer to the challenge set by the aims of space technology. The paper refers to an extendable jib which incorporates the advantage of tailored booms to be optimal in weight and alignment accuracy with the flexibility required for use at manipulators.

DESIGN REQUIREMENTS

For application within the development of the extendable jib the generally formulated requirements given in the introduction have to be formulated precisely to get their rationally provable demands. Signified by head lines these requirements are for the experimental application case:

- large extension range (30 through 50 m),
- large positioning flexibility (continuous extension) with narrow-hold mode tolerances ($< | \pm 2.5$ cm $|$),
- guaranty of alignment within narrow tolerances ($< | \pm 1^{o} |$),
- tolerable dynamic response properties (vibration levels of launch, attitude control loads by vernier and primary thrusters of the supporting platform, preliminarily the space shuttle) regarding the jib strength capacity, the extension functions and control efficiency,
- small storage volume (mainly aspired to be smaller than one space shuttle pallet length) and weight (less than existing — and under restrictions applicable — competitive systems),
- clean environment (no gas, debris or contaminating fluids which could falsify experimental results or hamper their functions,
- easy adaptation to payload interfaces (e.g. development goal 200 kg payload).

The design requirements for manipulators are partly equal, partly not yet animated by final figures. The differences influence sizes or special parameters, e.g. in the case of experiments it is possible to wait up to the elastic vibrations are damped down; for manipulators one desires a behaviour which is nearly equal to the aperiodic boundary case. Nevertheless these differences do not make questionable the main design principle for jib extension.

CHOICE OF JIB STRUCTURE

For unfolding mechanisms several structural principles have proved their capability: the two hinges and the multi hinges booms, the boom built up by stiffly erected continuous material cords and the telescopic booms. Already for reason of the volume demands the first principle has to be excluded. By means of a design based on the second and third principle it is difficult to get the desired stiffness and alignment independently from the extension status. The only principle promising to cover all requirements is the telescopic structure.

The european GEOS satellite was equipped with two pairs of telescopic booms. Structural layout ideas could be expanded to general application. But for their drive system a new mechanism had to be developped to become able to fulfill the requirements. Several reasons (simple power supply, tolerable disturbance of the environment, short and direct methods for control operations) urge to use electric motors for energy feed in.

The conversion of the motor revolution into mutually telescopic tube linear motion is carried out by means of a spindle drive. The advantage and reason for choice is the short way for drive torques in motion and hold phases, e.g. if compared with rope drives. Weight saving reasons favour reception of the drive system in the tube assembly core. Some guiding and latching mechanisms have to work together with the drive.

In the following the whole system will be described. Fortunately this can be done separately for the main functions:

- procurement of stiff structure,
- drive,
- guiding, and latching for hold phases,
- control,
- power and signal transfer.

The two latter functions are only mentioned for completeness and not discussed in detail.

THE STIFF STRUCTURE

The stiff structure consists of an assembly of tubes with different diamter (Fig. 1), which are mounted into one another. They put together nearly fully in the stowed condition and only partly up to a final overlap length in unfolded conditions.

The tubes do not have necessarily a circular cross-section . The triangle too is an interestic shape with some advantages for guiding. The circular shape presents advantages for manufacture and is chosen as a basis for design estimations.

For constructional reasons, namely to mount the drive mechanism, the smallest tube should have a diameter not smaller than 60 mm. Advantages for manufacture can be deduced if the increase of diameter is performed by constant steps, thus getting constant gap widths between the tubes to place identical latching mechanisms within. The ratio of the smallest to the largest diameter (i) can be optimized with regard to the desired response behaviour, assuming a constant ratio between inner and outer diameter (a) for each tube. The ratio i is bigger than tolerable from the manufactural view point. Therefore a constant (a) policy for all tubes is not practicable. But this influence is not so important that for further estimations this aspect will be expanded here.

The design goal is to get a sufficiently stiff construction with minimum of weight. Representative for stiffness is the deflection (δ) under static loads. To describe the dependencies Fig. 2 has been drawn. The abscissa presents the acceleration environment at the space shuttle spread over the range from vernier thruster to primary thruster pulses. The vernier thruster pulses may induce a boom oscillation with amplified amplitudes within the first half of the described range. The graphs are valid for a construction with one kind of material, constant wall thickness ratio (a) and constant resulting deflection (δ). Additional deflection caused by backlash is not considered. The graphs describe weight expense, readable at the ordinate of the figure. The additional weight by overlapping of the adjacent tubes and by the drive mechanism is considered. Competitive materialsare only aluminum alloy and CFP.

From the Fig. 2 it can be deduced furthermore the tube wall thickness has a tremendous influence on the total weight. It should be as small as possible and as far as the pertinent increase of diameter allows. Further it can be deduced that the increase of stiffness by the factor of ten means increase of weight by the factor of three. In this situation the aluminum alloy boom can be replaced by a CFP construction gaining half of the weight.

In Fig. 3 the design goal stiffness is checked against strength, resp. manufactural and constructional view points. The diagrams demonstrates that there exist lower and upper limits for the jib diameter. The lower limit is bounded to a wall thickness smaller than it would be practicable for a plain CFP shell. This suggests a network construction seems to be adequate for the material.

Concerning the upper boundary more detailed investigations are necessary.

An important viewpoint is the thermal stability. At CFP designs by its special properties this is reachable with special variation of the directions of the fibers. In case of aluminum constructions it may be necessary to perforate the boom, mainly at tubes with small diameter because the temperature dependent deflection is inversely proportional to the tube diameter. But this technology is bounded to weight expense.

Not included in the description of basic design aspects and parametric relations but necessary to investigate are local reinforcements at latching points and guiding tracks.

THE DRIVE MECHANISM

Two elements of the drive mechanism have been already mentioned: the motor and the spindle. The spindle has a threaded and an unthreaded section. In Fig. 1 this section is located between the motor and the upper spindle part. Further elements required for the drive are screws elastically suspended at the bottom of each tube and finally keyway rails at the shell surface of each tube to prevent mutual rotation of the tubes.

In the stowage mode, when the tubes are nearly completely fitted into one another, the screws are stringed up over the unthreaded store – section of the spindle. Only the uppermost screw is thrown into gear (Fig. 4).

The deployment mode starts with shift of the upper screw along the spindle, when it starts to turn. To prevent the other screws and therewith the other tubes to follow these tubes are latched with one another by pins. This will be described in detail later.

Shortly before the moving screw leaves the spindle a skewed ring of the moving tube comes into contact with a counter ring fixed at the upper end of the neighbouring outer tube (see Fig. 5). Now this tube is urged to leave the store. After its bottom screw has been thrown into gear the bottom screw of the preceding tube leaves the spindle not before the coupling between both tubes is performed.

The coupled tubes are now together the moving part. The described sequence from the start of deployment will be repeated up to fully boom extension. At any longitudinal extension is a stop of the motion (hold phase) and also a reversal of motion possible.

In the totally extended condition the holding phase is signified by the fact that all screws are outside the spindle without one. The reachable position of the last screw depends on the length of the container tube. For direct coupling of the last moving tube with the container tube the screw should reach the upper end of the spindle to release the coupling mechanism as in the cases before. Then the most outer (container) tube has to have nearly the block length (L_B) of the telescopic boom, whilst all other tubes have the length $L_B - (n-1) \cdot L_S$. L_S is the thickness of the bottom sections with the suspended screws and assumed to be equal for all tubes and n is the number of moving tubes. The described construction has the advantage that in the most unfolded condition the spindle is eased from loads. These have to take the direct path through the tube walls.

In Fig. 6 our functional model is sketched, all tubes having the same length. The desired end positioning of the last screw is maintained by loss of overlapping between the last two tubes, which is not a preferred design. Loss of overlapping means loss of stiffness and alignment accuracy.

The choice of the motor for the drive system depends on the awaited motion performances. Those are not finally fenced in, therefore this problem will not be discussed here. The choice of the coupling between the motor and the spindle and the supporting of the spindle which has to be suited and therefore different for operation and launch, has been excluded too.

THE LATCHING AND GUIDING DEVICES

The control of the sequence of motion and the blocking of the tubes in mutual end positions are performed by latches and pins. In the stowage mode each tube is blocked with the neighbouring outer tube by at least three pins (see Fig. 4). With exception of the pins of the most upper tube all other pins are blocked by additional pins which dive from the bottom of each tube into the bottom section of the adjacent tube.

During the deployment mode the lifting bottom pulls its blocking pin out of the next resting bottom. There the fixation of the coupling pins is solved and the resting tube can be set into motion as soon as a force along side the resting tube is high enough to overcome the lateral forces at the coupling pins from the skewed resting hole borders. The force required will be set free, by the drive system and introduced into the resting tube by the above mentioned contact rings (Fig. 5).

The amount of the force has to be significantly larger than friction between the moving tube and the resting tube, accelleration forces gathered directly from the single resting tube.

For the last (bottom section) coupling pins a suitable number of resting positions (n—1) in equal distances along side the container tube has to be provided. This is necessary to warrant the blocking and unique positioning of the tube packages.

The coupling of moving tubes is performed by latches, three for each bottom section as visible in Fig. 7. A skewed plug of each latch is pushed into appertaining holes of the neighbouring outer tube by a compression spring. This latching can occur as soon as latch pins give the latch free to rotate. These pins on the other hand are blocked by the spindel. Only when the bottom section with the pins is outside the spindle length the pins release the latch.

For the reversal, that is the opening of latching, the spindle head cone has to penetrate the pin section and to push the pins outside. Then the pins will turn the latches back with drawing their plugs out of the resting holes.

The latching pins are mounted in the same bottom section as the coupling pins. The latching pins serve only for one task. In the case of booms with a sufficiently stiff structure the coupling pins can be used in addition for realization of a jib free of backlash, bridging the necessary gap to prevent jamming between two tubes by spring elasticity. But it may be required to solve the task by means of different elements. And this has to be handled together with the bridging of the gap between the stop rings. The problem has to be handled very cautiously because all failures will be augmented by the number of tubes.

A final remark has to be made referring to the keyway rails which prevent the mutual torsion of the tubes. Because only in maximum two rails are in relative motion simultaneously their toler-

ances and gaps between their keyways induce no problems for alignment. The locked tubes can be hold in unique positions thus creating no additional geometric deviations.

INTERFERENCE OF REQUIREMENTS AT THE SPINDLE

The topics presented up to now were functional components built up by sets of structural elements. These elements have to be chosen appropriately. The spindle is an example.

If the length of the fully extended boom is specified then the length of the spindle depends on several parameters. At first there is the number of tubes and this number (n) depends on alignment requirements ($\Delta\delta$), the desired stowed boom block length (L_B), on the tubes overlapping length (L_U) and the tube bottom section thickness (L_S). The last parameter interferes with the thread pitch. The elastically suspended screw should have the possibility of performing the elastic motion equal to two spindle revolutions in both axial boom directions. This drive at a low pitch number. The necessity for self locking if the motor gear does not perform this work in intermediate boom positions also claims to a low pitch number.

The requirement to minimize weight asks for a small number of tubes. Finally dynamic response estimations as well as aspects of strength have to be considered. In Fig. 8 the main influencing parameters are gathered. The abscisse of the diagram refers to the number of tube elements. The ordinate refers to ratio between the induced alignment error and the diameter tolerances. The latter are the reason for alignment errors. The lines in the diagram are signified by constant overlapping length, constant block length, or constant spindle length.

It is visible that the overlapping length has a very significant influence on the alignment. Better alignment calls for more overlapping. This in addition has as result a larger block length. Only with a special number of tubes a minimum of alignment errors is reachable.

A realistic compromise for greater 0.8 m diameter booms will be 3.5 m block length, 17 tubes and 2.5 m spindle length (threaded part). For reason of the oscillation behaviour this spindle should have about 25 mm diameter. Then the amplification of boom dependent inputs for the spindle will be in any case smaller 6 dB.

CONCLUSION

A summary of important design details of the telescopic jib has been presented. The estimation of the interference of all details is not closed. By means of a functional model it has been proved that the drive and latching mechanism works satisfactorily. Further efforts therefore will be to develop a jib based on the initial success and experiences. Thus mating by the presented estimations the initial design idea with the required properties. The main steps will be:

- guaranty of latching system reliability,
- increase of the spindle/screw efficiency,
- development of a stiff tube structure.

The first two tasks will be signified by a lot of test activities.

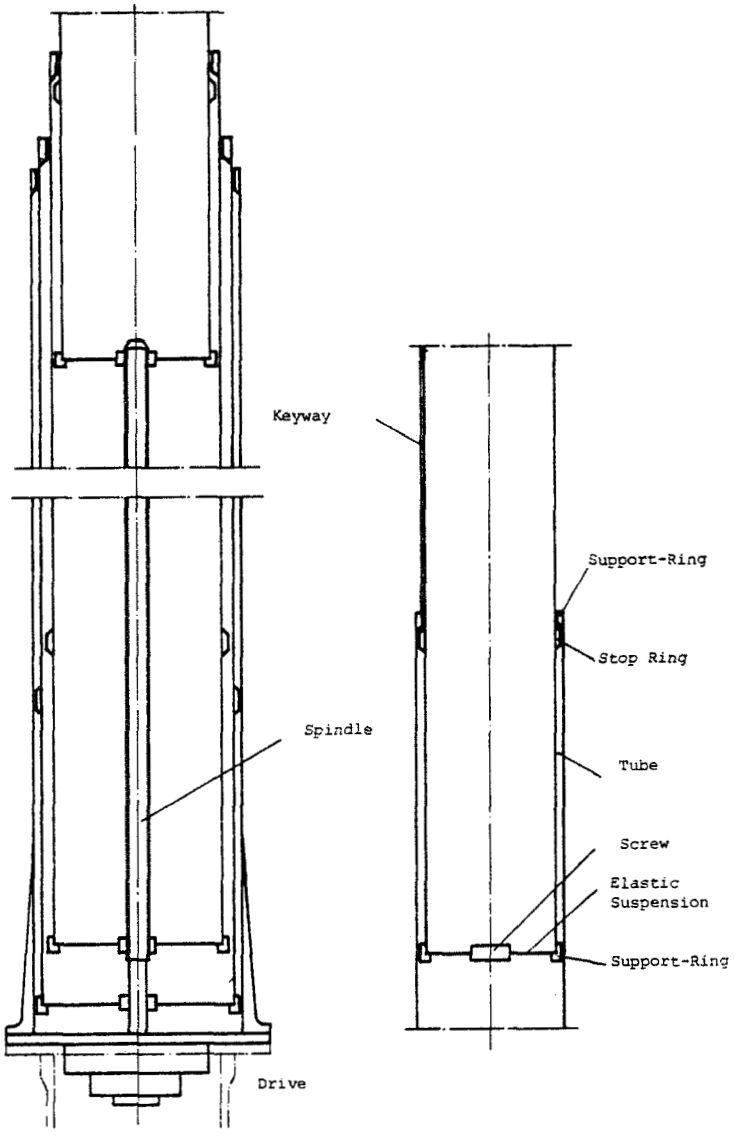

Fig. 1 : The Main Elements of the Telescopic Jib

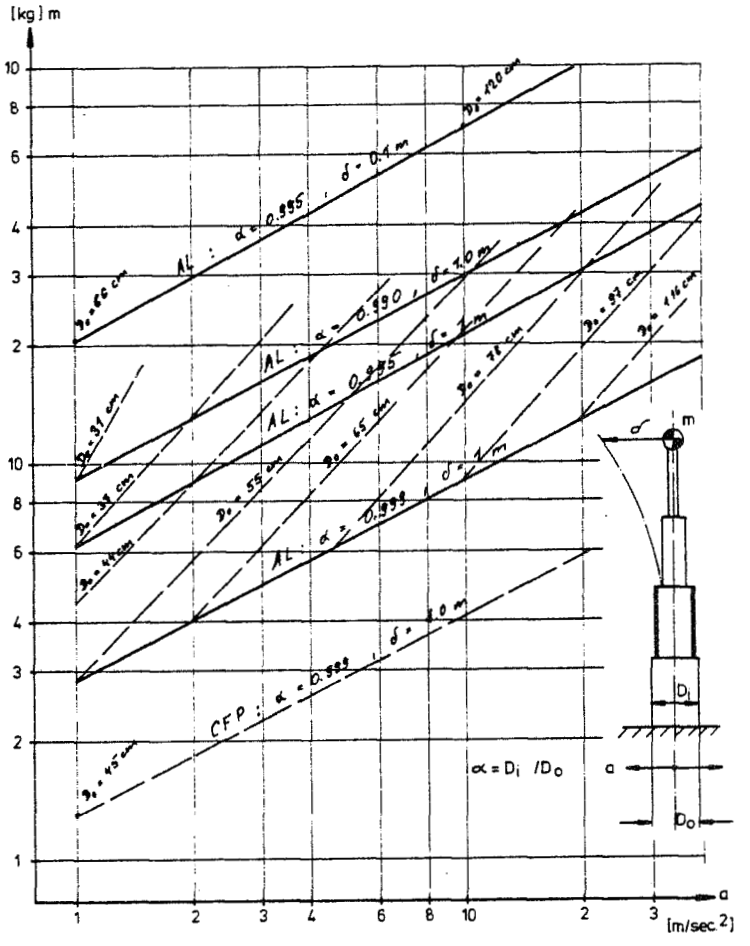

Fig. 2 : Telescopic Jib Dimensions and Weight Depending on Stiffness and Lateral Load

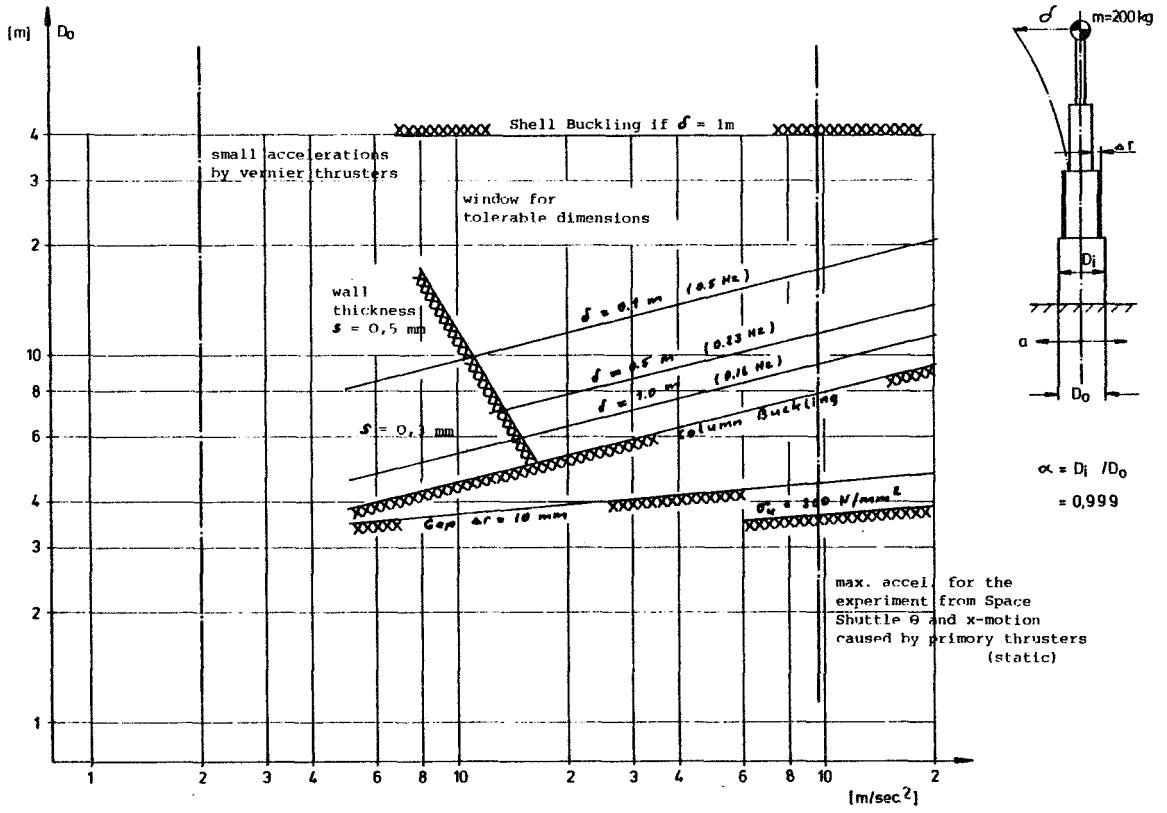

Fig. 3 : Limits for the Tube Diameter Choice of a 30 m Jib

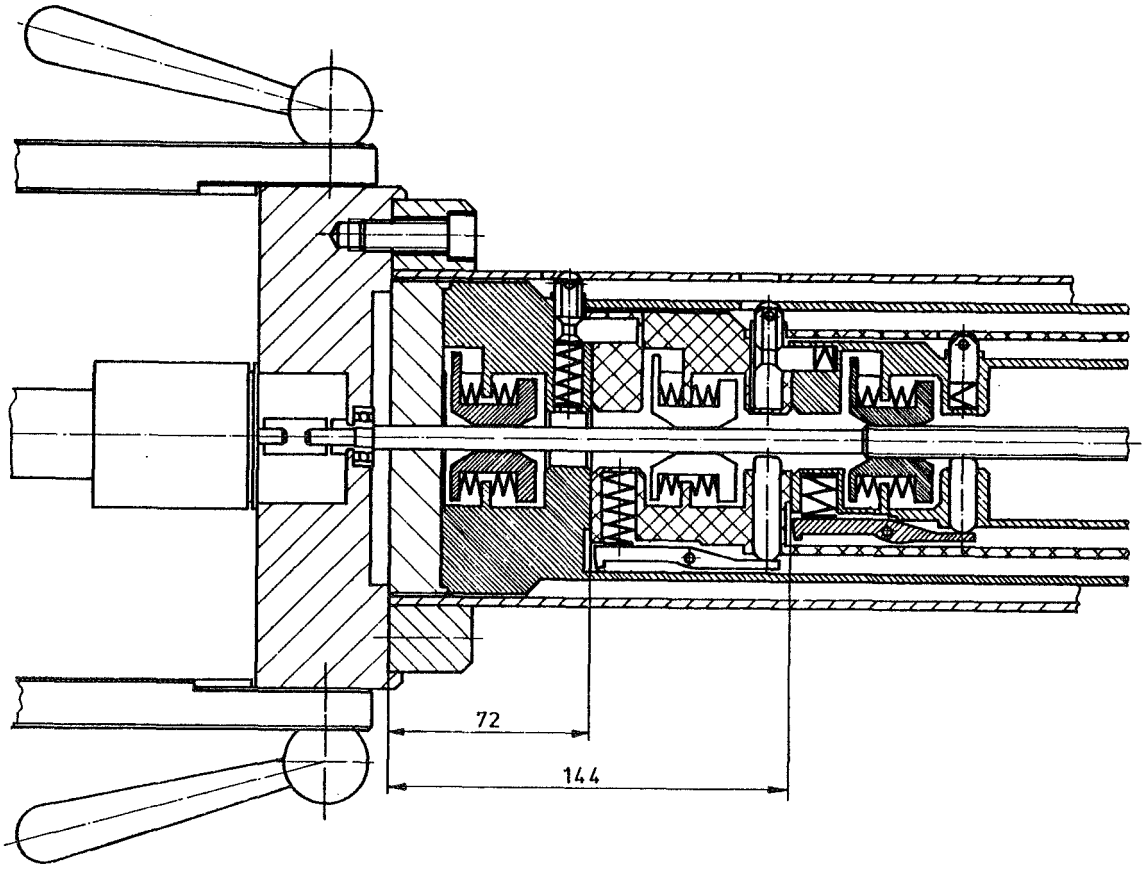

Fig. 4 : Storage and Release Mechanisms

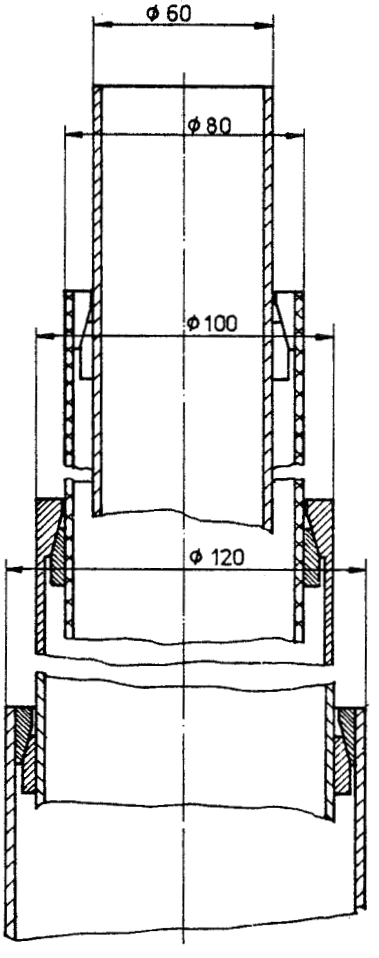

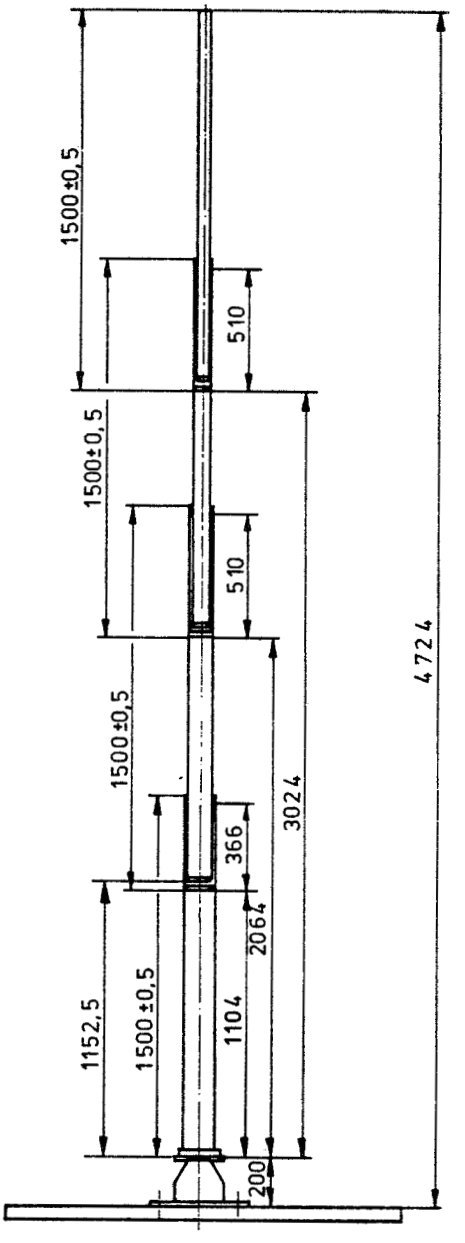

Fig. 5 : Limit of Relative Motion by Stop Rings

Fig. 6 : Functional Model Full Deployed

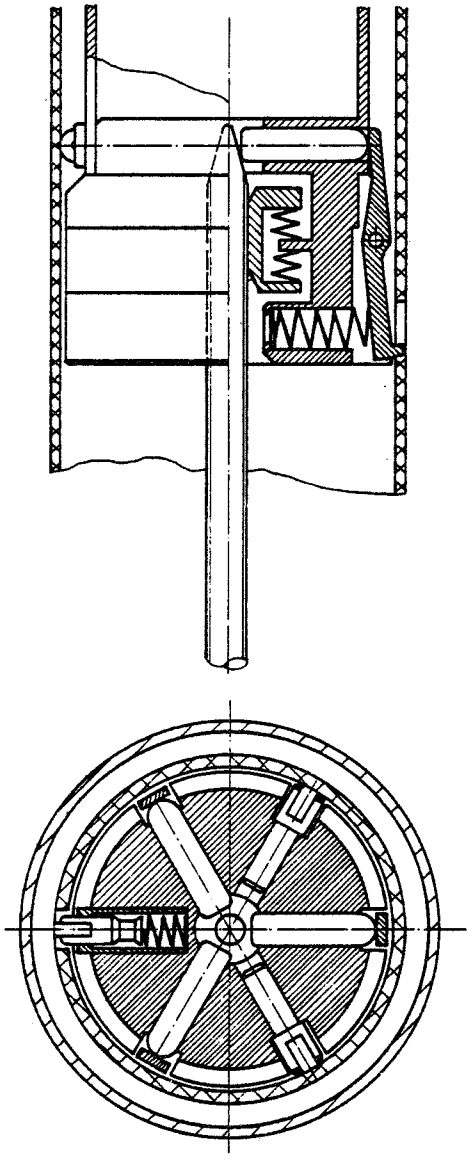

Fig. 7 : Clutching of Boom Tubes

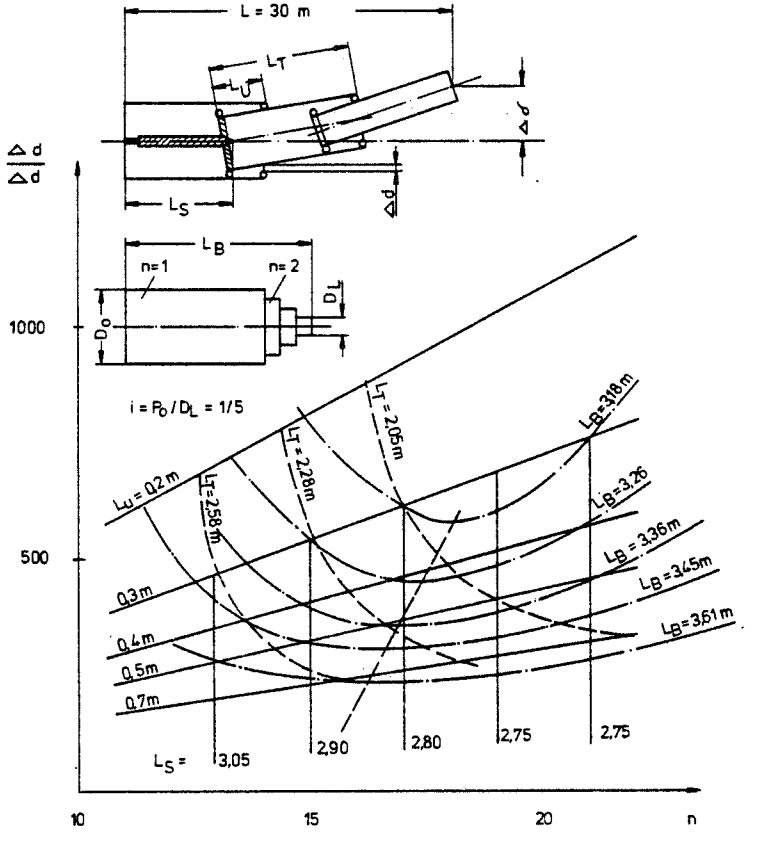

Fig. 8 : Fingerprintdiagram for Choice of Spindle Length

DESIGN OF A PIEZOELECTRIC SHAKER FOR CENTRIFUGE TESTING

By Jeffrey G. Canclini
NASA-Ames Research Center

Jerald M. Henderson
University of California, Davis

ABSTRACT

Centrifuge testing is a new experimental technique designed to test models of large earthen structures. Using centrifuge modeling to study the effects of earthquake ground motion requires a compact lightweight actuator that can produce large forces at high frequencies.

This paper describes the design of a prototype piezoelectric shaker and its development to date. Although certain design problems remain to be solved, the piezoelectric system shows promise for adaptation to a larger payload system such as the proposed geotechnical centrifuge at the Ames Research Center.

INTRODUCTION

A centrifuge can simulate gravity-induced stresses on foundations and earth structures at a reduced geometric scale through centrifuge loading. Using this technique, large structures of a size that cannot be tested practically in any other fashion can be modeled. In addition, centrifuge modeling is potentially a more accurate testing method and therefore can be used to verify and improve present finite element analysis techniques. In centrifuge model testing, a soil payload experiences increased soil pore pressure due to the normal (centripetal) acceleration produced by the centrifuge rotation. This increased pressure causes the soil to behave as though it was at a deeper level. For example, a 100 foot deep earthen dam can be represented by a 1 foot deep embankment when subjected to a 100 g normal acceleration.

Centrifuge modeling can be used to study the effect of earthquake ground motion on earthen embankments. To correctly simulate real world conditions in an N times g normal acceleration test, the centrifuge model laws require the simulated earthquake motion to have N times the acceleration, N times the frequency and 1/N times the duration of the real world motion. With an actual peak acceleration of .25 g's, a frequency of 4 Hz and a time duration of 10 seconds, a model payload rotating with a 100 g normal acceleration would need to experience a 25 g peak acceleration with a frequency of 400 Hz lasting for 0.1 seconds.

In 1976, at the University of California, Davis, the Department of Civil and Mechanical Engineering, in collaboration with the NASA-Ames Research Center, undertook a study to develop an earthquake simulator system. It was proposed that the feasibility of the system be tested in the Schaevitz 3-meter-arm centrifuge at Davis. The system components include:

1. An actuator capable of producing the desired earthquake motion on a test payload.

2. A payload box (container) to hold model earthen embankments.

3. A mounting and drive system to attach the actuator and payload box to each other and secure them to the centrifuge.

4. A monitoring system to record the earthquake motion and its subsequent effects on the test payload.

Using this system, preliminary data was obtained to check the accuracy of the model laws and to determine the feasibility of developing this system for use in a larger centrifuge.

DESIGN

Discussions between the organizations involved and other geotechnical researchers resulted in the following design requirements:

1. The actuation need only produce motion in one dimension. The desired model factor is N=100 (i.e., the test payload will experience a 100 g normal acceleration).

2. The shaking system is to be mounted in the outer, free-swinging bucket presently attached to the centrifuge. Some additional space is available at the center of the centrifuge for equipment mounting.

3. The total useful load mounted inside the outer bucket may not exceed 100 pounds (this includes soil, payload box, actuator, and instrumentation mounted in the outer bucket).

4. The instrumentation will include a videotape camera (mounted in the center of the centrifuge), an accelerometer attached to the payload box, and a pore pressure transducer.

5. The shaker mechanism must be made as light as possible in order to maximize the amount of soil that can be used in a centrifuge test.

6. The soil payload depth will not exceed 5 inches.

7. The shaker should be able to model real world accelerations of .2 to .5 g.

8. The exact simulation of a given earthquake record is desired, but a shaker which can produce sinusoidal motion from 200 to 600 Hz frequency range is considered acceptable.

METHOD CHOSEN

Seven possible actuator methods were considered. These were electrodynamic, rotating counterweights, explosive firing, spark gap (electric arc discharge), electrohydraulic, natural oscillation of a spring-mass system and piezoelectric. The piezoelectric method was found to best satisfy the design requirements. It is simple, light, compact, and can potentially model an exact earthquake record.

A piezoelectric ceramic element is an artificially-polarized wafer which deforms when an electric field is applied across its polarized surfaces. The magnitude of the strain is directly proportional to the magnitude of the electric field applied. To obtain the desired displacements, it is necessary to stack a number of elements in series and pre-stress them in compression. Since the strain is related to the electric field applied, it is possible to control the motion by varying the electrical input signal.

SYSTEM COMPONENTS

The design of the piezoelectric actuator system was divided into five areas:

1. Piezoelectric elements.
2. Electrical system.
3. Piezoelectric stack support and insulation.
4. Preload and drive system.
5. Payload box and its support.

Piezoelectric Elements

The piezoelectric material chosen was a lead titanate ceramic called PZT-4. This material has the highest strain per unit length of any available material when operated just below its maximum depoling field. It has a low compliance and can withstand the most compressive stress of the piezoelectric materials manufactured. Its relatively low capacitance combined with a high d_{33} constant (d_{33} is a measure of the strain produced for a given applied electric field) reduces the power necessary to operate it. For PZT-4 operating at low voltage levels d_{33} is approximately 2.89×10^{-10} meters/volt. The largest standard thickness available (0.5 inches) was chosen to reduce the number of electrical connections. To reduce the power requirements, primary tests conducted used a 6-inch stack (12 piezoelectric elements) to drive the payload. The proposed final design is to use an 8-inch stack (16 piezoelectric elements).

Electrical System

Figure 1 shows the basic electromechanical model of a piezoelectric element for a non-resonant system. The leakage resistance R_L is, for this application,

so large that it can be treated as an open circuit. The electrical portion of the model reduces simply to a capacitor with a reactance of $I/\omega C_e$. Because of the large impedance and high voltage requirements of the piezoelectric stack, it is estimated that the power required to operate at maximum amplitude would be near 28 kw (a 6 inch stack operated sinusoidally at 500 Hz). To evaluate the system without the use of a larger power supply the system is incorporated into an LRC resonant circuit. In this circuit the piezoelectric stack behaves as a capacitor while a variable inductor is used to peak the applied electric voltage at different frequencies.

As shown in Figure 2, the piezoelectric elements are connected electrically in parallel by thin shims placed between each element.

Piezoelectric Stack Support and Insulation

To insulate and protect the piezoelectric elements from other components in the system and to hold the stainless steel shims in place, a hollow polyvinylchloride (PVC) cylinder (Figure 2) surrounds the piezoelectric stack. As an additional safeguard to prevent electrical arcing, anticorona coating is sprayed on the outer sides of the elements. To separate the outer edges of the positive shims from the groundwire, and visa versa, each shim has a terminal strip which passes through a slot in the PVC shell and allows connections outside the shell. The positive and negative terminals are connected on opposite sides of the shell. The PVC shell also acts as a support for the piezoelectric elements and helps to keep them aligned.

Piezoelectric Preload and Drive System

The stack is preloaded using disc springs to hold the stack tightly together as it expands and contracts (Figure 2). Using disc springs with a total spring constant much less than the spring constant of the stack drive system allows the higher spring constant to control the resonant frequency. Preloading can be varied from 0 - 6500 pounds. Most tests were conducted with a 4500 pound preload. The piston actuator slides through the hollow center of the disc springs and the preloading bar. The preloading bolts are insulated from the preloading bar by bakelite collars preventing a ground loop which would reduce the current passing through the elements.

The piezoelectric stack and drive system is mounted underneath the baseplate of the payload box as shown in Figure 3. Although mounting the stack to the baseplate of the payload box would provide a more rigid connection, this was not possible due to the dimensions of the outer bucket in the centrifuge. The stack is compressed on one end by a baseplate which in turn is bolted to the outer centrifuge bucket. In addition to compressing the piezoelectric stack the baseplate distributes the force acting on the outer bucket wall, reducing the stress and deflection in this wall. The outer end of the stack is compressed by the piston actuator which in turn is threaded and bolted to a mounting plate attached to the bottom of the payload box.

Payload Box and Its Support System

The payload box is shown in Figures 3 and 4. Weight, size, stress, resonance, and providing a very stiff attaching platform were the five major considerations used in developing the box.

The payload box is constructed of 6061-T651 aluminum alloy. To increase the rigidity between the payload box and the piston actuator, stiffening ribs are welded to the bottom of the box (Figure 3). With this reinforcement, the stiffness of the baseplate is estimated to be between 10 and 100 times greater than that of the four cantilever supports.

The dimensions of the cantilever supports represent a compromise between the need for low stresses and a high resonance frequency and the desire for low compliance and minimum mass.

Description of Overall System

Figure 5 portrays the current test setup. When the frequency generator is manually triggered, a low voltage AC signal is sent to the power amplifier for a prescribed time interval. The output signal from the power amplifier is fed through the autotransformer and into the inductor. This high voltage sinusoidal signal is fed to the piezoelectric elements producing a sinusoidal motion proportional to the electric field across them. The signal generator also triggers the oscilloscope sweep and sends a signal to the digital counter which records the time interval of the test run.

The voltage across the entire LRC system, the voltage across the piezoelectric elements and the current through the LRC system is monitored by voltage and current probes connected to an oscilloscope. The acceleration produced is measured by an accelerometer rigidly attached to either the piston actuator or the payload box. A video camera attached on the center platform inside the centrifuge is used to observe the payload.

Slip rings on the main shaft of the centrifuge provide electrical connections for dynamic tests. The charge amplifier is mounted inside the centrifuge to reduce the effects of electrical noise generated when the signal passes through the slip rings. A solenoid remotely triggered by a DC power supply grounds the charge amplifier and clears it of transient signals. The bandpass filter screens out 60 Hz noise and other high frequency electrical and mechanical noise.

RESULTS

Static tests (conducted without the centrifuge rotating) produced accelerations at or above the level expected. Mechanical resonance of the shaker payload system occurred at a lower frequency than predicted amplifying the acceleration produced near 500 Hz. This resonance can be observed in Figure 6 where acceleration peaks even though the applied voltage is declining.

Dynamic tests produced acceleration which declined as RPM's increased. Part of this decline is due to the normal acceleration affecting the mechanical resonance frequency. Another part is due to the normal force acting on the mechanical coupling between the piezoelectric stack and the payload bucket. A number of modifications have been tested but none have completely eliminated the decline. Other factors that may contribute to the decline are under investigation.

Current tests were conducted at 40% of the piezoelectric systems rated capacity. The system is being modified to operate at higher power levels in addition to modifications that will hopefully eliminate the decline in acceleration or at least lead to an understanding of why it exists.

CONCLUSIONS

To date the results of this study have shown:

1. The feasibility of producing large forces using the piezoelectric system.

2. The feasibility of easily controlling and varying the frequency, the amplitude of acceleration and the time duration of motion.

3. The system shows promise for adaptation to a larger payload system.

Before a complete evaluation can be made, the system needs to be better understood. Elimination of the decline when the centrifuge is rotating, tests conducted with a "stiffer" system to eliminate the influence of mechanical resonance, and tests conducted at higher power levels are necessary before valid geotechnical studies can be successfully conducted.

ACKNOWLEDGEMENTS

The authors thank Professor Kandiah Arulanandan, the originator of this project, for his support and assistance. We are also grateful the knowledgeable advice concerning the characteristics of the piezoelectric ceramics provided by Mel Kullen, Senior Research Engineer for Vernitron, manufacturer of the ceramics.

REFERENCES

1. Arulanadan, K. "Centrifuge Testing in Geotechnical Engineering", University of California, Davis, Department of Civil Engineering, Technical Report 1977.

2. Canclini, Jeffrey G. "The Design and Development of a Piezoelectric Shaker for Simulating Earthquakes", Master of Engineering Report, University of California, Davis, June 1978.

3. Pokrovsky, G. I. and Fyodorov, I.S., "Centrifuge Model Testing in the Construction Industry", Vol II, Draft Translation by V. K. Building Establishment, 1975.

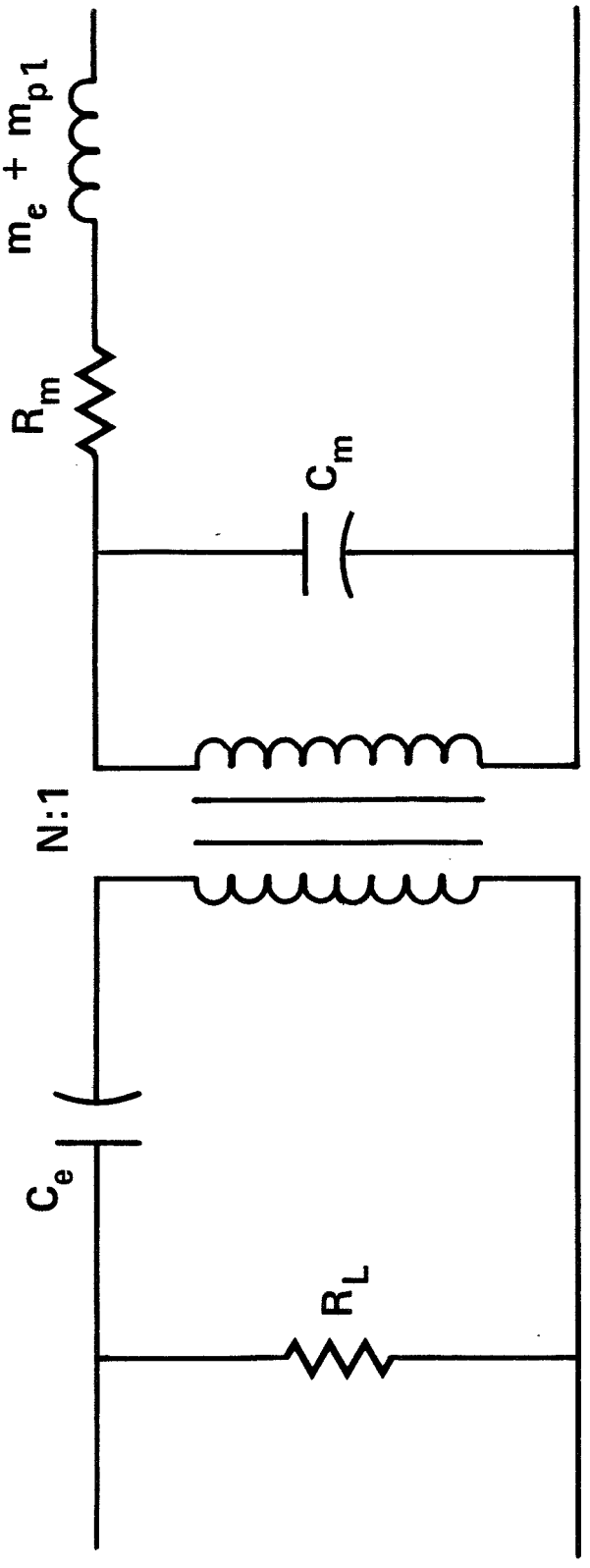

FIGURE 1 - Electromechanical model of a piezoelectric element. R_L is the leakage resistance, C_e the electrical capacitance, N the transformation ratio, C_m the mechanical compliance, m_e the effective mass, R_m the mechanical resistance, and m_{PL} the mass of the payload.

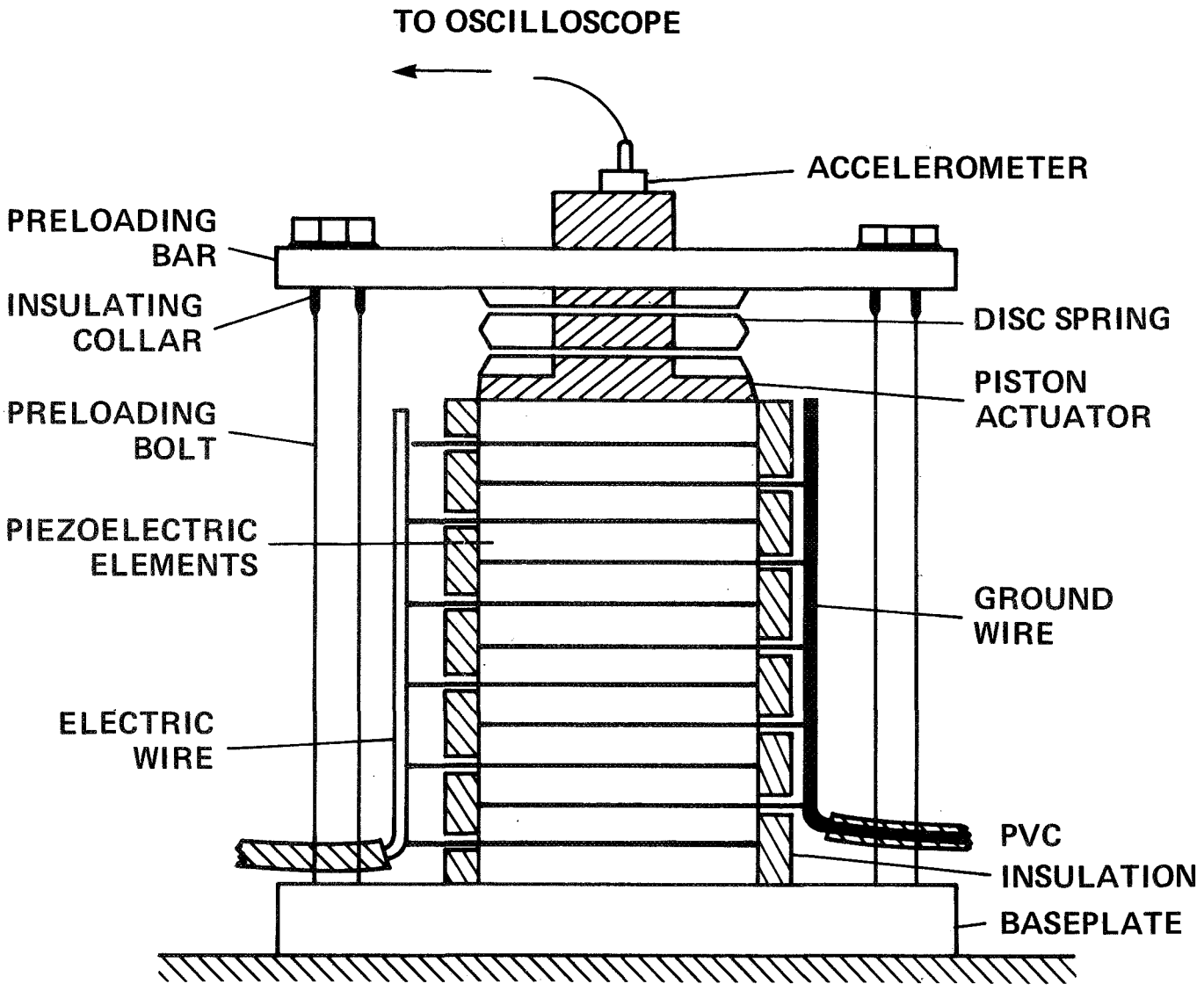

FIGURE 2 - Piezoelectric stack shown with preloading system and electrical wiring. The piston actuator shown is used to measure acceleration of the system when no payload bucket is attached.

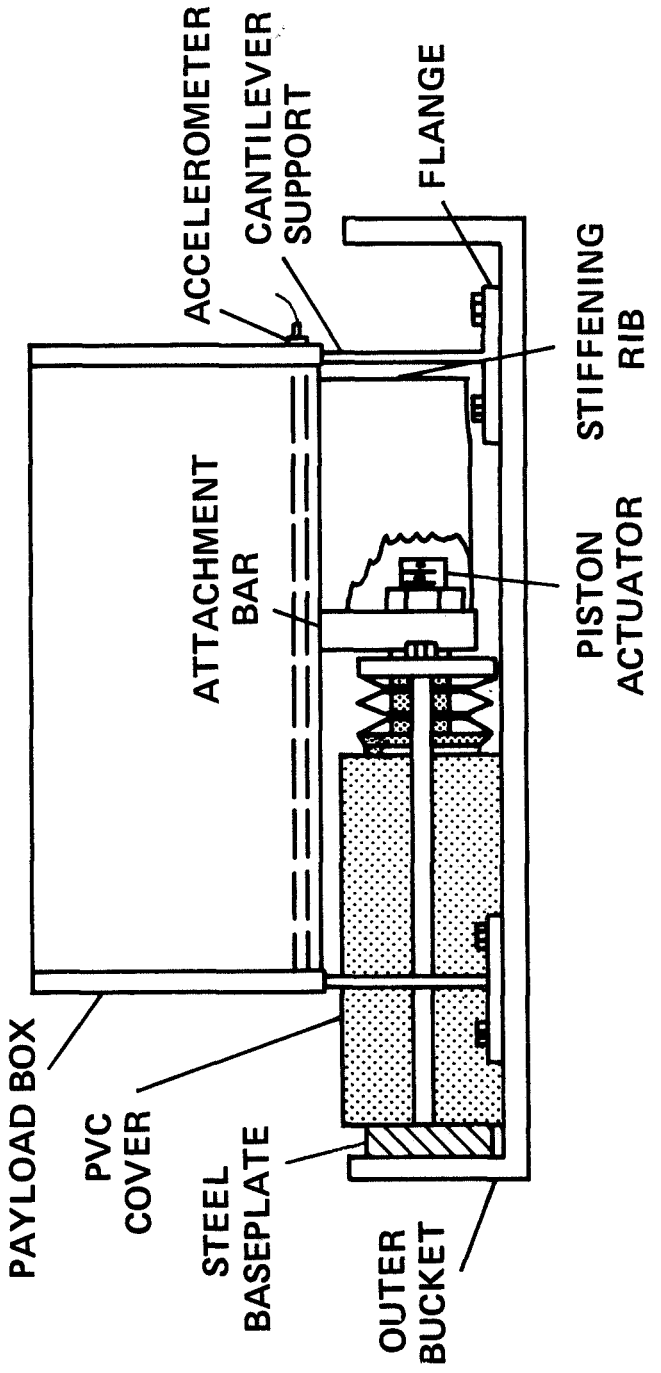

FIGURE 3 - Side view of piezoelectric system showing attachement of the piston actuator to the payload bucket. Electric wiring is not shown.

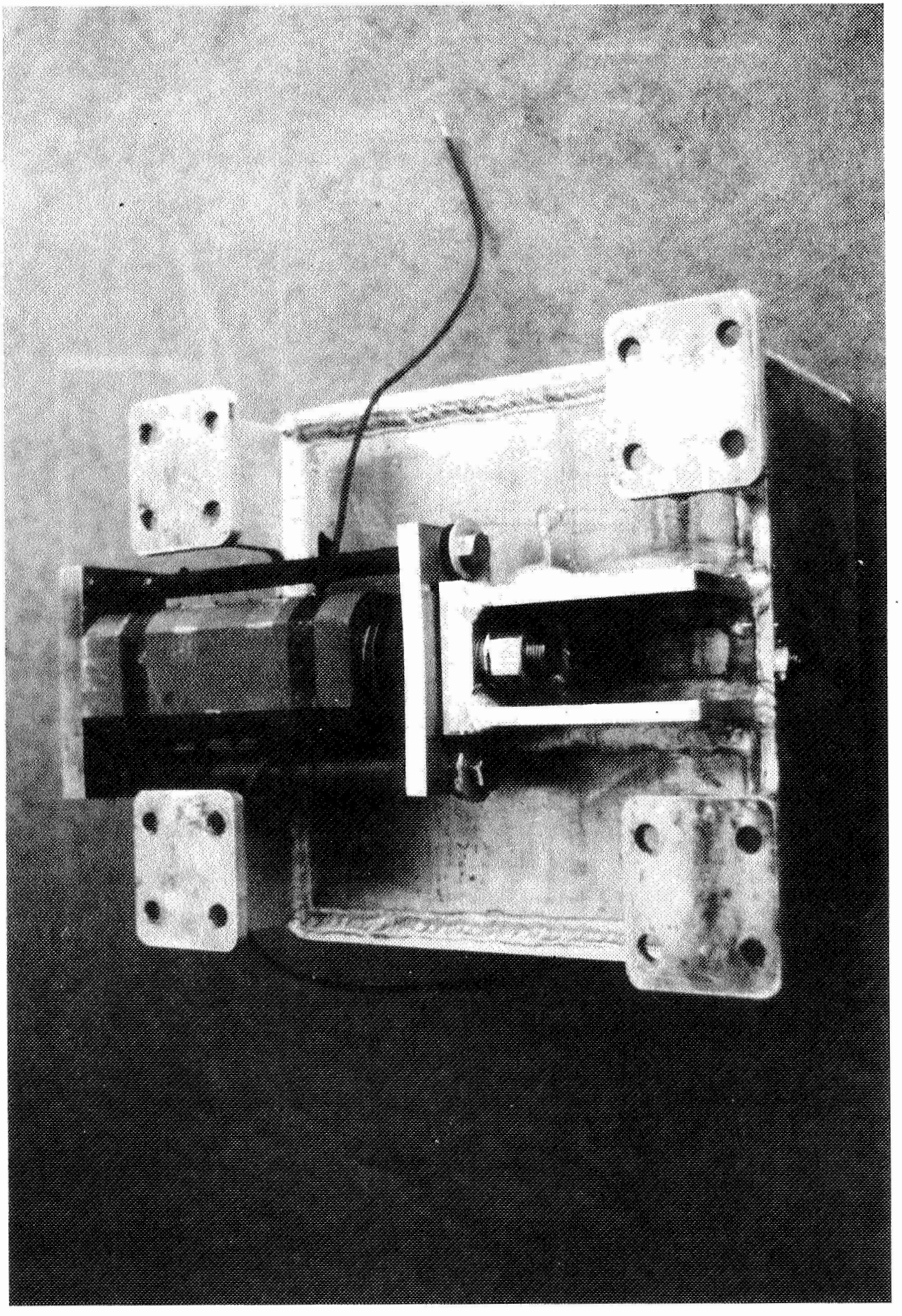

FIGURE 4 - Bottom view of payload bucket with piezoelectric stack and driving system attached.

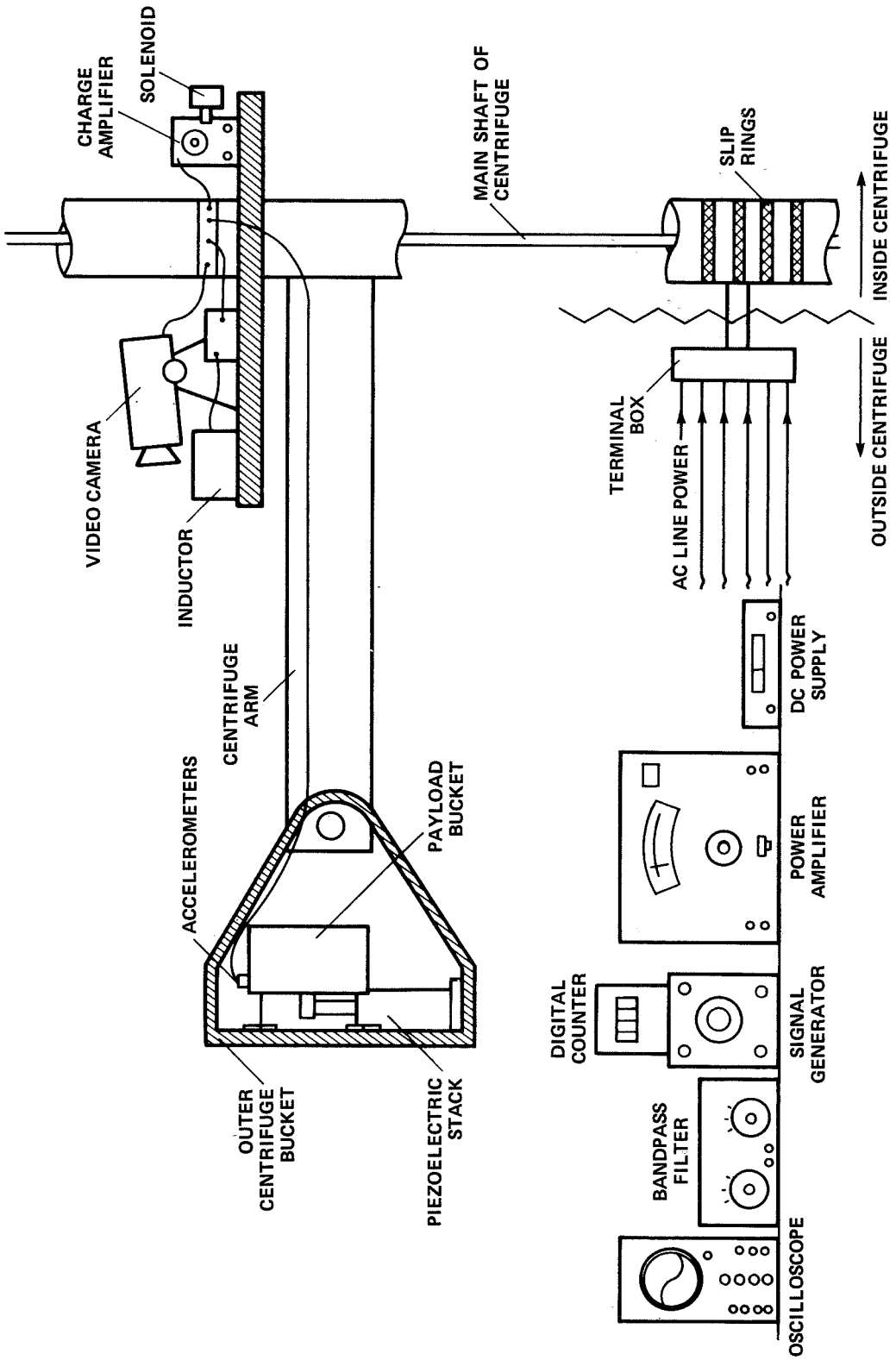

FIGURE 5 - Geographic location of piezoelectric system components.

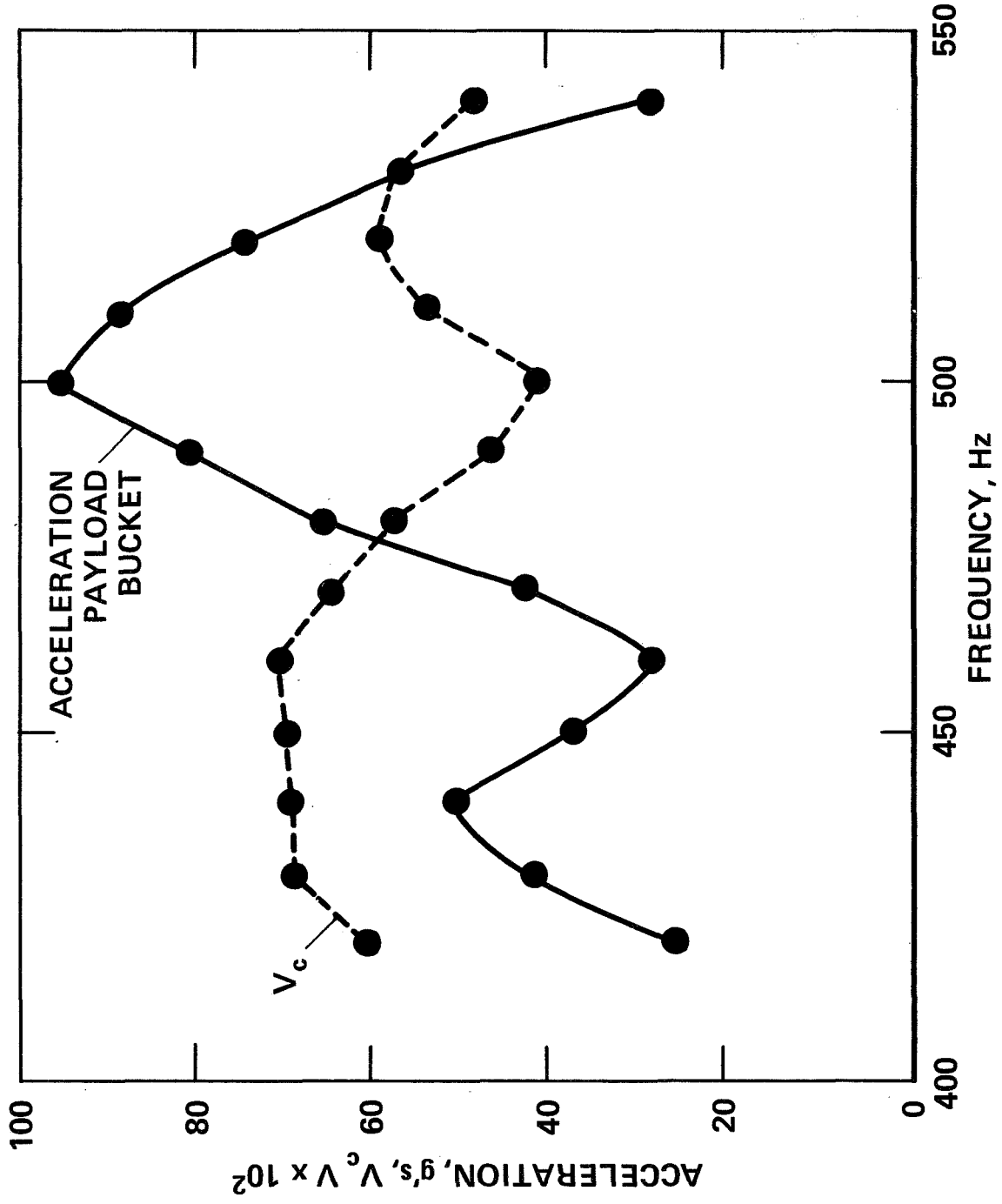

FIGURE 6 - Acceleration and Voltage Versus Frequency for 50 lb_m Soil Payload.

GIMBAL BEARING DESIGN CONSIDERATIONS

AND FRICTION CONTROL

By Nathan R. Kramer
Hughes Aircraft Company

ABSTRACT

The design considerations of bearing selection, bearing fits, bearing installation and thermal control are discussed for a gimbal with a high stiffness, low friction torque requirement. Tradeoffs between a quad set of small diameter spread apart or a large diameter bearing pair resulted in a cleaner, lighter, stiffer unit with the latter selection.

Bearing fits were designed to eliminate clearances with tolerances of 127×10^{-5} mm (50×10^{-6} in) on the bearing shafts and housings. The problems in metrology are discussed and a preferred technique for measurement of small cross-section bearings described. A technique for installation to assure proper seating of the bearing is offered.

Finally, where transient thermal conditions are involved, a method of controlling bearing friction by active control of bearing temperature gradients including the use of bearing unload test curves is described.

INTRODUCTION

When adequate stiffness of a device requires tight bearing fits but other considerations preclude high bearing stresses and high bearing friction, and on top of that there exists high launch loads, a dynamic thermal environment and weight and space limitations, how does one handle this delimma? This paper describes an approach that evolved for handling a case of this nature.

BEARING SELECTION

The problem concerned a two axis gimbal, Figure 1, in which the structure was required to have a stiffness of approximately 40 Hz. At the same time the friction had to be kept to a minimum for proper servo operation. The size, weight and power available were also critical. The azimuth bearing was the key element of the gimbal design in controlling both the stiffness and the friction values. Inasmuch as these two characteristics are direct functions of each other, i.e., an increase in preload for greater stiffness results in an increase in friction, the situation was like trying to walk a tightrope between adequate stiffness and acceptable friction torque levels.

Initial design studies looked at quad sets of bearings with the upper and lower pairs spaced apart to provide overturning moment stiffness. See Figure 2. However one large bearing pair with a high contact angle provided a much cleaner, more compact, lighter weight and stiffer design. The bearing selected was 26.7 cm (10.5 inch) I.D. x 29.5 cm (11.6 inch) O.D. x 2.54 cm (1.00 inch) wide with ninety (90) .635 cm (.250 inch) diameter balls in each row. The material is 440C stainless steel and the bearings are assembled in a DB arrangement with a preload of 125 pounds. For the elevation

axis, where the distance between bearings is approximately 20 inches, two DF pairs having 12.7 cm (5.0 inch) bores with a .95 cm (.375 inch) crossection were selected.

The bearings were dry film lubricated with molybdenum disulfide and Rulon A. And a Rulon A plus 5% MoS_2 retainer provides a lubricant reservoir.

BEARING FITS

In order to maintain the stiffness throughout the temperature range an interference fit of 760 to 890 x 10^{-5} mm (300 to 350 x 10^{-6} inch) was specified with the shaft of the azimuth bearing and 0 to 127 x 10^{-5} mm (0 to 50 x 10^{-6} inch) clearance fit with the housing, prior to preloading. For the elevation bearing, 127 to 254 x 10^{-5} mm (50 to 100 x 10^{-6} inch) clearance was specified for both inner and outer diameters prior to preloading. Since the I.D. contracts and the O.D. expands approximately 254 x 10^{-5} mm (100 x 10^{-6} inch) when the preload is applied, all clearances are removed, and stiffness is maintained.

In order to achieve the bearing fits specified, it required very accurate measurements of the bearing diameters and then fabrication of the shafts and housings to fit the selected bearings. However, it was soon found that measuring the diameters of small crossection bearings is not a simple thing to do. As an experiment three sets of bearings were sent for measurement to two sources which are reputed to be experts in metrology and the results were compared with the bearing vendor-supplied data. A typical set of results are shown in Table I.

TABLE I

	O.D. mm(in.)	I.D. (-1) mm (in.)	I.D.(-2) mm(in.)
VENDOR	294.63550 (11.599823)	266.69652 (10.499863)	266.69619 (10.499850)
A	294.63218 (11.599692)	266.69937 (10.49975)	266.69683 (10.499875)
B	294.63111 (11.599650)	266.69594 (10.499840)	266.69467 10.499790)
MEAN	294.63294 (11.599722)	266.69728 (10.499893)	266.69589 (10.499838)
MEAN DEVIATION	0.00170 (0.000067)	0.00140 (0.000055)	0.0081 (0.000032)
MAX. DIFFERENCE	0.00439 (0.000273)	0.00343 (0.000135)	0.00216 (0.000085)

In another experiment, one of the sources was asked to measure the same diameter each day for five successive days using the same operator and same instruments. The difference in the results averaged approximately 100 x 10^{-4} mm (40 x 10^{-6} inch) with a total spread of about 315 x 10^{-4} mm (125 x 10^{-6} inch).

It was found that picking up a small crossection bearing is very much like picking up a wet noodle that has been formed into a ring. The diameter will move in the direction in which hand pressure is applied. To overcome this effect, the procedure for measurement which was adopted provides an integrated average of the radius around the entire perimeter. This is done by utilizing a set of gage blocks stacked to the nominal diameter to be measured. This stack is centered on an Indiron table. A two gram force indicator probe is used to plot the location of the ends of the stack on the Indiron Chart with the scale set for 254 x 10^{-6} inch) per division. A circle drawn between the two diametrically opposed low points represents the nominal diameter, see Figure 3. Without changing the setting, the gage blocks are removed and the ring to be measured centered on the Indiron Table. The ring diameter is then run with the two gram probe and plotted on the same chart. The average difference between this plot and the nominal diameter circle is then determined from which the bearing diameter is established.

BEARING INSTALLATION

Bearing installation was carefully supervised to be sure that the bearings were properly oriented and aligned but of most concern was making sure that the bearings were fully seated without applying excessive forces to the bearings. There is no problem seating an unloaded bearing. With the threads lubricated, the torque to be applied to the screws or threaded retainer which will result in a reasonable force to be applied to the bearing can readily be calculated. For a DB bearing pair, the housing can be heated, the bearing inserted and the retainer torqued down. The housing and bearing subassembly is then heated and installed on the shaft. The shaft retainer is then torqued down. On the surface that would appear to be all there is to it. However, due to the difference in temperature between the bearing and its mating part at the time it is clamped by the retainer, the bearing may not be centered or properly preloaded. Therefore, the procedure that was used was to allow the assembly to cool down until it was close to room temperature. The retainers were then loosened to allow the bearings to center themselves and then retightened. For the outer races and housing, this is adequate. However, for the inner races and shaft, with a DB pair, the preload in the bearing tends to separate the races. When the retainer is retightened, it is necessary to overcome the friction between the bearing and shaft as well as the preload and friction in the threads. This does not lend itself readily to calculation since the normal force between bearing and shaft is difficult to determine. The approach that was used was to tighten the retainer in incremental steps and measure the friction torque of the bearing at each step. A running plot of the friction torque versus the tightening torque was made, see Figure 4. When the slope of the plot flattened out so that the friction was essentially the same for three values of tightening torque the bearing was considered to be seated. For the DF bearings, the procedure requires that the shaft be installed first and then the housing added.

THERMAL CONTROL

The above procedures may be adequate for stable temperatures, however transient thermal conditions can create large temperature gradients across the bearings. These can induce conditions of excessive bearing loads, stresses and friction at one extreme and cause the bearings to become unloaded

resulting in a loss of stiffness at the other extreme. To overcome this problem, active thermal control of the temperature gradients can be applied. In this form of thermal control, the bulk temperature is permitted to vary, but the temperature difference between the shaft and housing is maintained at a selected value which will result in a moderate positive load on the bearings.

As shown in Figure 5, the effect on friction and stress of the temperature gradient, ΔT, across a bearing is much greater than that of the bulk temperature. In the subject gimbal, thermal analysis indicated that the azimuth bearing shaft always tended to be cooler than the housing. Therefore heaters were required only on the shaft to prevent the bearings from becoming unloaded. With the elevation bearings the reverse was true, therefore heaters were required only on the housings to prevent excessive loads.

To establish the levels of temperature gradient (ΔT) which should be maintained, heaters and temperature sensors were applied to the housings and shafts and bearing unload test curves were plotted, see Figure 6. This is a technique where the temperature gradient across the bearing is varied and the bearing friction torque values (T_F) measured and plotted. ΔT is varied from zero or some negative value, where the shaft is warmer than the housing to increasing positive values. As the housing becomes warmer, T_F will continue to decrease until the bearing becomes unloaded after which T_F will remain constant. From the unload curve a value of ΔT can be selected where the friction is some safe value above unload and the associated stresses can be computed.

A system of thermal control of ΔT was then applied to maintain the selected value. Provision was also made to increase ΔT if for some reason an undesirable increase in friction torque occurred. See Figure 7. Conversely, ΔT may be decreased in the event that the bearing approaches an unloaded condition.

CONCLUSIONS

When the requirements for a gimbal specify a stiff structure and low friction, the bearing will probably be the most critical element. Careful selection, measurement, fitting and installation are essential. Careful analysis of thermal conditions may reveal a need for active thermal control. Control of bearing temperature gradients provides a means for controlling friction.

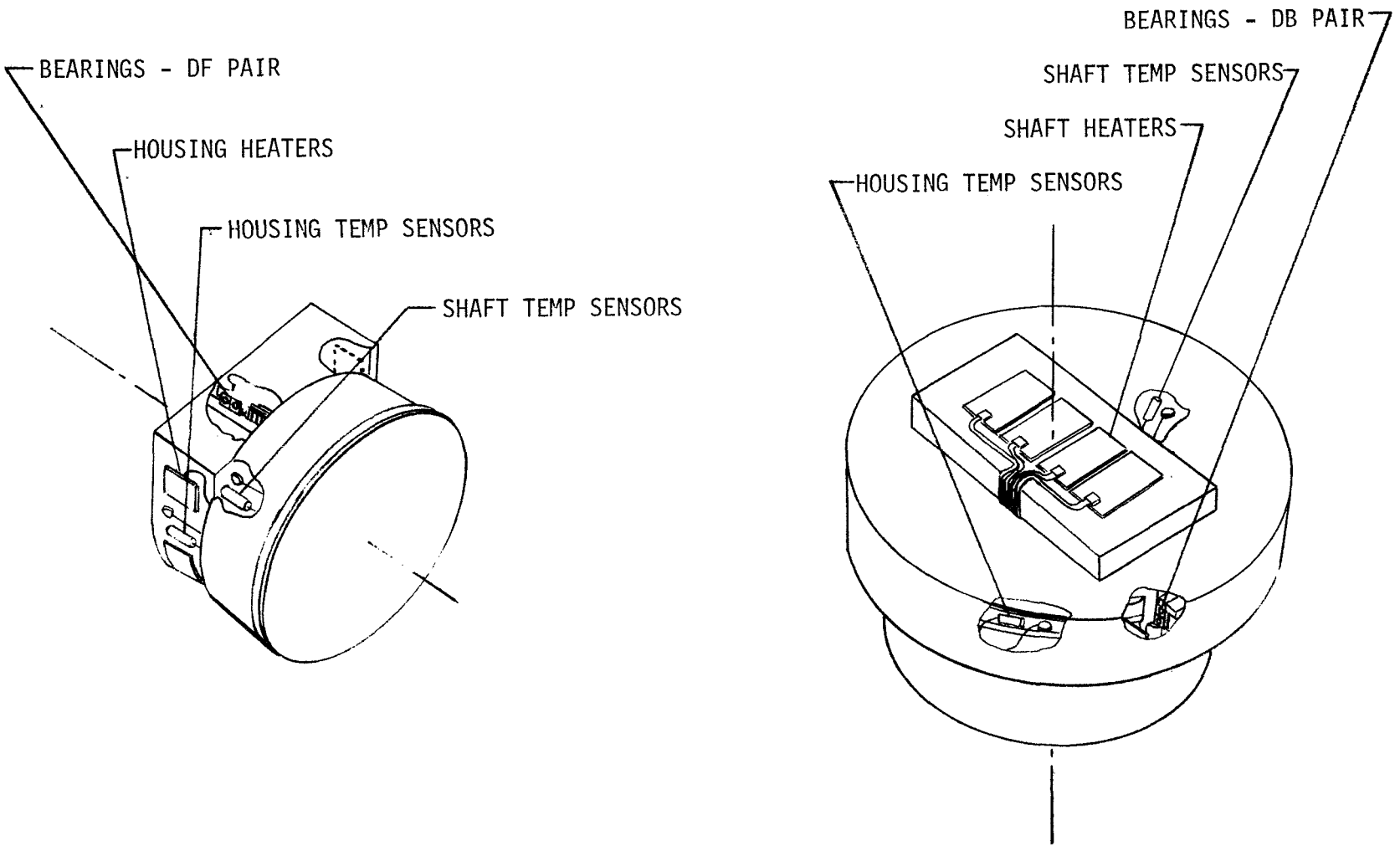

FIGURE 1 - TWO AXIS GIMBAL

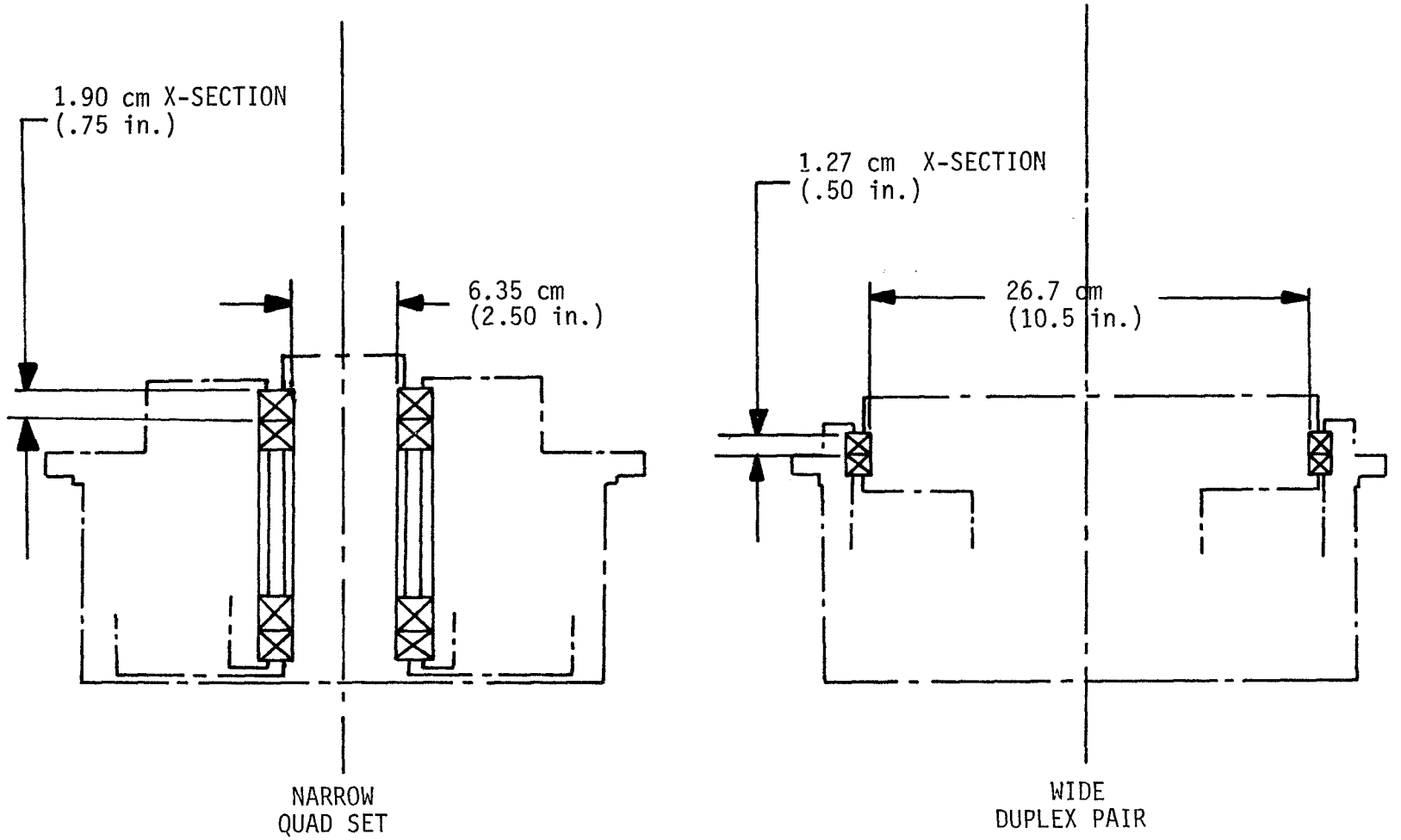

FIGURE 2 - BEARING SELECTION

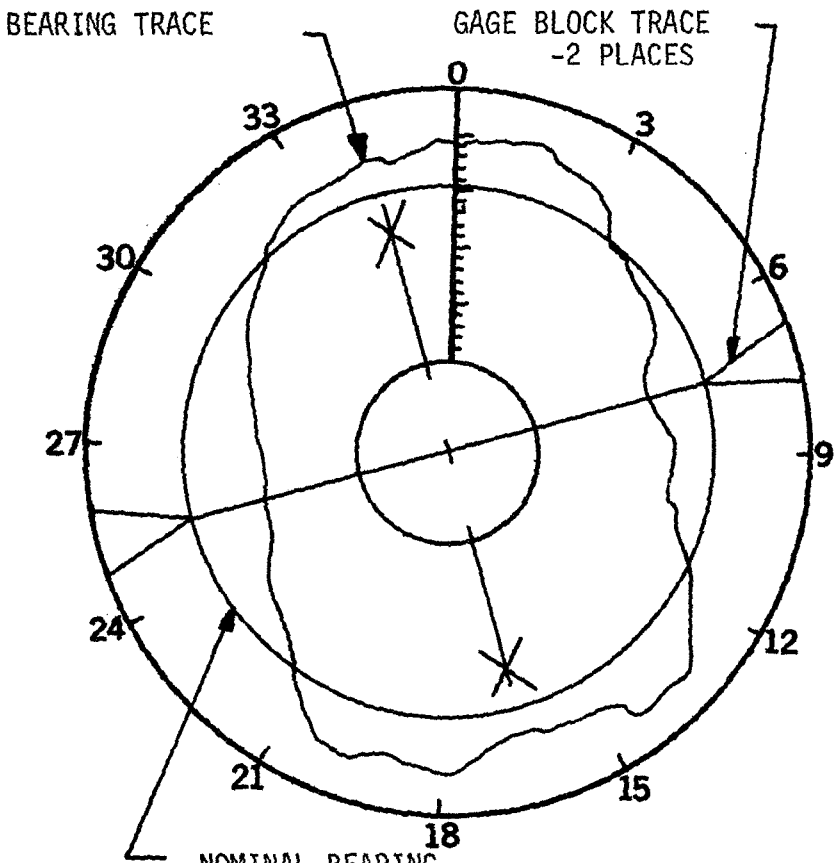

FIGURE 3 - INDIRON PLOT

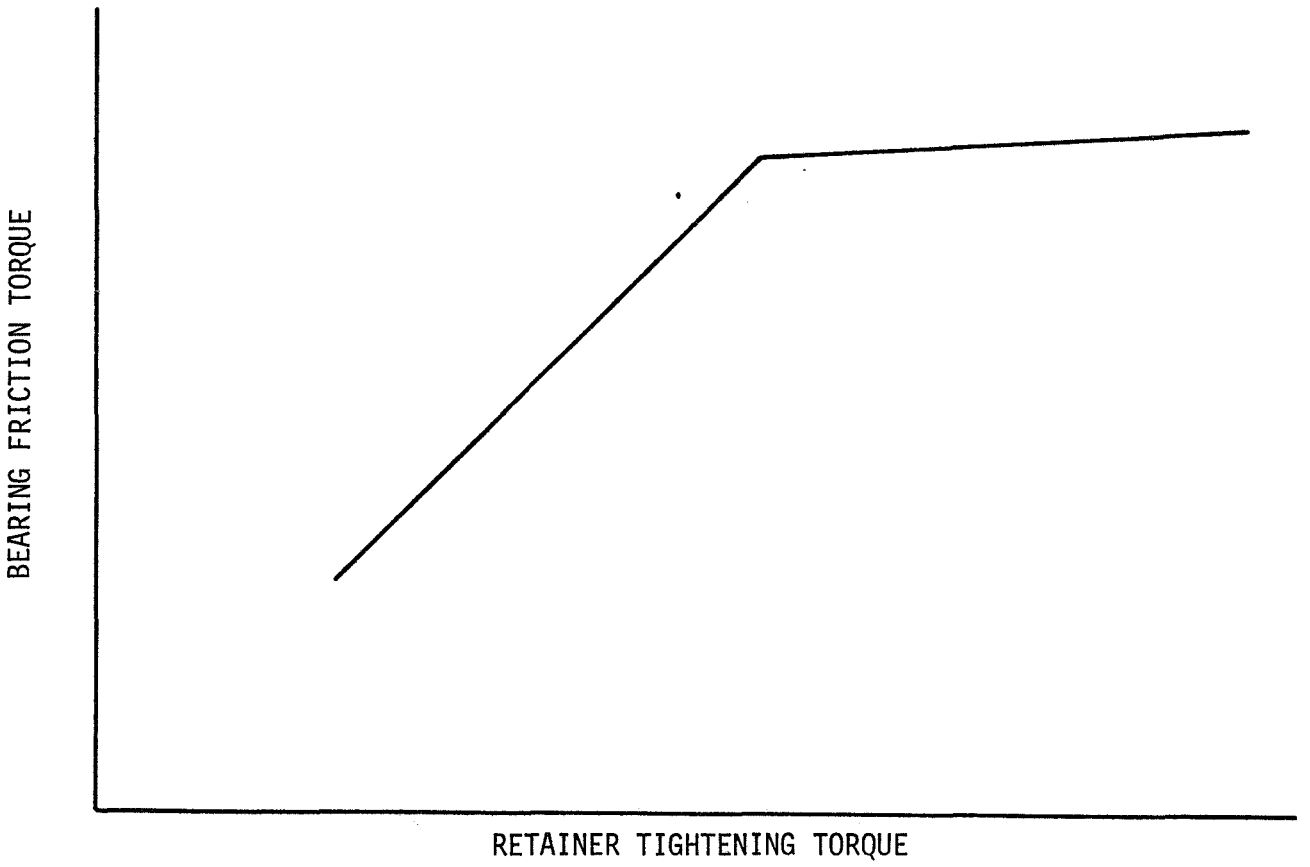

FIGURE 4 - BEARING INSTALLATION PLOT

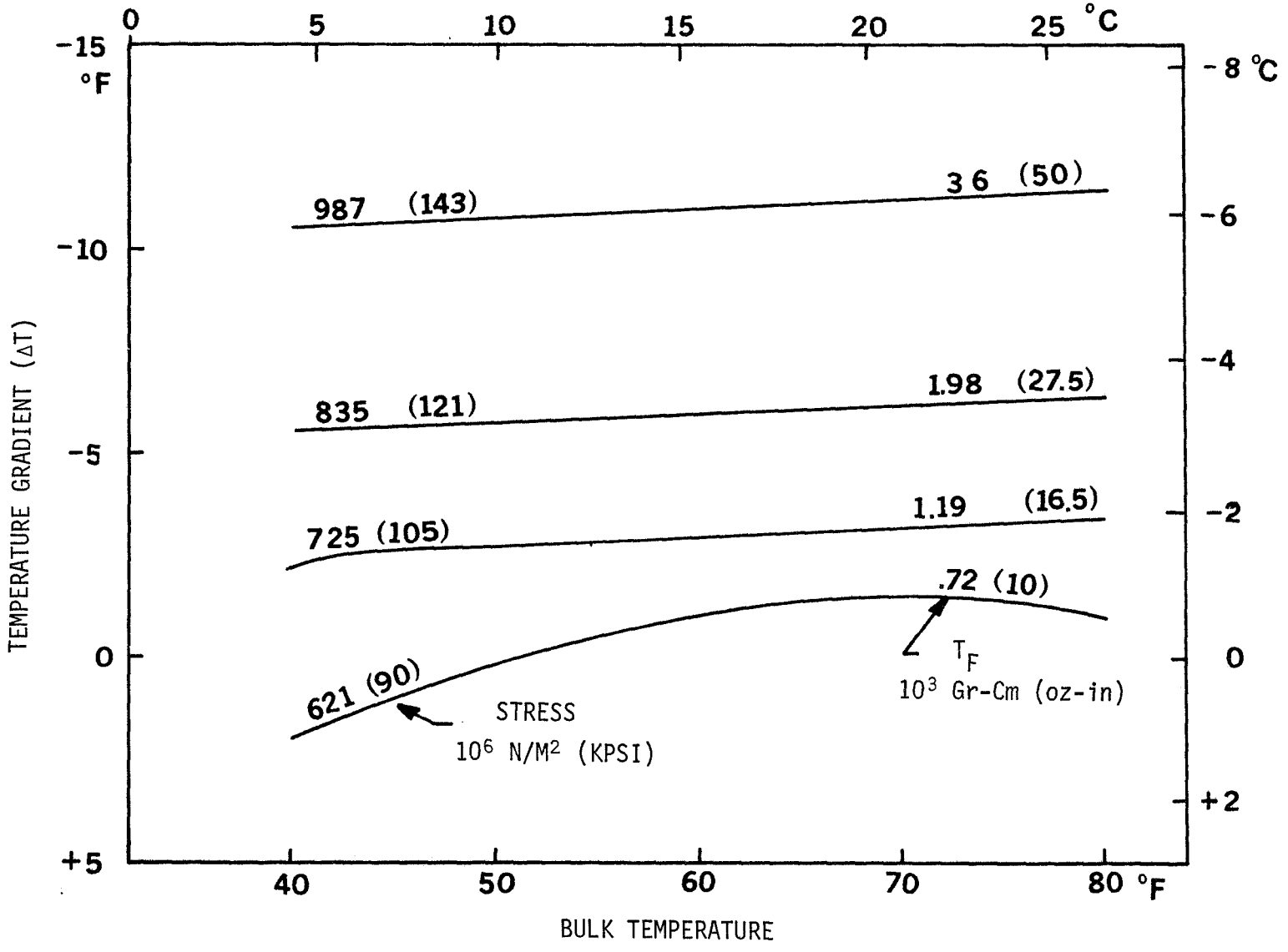

FIGURE 5 - TEMPERATURE EFFECTS (THEORETICAL)

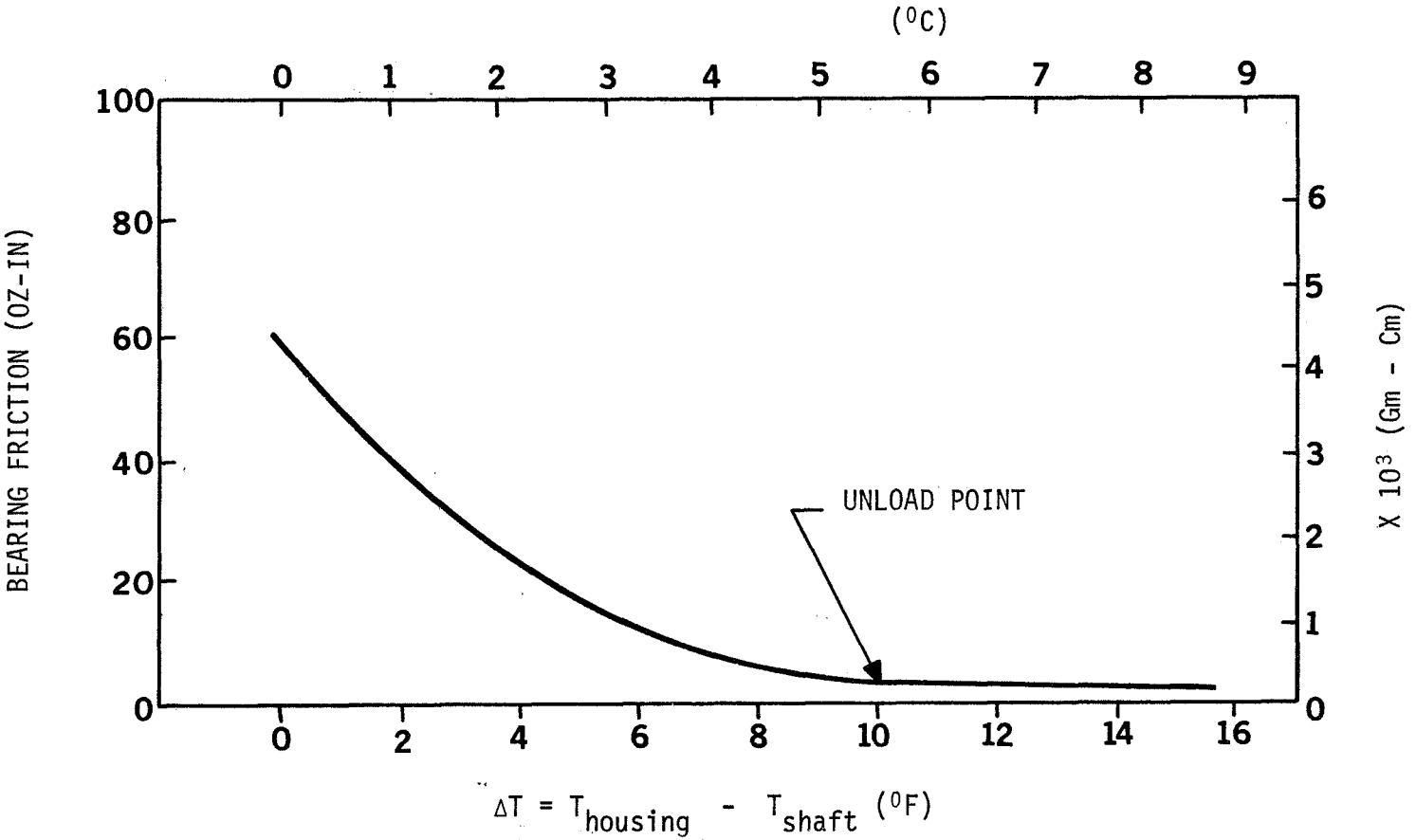

FIGURE 6 - UNLOAD CURVE

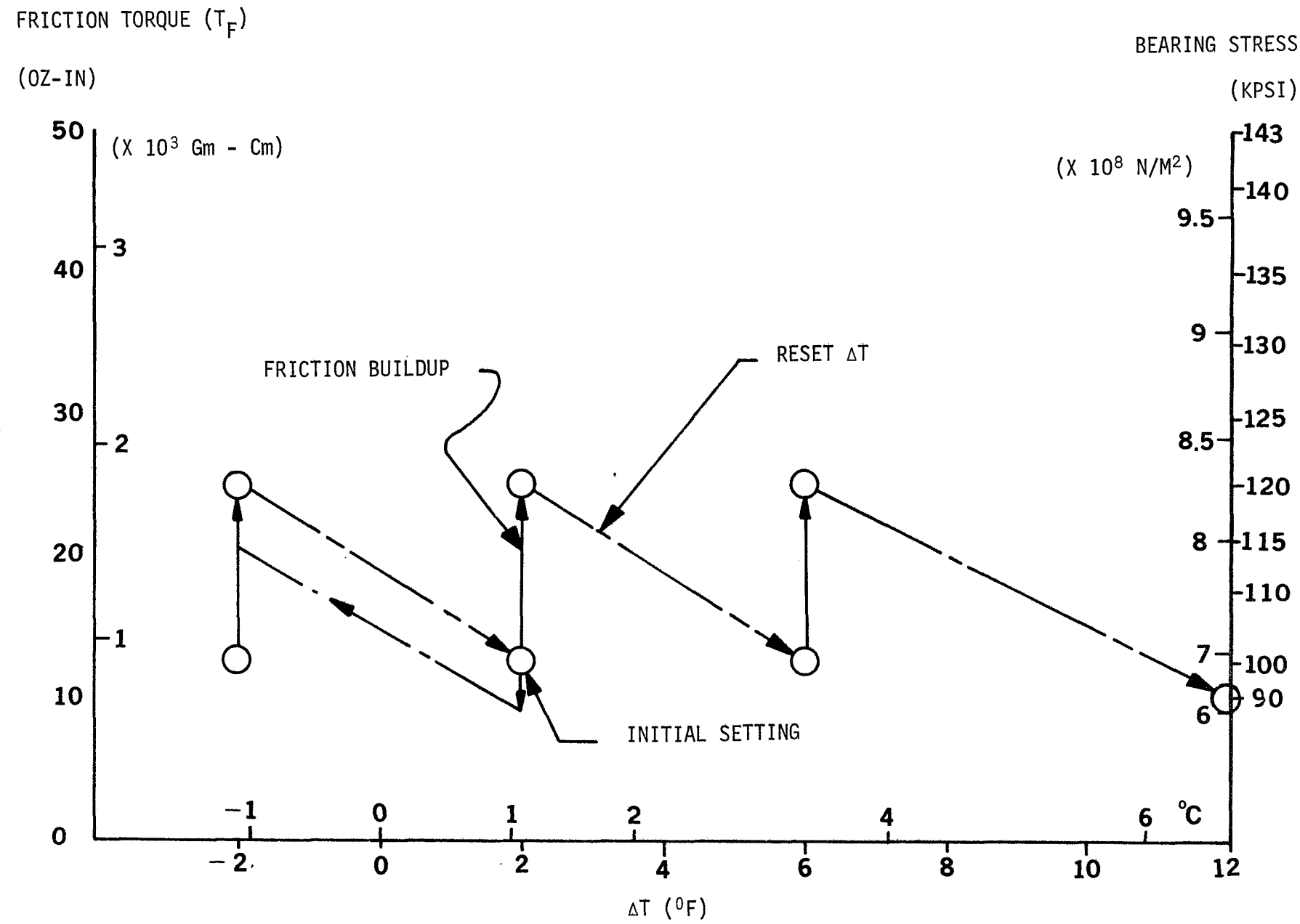

FIGURE 7 - THERMAL CONTROL

HELICAL GRIP FOR THE CABLE CARS OF SAN FRANCISCO

By Richard J. Peyran
NASA-Ames Research Center

ABSTRACT

A Helical Cable Car Grip to minimize high maintenance costs of San Francisco's cable car operation is presented. The grip establishes a rolling contact between the cable and grip to reduce sliding friction and associated cable wear. This paper describes the design, development, and testing of the Helical Cable Car Grip.

INTRODUCTION

The San Francisco cable cars (Figure 1) currently utilize a manually operated mechanical grip to force two replaceable soft steel dies against a 3.33 cm (1.31 in.) diameter cable to accelerate the car from rest to cable speed of 4 m/s (9 mph). Friction between the cable and dies creates high temperatures and rapid wear resulting in a die life of 3-4 days and a cable life of 3-4 months. Associated maintenance costs are $500,000 per year.

A joint effort of the NASA-Ames Research Center and Stanford University created a design for a cable car grip that minimizes maintenance costs while preserving the traditional appearance and operation of the cars. The 10,900 Kg (24,000 lbm) cable cars climb 21% grades at speeds from 0 to 4 m/s (9 mph) and accelerate at 0.1 g. The grip mechanism must release and re-engage the cable at cable intersections and operate within the confines of the cable conduit under the street.

GRIP DESIGN

This study concentrates on the design of the cable gripping mechanism which operates below the surface of the street. The Helical Grip design reduces sliding friction and cable wear compared to the existing grip. Drive wheels are grooved with a helical pattern that meshes with the lay of the cable in a manner similar to a worm and gear set. The cable is gripped between the drive wheels and guide rollers (Figure 2) and the cable car pulled along as the rotation of the drive wheels is slowed by hydraulic clutches. The drive wheels maintain rolling contact with the cable without the wear-producing slippage of the soft steel dies. The meshing action between the drive wheels and the cable enhances the gripping ability and reduces the clamping forces needed to maintain the wheel's grip on the cable. Without the helical grooves, the clamping force required to prevent slippage between the drive wheels and cable is so great that cold rolling of the cable would occur.

The complete grip (Figure 3) uses four drive wheels 10.7 cm (4.2 in.) in diameter. Two hydraulic wet clutches brake each drive wheel. The clutches are a multiple plate type with an oil film separating the individual plates. Fluid shear brakes the drive wheels as the plates are forced together. Metal to metal contact of the plates occurs only when the drive wheels are locked (fullgrip). To operate the clutches, a 0.4 hp hydraulic pump and oil reservoir are required to supply oil at a pressure of 1.03 MPa (150 psi). This pump could be located in the cable car away from the grip. A separate oil system to circulate oil through the clutch plates could be incorporated to facilitate heat removal. Sixteen guide rollers position the cable against the drive wheels and prevent separation between the cable and drive wheels while gripping the cable. Lift arms link the rollers with the shank plate (Figure 3). Downward motion of the shank plate presses the rollers tight against the cable. Upward motion of the shank plate retracts the rollers to allow the cable to drop away from the grip at cable intersections. Once passed the intersection, the grip may re-engage the cable.

MODEL TESTING

To determine if the Helical Cable Car Grip concept was feasible, a test plan examining the basic principles was needed. For a feasible design, the test needed to show that no slippage occurred between cable and drive wheel, that sufficient force, 32,000 N (7200 lbf), was developed to pull the cable car, and that the clutches lock the drive wheels against the cable. A prototype model to be tested under laboratory conditions was designed (Figure 4). The test model consisted of a single drive wheel, two clutches, and four pressure rollers which correspond to one-quarter of a full grip assembly. Two arms adjusted the pressure rollers by a threaded rod. Each clutch was actuated through a high pressure oil line and a lower pressure bleed was used for lubrication and cooling. The grip was bolted to the floor and remained stationary during the tests (Figure 5).

The drive wheel was cut to mesh with a 1.91 cm (0.75 in.) diameter cable. The helical pattern (Figure 6) was cut using a high speed milling cutter 0.95 cm (0.375 in.) diameter and 6.99 cm (2.75 in.) pitch on a helical gear cutting machine.

The test set-up (Figure 7) used a 15.3 m (50 ft.) loop of 1.91 cm (0.75 in.) diameter cable. The cable was made of six strands around a hemp core and was similar in construction to the 3.33 cm (1.31 in.) diameter cable in actual use but its smaller diameter allowed for a simpler test apparatus. A jack shaft assembly connected a 3 hp motor to the cable drive. A hydraulic pump with a 2.84 ℓ (0.75 gallon) reservoir supplied oil to the clutch assemblies.

Static tests on the grip model simulated the car moving at cable speed. The test was conducted by loading the cable with a manual winch to force it through the grip with the clutches engaged (Figure 8). Loads were one-quarter of full scale, 8000 N (1800 lbf), corresponding to one of four drive wheels. A dynamic test simulated the cable car accelerating to cable speed. The cable was motor driven as clutch pressure was increased. By measuring motor current the load transmitted from the cable to the grip was calculated. Another dynamic test simulated the stationary cable car with the cable running free through the grip. Cable speed and drive wheel speed were measured with a strobotach and compared to detect slippage.

CONCLUSIONS

Grip model tests show that the Helical Grip design is feasible. No sliding between the cable and drive wheel was detected during the dynamic tests, which indicates that cable and grip wear will be minimized. The static tests have demonstrated that the grip will provide enough force to pull the cable car. The clutch system worked properly, stopping the drive wheel against the cable.

Further development of the grip is planned. Long term wear tests on the model, investigations into guide roller and clutch interfaces and actuation on the full-scale grip are required. Eventually a full-scale grip will be tested on the cable car system in San Francisco.

REFERENCES

1. Giovannetti, A., "Study of San Francisco Municipal Railway Cable Car System", NASA-Ames Research Center, Moffett Field, CA, September 23, 1975.

2. Lepetich, James A., "Redesign of San Francisco Cable Car Gripping Mechanism", University of Santa Clara, CA, 1977.

3. Haahr, Mary Ellen, Peyran, Richard J., and Divine, Michel, "A Redesign of the San Francisco Cable Car Grip", Stanford University, CA, 1978.

(CALIFORNIA STREET CABLE CAR R.R. COMPANY)

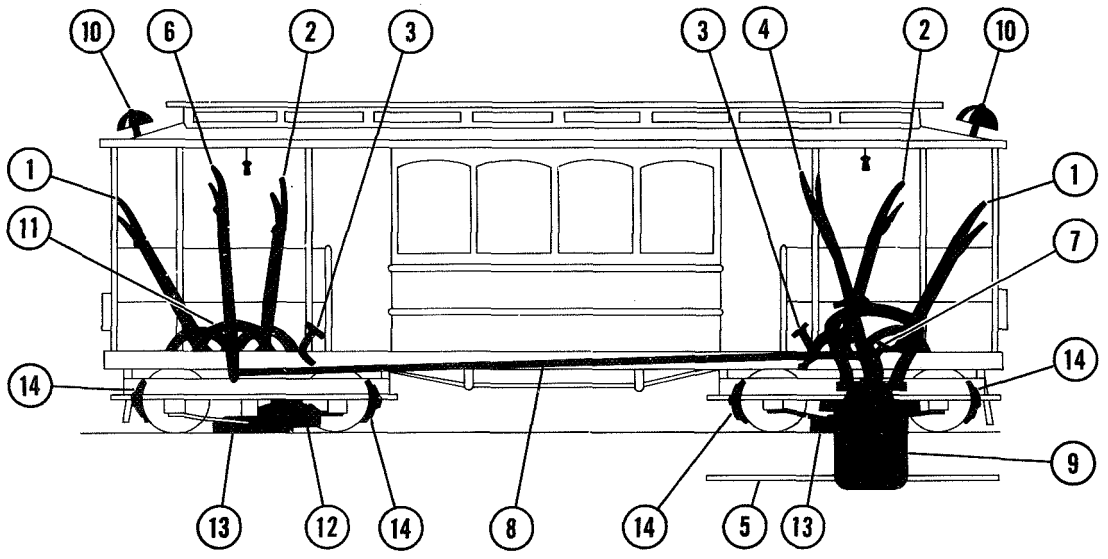

1. EMERGENCY BRAKE LEVER
2. TRACK BRAKE LEVER
3. WHEEL BRAKE FOOT PEDAL
4. GRIP LEVER
5. CABLE
6. GRIP LEVER (ALTERNATE)
7. ADJUSTING LEVER
8. CONNECTING ROD
9. THE GRIP
10. BELL
11. QUADRANT FOR GRIP LEVER
12. EMERGENCY BRAKE
13. TRACK BRAKE
14. WHEEL BRAKE

FIGURE 1. - SAN FRANCISCO CABLE CAR

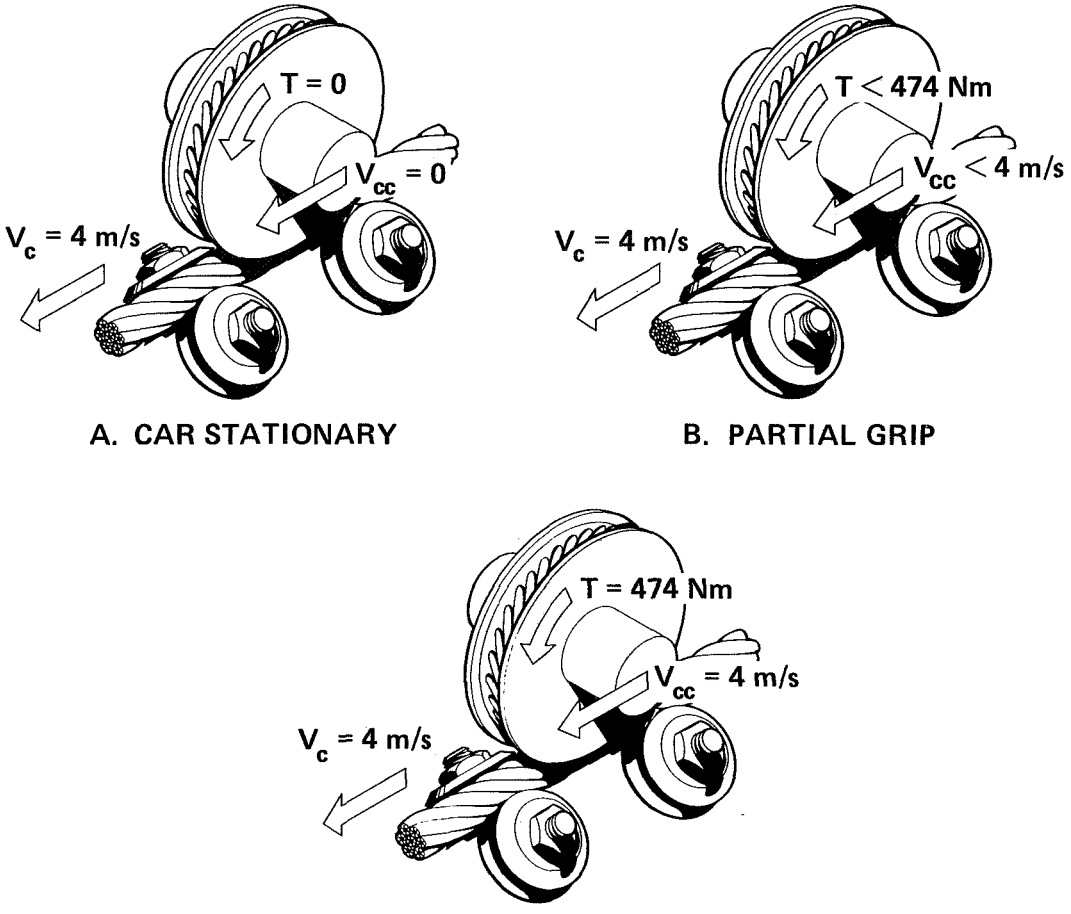

V_c = CABLE SPEED
V_{cc} = CABLE CAR SPEED
T = NET TORQUE ON DRIVE WHEEL FROM HYDRAULIC BRAKING

FIGURE 2. - DRIVE WHEEL-CABLE INTERACTION

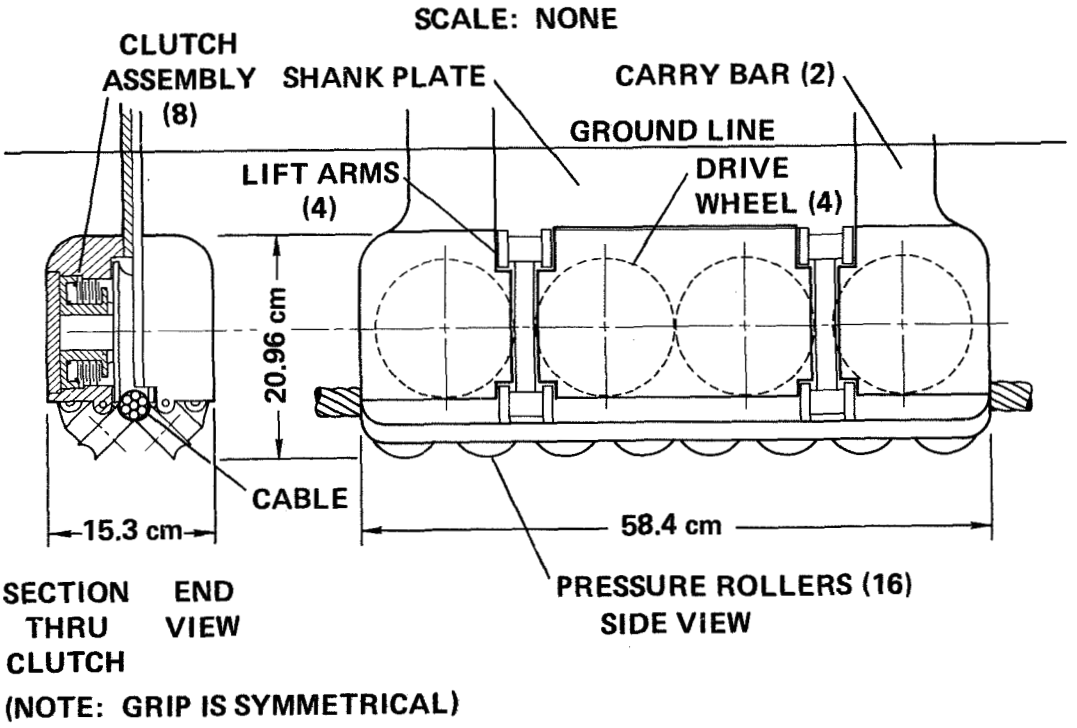

FIGURE 3. - COMPLETE HELICAL GRIP

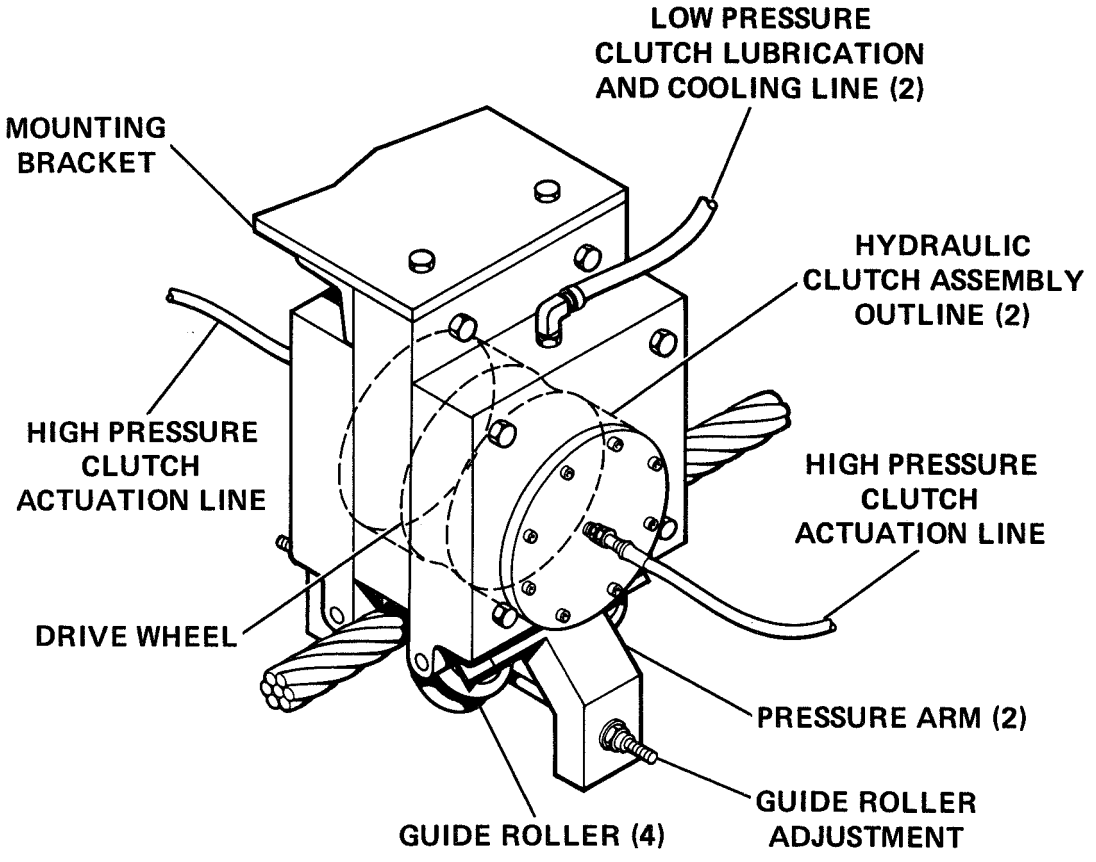

FIGURE 4. - GRIP TEST MODEL

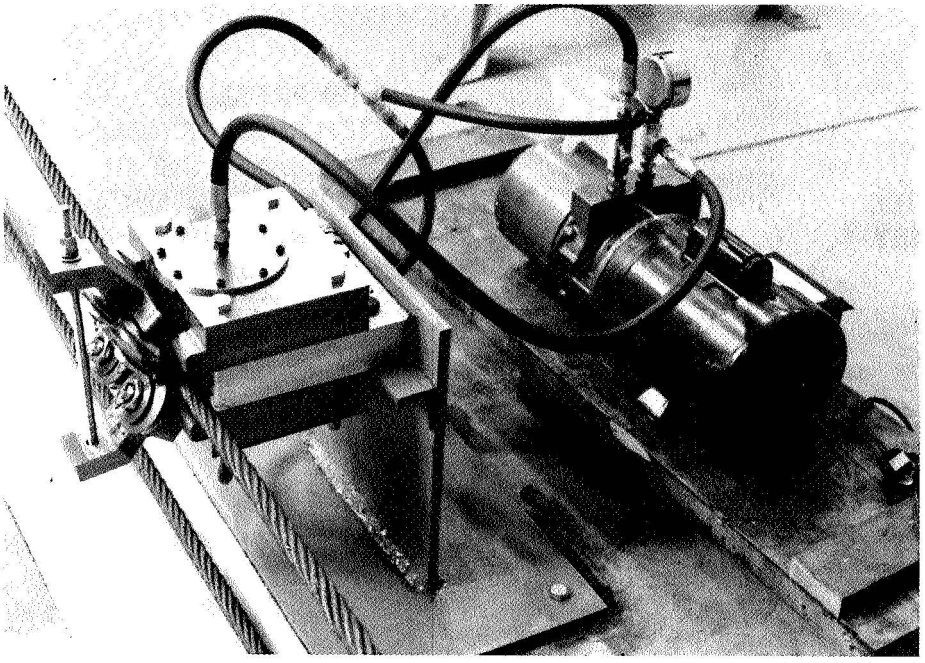

FIGURE 5. - TEST GRIP AND PUMP

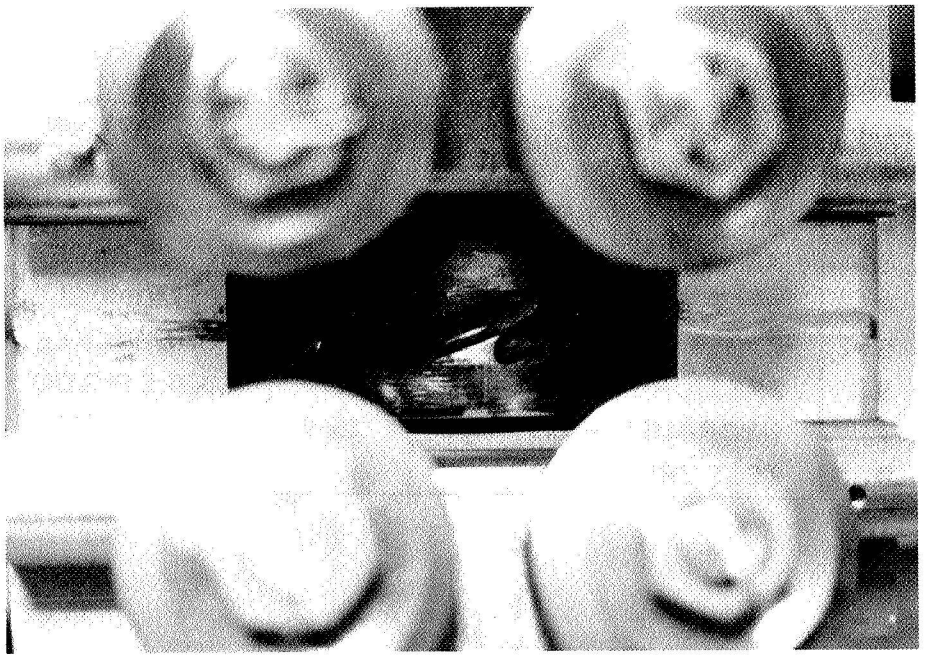

FIGURE 6. - DRIVE WHEEL DETAIL

ITEM	DESCRIPTION	ITEM	DESCRIPTION
1	3 HP MOTOR	9	KLINE GRIP
2	JACK SHAFT ASSEM.	10	WINCH
3	AMMETER	11	FORCE GAGE
4	BELT TENSIONER	12	10 in. DIA. BLOCK
5	CABLE LOOP	13	TURNBUCKLE
6	PRESSURE GAGE	14	CABLE PYLON
7	HYDRAULIC PUMP	15	GRIP PYLON
8	TEST GRIP		

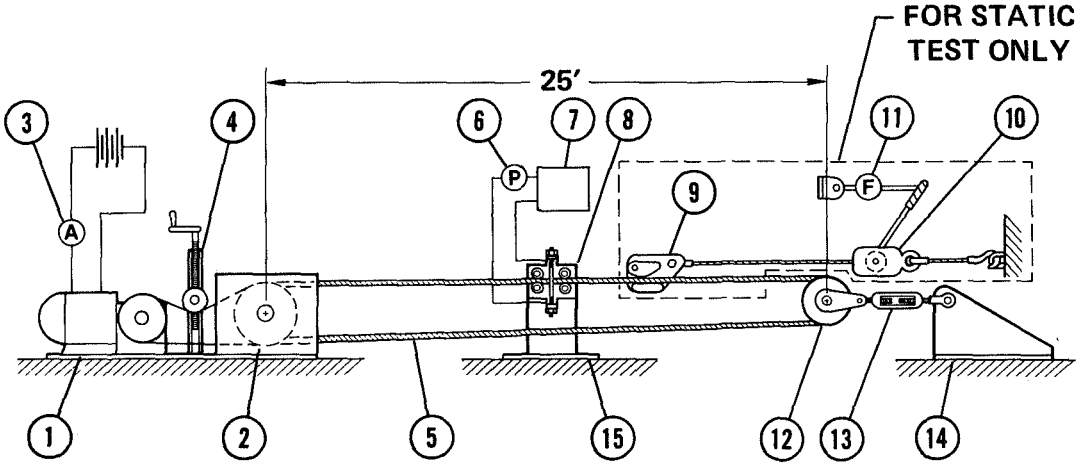

FIGURE 7. - TEST SET UP

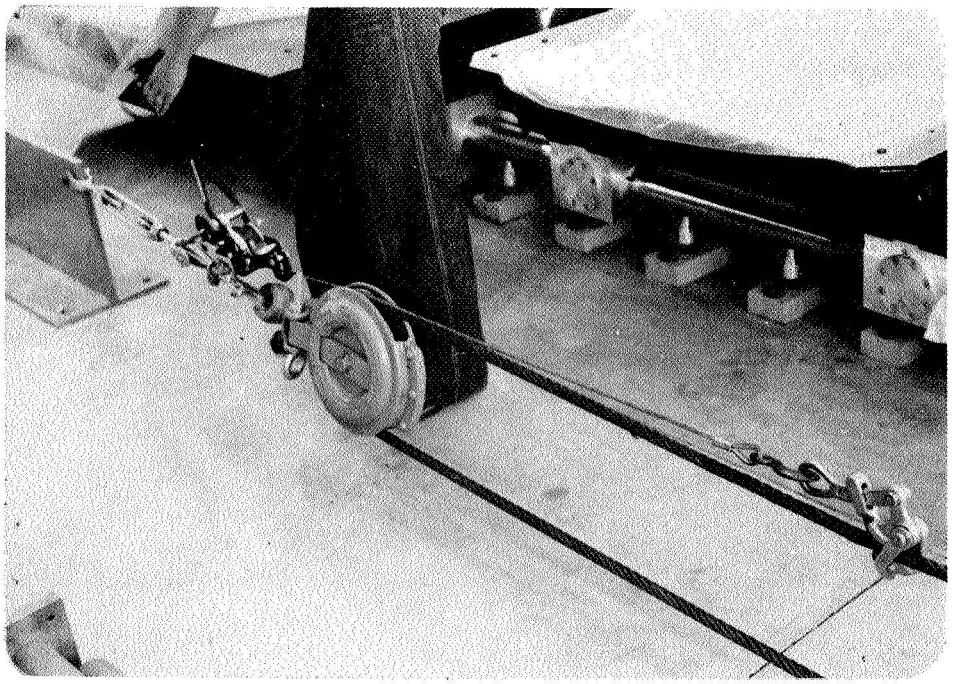

FIGURE 8. - STATIC TEST WITH MANUAL WINCH

LOAD PROPORTIONAL SAFETY BRAKE

Michael J. Cacciola

Boeing Commercial Airplane Company

INTRODUCTION

This brake is a self-energizing mechanical friction brake and is intended for use in a rotary drive system. It incorporates a torque sensor which cuts power to the power unit on any overload condition. The brake is capable of driving against an opposing load or driving, paying-out, an aiding load in either direction of rotation. The brake also acts as a no-back device when torque is applied to the output shaft.

The advantages of using this type of device are:

1. Low frictional drag when driving.
2. Smooth paying-out of an aiding load with no runaway danger.
3. Energy absorption proportional to load.
4. No-back activates within a few degrees of output shaft rotation and resets automatically.
5. Built-in overload protection.

DESCRIPTION

Figure 1 shows a section view of the brake which is made up of two major components, the braking component and the torque sensing component. The braking component is comprised of three separate elements; the energizing brake, the load sensing cams, and the holding brake. The torque sensor is comprised of load sensing detents, load reacting springs and a switch assembly. The brake absorbs energy in proportion to the load and dissipates the energy as heat through an oil filled, finned aluminum housing.

Figure 2 shows the brake assembly without the torque sensing element attached. This type of brake can be used in applications which do not require overload protection.

The input shaft (1) has one outer and one inner set of driving slots, see Figures 1 and 3. The inner set of slots contact lugs on the main brake shaft (2) and provide a straight through drive. They also provide a secondary load path in case of brake failure. The outer driving slots contact lugs on the spring cage (6) which is index splined to the input cam plate (10). This arrangement of driving slots and lugs maintains alignment of the ball detent position on the cam plates (10) (12) and keeps the holding brake de-energized. Because of the symmetry of these parts, the brake will

function when driven in either direction. Return springs (33) provide an axial force to the output cam plate (12) which keeps the three balls (11) seated in their detent position and maintains a gap at the brake plates to eliminate holding brake drag. The energizing springs (7) which are retained in the spring cage (6) provide an axial force to the energizing brake which generates a reaction torque for energizing the holding brake. The reaction torque is transmitted by the stator plates (9) which are grounded to the external housing (3) through spline teeth on the stator (37). Anti-friction thrust bearings (5) (35) are used to carry the force of the energizing springs (7) to minimize frictional drag developed by the relative rotation of the input cam plate (10) and main brake shaft (2) during brake application. Nut (4) is used to react the energizing spring force and to adjust the gap at the energizing brake plates. The load sensing element of the brake is made up of circular ball cams on both the input and output cam plates (10) (12), three balls (11), and a ball cage (36), see Figure 4 and 5. The ball cams are designed to operate in either direction. The cam slope forms a vee which has a radius smaller than the ball radius. This provides a detent effect which prevents movement until the transmitted torque actuates the cam plates. Transverse to the direction of rotation the cam radius is larger than the ball radius. This allows the balls to seek a position where all the balls share the load, and compensates for tolerances on the individual parts. The ball cage (36) is used to capture the three balls and forces the balls to move in unison up the cam surfaces. The brake plates (8) (13) are a special design which have a controlled uniform coefficient of friction. The friction lining is non-metallic and is bonded to a steel core which is splined to the cam plates. The stator plates (9) (14) have an external spline with every other tooth removed, see Figure 3, and provide the mating surface for the brake plates (8) (13). The stator (37) also has every other tooth removed on the internal spline in the area of the holding brake only. Spacers (15) are provided in both the energizing and holding brake to change the braking capacity depending on the load. The load springs (34) are retained in spring cage (16). They supply an axial force to the holding brake in direct proportion to the load. The springs are selected so that the force generated by the load sensing cams is within their working range. This enhances the smoothness of the brake when driving an aiding load. Shim (32) is a laminated shim used to adjust the gap on the holding brake. Nut (18) is used to lock the pressure plate (17) to the main brake shaft (2) for reacting the load spring force. The torque sensor has an input and output detent shaft which retain three balls (20) in countersunk detents. The input detent shaft (19) is splined to the main brake shaft (2) and transfers load to the output detent shaft (31) through the three balls (20). In case of ball disintegration, a secondary load path is provided through a pair of driving lugs with enlarged clearances to allow normal operation. The output detent shaft (31) is splined to the output shaft (26) and has a flange which, when displaced, contacts an anti-friction bearing (22) on the switch assembly. Five belleville springs (30) provide the force to the output detent shaft for retaining three balls (20) in the detents. The spring force is reacted to the input detent shaft through washers (28), an anti-friction thrust bearing (29), and nut (27). A lever (24) and shaft (23) are used to transfer the detent shaft motion to actuate the switch (21). An adjustable stop (25) is provided for the lever (24) to maintain a clearance gap at anti-friction bearing (22) during normal operation.

PRINCIPLES OF OPERATION

Driving Against A Load (Figure 6)

When driving from a stopped position with the brake fully energized, (no-back activated) the initial rotation of the input shaft (1) releases the holding brake. The input shaft (1) supplies torque directly to the main brake shaft (2) through a pair of driving lugs, see Figure 3. The output cam plate (12) is driven by the main brake shaft (2) to align the ball detents. The holding brake allows the cam plate (12) to rotate because of the enlarged clearance between the stator plate (14) and the stator (37) spline teeth. The input shaft (1) simultaneously drives the spring cage (6) through another pair of driving lugs which provide torque to the input cam plate (10) to overcome the energizing brake torque. The cam plates are keyed so that the ball detents are aligned when the driving faces of both sets of lugs are in contact. With the ball detents aligned the return springs (33) provide an axial force to the output cam plate (12) which keeps the three balls(11) seated in the detents. Since the three balls (11) cannot rise up the cam surfaces the brake remains de-energized. Torque is then applied through a spline to the input detent shaft (19) of the torque sensor and transferred through three balls (20) to the detent shaft (31). The output detent shaft (31) is coupled to the output shaft (26) through a spline and transmits the torque to the drive system. When an overload condition is developed the load reacting springs (30) are not supplying enough force to keep the three balls (20) seated in the detents. The output detent shaft (31) is then displaced axially to operate a lever (24) which trips the switch (21) in the electrical control circuit and cuts power to the drive motor.

Stopped-No-Back (Figure 7)

When the drive motor is stopped, the load back drives the main brake shaft (2) and the output cam plate (12). The energizing springs (7) maintain a force on the energizing brake plates which provide a reaction torque to the load through the three balls (11). As torque is applied, relative rotation occurs between the input cam plate (10) and the output cam plate (12). This causes the output cam plate (12) to displace axially as the three balls (11) rise up the cam surfaces and remove the holding brake plate clearance. Further increase in back driving torque displaces the output cam plate (12) to compress the load springs (34) to some force level. When the spring force applied to the holding brake plates (13) (14) generates sufficient torque all movement stops and the load is fully reacted.

Driving An Aiding Load - Paying Out (Figure 8)

When driving an aiding load, the input shaft (1) rotates in the direction of the load and the outer set of driving lugs contact the spring cage (6) which applies torque to the input cam plate (10), see Figure 3. When this torque exceeds the difference between the energizing brake torque and the reaction torque of the three balls (11), the main brake shaft (2) rotates under the influence of the load. The load springs (34) modulate the force of the load sensing cams on the holding brake plates (13) (14) which generate a holding torque permitting the load to pay out smoothly at drive motor speed.

SYMBOLS

T_1	=	Input Torque	T_o	=	Output Torque
T_D	=	Drag Torque	T_M	=	Main Brake Torque
T_B	=	Torque Across Ball	F_E	=	Energizing Spring Force
F_M	=	Modulating Spring Force	F_R	=	Return Spring Force
F_A	=	Axial Force At Ball	F_t	=	Tangential Force At Ball
μ	=	Coefficient Of Friction	r_D	=	Drag Brake Plate Radius
r_M	=	Main Brake Plate Radius	r_B	=	Radius To Ball
n_D	=	Number Of Drag Brake Surfaces	n_M	=	Number Of Main Brake Surfaces
$\emptyset$	=	Cam Slope Angle			

MAXIMUM CAM SLOPE ANGLE

For a given load the axial force on the ball is: (See Figure 7)

$$T_o = F_A(\mu r_M n_M + \text{Tan}\emptyset r_B) - F_R \mu r_M n_M$$

$$F_A = \frac{T_o + F_R \mu r_M n_M}{\mu r_M n_M + \text{Tan}\emptyset r_B}$$

Minimum Holding Brake is:

$$T_D = T_B$$

$$F_A \mu r_D n_D = F_A \tan\emptyset r_B$$

Substituting for F_A:

$$\frac{T_o + F_R \mu r_M n_M}{\mu r_M n_M + \tan\emptyset r_B}(\mu r_D n_D) = \frac{T_o + F_R \mu r_M n_M}{\mu r_M n_M + \tan\emptyset r_B}(\tan\emptyset r_B)$$

Solution of the above equation resolves into a quadratic of the form:

$$A \tan\emptyset^2 + B \tan\emptyset - C = 0$$

Substituting values for all the known terms and solving for $\emptyset$ will give the maximum cam slope angle which will hold the load without slipping.

BRAKE STABILITY

The brake as described in Figures 1 and 2 is easily proportioned to be self-energizing and capable of holding a load in the static or stopped

condition. The critical condition is driving or paying out an aiding load smoothly without brake chatter. Chatter is an unstable condition in which the brake is rapidly cycling between locked-up and released.

The following items are required to insure stable operation of the brake:

1. Friction material with a stable coefficient of friction throughout the operating range of temperature and brake plate pressure.

2. Combination of friction material and oil which minimizes the fluctuation between static and dynamic coefficient of friction.

3. Correct load balance between the energizing brake and the main holding brake.

4. Modulating spring rate to balance maximum axial load developed by the ball cams.

Another method of producing a stable brake is to reduce the torque capacity of the energizing brake to a value below the ball torque and then add a constant drag brake to the input shaft. The affect of reducing the energizing brake is to make the brake reversible, but the addition of the constant drag brake in conjunction with the other braking elements makes the brake irreversible and capable of reacting the full load. When driving an aiding load, the input torque need only overcome the margin of the constant drag brake which allows the load to pay-out. Figure 9 shows a constant drag brake applied to the input shaft with a ratcheting device which bypasses the brake when driving against a load.

Figure 10 shows the drive system of the Boeing Model 747 On-Board Loader which used two brakes in a dual load path arrangement. The final design of the brake as delivered was as shown in Figure 1.

ANALYSIS OF ON-BOARD LOADER BRAKE

Weight of platform and payload - 34,000 lb.
Torque at cable drum - 102,000 in-lb.
Torque at brake - 1,090 in-lb.

Brake Design Parameters:

r_D = 2.47 in.
r_M = 2.47 in.
r_B = 2.50 in.
n_D = 4
n_M = 6

F_E = 60 lb.
F_R = 30 lb.
F_M = 552 lb.
μ = .12-.10 oper.
μ = .06 Min.

CHECK CAM SLOPE ANGLE

$$\frac{T_o + F_R \mu r_M n_M}{\mu r_M n_M + \tan\phi r_B} (\mu r_D n_D) = \frac{T_o + F_R \mu r_M n_M}{\mu r_M n_M + \tan\phi r_B} (\tan\phi r_B)$$

Substituting values for all known terms and the minimum coefficient of friction, the above equation resolves into the following quadratic:

$$172.975 \tan \phi^2 + 20.5079 \phi - 14.5885 = 0$$

Solution of the quadratic gives the maximum cam slope angle which will allow the brake to support the load without slipping.

Solution: $\phi = 13.34^o$

To allow for tolerances we will use $\phi = 12.50^o$

DRIVING AN OPPOSING LOAD (See Figure 6)

Input Torque:

$$T_1 = F_E \mu r_D n_D + T_o$$

$$= 60 (.11) 2.47 (4) + 1090$$

$$T_1 = 1155 \text{ in-lb}$$

STOPPED WITH LOAD APPLIED (See Figure 7)

Axial Force:

$$F_A = \frac{T_o + F_r \mu r_M n_M}{\mu r_M n_M + \tan\phi r_B}$$

$$= \frac{1090 + 30 (.11) 2.47 (6)}{.11 (2.47) 6 + \tan 12.50^o (2.5)}$$

$$F_A = 521.4 \text{ lb}$$

For brake to be irreversible:

$$T_D > T_B$$

$$T_D = F_A \mu r_D n_D$$

$$= 521.4 (.11) 2.47 (4)$$

$$T_D = 566.7 \text{ in-lb}$$

$$T_B = F_t r_B$$

$$= F_A \tan\phi r_B$$

$$= 521.4 \tan 12.50^{o} (2.5)$$

$$T_B = 288.9 \text{ in-lb}$$

$$T_D > T_B$$

$566.7 > 288.9$ ∴Brake is irreversible

BRAKE HOLDING MARGIN

$$T_M = F_M \mu r_M n_M$$

$$= (521.4 - 30) .11 (2.47) 6$$

$$T_M = 801.1 \text{ in-lb}$$

Margin:

$$\frac{T_D + T_M}{T_o} = \frac{566.7 + 801.1}{1090}$$

Margin = 1.25

DRIVING AN AIDING LOAD (See Figure 8)

Input Torque:

$$T_1 = F_A (\mu r_D n_D - \tan\phi r_B)$$

$$= 521.4 \left[.11 (2.47) 4 - \tan 12.50^{o} (2.5) \right]$$

$$= 566.7 - 288.9$$

$$T_1 = 277.8 \text{ in-lb}$$

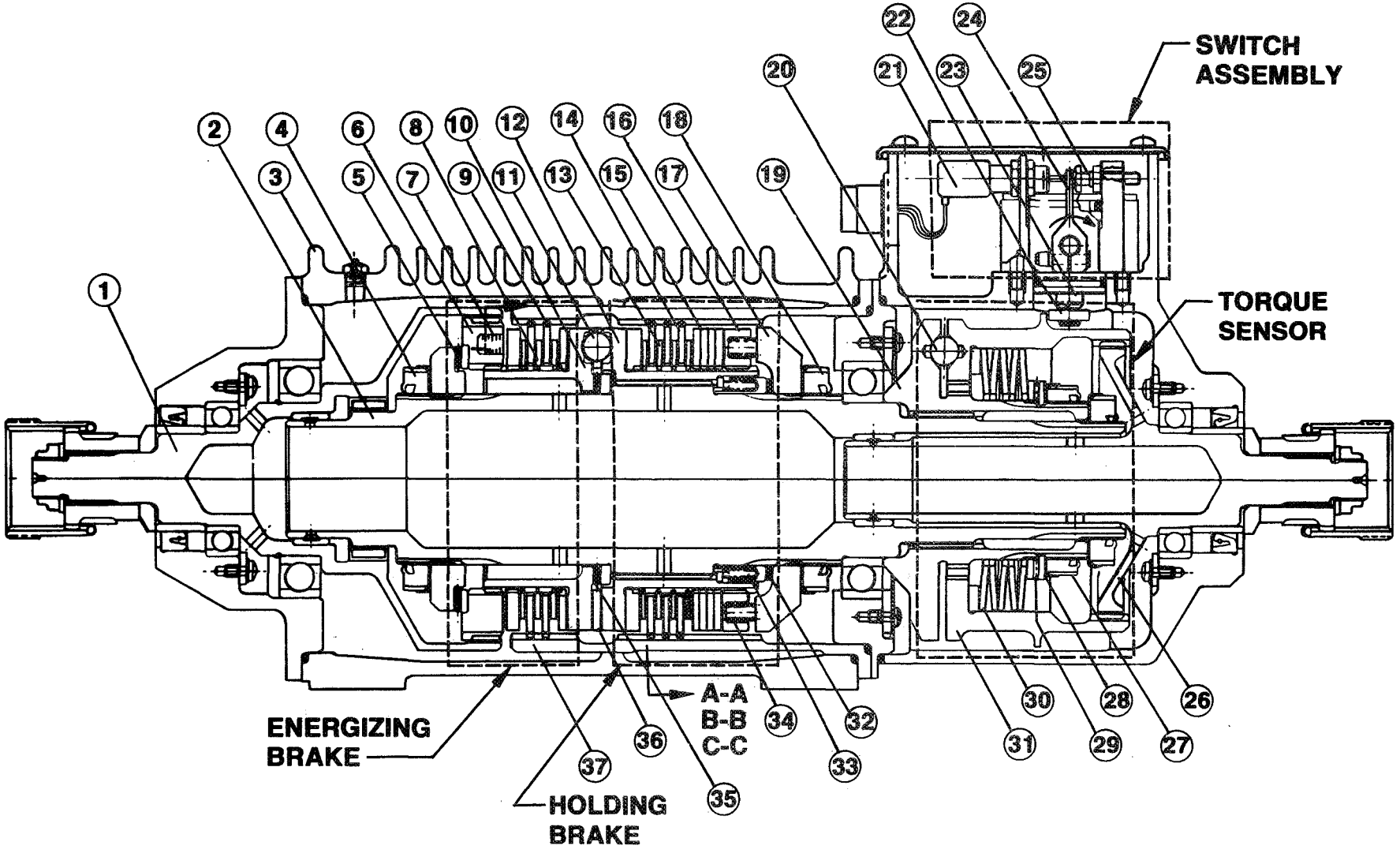

Figure 1

Energy Absorbing Brake With Torque Sensor

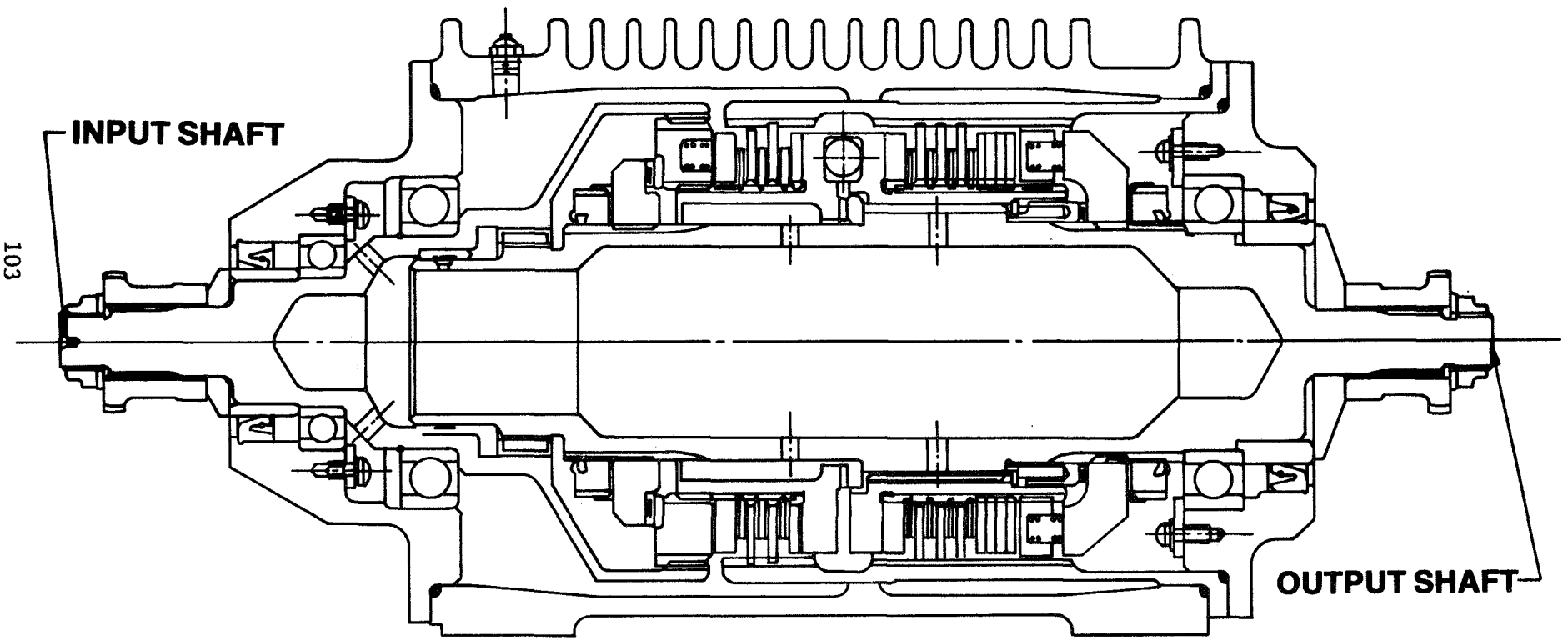

Figure 2

Energy Absorbing Brake

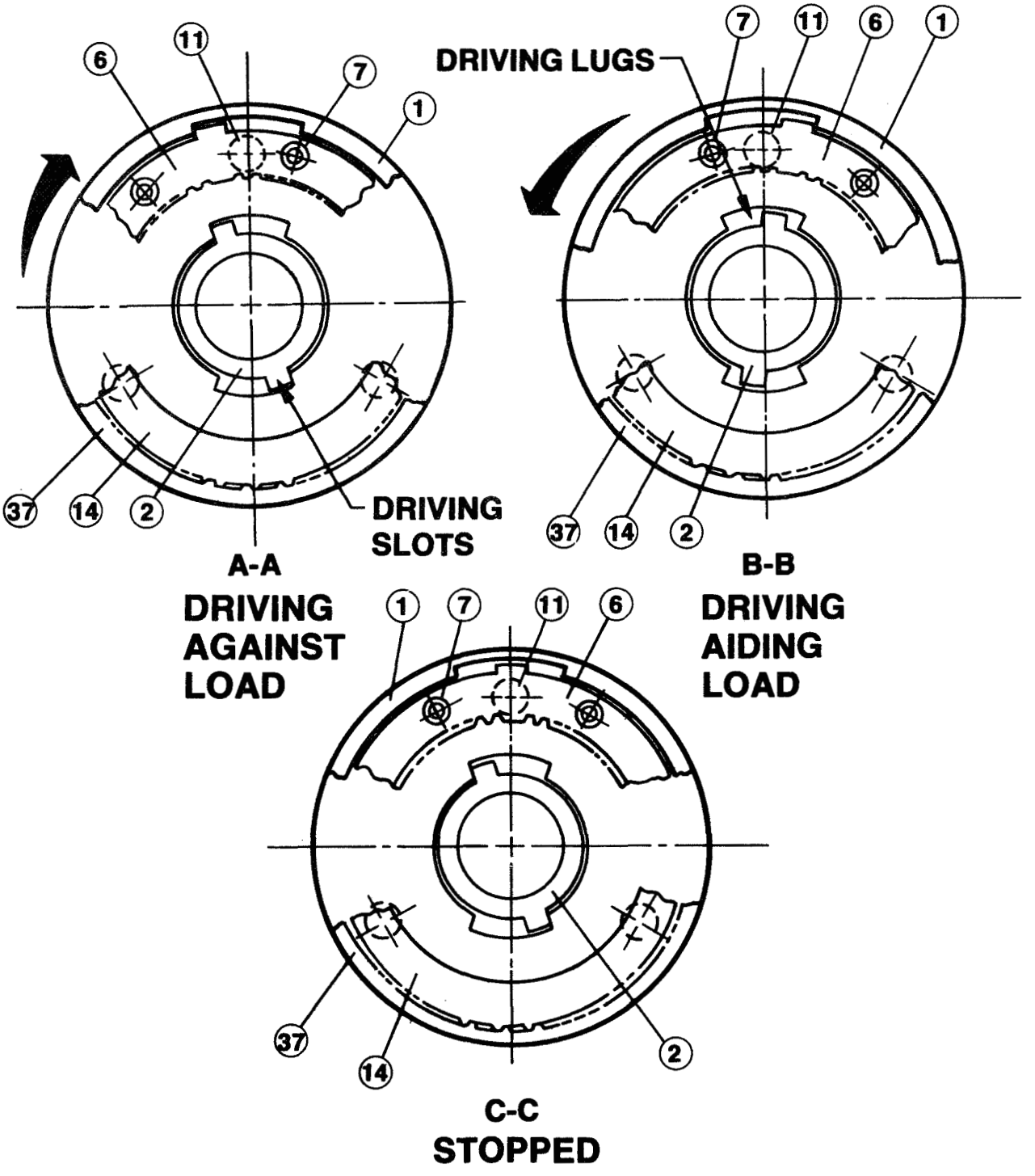

Figure 3

Sections Through Driving Members

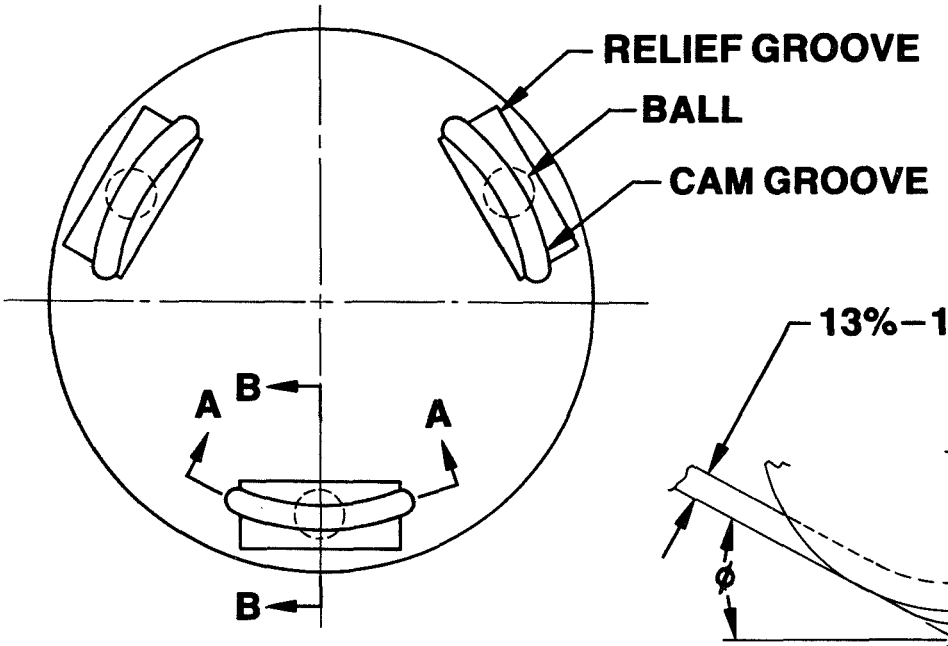

PLAN VIEW

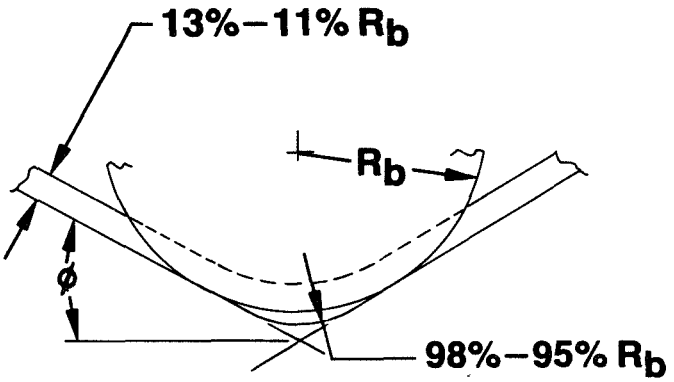

SECTION A-A
(UNWRAPPED)

Figure 4

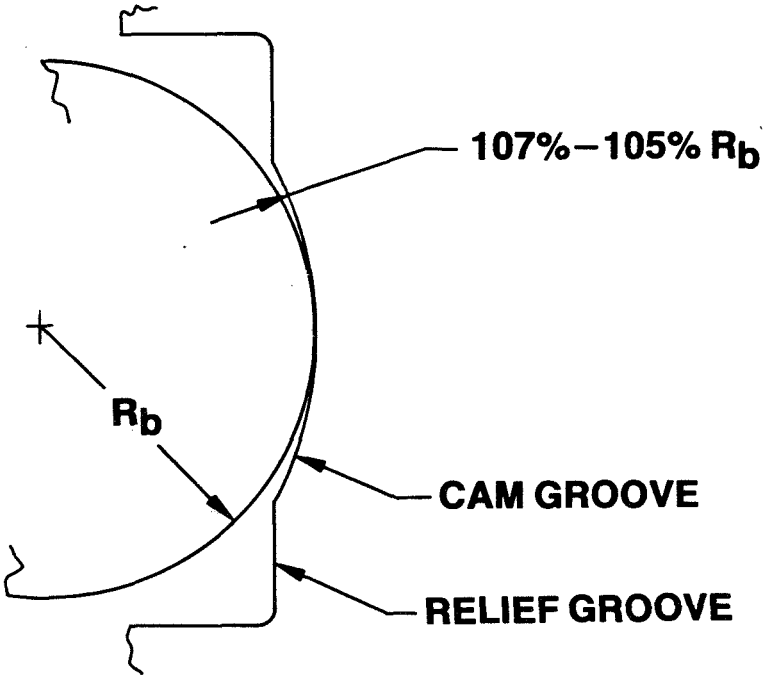

SECTION B-B

Figure 5

Ball Cam Groove

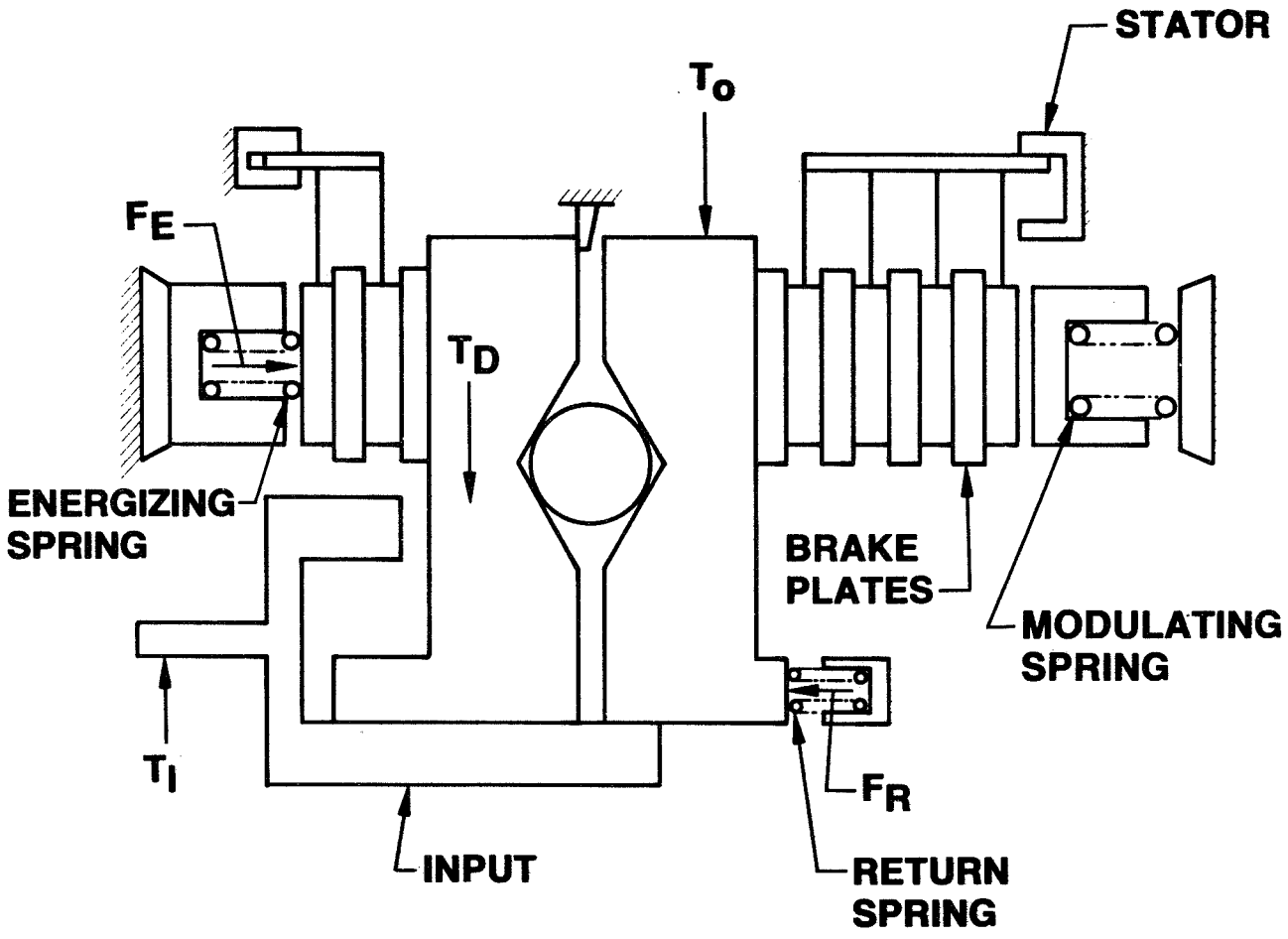

$$T_I = T_D + T_O \qquad T_D = F_E \mu r_D n_D$$

$$T_I = F_E \mu r_D n_D + T_O$$

Figure 6

Driving an Opposing Load

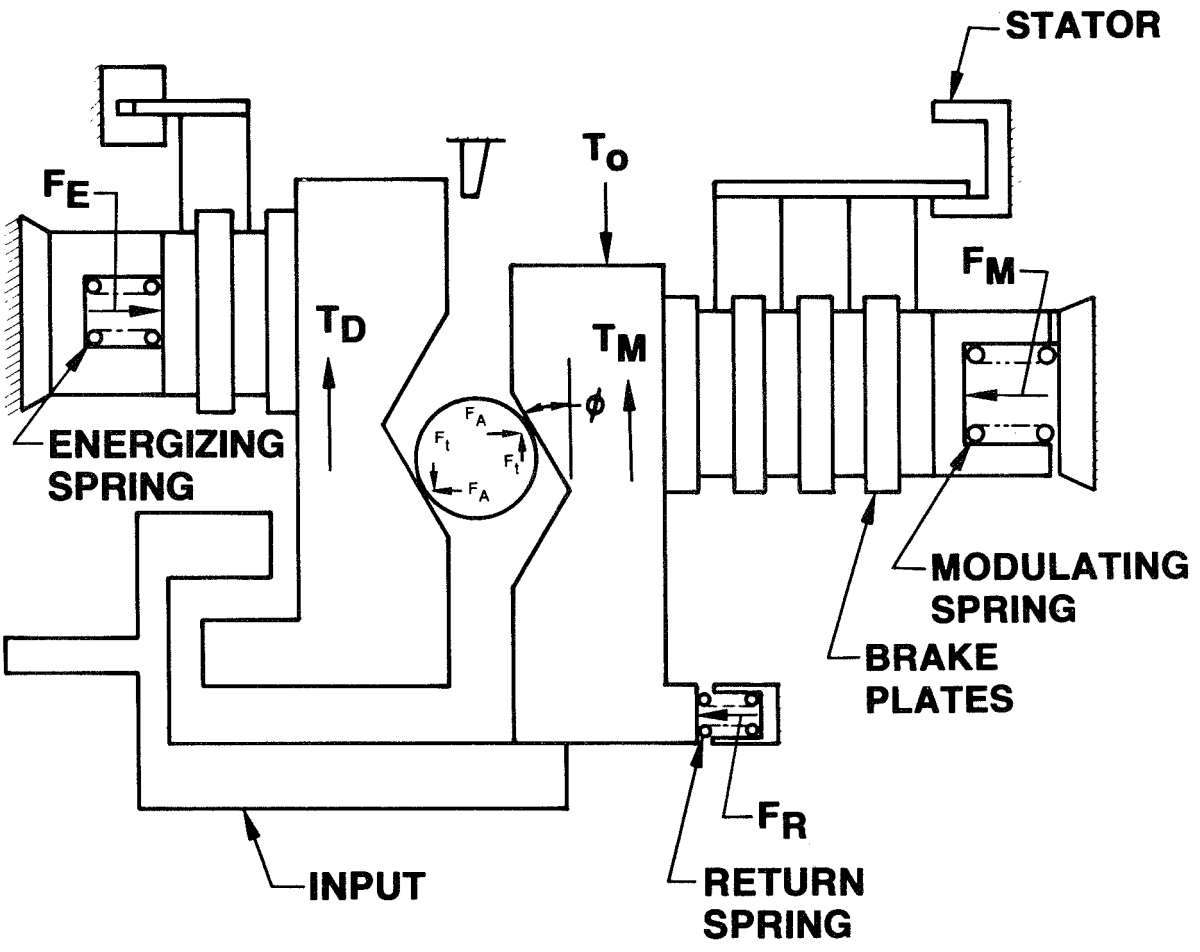

$$T_O = T_M + T_B$$
$$T_O = F_M \mu r_M n_M + F_t r_B$$
$$T_O = (F_A - F_R)\mu r_M n_M + F_A \tan\phi r_B$$
$$T_O = F_A(\mu r_M n_M + \tan\phi r_B) - F_R \mu r_M n_M$$

$$T_M = F_M \mu r_M n_M$$
$$T_B = F_t r_B$$
$$F_A = F_M + F_R$$
$$F_t = F_A \tan\phi$$

FOR BRAKE IRREVERSIBLE:

$T_D > T_B$

$$T_D = F_A \mu r_D n_D$$

Figure 7

Stopped With Load Applied

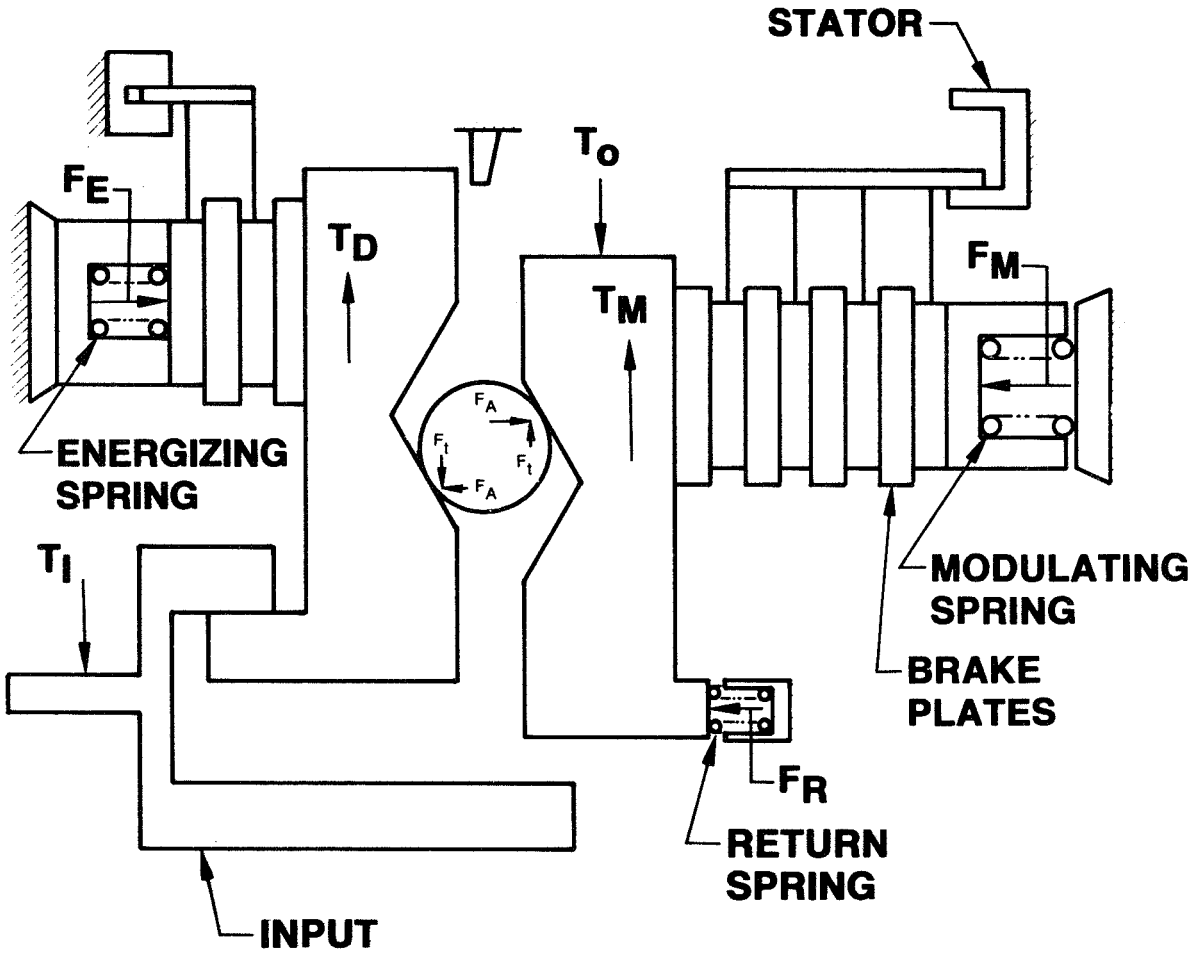

$$T_I = T_D - T_B$$
$$T_I = F_A \mu r_D n_D - F_t r_B$$
$$T_I = F_A \mu r_D n_D - F_A \tan\phi\, r_B$$
$$T_I = F_A (\mu r_D n_D - \tan\phi\, r_B)$$

$$T_D = F_A \mu r_D n_D$$
$$T_B = F_t r_B$$
$$F_t = F_A \tan\phi$$

Figure 8

Driving An Aiding Load

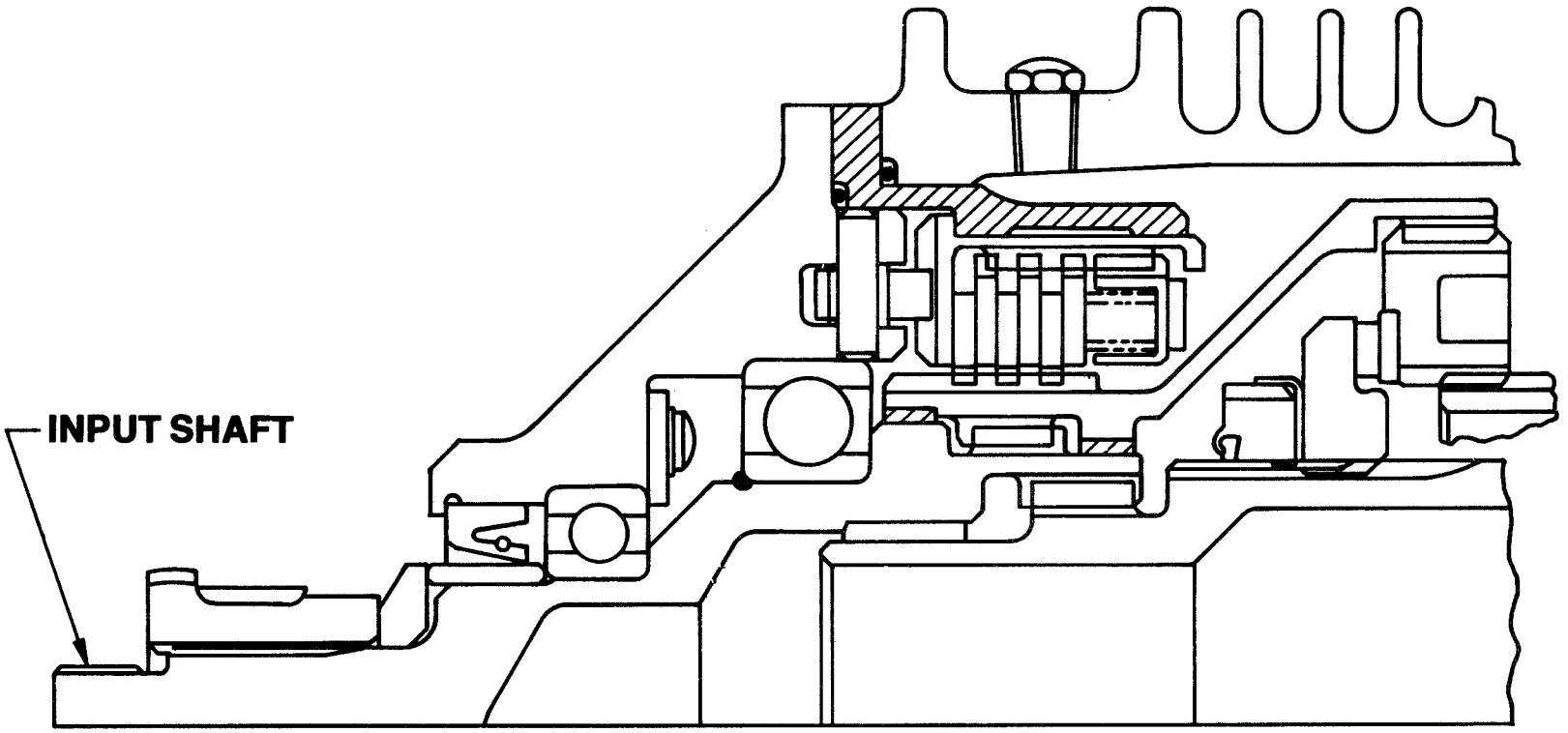

Figure 9

Constant Drag Brake

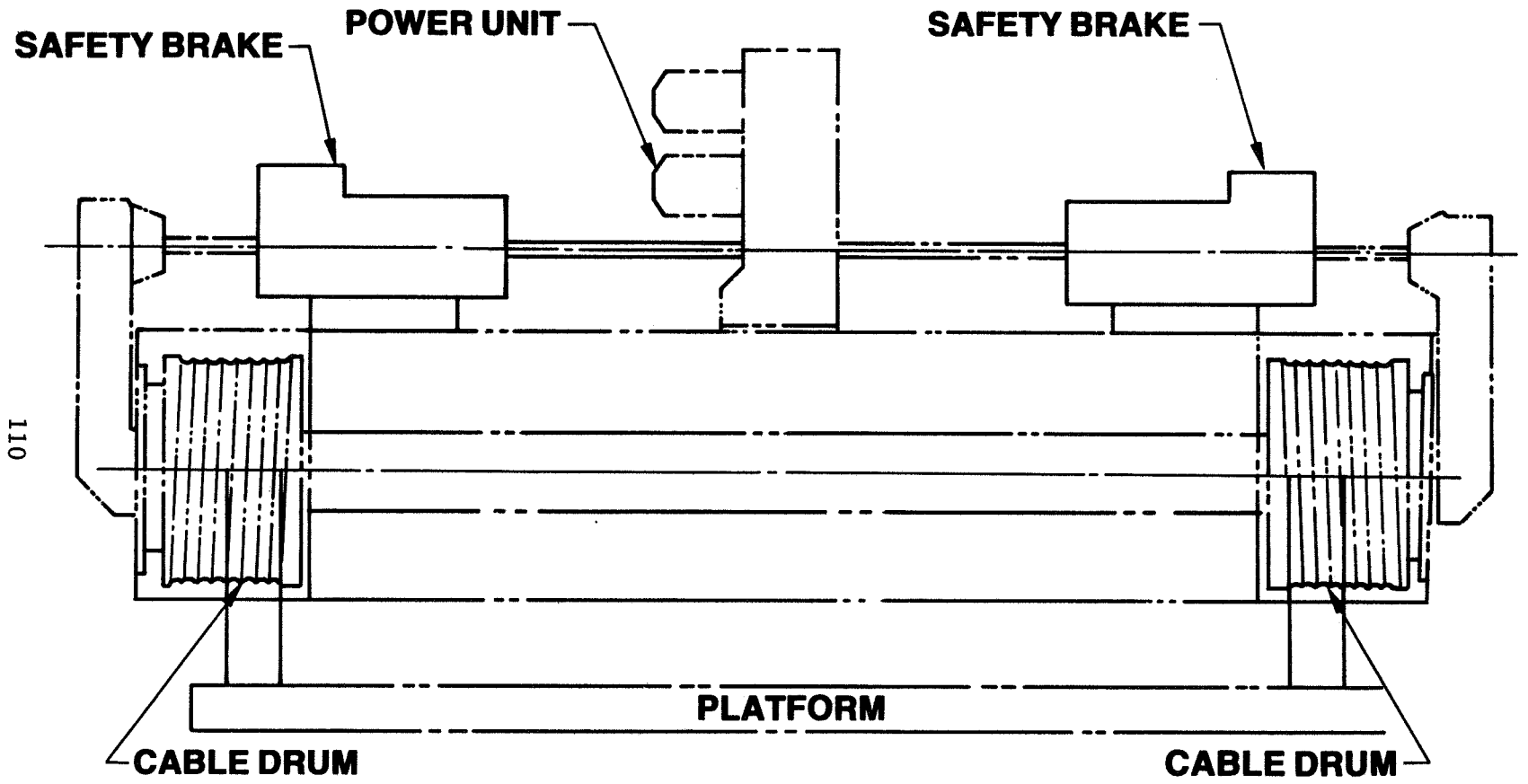

Figure 10

On-Board Loader Drive System

A ZERO "G" FLUID DROP INJECTOR FOR THE DROP DYNAMICS MODULE SPACELAB EXPERIMENT

by George M. Hotz*

ABSTRACT

A fluid drop injector has been developed to form and release fluid drops into free drift within an experimental apparatus known as the Drop Dynamics Module which is to be flown on an earth orbiting Spacelab. To verify the design concept, a breadboard injector was flown on the NASA KC-135 zero "g" airplane after which more extensive laboratory 1 g tests were performed to improve the injector design and enable it to meet the module's functional requirements. The breadboard fluid drop injector will be modified and upgraded to flight hardware.

INTRODUCTION

A fluid drop injector has been designed, breadboarded, and tested for use in a science experiment facility known as the Drop Dynamics Module (DDM). The experiment is expected to be flown initially on Spacelab III. This zero "g" experiment facility will be used for various fluid drop experiments, the first of which is to study the dynamics of free fluid drops to verify existing theory, with potential application to droplet behavior in chemical processing, containerless processing of molten material and meteorology. The DDM will be installed in a double rack in a pressurized payload module, thus operating in a "shirtsleeve" environment.

The experimental apparatus comprises a chamber into which fluid drops are formed and released, an acoustical drop positioning and manipulating system, and a data collection system consisting of a movie camera which views the drops from three directions, see figure 1. The acoustical positioning and manipulation system produces drop centering forces through pressure gradients produced by standing waves generated by three acoustical drivers. The acoustics can also rotate or oscillate the drop through variation of the phase and amplitude of the acoustic waves. The DDM is being implemented as an

* Jet Propulsion Laboratory, Pasadena, CA 91103

automated experiment to minimize attention by the Payload Specialist, who will be required only to perform such tasks as replacing consumables, viz, changing fluid containers, film magazines and data tape cassettes, and chamber cleanup in experiments where fluid drops fragment and strike the chamber walls.

The fluid drop injector is required to produce drops of various fluids such as water and silicone oils of widely varying viscosities, surface tensions and densities, and of various sizes from about 0.6-2.5 cm (¼-1") in diameter. It must then release the drops in the center of a nearly cubical transparent chamber of about 15 cm cube (6") with essentially zero drift velocity and with minimal rotation, oscillation or production of secondary droplets and then must retract from the chamber.

FLUID INJECTOR REQUIREMENTS

Drop Volume,	0.25-10 cc (accurate to $\pm$0.03cc)
Fluid Viscosity Range	1-1000 centistoke(cs)
Fluid Pumping Rate	0.1-1.0 cc/sec
Maximum Drop Velocity (after release)	0.1 cm/sec
Maximum Secondary Droplet Volume	0.10% of drop volume

No contamination of drop with previous liquid used.
Form drops in 10^{-3} g field with no acoustical force field.
Release drop with minimum oscillation and rotation.

INITIAL FLUID INJECTOR DESIGN

1. To prevent cross contamination of fluids, all parts which contacted the fluid, such as pumps and injectors, would handle only a single fluid.

2. To provide accurate metering and minimize the net momentum of the drop, dual positive displacement pumps would be employed, operated by a single stepper motor. Each pump would discharge fluid through opposite facing injectors, thus providing equal flow rates with total volume proportional to the number of commanded motor steps.

3. Since the optimum positioning of injectors during drop growth and the optimum positioning and velocity of injectors during release of the drop were unknown, it was decided that programmable injector position and velocity servos would be employed for maximum design flexibility.

4. Since injector tip design was unknown, tips would be made replaceable. If possible, injector tips would utilize surface tension forces to stabilize the drops during drop growth.

5. Major unknowns in the design were parameters which controlled the production of secondary droplets.

BREADBOARD FLUID PUMP, INJECTORS & INJECTOR DRIVERS

Breadboard fluid drop producing devices were built in accordance with the initial design noted above. The pump, shown in figure 2, uses a computer controlled 200 step/revolution stepper motor to rotate a lead screw - a 5 cm (2") travel micrometer head - through suitable gearing to provide about 4.8 cm (1.9") of travel to a pump driver which pushes the plungers of two 50 cc gastight fluid filled syringes.

The driver is guided by three miniature ball bushings running on two guide rods. The gearing was selected to produce a fluid flow of very nearly 0.002 cc/motor step; thus, a 10 cc drop requires 5000 motor pulses which can be stepped in from 10 to 100 seconds. The motor is operated in the open loop mode.

Fluid discharged from the syringes flows through fluorocarbon elastomeric tubing to two oppositely facing injector tubes installed along a line passing through the center of the chamber. The injectors are, in turn, moved in and out of the chamber as desired by motor operated injector drivers, see figure 3, which are position and velocity servo controlled by computer operated controllers.

Each injector is installed in the hollow injector driver which is positioned axially by a rack machined into the driver. The driver is guided by three sets of rollers, one of which is spring loaded, and is driven by an aircraft quality dc motor through two stages of anti-backlash reduction gears. The drive gear for the rack also directly rotates both the injector position (single turn) potentiometer and, through suitable gearing, a small ironless armature dc motor which generates the voltage employed by the injector velocity servo. The injectors are guided by the rollers with sufficient accuracy to align their centerlines within a few thousandths of an inch when they meet at the chamber center. Although the functional requirements originally called for a minimum retraction velocity velocity of 100 cm/second in a distance of 0.5 cm - and the velocity of the breadboard injectors and drivers approached that velocity - investigations to be described later showed that the optimum retraction velocity was less than half that figure. The lower velocity was achieved by operating the motors at reduced voltage.

Replaceable injector tips are installed at the outlet end of each injector to suit the fluid characteristics and discharge rate. Replacement of syringes, injectors and flexible tubing is facilitated through the use of split, hinged clamps which secure the syringe barrels and plungers. Bubble free filling of fluid containers is essential and is expected to be a ground based operation.

FLUID DROP STABILITY ON A SINGLE INJECTOR TIP

Investigations indicated that there is a basic difference in the equilibrium positioning of fluid drops suspended on an injector tip in zero "g" if the contact angle between the drop and the tip is greater than 90^{o} in the one case and less than 90^{o} in the other. Figure 4 illustrates this point. If the fluid/tip contact angle is greater than 90^{o}, as is the case for a water drop on a wax coated metal tip, the drop will not allow itself to be impaled on the injector tip but will move tangent to the end of the tip to maximize its surface energy. Figure 4 also shows that for liquid/tip

contact angles of less than 90^{o}, e.g., a silicone oil drop on a PFOMA* coated metal tip, the drop cannot be made to stay tangent to the end of the tip (without the application of an external force) but will move back until the front of the drop is tangent to the end of the tip (i.e., the drop is impaled on the tip).

This difference in drop behavior (oil vs. water) can be eliminated by making both oil and water have a contact angle of 0^{o} which would make both behave like oil, with drops impaled on the tip. This idea was discarded as was the use of a single injector tip for three reasons:

(a) Deep immersion of the drop in the injector was suspected as being a contributor to the production of secondary droplets.
(b) Release of the drop with near zero net momentum in the absence of an acoustical centering force field appeared difficult.
(c) Achieving a 0^{o} contact angle required careful cleaning of the surfaces being contacted and high purity of the fluids. Maintenance of required tip cleanliness for multiple injections under flight experiment conditions would be difficult.

Accordingly the use of two PFOMA coated injectors was selected.

FLUID DROP STABILITY ON TWO INJECTOR TIPS

Figure 5 illustrates three possible injector tip shapes and indicates the net stability of a drop in the axial and radial directions resulting from the surface tension forces for fluid and tip coatings having contact angles 1) greater than 90^{o}; e.g., water/paraffin, glycerine/teflon, mercury/iron, etc., and 2) less than 90^{o}; e.g., petroleum or silicone oil/PFOMA, kerosene/glass, etc. It shows that for water on a "non-wetting" coating such as paraffin, drop stability can be achieved at the chamber center through the use of truncated cone shaped tips with small ends facing, whereas for silicone oil on a "non-wetting" coating such as PFOMA, stability can be achieved with truncated cones with bases facing each other. Therefore, other conditions

* poly (1,1-dihydropentadecaflourooctylmethacrylate)

permitting, the two cone shaped injector tips noted would be used.

IS PROGRAMMED INJECTOR MOTION NECESSARY?

The difference in direction of the axial force vectors for oil and water drops in contact with PFOMA* coated injector tips, figure 5, implies that oil drops and water drops require different injector positions during drop growth if programming of the motion is to be avoided. With water drops, the tips should be moved apart to a separation equal to or somewhat greater than the final drop diameter, and kept fixed during drop growth, whereas with oil the tips must be moved to a separation equal to the tip inside diameter or less and then held there until the drop is fully grown. Alternatively for both fluids, the tips can be moved together until they almost touch, then the fluid pumped until the two streams coalesce into a single drop, after which the injectors must be withdrawn at a varying rate so as to keep the drop periphery tangent to the two tips.

Determination of which motion technique was better awaited test results.

KC-135 ZERO "G" TEST

The breadboard pumps, injectors, and injector drivers, shown in figures 2 and 3 were tested qualitatively in three flights of the NASA KC-135 airplane at Clearwater, Texas in mid-1978, and demonstrated that water and silicone oil drops could be formed in zero "g" with and without the acoustical field, see figure 6. However, the flights did not demonstrate that the functional requirements could be met since the severe time limitations of zero "g"** and generally poor "g" conditions preceding and following "free float" necessitated injector tip geometries and fluid pumping rates not conducive to meeting these requirements, e.g., large diameter tips and high fluid pumping rates. The high speed motion pictures taken on the KC-135 flights did not provide adequate resolution to make accurate assessments of satellite (secondary) droplet sizes, but it was apparent that secondary drop volumes

* There is no known coating capable of increasing the contact angle of silicone oil to >90°.

** Zero "g" float durations were usually 5-10 seconds.

were much greater (20-30 times greater) than the 0.1% permitted by the functional requirements. Residual drop velocity was also difficult to determine and it was seldom possible to assess whether the airplane and/or experiment operators contributed to the drop velocity rather than the fluid injectors.

The KC-135 tests showed that the sources of drop disturbance and secondary droplets produced in drop release were the columns of fluid extending from either side of the drop in the wake of rapidly retracting injector tips. It was not known whether the sources of these columns were fluid pulled from the drop or fluid trailed from the rapidly accelerating injectors. In any case, after the columns attained some maximum length, they broke up into droplets whose diameter was approximately the column diameter.

In the formation of silicone oil drops on the KC-135, due to a programming error, the injector tips were moved apart before sufficient oil had been pumped and resulted in the formation of two drops instead of one. After several such runs, the controller was switched to manual operation and the injector tips were held close together during the entire fluid pumping period which resulted in the formation of single oil drops.

LABORATORY INJECTOR PARAMETRIC TESTS

Next laboratory tests were conducted to optimize injector parameters to (a) reduce the production of satellite droplets to less than 0.1% of the drop volume as called for in the functional requirements, and (b) minimize the disturbance to the drop caused by injector withdrawal. In addition, since only water and 100 cs silicone oil were injected on the KC-135 flights, oil of other viscosities, viz.,1000 cs and 10 cs were also tested. Injector tips and operating parameters were included which were identical to those used on the KC-135 flights for comparison. Parameters investigated included tip diameter, cone angle (for water tips), immersion depth into drop, and injector retraction velocity.

Since the KC-135 tests with 100 cs silicone oil had indicated that the total volume of secondary droplets was essentially independent of drop size, it was decided that the simplest test procedure would be to use a cup filled with oil (or water), simulating a drop of infinite radius and mount a single injector with its drive mechanism over the cup, immerse the injector tip to the desired depth in the fluid and withdraw the tip vertically upward at the desired speed while taking high speed motion pictures of the tip, surface disturbance and column or droplets of fluid.

Preliminary runs with various fluids noted indicated that the test procedure described above was adequate for determination of relative drop disturbance of all fluids. It was also adequate for testing relative secondary droplet volumes for water and 10 cs silicone oil, but it was marginal to poor for 100 cs silicone oil and totally unsatisfactory for 1000 cs silicone oil. This was due to the higher viscosity fluids stringing out to a length corresponding to full travel of the injector, then streaming down from the motionless injector under the influence of gravity until they had necked down to a smaller diameter column which finally broke up into satellite droplets, but not of the correct size nor volume.

As a consequence, it was decided to employ another technique for satellite droplet volume determination. This technique involved the operation of the injector in a horizontal or near horizontal attitude instead of vertical. Two arrangements were tried, the first having the tip pass through a clearance hole in the side of a cup. The hole was located close to the fluid top surface and sized so that fluid surface tension prevented leakage of fluid from the cup when the tip was inserted through the hole. The second arrangement used a cup filled to the top, into the surface of which the tip was inserted at an angle of about 15^{o} above horizontal. Both of these techniques were satisfactory.

Another preliminary test was made to determine the source of the fluid which formed the column of fluid and, in turn, produced the secondary droplets. Injector tips were connected to a hypodermic syringe filled with the appropriate fluid and fluid was forced from the tip into the simulated drop (i.e., the

cup) just before tip retraction. The tip was then retracted and the column and secondary droplets photographed (see figure 7). Similar tests were performed using tips with no orifices (rods were used instead of tubes). As results indicated only a minor difference in drop disturbances or production of satellite droplets with the two techniques, rods were used for subsequent tests and the conclusion reached was that the fluid forming the columns came from the drop.

LABORATORY TEST RESULT TRENDS

Test results generally confirmed expected trends, i.e.:

1) Smaller diameter injector tips produced smaller drop disturbances and smaller volumes of secondary droplets.
2) Smaller tip immersions produced smaller drop disturbances and decreased secondary droplet volumes.

Unexpected trends included the following:

3) Decreased injector withdrawal velocities (within the range tested) produced smaller secondary droplet volumes.

LABORATORY TEST RESULT - DISCUSSION

Results shown in figure 8 indicated that the secondary droplet volumes specified by the functional requirements could only be met through the use of very small size tips and/or minimal immersion of the tips into the drops. Minimal immersion of injectors meant that accurate programming of injector motion during the growth of oil drops was essential. The feasibility of these parameters depended upon other factors such as:

1) Could the small tip diameter produce sufficient stabilizing surface tension forces to retain the drop in a 10^{-3} g force field?
2) Was the injector driver servo resolution sufficient to permit small injector tip immersions?

3) Did the small tip allow acceptable fluid pumping rates with high viscosity fluids?

A calculation of the diameter of injector tip required to retain a 10 cc water drop in a 10^{-3} g field indicated that a minimum diameter of 0.04 cm (.016") is required. This is consistent with the 0.05 cm (.020") minimum O.D. of the sharp cone tested and found to meet the secondary droplet maximum volume allowed for a 0.25 cc drop at an immersion of 0.16 cm (1/16") Thus, a single tip size will be satisfactory for water drops of all sizes since controlling the position of each injector, hence the tip immersion to 0.04 cm (.015") is achievable. Finally, water can be pumped through an 0.04 cm (.016") diameter injector at the maximum required pumping rate of 1 cc/second.

A similar calculation for silicone oil drops indicated that a minimum tip outside diameter of 0.18 cm (.070") is required to support a 10 cc drop on them in a 10^{-3} g field; a 0.24 cm O.D. (.093") by 0.20 cm I.D. (.078") tip was selected. Test results (see figure 8) indicated that the minimum satellite volume can be met at a reasonable immersion only for drops larger than about 1 cc. Consequently, the use of a second, smaller injector tip size 0.11 cm O.D. (.042") x 0.07 cm I.D. (.03"), is required for oil drops from 0.25-1.0 cc volume. Since the maximum tip separation to insure coalescing of oil into one drop is .07 cm (.03") which is about the resolution limit of the position servo, the injector tips will be positioned to touch (i.e. zero gap). It is not possible to pump the higher viscosity oils through the small tip at rates much above the minimum, i.e., 0.1 cc/sec because of the very high pressure drop which swells the elastomeric tubing excessively and stalls the pump motor; however, a pumping time of 10 seconds for a 1 cc drop is quite acceptable. The larger size oil tip permits a pumping rate of 1 cc/sec with 1000 cs oil.

The use of the inverted cone shape for silicone oil injector tips to achieve axial drop stability was discarded since this shape results in increased satellite droplet volume and/or decreased fluid pumping rates because of smaller injector tip inside diameters.

Cylindrical (tubular) shaped tips were selected for the oil injector tips since these result in a minimum tip outlet diameter, produce positive drop stability in the radial direction and neutral drop stability in the axial direction.

CONCLUSION

A practical fluid drop injection system has been developed for the Drop Dynamics Module, capable of forming drops of a range of commandable sizes from liquids having a wide range of physical characteristics. This system employs:

- A volume and rate commandable stepper motor operated dual outlet positive displacement pump.
- Two oppositely discharging programmable servoed injectors which move from outside the test chamber to its center as programmed.
- Surface tension forces to provide drop stability during drop growth and release.
- An initial tip separation of less than the tip radius.
- An injector retraction motion which keeps the growing drop periphery tangent to the injector tip outlets.
- One size injector tip for water drops of all sizes (¼ - 10 cc).
- Two sizes of injector tips for oil drops: one for drops from ¼ - 1 cc and the second for drops from 1¼ - 10 cc volume.
- Programmed injector tip motions together with tip sizes which minimize the production of satellite droplets and disturbance to the drop during its release into free drift.

The research described in this paper was carried out at the Jet Propulsion Laboratory, California Institute of Technology, under NASA Contract NAS7-100.

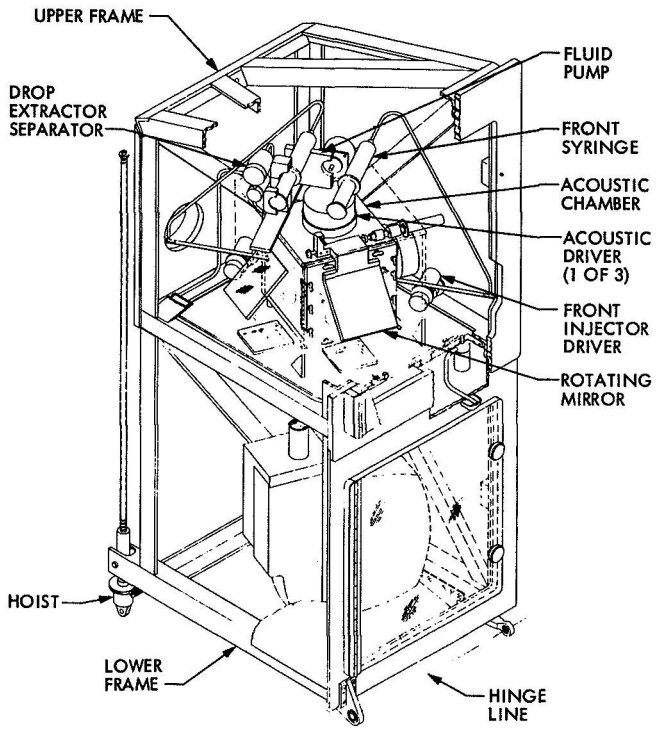

Fig. 1. Drop Dynamics Module Mechanical Module

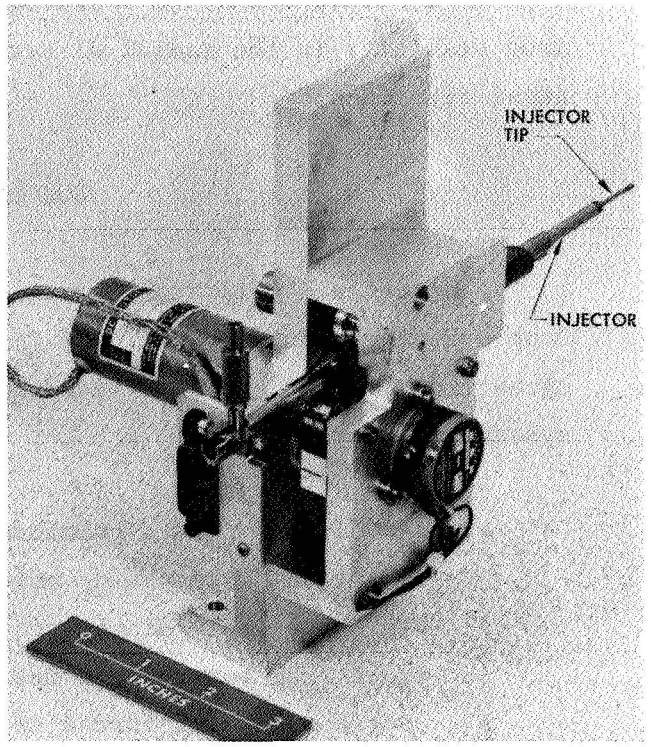

Fig. 3. DDM Fluid Injector and Driver

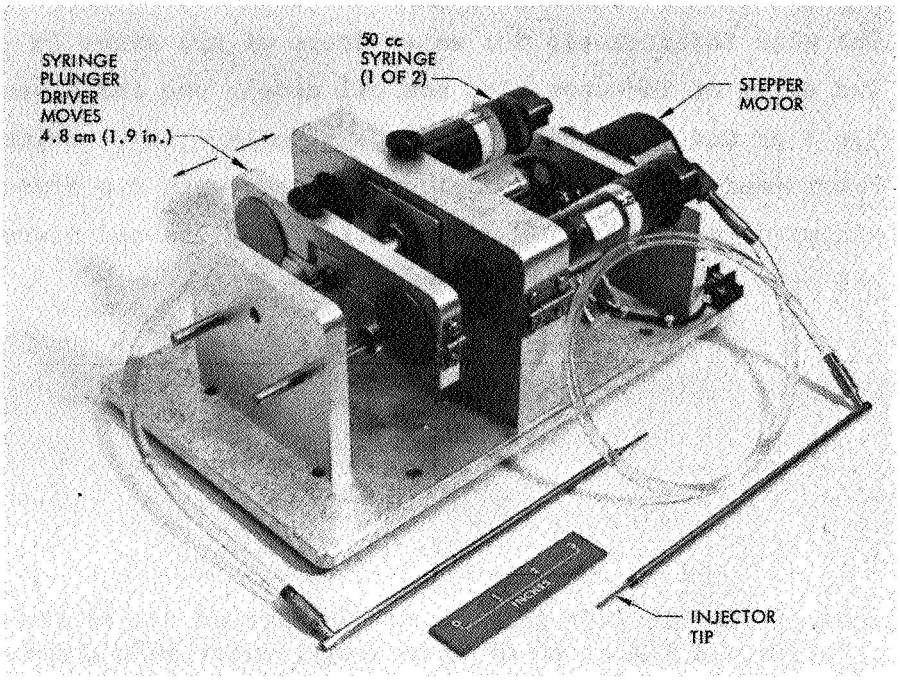

Fig. 2. DDM Fluid Pump

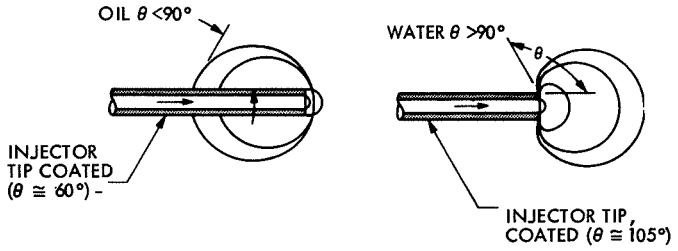

Fig. 4. Basic Drop Formation on Single Injector Tip

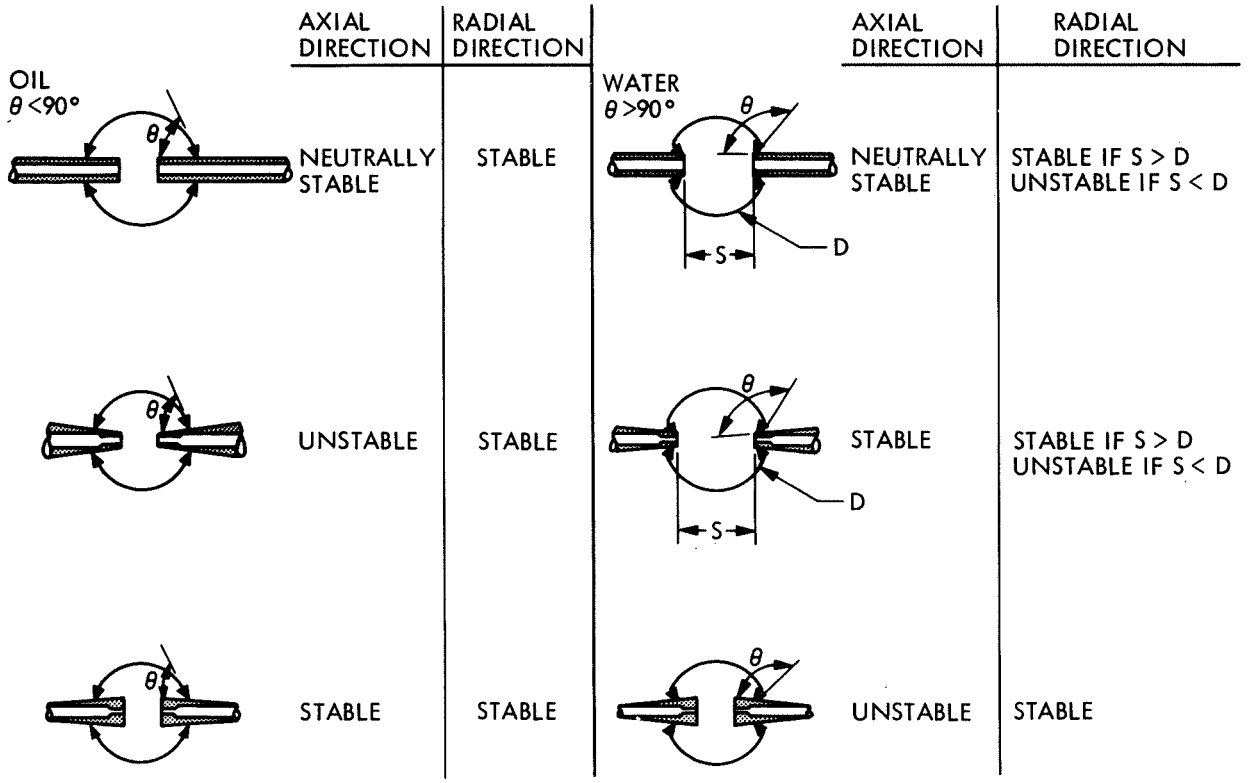

Fig. 5. Stability of Fluid Drops on Two Injector Tips vs Tip Geometry

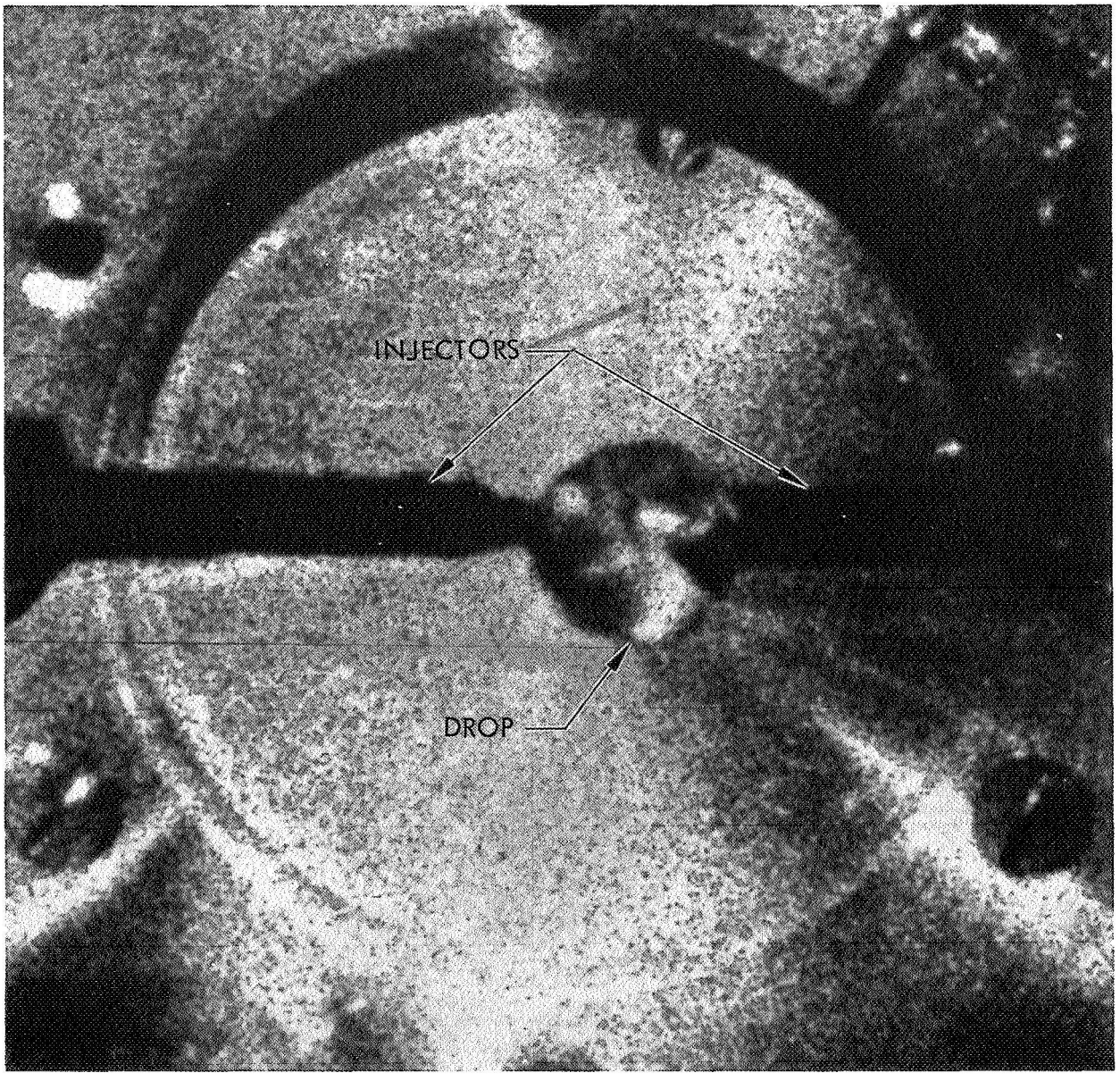

Fig. 6. KC135 Flight - Water Drop Forming in Zero "G"

DDM SATELLITE DROP FORMATION-LABORATORY TESTS

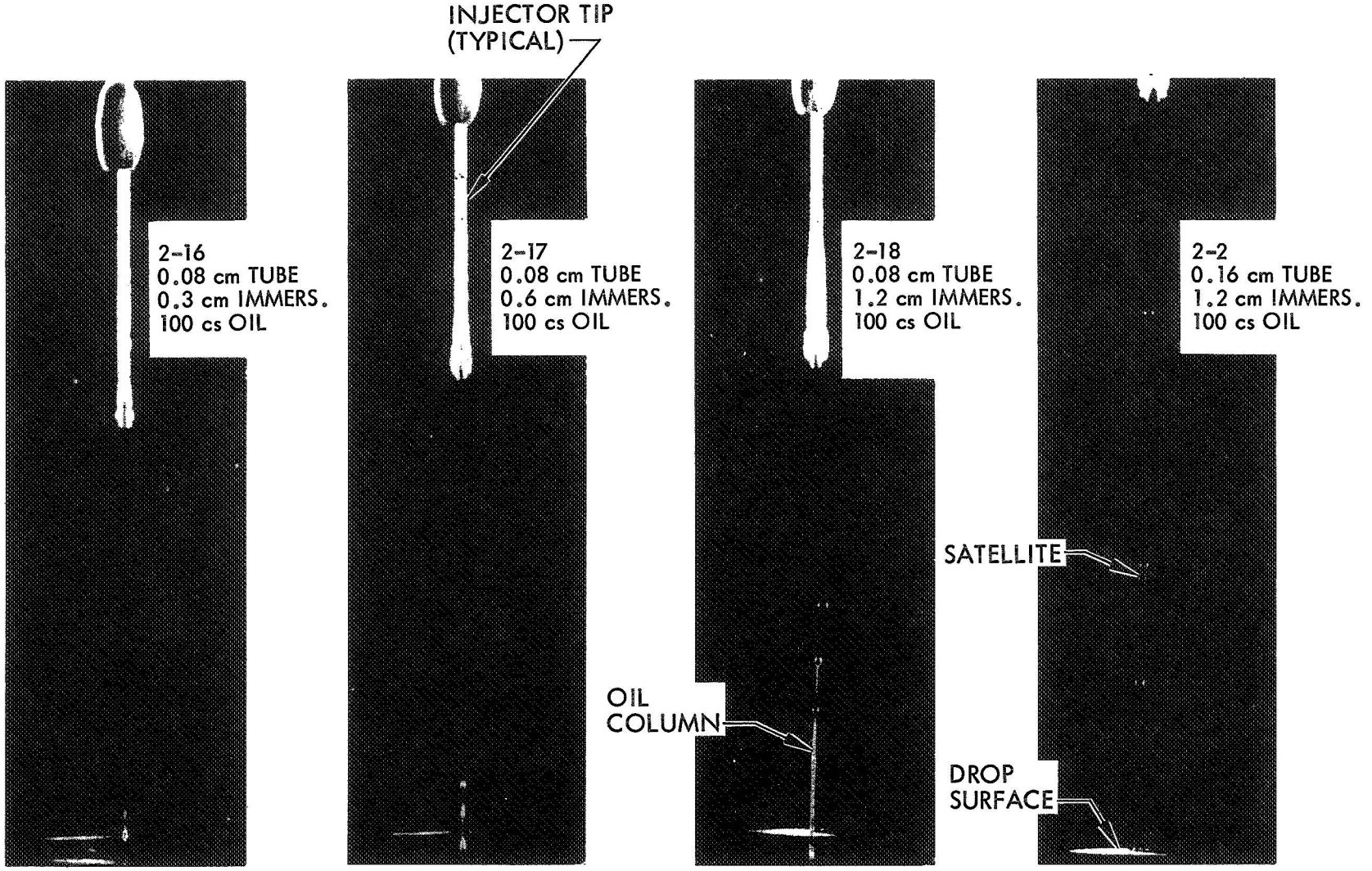

Fig. 7. DDM Satellite Drop Formation - Laboratory Tests

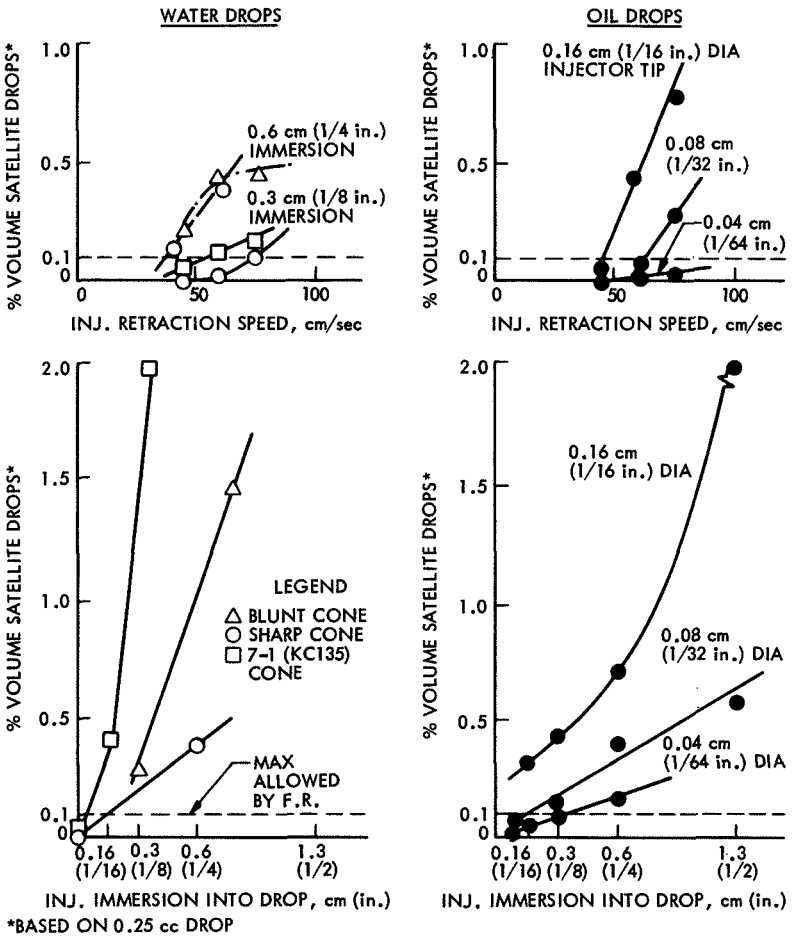

Fig. 8. Laboratory Test Results - Injector Parameters - Effect on Satellite Drop Volume

ON THE DESIGN OF AN ADJUSTABLE HIGH PRECISION LATCHING HINGE

John W. Ribble & William D. Wade

Lockheed Missiles and Space Company

Abstract

The design and test details of a high precision hinge and locking mechanism created principally in support of the Lockheed space deployable Flex-rib Parabolic Antenna concept are presented. These developed improvements in the detail design of ultra-precise rib hinge and contour adjustment mechanisms will allow radio frequency antenna reflectors to expand into the 15-50 meter diameter size class and to support the .013 mm. deployment repeatability tolerance required to support the 12+ GHz frequency range.

Introduction

In the spring of 1974 a 9.1 meter diameter Parabolic Antenna designed for use at frequencies up to 8 GHz was successfully placed in orbit. This reflector, shown in Figure 1 in its final deployed state, has operated satisfactorially ever since. The design is of the flexing wrap rib type, which consists of a number (variable) of radial ribs or beams which are cantilevered from a central hub structure. Each of the ribs is attached to this hub through a hinge. This radial spoke system provides the mounting for the antenna surface structure. Arrays are formed by mounting a membrane with elements on the front edge of the ribs and, if required, a ground plane on the rear edge. For parabolic or other curved reflectors, the ribs are formed in the required shape, and reflective pie-shaped gores are attached between the ribs. An overview of such a deployed system is presented in Figure 2.

The rib cross section and material are chosen to permit elastic buckling of the ribs. This is to allow the ribs to be wrapped around the hub structure in the ascent or stowed package configuration.

In the stowing process, the ribs and attached surface are rotated about the rib hinges until the ribs are tangent to the hub. After this rotation, the ribs are flattened and wrapped circumferentially around the hub. The elastic buckling of each rib accommodates this action. The surface material is allowed to form a package between the ribs. The elastic energy stored in the wrapped ribs is sufficient to accomplish deployment of the reflector. The stowed package is contained by a series of hinged doors which are held in place by a restraining cable. Deployment occurs when the cable is severed.

It was in the detail design of the rib hinge and latching mechanisms that need for design improvement was noted for larger, higher frequency designs. During the reflector assembly, excessive time was consumed in adjusting the rib tips to the required contour position tolerance of $\pm$.965 mm.

In addition, during testing larger-than-expected deviations from the "as adjusted" contour were experienced. While these items caused no significant performance degredations on that reflector, it was recognized that unless improvements were made, additional capability in either operational frequency or reflector diameter would be limited by these mechanism errors.

These concerns led to the initiation of a development study aimed at producing a mechanical reflector design showing improved setability and repeatability.

Symbols

η = efficiency
π = pi = 3.141592654
D = diameter
λ = wavelength of the electromagnetic wave
f = focal length of the antenna
c = local speed of light
G = gain
δ = RMS distortion

Reflector Performance

The need for improved antenna surface tolerance control can be understood by a brief discussion of antenna performance. The gain of an antenna may be directly related to the physical properties of the antenna surface. Consider the case of a round aperture having a diameter D. In this instance, the antenna gain is directly related to the diameter by the simple expression

$$G = \eta_E \left(\frac{\pi D}{\lambda}\right)^2 \qquad (1)$$

The above formula indicates that the gain of an antenna is directly proportional to the square of the diameter and the square of increasing frequency. The efficiency factor (η_E) accounts for the normally encountered degrading factors in any antenna system, including, among many other effects, resistive losses, reflection losses, aperture distribution losses, and blockage losses. Highly efficient systems have an efficiency of nearly 70 percent. Broad bandwidth systems have an efficiency of approximately 30 percent to 40 percent; moderate bandwidth systems of conventional performance generally have efficiencies in the 50 to 55 percent region. By specific exclusion, this efficiency factor does not include the impact of distortions.

For estimation purposes distortions of large structures can be considered as random errors in the surface. Exact treatment of the performance degradation caused by the actual distortions is a very complex issue, related to the type of antenna used, the distribution of errors, and many other factors. However, a reasonably well accepted and accurate relationship between gain in the ideal case and that achieved in the presence of small structural

distortions is represented by the relationship

$$G_d = G\, e^{-\left(\frac{4\pi\delta}{\lambda}\right)^2} \qquad (2)$$

where λ is the wavelength and δ is the RMS surface error. This can be rewritten in terms of reflector efficiency as

$$G_d = \eta_\delta\, G \text{ where } \eta_\delta = e^{-\left(\frac{4\pi\delta}{\lambda}\right)^2} \text{ ; mechanical effeciency} \qquad (3)$$

If we are dealing with statistically independent error sources, then δ is the RSS of the individual error sources. The overall efficiency equation can now be written as

$$\eta = \eta_E\, e^{\frac{-16\pi^2}{\lambda^2}\left(\delta_S^2 + \delta_A^2 + \delta_T^2\right)} \qquad (4)$$

where δ_S is the surface error caused by manufacturing error and deployment non-repeatability, δ_A is the surface approximation error, and δ_T is the thermal distortion error.

The repeatability error term may now be investigated parametrically by plotting its efficiency against RMS distortion error divided by wavelength in order to normalize the results with respect to frequency. This result is shown in Figure 3. Based on previous experience in error allocation budgets for antenna systems, a reasonable efficiency contribution for repeatability is 95%. Thus it can be seen that in order to obtain a high overall reflector efficiency, the reflector mechanisms distortions must be kept small (i.e. $\leq 1/50$) compared to the wavelength of the radiated energy.

Mechanical Development

In response to the recognized need for reduced surface distortions and improved surface repeatability for evolving antenna needs, a development program was initiated in 1975 to isolate the sources of the errors encountered with the 9.1 meter diameter reflector and to reduce them with detail design improvements. As previously discussed, one error in the design was traced to the rib latch mechanism, shown pictorially in Figure 4.

The latch consisted of a taper-ended plunger situated parallel to the rib hinge line and preloaded by a 22 newton spring. The plunger rode against a quadrant located on the rib. When the rib reached the fully-deployed position, the plunger would travel beyond the end of the quadrant and snap into the latched position. A loading diagram of the hinge portion of this latch mechanism is shown in Figure 5. This latch orientation induced torque moments T about the long axis of the rib which caused it to deflect from the desired contour position. In addition, this torque varied according to the

exact final position of the plunger each time the rib was deployed, giving rise to variations in the rib position each time it was operated.

A second area of concern in the reflector was the method used to adjust the rib positions to establish the required contour. Three rib hinge adjustments were required to be made simultaneously. The rib was adjusted vertically at the hub, rotated with respect to the hinge axis in order to provide vertical adjustment at the tip, and the fully deployed position was adjusted to insure that the rib extended in an exactly radial direction. The radial position stop was a screw adjustable stop, which operated quite satisfactorially. The other adjustments, however, in practice required the expenditure of large amounts of time to achieve the required accuracy. The hub end of the rib was adjusted vertically by exchanging matched pairs of graduated shims. While the shims functioned well, changing and checking these matched pairs was extremely time consuming. The angular adjustment at the hinge required to achieve vertical adjustment at the rib tip was accomplished by tapping a sliding block housing for the hinge bearing with a suitable hammer. This proved to be a trying process. Therefore, design efforts in the development program were directed at eliminating these causes for concern.

Design requirements for a new reflector were based on typical known large reflector needs. An attempt was made where economics allowed, to better these requirements, recognizing future needs to extend both the size and operating frequency of parabolic antennas. Table I lists the assumed requirements for the study. The hinge design which evolved is shown in Figure 6. In that design the plunger was relocated to the rib and positioned to move in a direction perpendicular to the hinge line halfway between the hinge bearings. Thus, no torque is transmitted to the rib from variations in latch loads, eliminating one source of contour non-repeatability.

The elimination of induced torque due to latching loads also allowed the latch mechanism to be utilized to eliminate bearing freeplay. The use of a rib hinge always creates hinge bearing clearance problems which manifest themselves as contour inaccuracies. In the case of the new design the bearing freeplay magnification ratio (i.e., length of rib/bearing separation) is 50:1. Therefore in order to produce a reflector contour which is repeatable, the bearing freeplay was eliminated at the completion of deployment by utilizing a very high force spring to drive the latching plunger. A further complication is the one-g environment under which the contour must be set and measured. The latch spring was also designed to drive the rib bearings to a repeatable position whether the reflector is deployed with the concave side up or down, thus eliminating the one-g deadband in the bearings.

The other major change incorporated into the new design is the method of achieving vertical adjustments at the rib root and tip. The resulting vernier rib adjustment mechanism which was developed is shown in Figure 7. The design goals which led to this adjustment device were:

(1) Adjustment Fineness - The ability of the mechanic to "feel" $\pm$.25 mm tip motion.

(2) Repeatability - Once the adjustment was made, it could be expected to remain in that position.

(3) Readjustability - If for some reason it was found necessary to change the setting, disassembly would not be required.

The bottom (side away from contoured side of rib) hinge bearing is held by a housing which is adjusted radially by a differential screw device. Turning the adjusting collar 18^{0} results in a .25MM vertical rib motion at the rib root vertical adjustments can be made by changing one shim, thus eliminating the need for matched shim pairs.

Design Verification

The hinge model shown in Figure 6 was subjected to repeatability tests during the spring of 1978. Results of those tests are summarized in Table II. Initial tests showed excessive deflections in the hinge. The difficulty was traced to deflection in the lower hinge pin (see Figure 8). The deflection in this pin caused by the latching loads from the plunger spring were in the order of 0.2 mm, which could result in a mechanical efficiency contribution in the projected design of 36%. The pin was therefore redesigned and stiffened as shown in Figure 8. The new pin was installed and the results of Table II obtained, resulting in a projected mechanical efficiency contribution of 98% for the design which was well above the 95% goal.

The results of these tests enabled a go-ahead to manufacture and assemble a 4-rib, 3-gore section of a complete 15 meter diameter reflector. This model (Figure 9) has been completed and is currently scheduled to undergo engineering development testing to verify deployment dynamics and contour repeatability.

Conclusions

The design of a latching hinge capable of supporting antenna reflectors in the 15-50 meter diameter range and 12+ GHz frequency range has been achieved. This hinge design achieves deployment repeatability of within $\pm$.010 mm across the bearings and allows positive vertical rib adjustments of $\pm$.05 mm at the root and .25 mm at the tip.

TABLE I

Requirement	Value	Compliance
Diameter Deployed	15 M	15.24 M
Diameter Stowed	<200 M	1.90 M
Reflector Weight	<138 Kg	122 Kg
Operating Frequency	9 GHz	8.5 GHz
Surface Approx Loss	<.5 dB	.5 dB
Thermal Dist. Loss	.1 dB	.045 dB
Torque Transmitted to S/C	<46.6 Newton-M	34 Newton-M
Launch Environment	$\pm$ 20 G's*	.08 M.S.
f/D Ratio	.44	.44
Mfg. & Repeatability/Loss	<.07 dB	.02 dB

* Applied in 3 orthogonal directions simultaneously - equivalent static inertial load

TABLE II

Load Condition	Deflection at 1g load	Deflection After Load Removal
Vertical Shear	.015	.010
Horizontal Shear (Toward Deployment Stop)	.012	.008
Horizontal Shear (Away from Deployment Stop)	.011	.0075

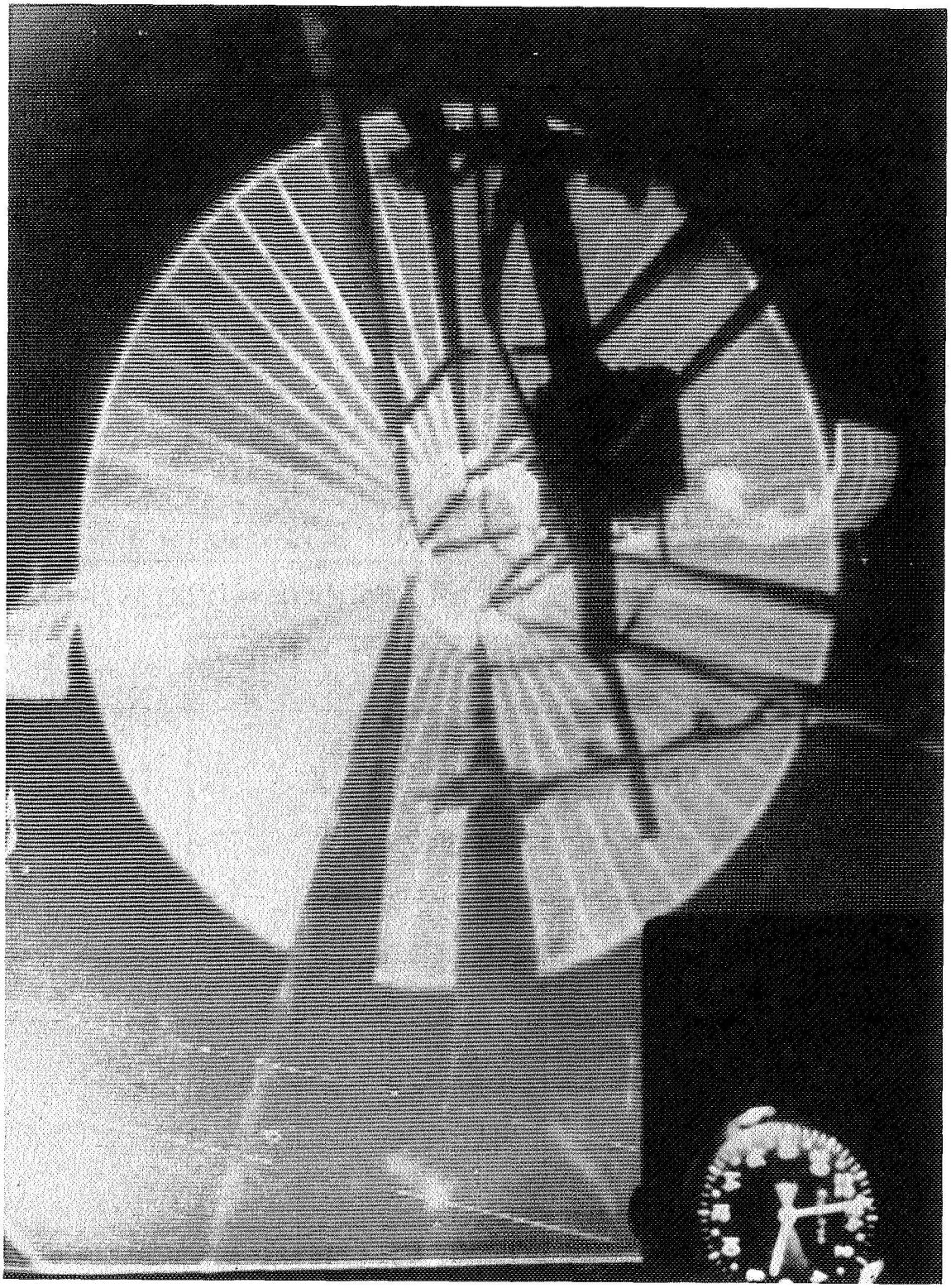

FIGURE 1
10 METER DIAMETER REFLECTOR DEPLOYED IN ORBIT

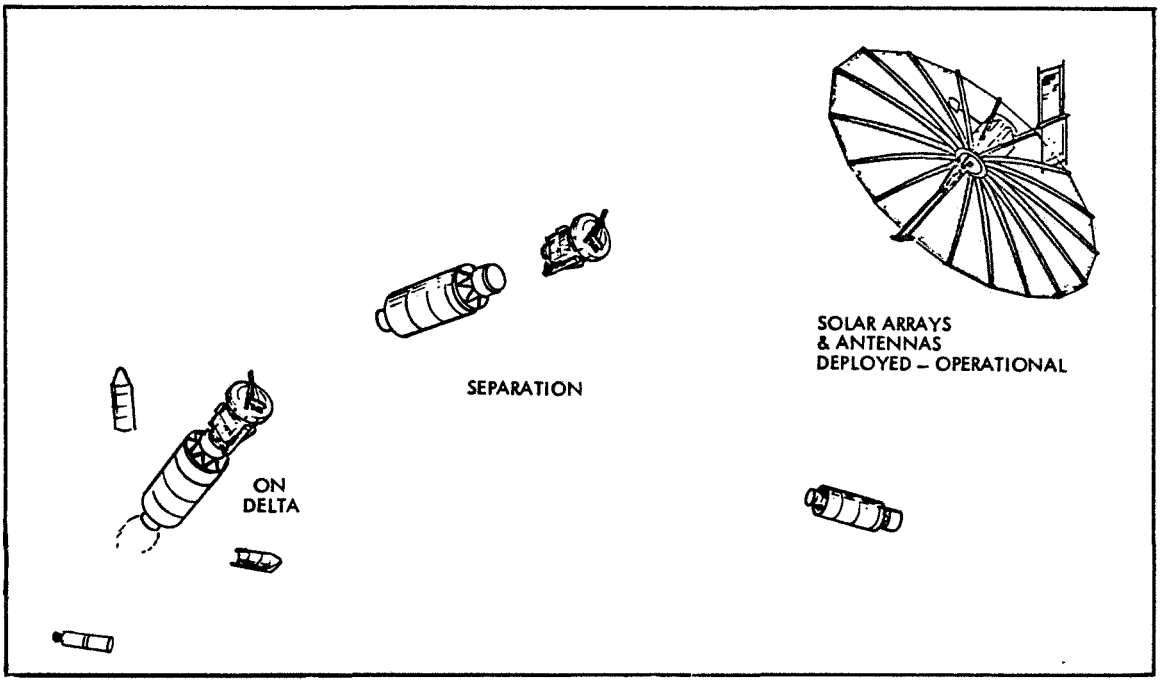

FIGURE 2 MISSION PROFILE-SATELLITE DELIVERY (OPTIONAL DELTA LAUNCH)

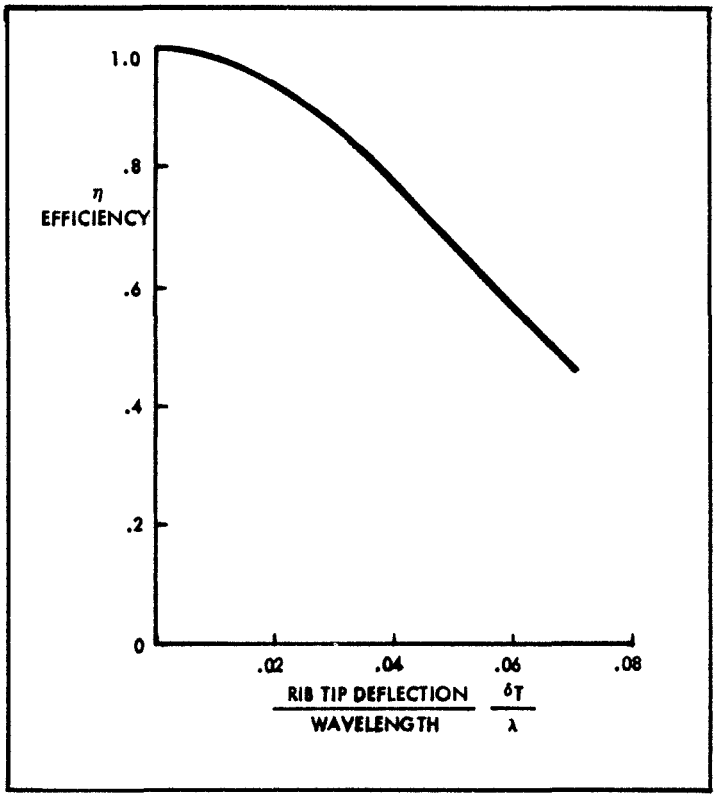

FIGURE 3 REFLECTOR EFFICIENCY EFFECT OF SURFACE DISTORTION

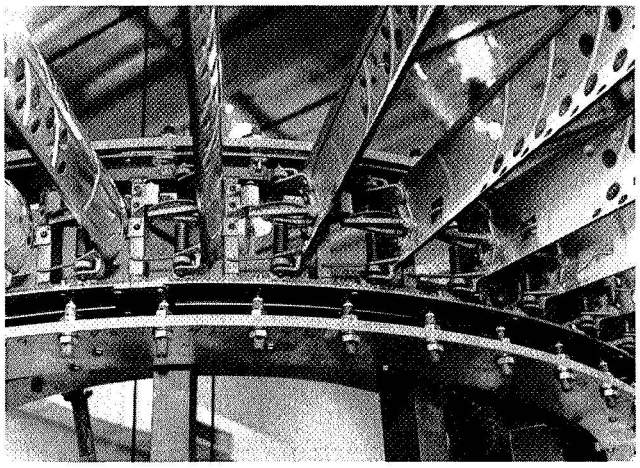

FIGURE 4
RIB HINGE & LATCH ASSEMBLY FOR 9.1 METER DIAMETER REFLECTOR

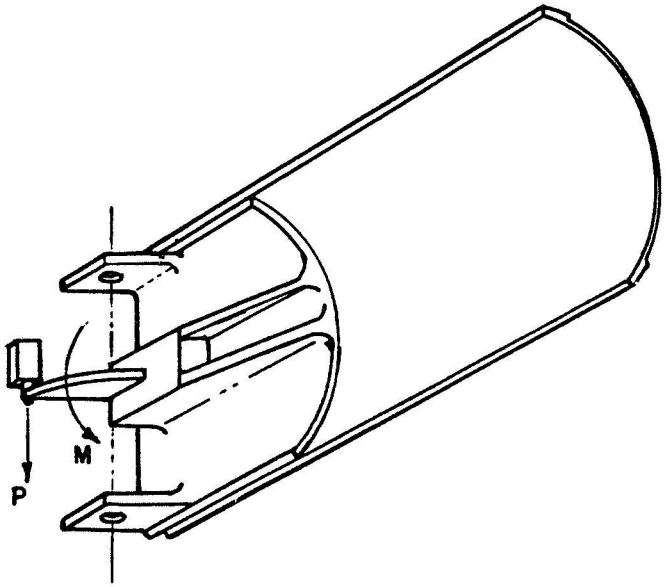

FIGURE 5 HINGE LOADING DIAGRAM

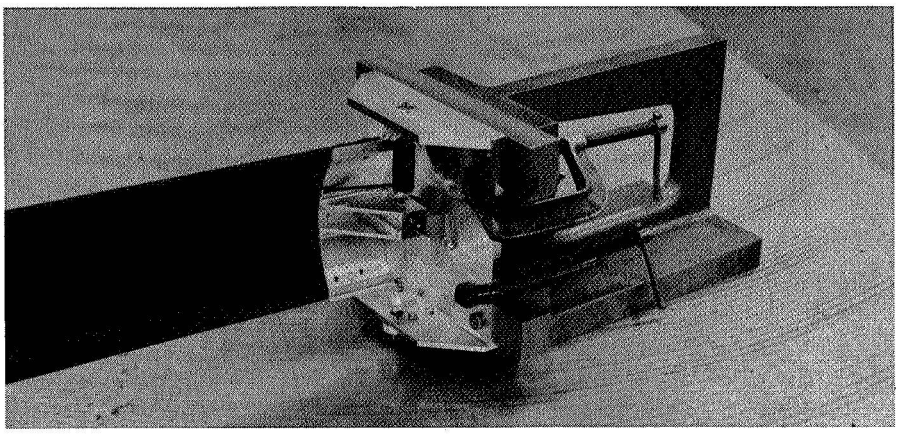

FIGURE 6
REDESIGNED RIB HINGE & LATCH ASSEMBLY FOR 15 METER DIAMETER REFLECTOR

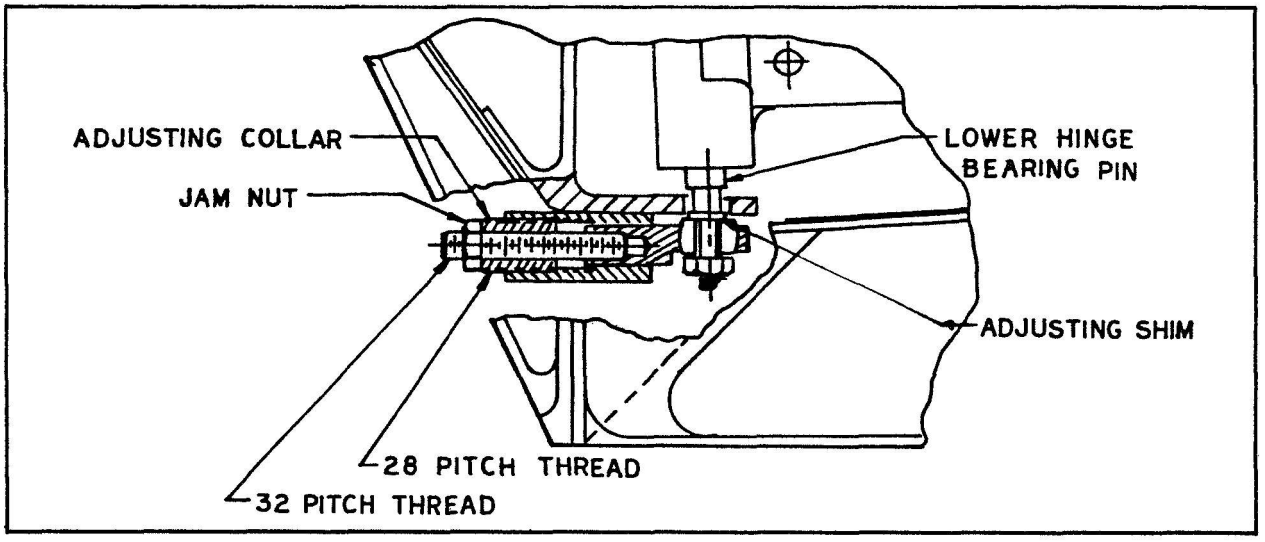

FIGURE 7

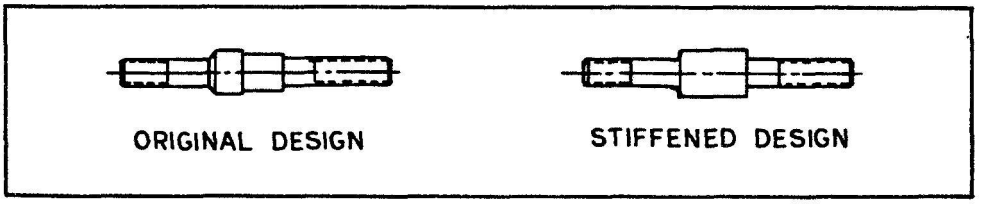

FIGURE 8

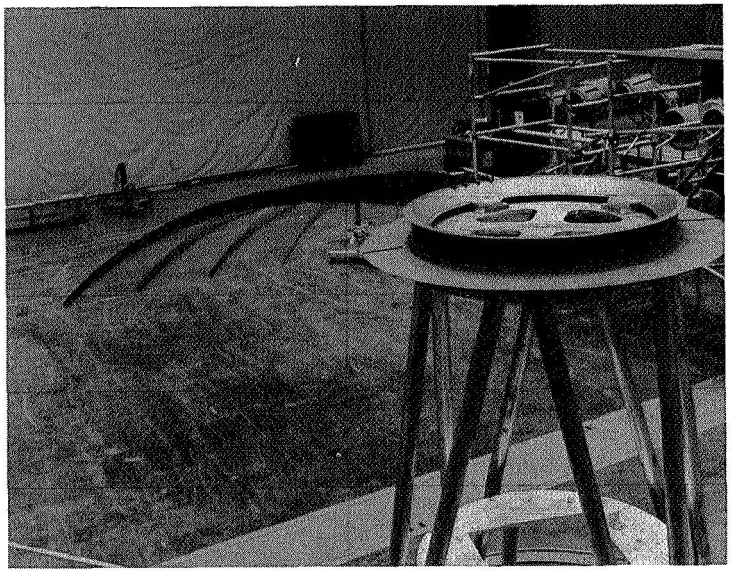

FIGURE 9

RELIABILITY BREAKTHROUGH: AN ANTENNA DEPLOYMENT/ POSITIONING MECHANISM WITH ELECTRICAL AND MECHANICAL REDUNDANCY

By M. C. Olson, L. W. Briggs and J. B. Pentecost
Hughes Aircraft Company

ABSTRACT

An Antenna Positioner Mechanism (APM) has been developed for deployment of an antenna reflector and for fine granularity closed loop tracking of the antenna in response to RF beacon error signals. By utilizing permanent magnet stepper motors, spur gearheads, irreversible single thread worm/wheel assemblies and a miter gear differential, full electrical and mechanical redundancy has been realized. Two versions of this design have been generated: one is a weight-optimized design with a clutch for overload protection and one is a more rugged unit without a clutch.

INTRODUCTION

The SBS (Satellite Business Systems) and the Anik C (Canadian Communications Satellite) spacecraft employ 1.8 meters (6 feet) diameter antennae which are restrained during launch by pyrotechnic devices and after orbit injection are deployed approximately 70° to their operating position. (See Figure I.) This deployment as well as the fine grain on-orbit steering are performed by the Antenna Positioner Mechanism shown in Figure II. Except where noted, all descriptions, test programs, etc. presented in this paper apply to the initial weight-optimized design. This unit because of the light weight features required a slip clutch to protect the gears from on-orbit backdriving loads from the antenna and from the full stall torque capability of the stepper motor. After completion of the development effort on this weight-optimized unit, a more detailed computer model revealed a torsional stiffness requirement an order of magnitude greater than that measured. Several quick-fix solutions were abandoned in favor of a complete redesign to satisfy the new stiffness requirements. The ruggedized version that evolved from this redesign effort is described briefly at the end of this paper. With the exception of the clutch, which because of the larger gears became unnecessary for load protection, the basic designs of the two versions are identical. Both contain the full electrical and mechanical redundancy features.

DESIGN REQUIREMENTS/CHARACTERISTICS

The key design requirements and characteristics of the APM are summarized in Table I. The output shaft motion granularity of 0.0025 degrees for each 45° motor step determined the overall gear ratio of 18000:1. For one of the failure modes, described later in this paper, the output step increment becomes 0.005 degrees which is still acceptable. During deployment the step rate is 25 steps per second while typical operation for antenna pointing is about 1 step every 18 minutes.

The torsional stiffness about the APM output shaft was initially undefined when the weight optimized unit was conceived, designed and developed. When this parameter was established, it was an order of magnitude higher than the value measured on the qualification unit and, of course, necessitated a redesign.

The antibacklash torque is the torque required at the output shaft to prevent pointing errors due to backlash in the gears. Normal in-orbit loads due to spacecraft wobble and nutation dictate this requirement.

DESIGN DESCRIPTION

The APM gear train layout is shown in Figure III and is illustrated in schematic form in Figure IV. Redundant permanent magnet stepper motors drive through reducing gearheads into worm/wheel sets and a miter gear differential. The revolving trunnion shaft of the differential carries a serrated tooth, spring loaded clutch as shown in Figure V. The differential gear system permits either motor to drive the output shaft. Rotation of the non-powered half of the system is prevented by the irreversible feature of the single thread worm/wheel gears supplemented by the permanent magnet detent of the motor acting through the gearhead and worm/wheel ratios.

Any failure in the motor, gearhead or worm/wheel components is overcome by switching to the standby system. In the case of a jammed bevel gear in the differential, both motors are energized simultaneously. This operating mode causes the entire differential to rotate as a common member and actually reduces the gear ratio by 1/2 to 9000:1. Step size at the output is increased to 0.005 degrees, but since both motors are driving, the output torque is the same as for normal operation.

The clutch, located between the output shaft and the fixed bevel gear of the differential, is spring loaded to slip at approximately 8.16 Newton-meters (6 ft-lbs) of torque. This value prevents damage to the mechanism in the event of high backdriving torques from the antenna due to spacecraft maneuvers, etc. It also is sized to limit the amount of amplified motor torque seen by the gearbox and thus permits use of smaller and lighter components. A fixed stop external to the APM prevents antenna overtravel to about 1 degree beyond the operating range when the clutch is activated.

A conductive plastic, infinite resolution potentiometer is mounted on the APM output shaft to provide telemetry information. Since it is not necessary for mission success, it is not redundant. For applications where position data is necessary for closed loop pointing, a redundant unit could easily be provided. This custom-made frameless potentiometer has an electrical angle of 75°. In order to obtain high resolution in the operating region, an off-center tap is provided. With 5 volts applied at the potentiometer ends and 0 volts at the tap, the sensitivity over the first 65° from the stowed position is about 77 millivolts/degree while in the remaining 10°, which includes the normal operating region, it is about 500 millivolts/degree.

Spring biasing of the output shaft is used to eliminate backlash or dead zone in the gear system. This spring starts at essentially zero torque in the stowed position and winds up over the 70° deployment angle to provide about 12 in-lbs in the operating region.

All bearings supporting the worm/wheel gears and differential are preloaded angular contact type. Ground shims are provided to set the proper wavy spring preload forces. Except for the main output shaft bearings, failure of any bearing in the system is overcome by switching to the standby motor/geartrain or to simultaneous stepping by both motors. The main output bearing redundancy is achieved by applying thin sputtered MoS_2 film to the close tolerance slip fits of bearing to shaft and bearing to housing. In effect this creates journal bearings at these interfaces that allow operation if the output bearings fail.

APM LIFE & LUBRICATION DESCRIPTION

The APM design life consists of the following combination of test and flight operating cycles:

1.	Unit Test	162,000 motor steps
2.	Spacecraft System Test	284,000 " "
3.	In-Orbit Deployment	28,000 " "
4.	In-Orbit Pointing	292,000 " "
	Total test & mission steps	766,000

The in-orbit positioning requirement was determined from the following assumptions:

- An average daily correction of $\pm$ 0.05 degrees, corresponding to 80 steps per day.
- A correction frequency of 1 step every 18 minutes, representing a correction of .0025 degree
- An in-orbit life of 10 years.
  (10 years X 365 days X 80 = 292,000)

The extremely large numbers of oscillatory cycles due to spacecraft nutation or wobble are not a factor since the magnitude of the torque loads is less than 1/10 that necessary to overcome the antibacklash spring on the APM output shaft. The in-orbit operational life can be expressed as 3650 cycles (365 days X 10 years) at a very low rate (1 step every 18 minutes) with an average amplitude as follows:

at motor	$\pm 900^{o}$ ($\pm$ 20 steps)
at output of gearhead & the worm gear	$\pm 12^{o}$
at worm wheel and input to bevel gears	$\pm 0.1^{o}$
at output shaft	$\pm 0.05^{o}$

The gear and bearing lubrication and processing are tabulated in Table II. A significant feature of the lubrication system is the extensive use of sputtered MoS_2 and ion plated lead for bearings and gears. The 2000°A lead film was chosen for the gearheads to be compatible with the small clearances and tight tolerances required for reliable operation. The sputtered MoS_2 on the bearing races and balls provides an extremely tenacious, uniform film for initial lubrication while the Duroid 5813 (primarily teflon & MoS_2) provides a space-proven replenishment system for long life. A bonded MoS_2 was employed for the difficult worm/wheel lubrication task because of the extensive previous experience in similar space applications and superior performance in tests where sliding friction occurs.

QUALIFICATION/LIFE TESTS

After completing a series of in-process functional/electrical tests, the weight-optimized unit was subjected to a design qualification test program. The key performance parameters evaluated during the tests included the following:

- Total excursion versus motor steps as measured by the control logic input pulse register and a mirror/autocollimator setup (performed for each of the redundant motor/gear systems).
- Small angle ($\pm$ 1 degree and $\pm$ 0.1 degree) step accuracy using the autocollimator system for each motor/gear system.
- Clutch release torque and antibacklash spring values.
- Torsional and cross-axis stiffness characteristics.

The unit environmental tests consisted of the following exposures:

- Qualification level random vibration of 21 g's rms overall along each of 3 axes.
- Qualification level thermal tests with a representative inertia load attached to the output shaft.

The unit performed flawlessly during all phases of the test program. In addition, an inspection after completion of unit and qualification spacecraft tests showed the gears and bearings design/lubrication to be compatible with the life requirement.

Since the life travel distance requirement was most severe for the gearheads, an additional special life test was conducted on a motor/gearhead combination driving a representative inertia load. For this test, the motor was programmed (at a rate of 25 pps) for continuous cyclic operation (7000 pulses CW and CCW each followed by a 4 second pause) for a total of one million pulses. After completion of the cyclic life test the gearhead was disassembled and visually inspected for lube wear and gear tooth damage. The results of this inspection revealed no gear tooth damage with the ion-plated lead film intact and in excellent condition.

ALTERNATE DESIGN DESCRIPTION

The cross-section of the alternate design developed to provide additional torsional stiffness is shown in Figure VI. Because of the larger shaft and gears needed to satisfy the requirement for an order of magnitude increase in stiffness, a clutch was not required for overload protection. This feature along with some minor design improvements has simplified the assembly procedures and reduced the overall complexity. The qualification model of this design, after completion of functional and environmental testing, will be subjected to a life test program.

CONCLUDING REMARKS

The APM for the SBS/Anik C programs was developed with the goal of achieving high reliability through full mechanical and electrical redundancy. The final configuration required a redesign effort in order to satisfy all the system requirements as well as the reliability goal. Although the initial weight-optimized unit proved the basic design concepts and will, of course, be valuable for future applications, an earlier definition of stiffness requirements could have eliminated this extra design iteration.

TABLE I - APM DESIGN REQUIREMENTS/CHARACTERISTICS
(WEIGHT-OPTIMIZED VERSION)

Parameter	Requirement/Characteristics
Deployment Travel Range	70 degrees
Deployment Time	19 minutes
Operating Travel Range	$\pm$ 1.0 degrees
Positioning Increment	0.0025 degrees/step (0.005 deg/step acceptable)
Step Rate	1 - 25 steps/second
Power Required	15 watts (28 V, 25^{o}C)
Load Inertia	1.632 X 10^{8} gm-cm^{2} (12.0 slug-ft^{2})
Torsional Stiffness	Requirement Undefined - unit achieved 9.52 Newton-meters/degree (7.0 ft-lbs/degree)
Antibacklash Torque	16.32 Newton-meters (12.0 in-lbs)
Clutch Slip Torque	8.16 Newton-meters (6 ft-lbs)
Temperature Range	-51^{o}C to 66^{o} (-60^{o}F to + 150^{o}F)
Weight	1.59 kgms (3.5 lbs)
Redundancy Required	Electrical & Mechanical

TABLE II - APM LIFE/BEARING/LUBRICATION SUMMARY

ITEM	DESIGN LIFE (REVOLUTIONS)	LUBRICATION/PROCESSING	
Motor Bearings	77,500	Duroid 5813 retainers - Bearings (in motor) run-in in controlled atmosphere (GN_2)	
Gearhead Bearings	1,025 to 27,000	Duroid 5813 Retainers	Bearings and Gears (in gearhead) run-in in controlled atmosphere
Gearhead Gears	1,025 to 27,000	2000 Å ion plated lead	
Worm & Wheel Gears	1,025 (worm) 8-1/2 (worm wheel)	Lubeco 905 (Bonded MoS_2) Run-in in controlled atmosphere	
Bevel Gears	8-1/2	Lubeco 905 - Run-in in controlled atmosphere	
Bevel Gear Bearings	8-1/2	Duroid 5813 retainers. Sputtered MoS_2 on balls & races. Run-in in controlled atmosphere.	
Output Shaft Bearings	4-1/4	Duroid 5813 retainers. Sputtered MoS_2 on balls & races. Run-in in controlled atmosphere.	

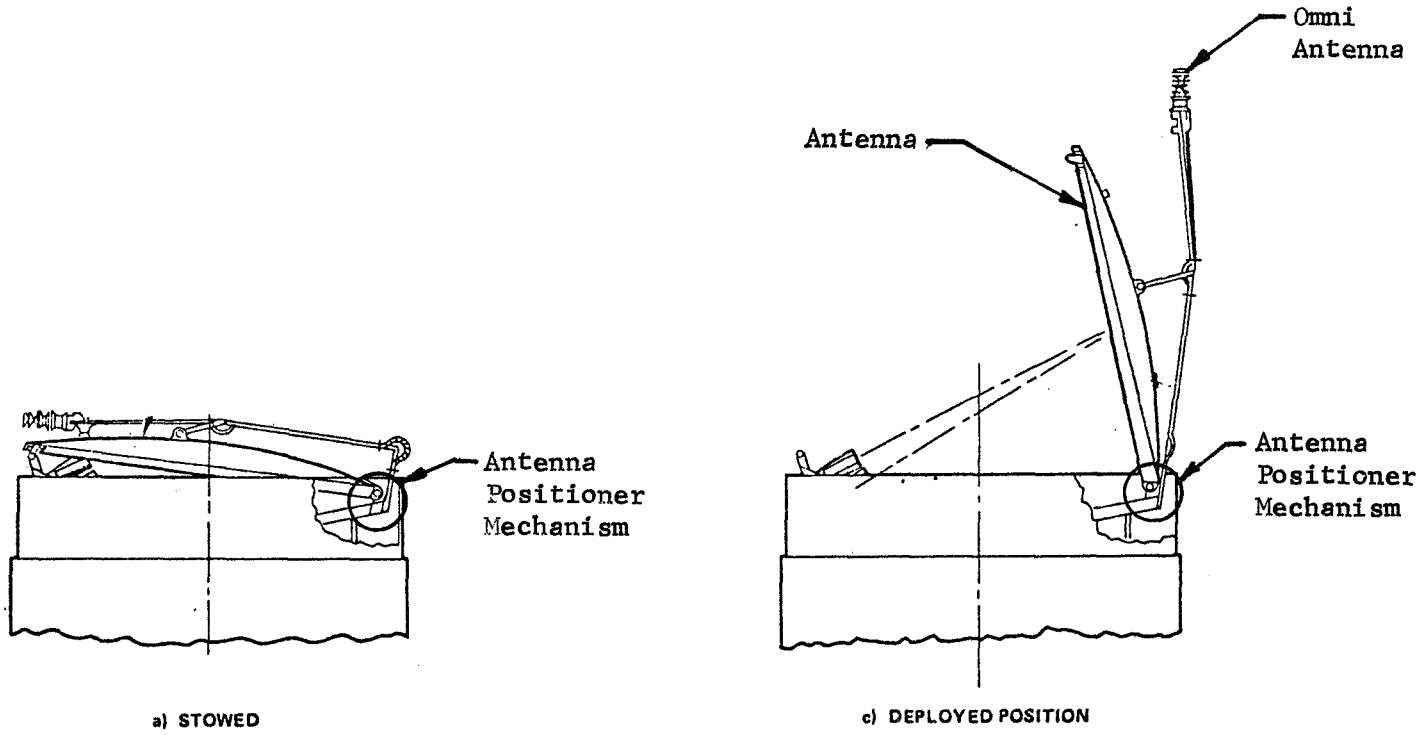

Figure I - SBS/Anik C Antenna Arrangement

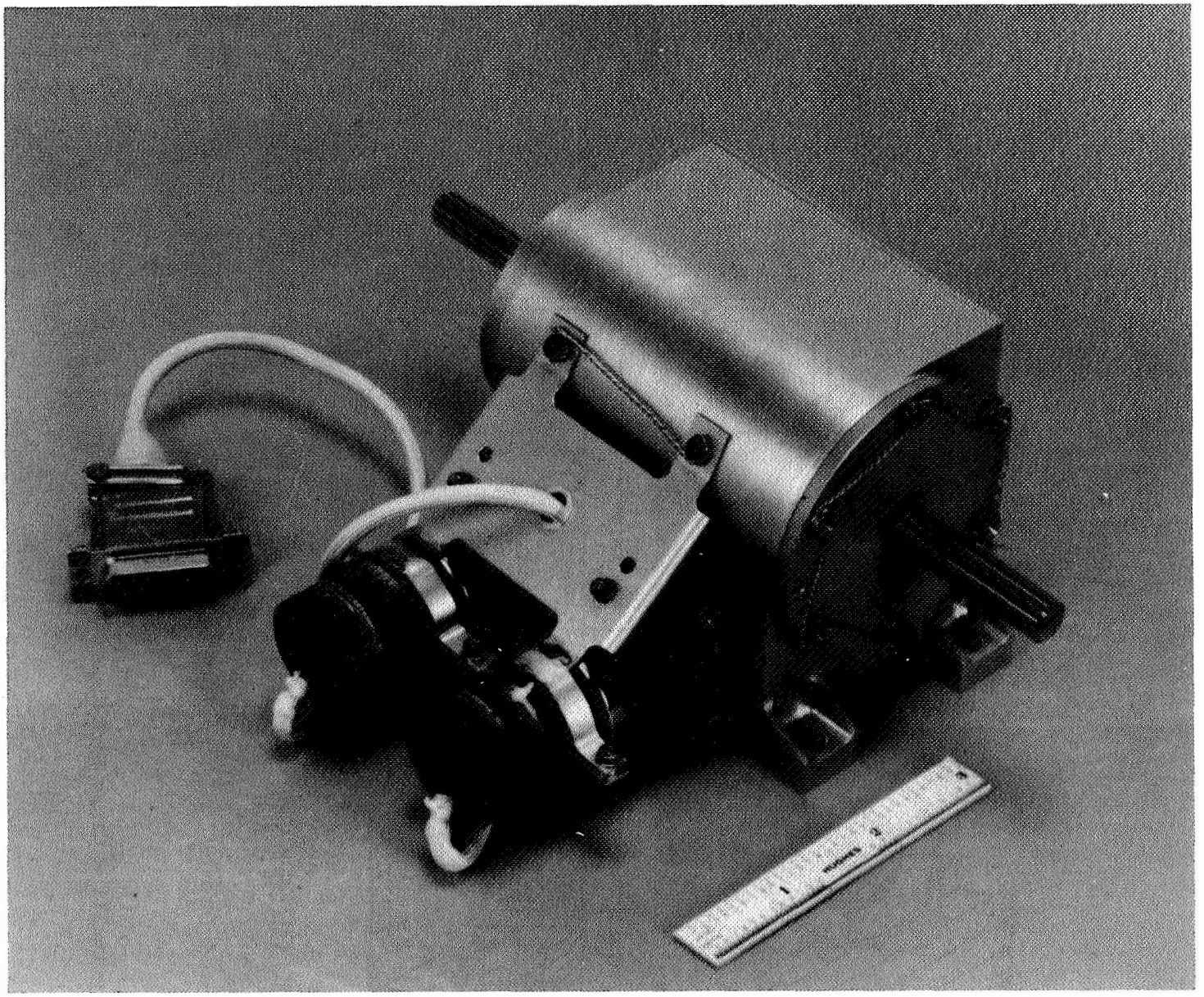

Figure II. Antenna Positioner Mechanism-Weight-Optimized Version

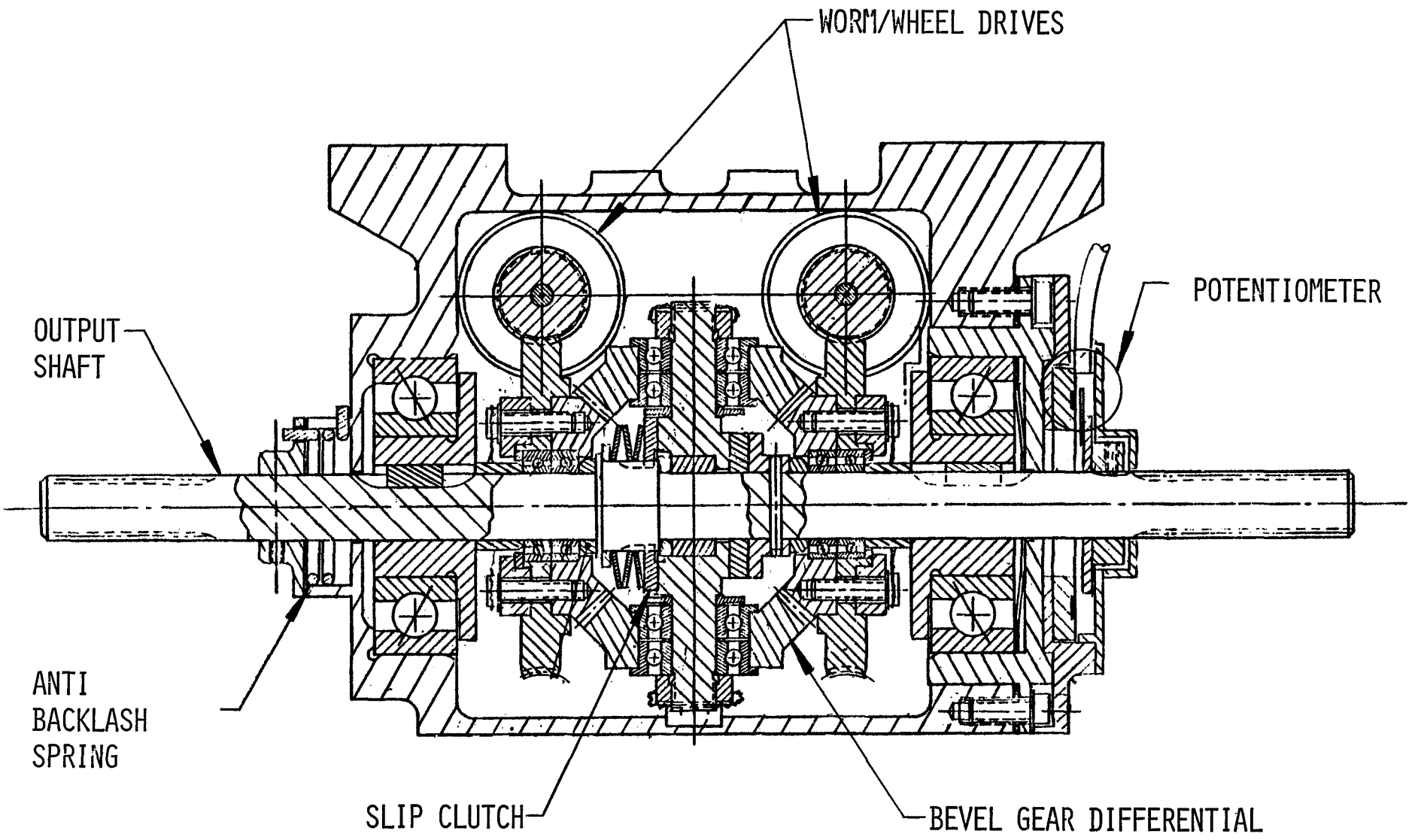

Figure III - Cross-Section of Weight-Optimized APM

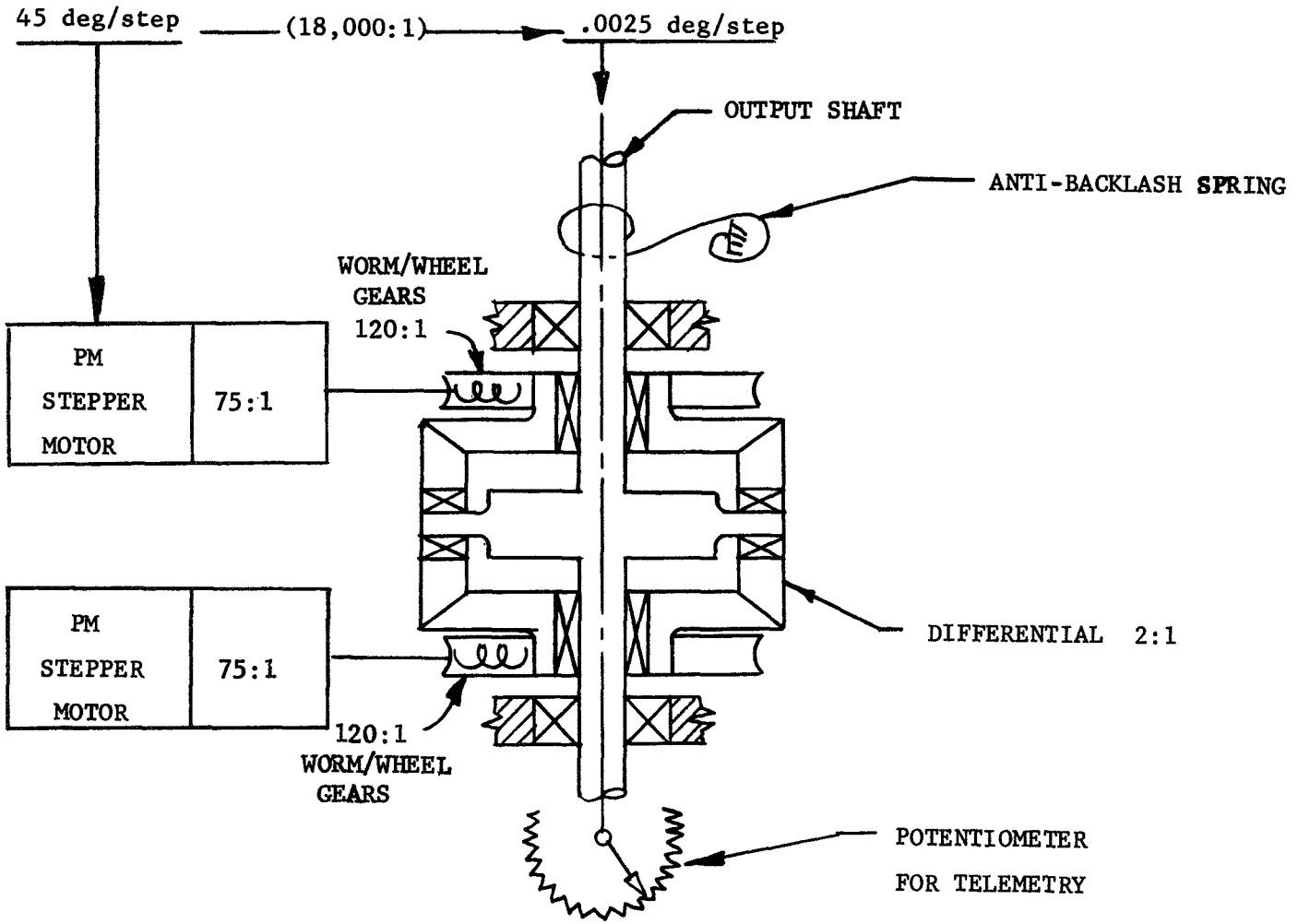

Figure IV - APM Mechanical Schematic

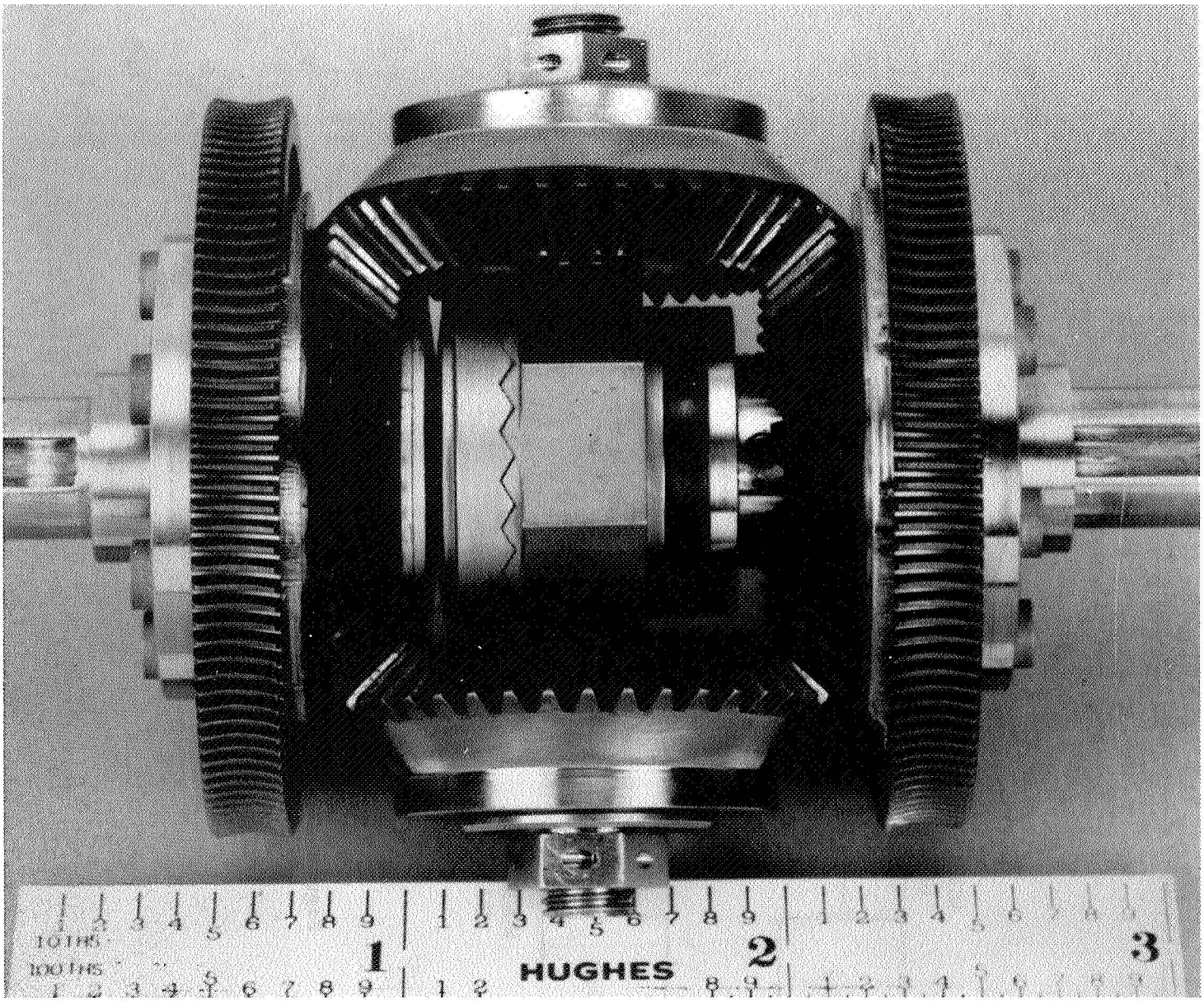

Figure V. APM Differential/Clutch System-Weight-Optimized Version

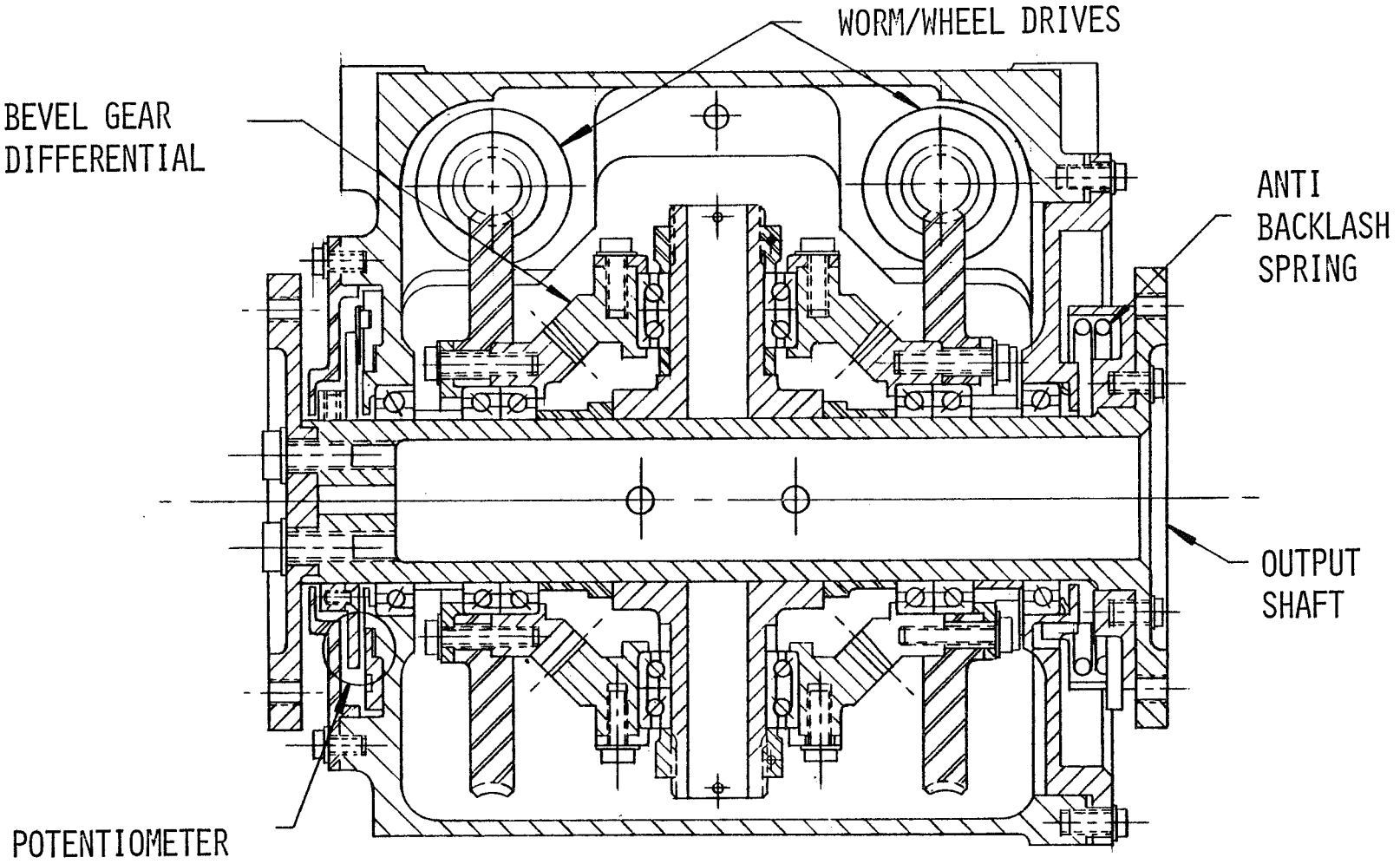

Figure VI - Cross-Section of Ruggedized APM

DEVELOPMENT OF DRIVE MECHANISMS FOR COMMUNICATION SATELLITES

by Arnold C. Schneider and Thomas D. McLay

General Electric Space Division
Valley Forge, Pennsylvania

ABSTRACT

A distinguished pedigree is an important asset in the development of Aerospace mechanisms. Four drives recently developed for communication satellites are outgrowths of a previously-proven drive configuration.

Pedigree by itself, however is not enough to generate success. Inevitably, design changes which are thought to be minor, are generally introduced to fine tune the pedigreed hardware to meet particular requirements of a specific new application. Such design changes are often viewed too casually and are not thoroughly tested in the early development stages of the program. This paper describes two areas of design change on the solar array drive applied to the Japanese Broadcast Satellite (BSE) which led to subsequent problems during the development phase of the program. The methods applied to establish the cause and the solution of these problems are described as well as the testing approach adapted to prevent similar occurrences on the current Communication Satellite Program, The Defense System Communications Satellite III (DSCS III).

INTRODUCTION

Today the solar array drive for the Japanese Broadcast Satellite (BSE) is performing perfectly in orbit. Likewise, the solar array drive and the gimbal antenna drives for the Defense Systems Communications Satellite III (DSCS III) have successfully passed their qualification tests. One of the primary reasons for the success of these drive mechanisms has been their common pedigree.

During 1971, GE developed a drive concept using company discretionary funds. This design concept was a fully redundant drive system utilizing two drive modules, each one consisting of a D.C. stepper motor, a harmonic drive speed reducer, spur gear speed reducer, and a wrap spring clutch. (Reported at the 8th Aerospace Mechanisms Conference in October, 1973).

The BSE solar array drive is a flight version of this original design concept with some minor changes in order to reduce weight. The DSCS III solar array drive is a modified version of the BSE drive providing a more compact assembly and a further reduction in weight.

The DSCS III gimbal dish antenna actuators use the basic parts from the drive system developed in 1971, including some simplifications that are possible because their reliability requirement can be met without redundancy.

DESIGN DESCRIPTION

BSE Solar Array Drive

The BSE solar array drive consists of two completely redundant unidirectional drive modules that are interconnected by two, passive, wrap spring clutches (see Figure 1). These clutches permit either drive to be energized with a resultant output torque of 18 Nm (160 Lb.In.) or both to be energized with a torque of 36 Nm (320 Lb.In.). Each drive contains a 1.8 degree step angle, stepper motor, a 100:1 harmonic drive speed reducer, and a 6.05:1 spur gear set. Power is transferred from the rotating solar array panels to the vehicle structure by means of a slip ring assembly consisting of 20 signal rings and four power rings. The slip ring assembly is mounted around the one-piece output shaft that connects the two redundant drives.

DSCS III Solar Array Drive

The DSCS III solar array drive is a modified version of the BSE drive (see Figure 2). The concept of redundant drive modules is maintained, but the output of the drive modules is a common bull gear rather than the output shaft. The assembly includes two slip ring modules which are integrated into the support housings to reduce weight and to eliminate extra bearings. A separate torque tube connects the driving half of the assembly to the non-driving half.

DSCS III Antenna Actuators

The DSCS III antenna actuators (see Figures 3 and 4) are exact replicas of the BSE drives from stepper motor to pinion gear. The spur gear has been changed to a segment, and the gear ratio has been reduced to minimize weight. A conductive film potentiometer and stops have been added (see Figure 5) to meet design requirements, and the wrap spring clutch has been deleted since the need for redundancy has been eliminated.

BSE Reed Switches

Reed switches are used in the BSE solar array drive to generate position inputs to the Attitude Control Subsystem for roll and yaw axis control. Two switches are mounted side by side in each of four position indicator switch assemblies. These assemblies are mounted at 90° spacing around the solar array drive shaft to indicate quadrant position. A bar magnet, which is installed into the position indicator switch assembly, normally keeps the contacts of the two reed switches closed. A disc with a 90° gap is attached to the solar array drive shaft and passes between the magnet and the switches (see Figures 6 and 7). When the 90° sector of the disc passes an assembly, the switches remain closed; but when the solid 270° sector passes an assembly, the magnetic field is interrupted and the switches open. Since the shaft normally rotates at an average speed of one revolution per day, each pair of switches is normally open for six hours per day and closed for 18 hours per day.

BSE Reed Switch Problem

The Reed Switches were purchased from a contractor to a detailed Switch specification. This detailed Switch specification was prepared using test methods for Reed Switches in accordance with MIL-S-55433. These switches worked well during acceptance testing, but during qualification testing of the entire solar array drive assembly, the following facts and theories became apparent.

Facts

1. Switches that operated successfully through extensive ambient and thermal cycling sometimes remained closed after vibration.

2. These switches eventually opened after:

   a) disturbance of magnetic field
   b) physical disturbance

Theories

1. Despite the presence of the disc, the magnetic field at the switch is significantly high.

2. Vibration causes switch blades, which closed, to stick. (It is a well known fact that switches do stick after subjection to vibration while closed. This phenomenon is listed as a theory since all our switches were tested for sticking per MIL-S-55433).

To prove the validity of these theories, we had to assume that switch design problems could exist that would not show up until sub-system installation. For example, all the switches had been tested for sticking per MIL-S-55433. Therefore, Theory No. 2 could only be valid if the subsystem installation environmental conditions caused greater stress than imposed by the specified piece part test.

In order to investigate Theory 1 above, a test was devised to plot magnetic field at the switch locations versus disc position (see Figures 8 and 9). With switches of differing known pull-in and drop-out values installed in the test fixture, the disc was moved in and out until both inner and outer switches actuated. A number of conclusions were evident from this testing:

1. With the disc in the switch open position, the magnetic field at the switches is considerable (16 ampere turns vs. 20 ampere turns drop-out).

2. The field strength at the outer switch is always higher than at the inner switch (due to magnetic leakage around the disc).

In order to investigate Theory 2, a test fixture was fabricated to allow vibration testing of the switches and disc disassembled from the complete assembly. During this testing, one of the switches remained closed despite: 1) replacement of the disc with a demagnetized disc, 2) reduction of the disc gap to zero (reduced magnetic field), and 3) replacement of the magnet with a weaker magnet. It opened when it was lightly tapped. The switch was revibrated and stuck again. This time the switch was left alone and opened by itself after approximately six hours. The vibration was then separated into bands by frequency with the following results:

Frequency	g level	Results
80 - 160 Hz	24	No Sticking
160 - 230 Hz	36	No Sticking
230 - 1100 Hz	26	Stuck
1100 - 1400 Hz	60	Stuck
1400 - 2000 Hz	13	No Sticking

An accelerometer mounted to the switch assembly indicated a resonance at around 900 Hz with an amplification of about 4.5X. It was felt that an increase in the natural frequency which would remove the resonance might prevent sticking. In order to test this theory, an .090" aluminum stiffener was bonded to the switch assembly. The switch did not stick after vibration. The stiffener was removed and again the switch stuck after vibration. The conclusion reached was that the switch sticks when the g level exceeds about 36 g's.

Discussions were held with the switch vendor regarding our failures. The vendor felt that the switch being used was "too small" for a critical application and that the next larger switch would perform better for the following reasons:

1. A heavier coating of rhodium
2. More snap action
3. Made on automatic equipment (i.e., better quality control)

The larger switches were purchased and fabricated into six (6) assemblies using identical procedures and materials. These switches were vibrated at the highest levels with gap settings equivalent to only two ampere turns margin without failure.

The following changes were implemented to eliminate the problem:

1. Changed switches to larger type.

2. Changed switch specification to tighten pull-in and drop-out ranges and to reject switches that stick by 1 ampere turn or more.

3. Redesigned bracket for higher stiffness.

4. Added a field strength requirement to the magnet drawing to control all magnets.

5. Tested all switch assemblies as follows:

   a) must pull-in with .40 oersted magnet
   b) must drop-out with .92 oersted magnet
   c) disc position @ drop-out must exceed vehicle setting by 1.5mm
   d) vibration test

BSE Wrap Spring Problem

Wrap springs are used in the BSE solar array drive to transmit torque from the two redundant drive modules to the common output shaft (see Figure 10). In transmitting this torque, each spring must bridge a gap between the driving hub and the driven shaft. Accurate control of this gap is necessary to prevent the spring from wedging itself into the gap.

Two significant changes were made between the original testing of the wrap springs and the flight configuration. In the original testing, a single spring drove the output shaft; whereas, in the flight configuration, two widely separated springs (56 cm between springs) were utilized. In addition, the flight springs had drastically reduced cross section in order to minimize weight. As a result of these two changes, the spring exhibited a tendence to wedge itself into the gap under extreme loading (20 to 30 times the anticipated torque). Analysis of the anomaly revealed the following facts:

1. Bearing axial play, shimming, thermal effects, and gap setting tolerances were producing a 0.84 mm gap.

2. Under extreme loading, the spring forces at the gap deflect the structure thereby causing the gap to open as much as 0.46 mm on one side.

3. The corner radii (or chamfers) on the spring cross section cause a wedging action on the shaft that permits the gap to increase as much as 0.38 mm due to structural flexibility.

Previous analysis of Item 1 had shown ample margin (.84 mm gap vs. a 1.47 mm cross sectional width of the lighter spring). It was determined during tests of the complete assembly that Items 2 and 3 in combination with Item 1 resulted in a gap that would exceed the spring widgh (.84 + .46 + .38 = 1.68 mm which is greater than 1.47 mm). Thus, the gap width should be sized by dynamic as well as static analysis. The dynamic effects may only be measured by performing tests on the component.

By accurately controlling the shimming of the bearings and the setting of the gaps, we are able to reduce the contribution of Item 1 to 0.45 mm. With these changes, the spring ceased to wedge into the gap. Under even the most severe loading and worst tolerances, the gap is 0.18 mm less than the spring cross sectional width.

DSCS III Approach to Testing

The approach to testing on the DSCS III program has been to perform as much in-process testing as possible in order to uncover potential problems as early as possible. A list of the significant tests performed on the DSCS III solar array drive and antenna drives is as follows:

1. Complete functional and environmental testing of an engineering model.

2. 100% run-in of bearings and gears for prime usage.

3. Precise monitoring of wrap spring gap.

4. Measurement of motor and harmonic drive friction torque at temperature extremes.

An engineering model of the solar array drive was fabricated including all of the critical piece parts (see Figure 11). The assembly was subjected to the full DSCS III qualification test levels for vibration and temperature. At the conclusion of these environmental tests, the assembly was completed disassembled and inspected for damage and/or wear. The inspection did not reveal any out of tolerance conditions.

All bearings and gears, including the harmonic drive, were run-in, inspected, and thoroughly cleaned before being installed into prime assemblies. This run-in assures a smooth running assembly with no possibility for high friction due to burrs, chips, or surface imperfections.

In the modified solar array drive configuration of DSCS III, the critical wrap spring gap is not capable of direct measurement. In order to prevent a repeat of the BSE wrap spring problem, the piece part tolerances were held extremely tight and the mating pieces were measured prior to assembly. As a result of these controls, the gap was held to 0.25 ± 0.10 mm which eliminated the possibility of a problem.

The most important pre-assembly test on DSCS III was a measurement of stepper motor and harmonic drive friction torque in a prime configuration at temperature extremes, This measurement yields a direct indication of the excess stepper motor torque, over and above internal friction, that is available to overcome external loads and inertia. This in-process test revealed a low temperature problem associated with the harmonic drive and a high temperature problem associated with the stepper motor. Both of these problems were readily identified and corrected. However, if this testing had not been performed, we would have experienced these problems for the first time at the assembly level. Since the problems occurred at both high and low temperature, it would have been extremely difficult to identify the two separate sources, motor and harmonic drive, at this level of assembly.

CONCLUSIONS

A proven pedigree plus early testing of all modifications insure a successful design. A successful design plus ample in-process testing produces quality hardware. These principles have been successfully applied in the development of four drive mechanisms for the BSE and DSCS III communication satellites.

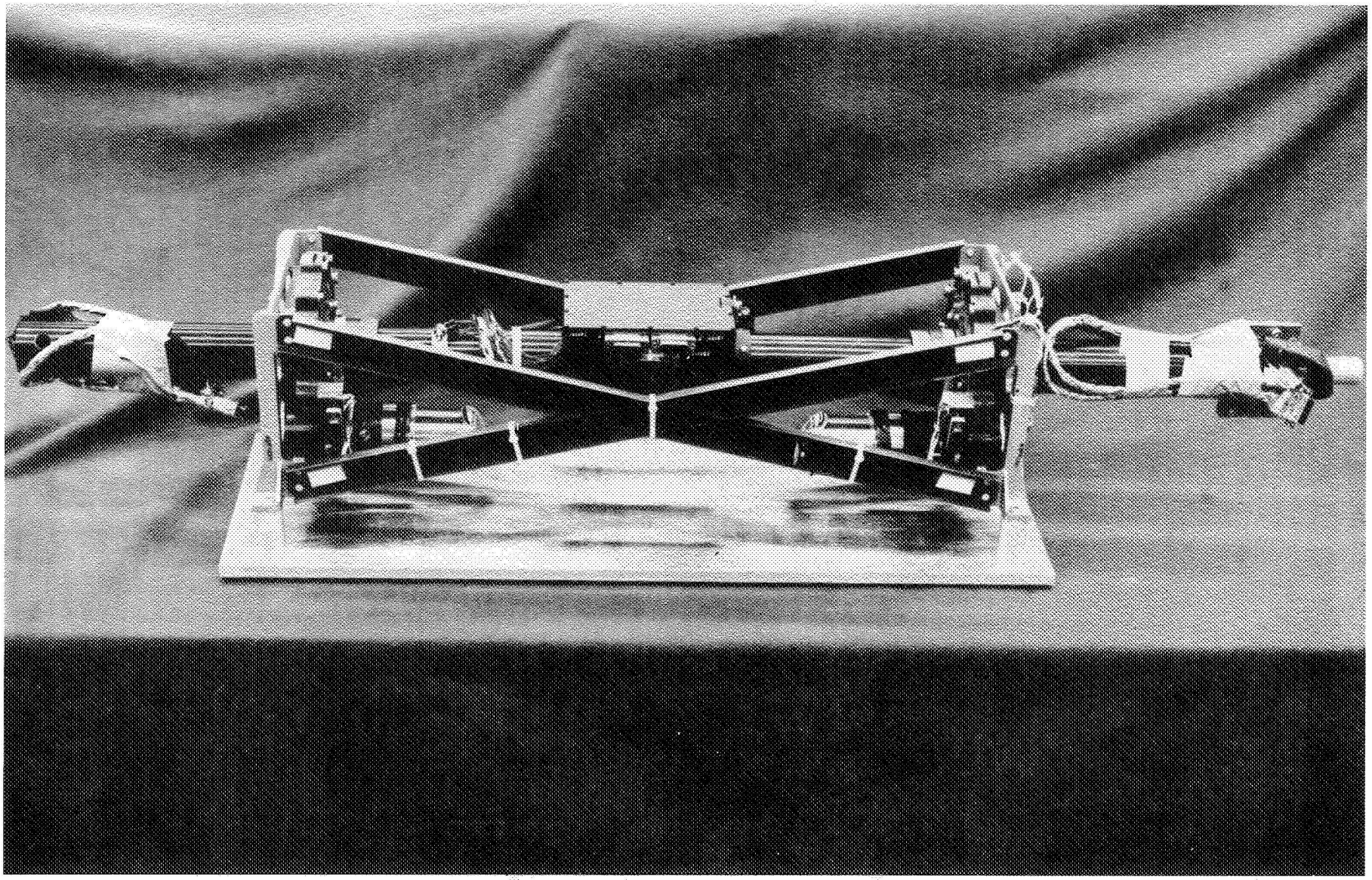

Figure 1. BSE Solar Array Drive

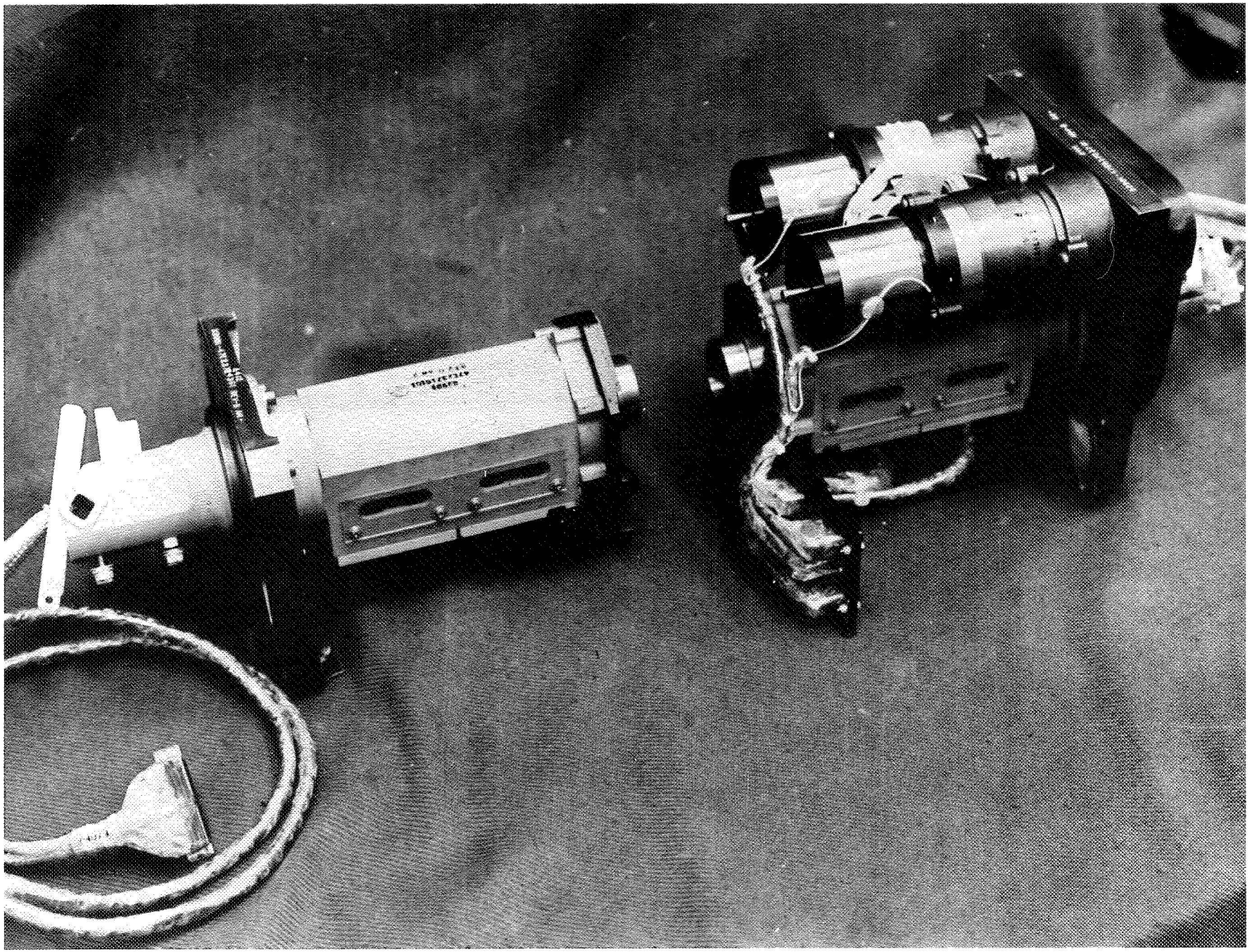

Figure 2. DSCS III Solar Array Drive (Torque Tube not Shown)

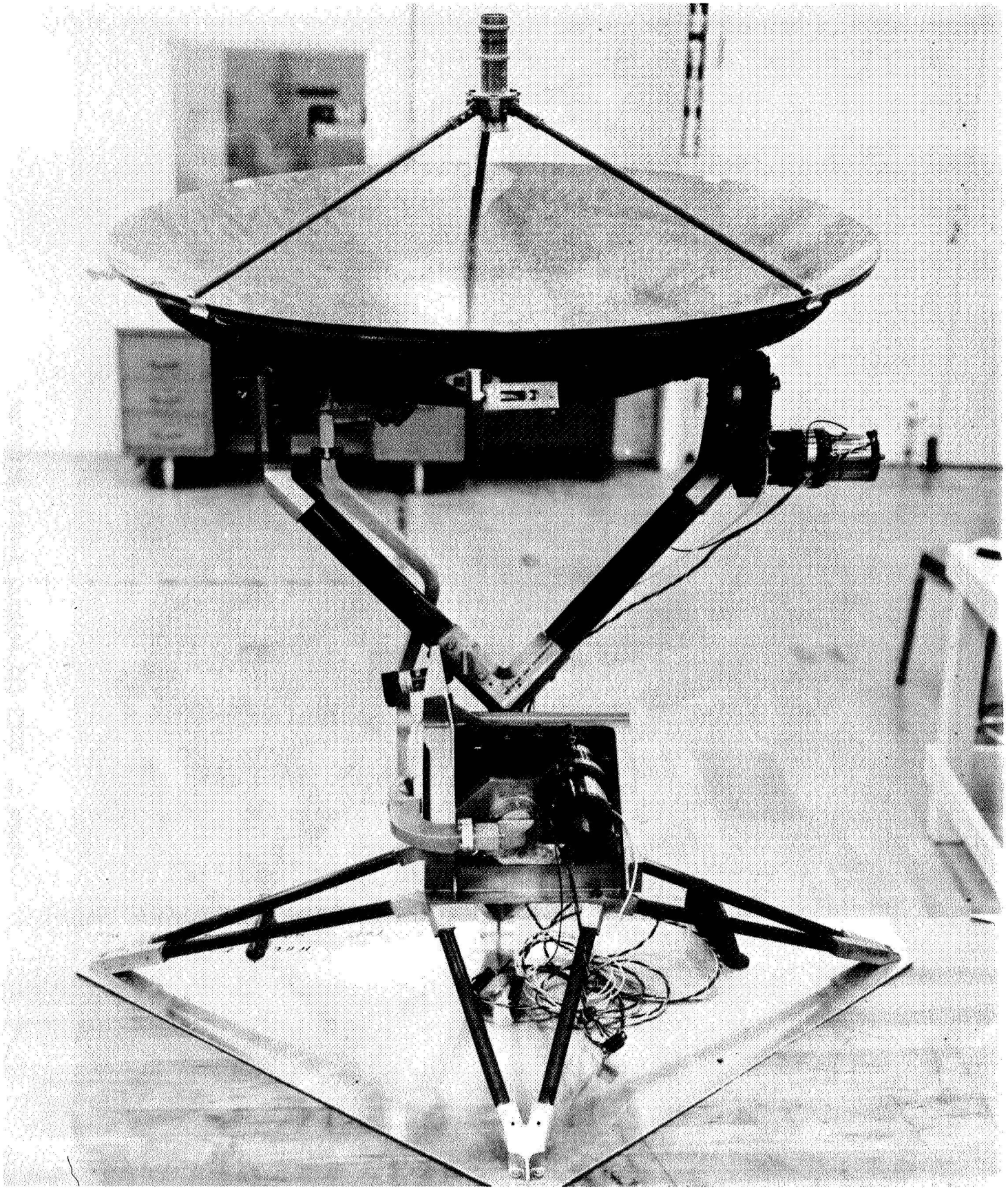

Figure 3. DSCS III Gimballed Antenna

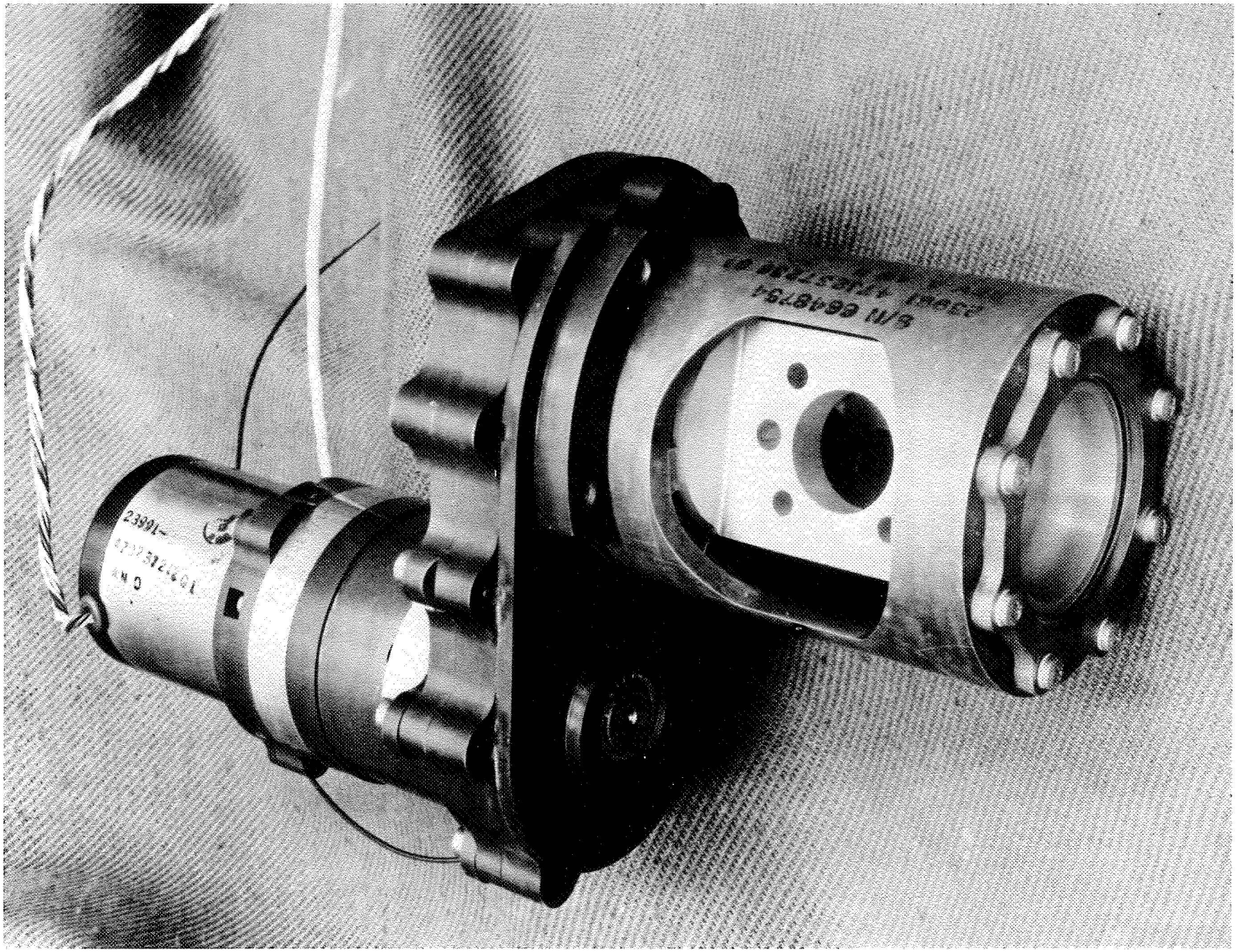

Figure 4. DSCS III Antenna X-Axis Actuator

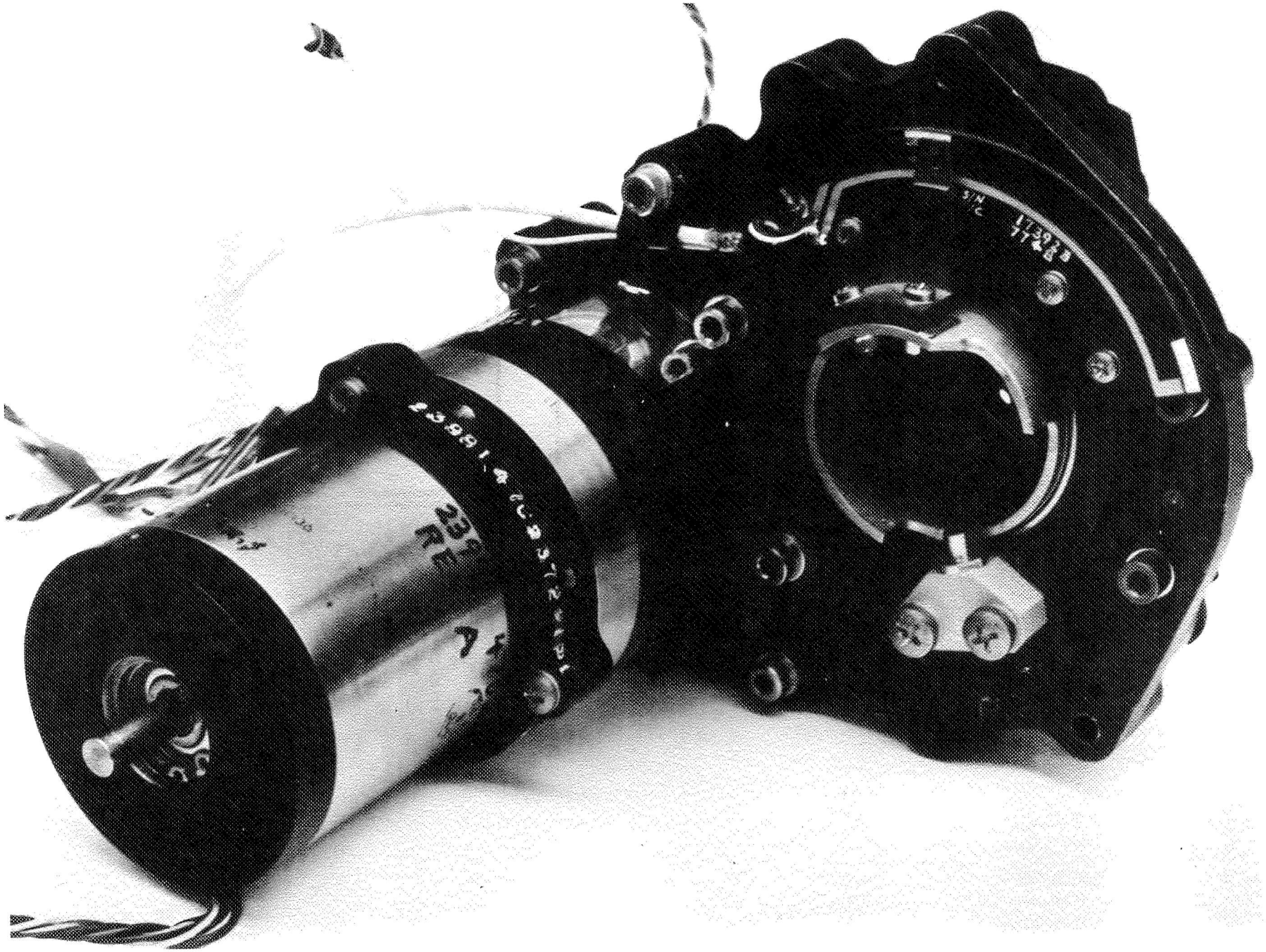

Figure 5. DSCS III Antenna Y-Axis Actuator

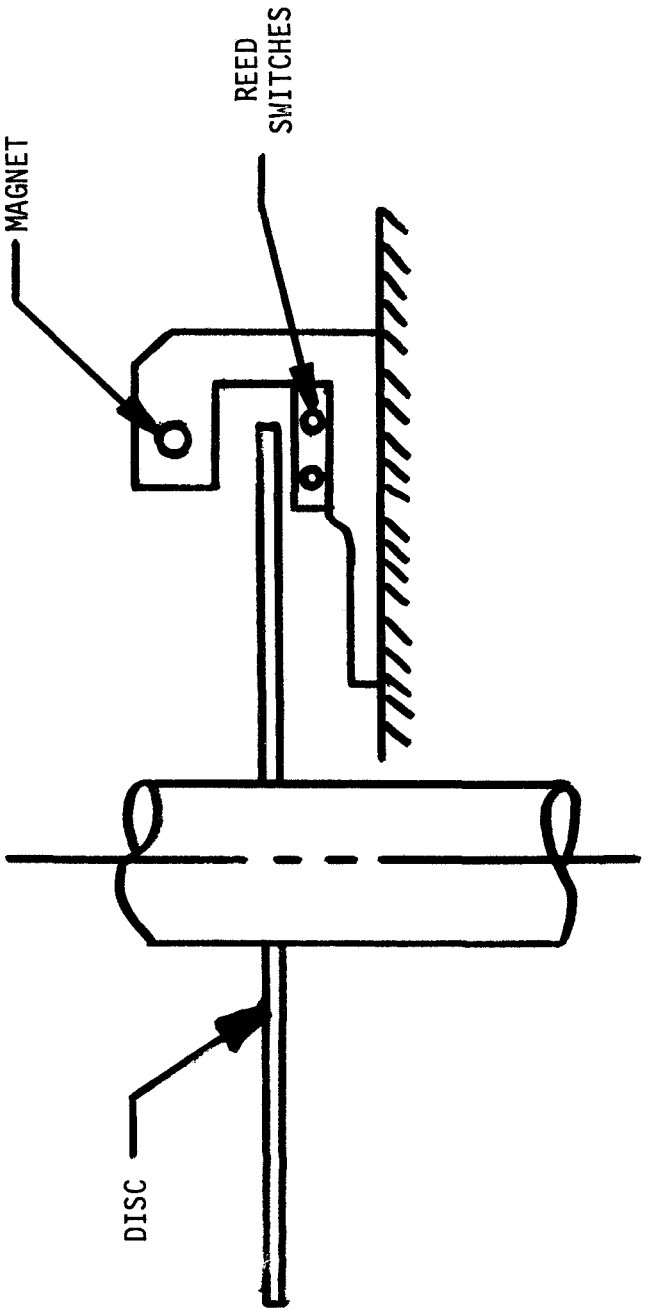

Figure 6. BSE Reed Switch Assembly

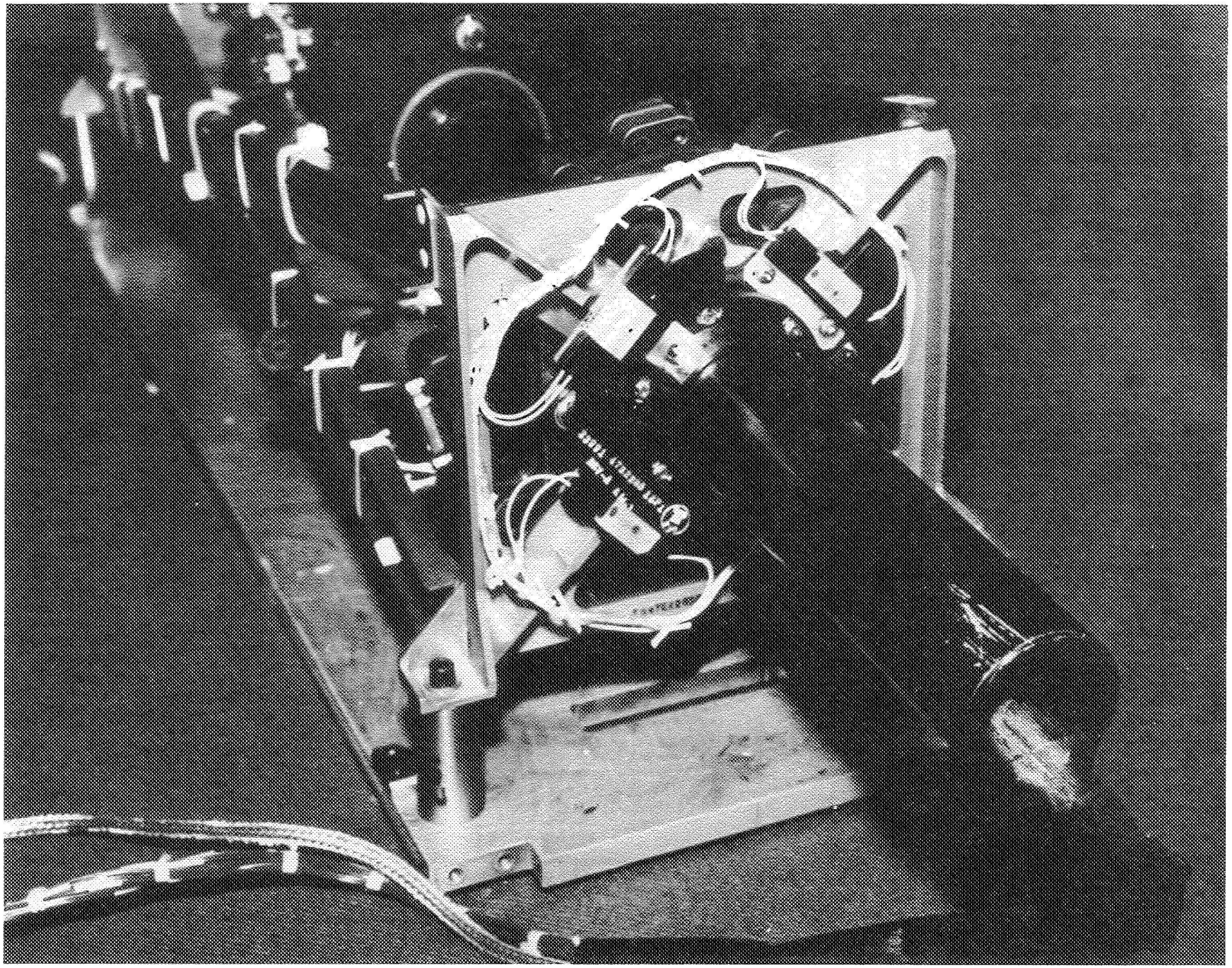

Figure 7. Reed Switches Assembled to BSE Solar Array Drive

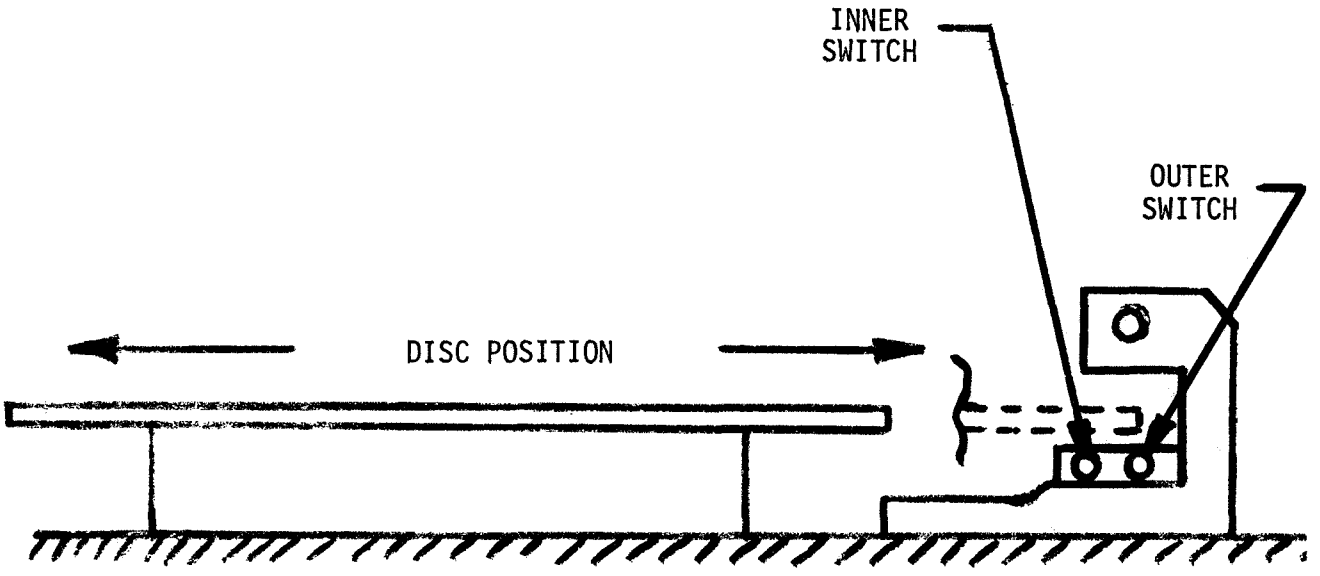

Figure 8. Reed Switch/Disc Test Fixture

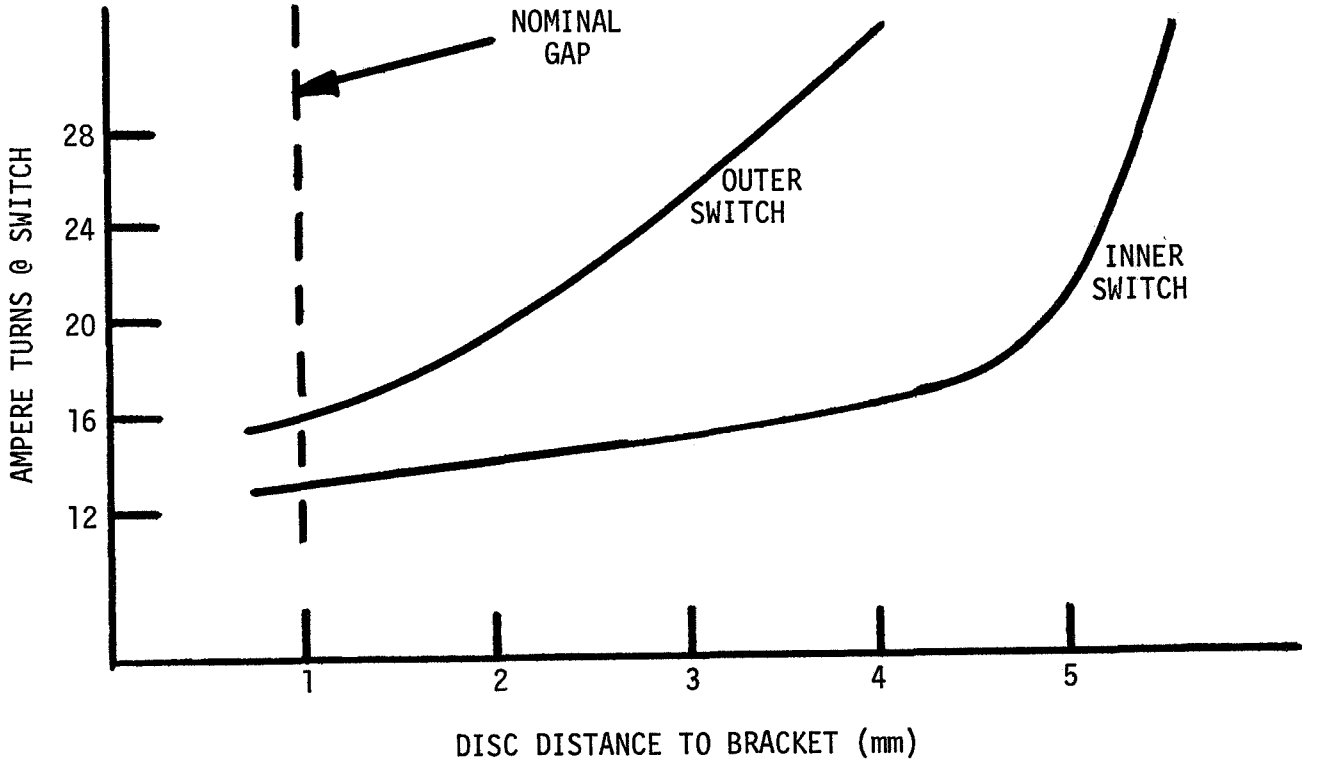

Figure 9. Effect of Disc Position on Magnetic Field

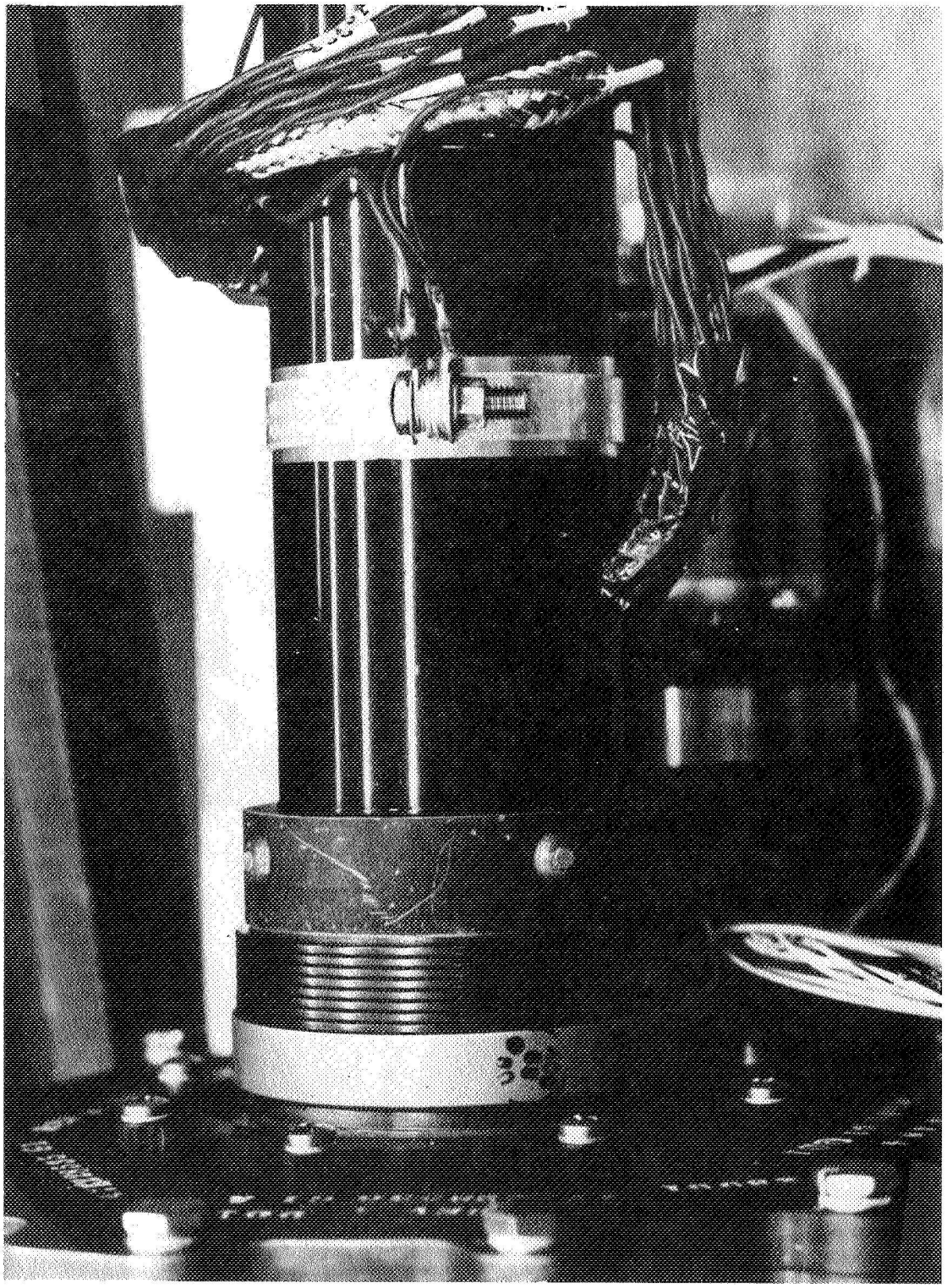

Figure 10. Wrap Spring Portion of BSE Solar Array Drive

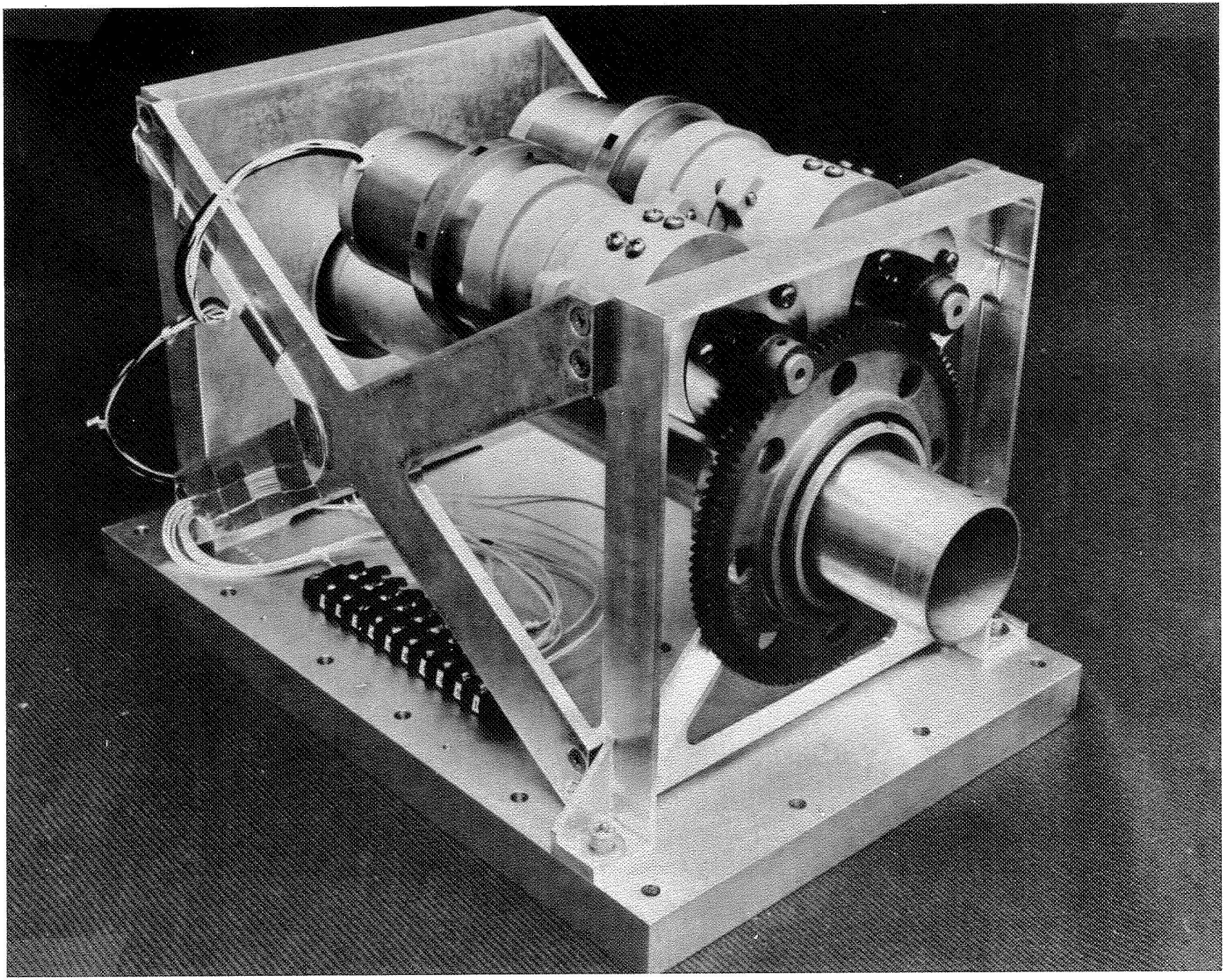

Figure 11. DSCS III Solar Array Drive - Engineering Model

TESTS OF A PROTECTIVE SHELL PASSIVE RELEASE MECHANISM FOR HYPERSONIC WIND-TUNNEL MODELS

Richard L. Puster* and James E. Dunn**

ABSTRACT

A protective shell mechanism for wind tunnel models was developed and tested. The mechanism is passive in operation, reliable, and imposes no new structural design changes for wind tunnel models. Methods of predicting the release time and the measured loads associated with the release of the shell are given. The mechanism was tested in a series of wind tunnel tests to validate the removal process and measure the pressure loads on the model. The protective shell can be used for wind tunnel models that require a step input of heating and loading such as a thin skin heat transfer model. The mechanism may have other potential applications.

INTRODUCTION

Hypersonic wind tunnel models sometimes require protection from pressure loads associated with the start or unstart of the wind tunnel, the loads caused by insertion into the test stream, and thermal and aerodynamic loads of the test medium until exposure of the model is desired. A passive system has been developed which shields a wind tunnel model from a hot hypersonic test medium and then exposes the model to a step input of aerodynamic heating and loading - a useful technique for experimental heat transfer studies. The protection system is novel in that no active electrical, mechanical, or explosive devices are required for the removal of the protective shell.

This paper will describe the design and performance of a protective shell mechanism that was tested in a wind tunnel to verify the operation of the mechanism and to measure the transient loads associated with the release of the protective shell.

SYMBOLS

h	heat transfer coefficient (W/m^2-K)
I	impulse (N/s)
K	heat input parameter (equation 1)
L	model length (cm)
M	Mach number
N_R	Unit Reynolds number per m
P	pressure (kPa or MPa)
$\overline{P}$	mean pressure (kPa or MPa)

*NASA Langley Research Center, Hampton, VA
**Prototype Development Associates, Santa Ana, CA

r	radius (cm)
R	gas constant $\frac{J}{kmol-K}$
s	surface distance (see figure 5)
t	time (s)
T	temperature (K)
$\overline{T}$	mean temperature (K)
X	axial distance along model (cm)
σ	standard deviation

Subscript:

b	base
c	cone
CI	center of impulse
oc	plenum conditions in combustor
p	test section pod
o	total or stagnation point or first exposure of forward split nut to aerodynamic heating
w	wall
zr	temperature at retaining ring failure
1	time to retaining ring failure
2	pitot or time for cavity between model and shell to fill and aft retaining ring to break
3	total time required for all of protective shell components to be downstream of model
∞	freestream

TEST MODEL ASSEMBLY AND OPERATION

Protective Shell Assembly

Figure 1 illustrates the components of the protective shell and the wind tunnel model. The shell was made of two longitudinally split fiberglass petals formed with support pads as shown in the figure. The petals are held in place by a forward restraint/release nut and an aft restraint band. The forward split release nut, shown in detail in figure 2, was fabricated of low brass (80% Cu;

20% Zn) in two pieces which were held together by a zinc retaining ring. The brass nut halves were lap finished at the part plane to produce essentially zero clearance when assembled. A zinc retaining ring was fitted into a circular groove at the rear of the nut, compressed to twice the yield strength of the zinc, and the excess zinc was then machined flush with the brass. A hole was then drilled and tapped into the aft face of the assembled nut. A brass bolt with a conical head was made to nest inside a matching internal conical cavity in the split halves of the petal. By screwing the split nut onto the bolt, the protective petal halves were held and compressed together at the forward end. At the aft end of the model an adaptor ring was installed on the base of the cone and the petal halves were held in place by an external, frangible fiberglass band.

Model

The wind tunnel model was a spherically blunted, 15 degree half-angle cone with a 3.6 cm nose radius, a length of 61 cm, and a base diameter of 38 cm. The model had a gas driven impulse turbine permitting it to be rotated between 1 to 5 revolutions per second. A photograph of the assembled model in the test section of the wind tunnel is shown in figure 3. A device was installed at the base of the model to catch the adapter ring for reuse and to prevent damage to the adapter ring or the model support sting.

The purpose of the rotation was to make the investigation general in scope so that the results could be applied to freely spinning flight bodies. Most wind tunnel models do not rotate and are inserted into the test medium at a zero degree angle of attack; therefore the release dynamics were investigated at this condition as well.

Operational Mechanism

The protective shell removal mechanism is relatively simple. When the model is inserted into the flow, aerodynamic heating to the split nut transfers heat inward raising the temperature of the retaining ring. When the retaining ring is hot enough to lose its strength the two halves of the split nut separate, exposing the annulus between the model and its protective shell to high aerodynamic pressure. As the petal-model annulus fills, the petals open further and break the aft restraining band. As a result of aerodynamic forces, the bolt and petals move away and outward from the model. Freestream turbulence, gravity, and flow misalignment cause the bolt to be removed from the nose. The petals fracture, and the fragments, the bolt, split nut halves, and the parts of the aft restraint band are all accelerated downstream.

Instrumentation

The model had twenty semiconductor pressure transducers (see ref. 1 and 2 for a description of this type of transducer). The temperature of the retaining ring of the forward split nut was measured using two spring loaded chromel alumel thermocouples mounted through the bolt. The spin rate of the model was measured using a fixed Hall effect proximity sensor and permanent magnets rotating with the model. A blunt nose with the same geometry as the forward split nut was made and instrumented with four Gardon-type heat flux gages and was used in separate tests to measure heat flux and its distribution on the flat faced portion of the nose. In another series of tests a sharp cone was fitted to the model and used with the surface pressure transducers to calibrate the test flowfield. Motion picture coverage at 400 and 1000 fps was used to record the protective shield removal process.

FACILITY AND TEST CONDITIONS

The tests were performed in the Langley 8-Foot High-Temperature Structures Tunnel, a hypersonic blow down wind tunnel. The high-energy test stream consists of the products of combustion obtained from a mixture of methane and air burned under pressure in a plenum chamber. The flow is expanded through an axisymmetric, contoured nozzle to approximately Mach 7 into an open-jet test section. The flow is decelerated in a supersonic diffuser. Additional information about the facility and test procedures may be found in references 3, 4, and 5. The nominal test conditions are given in Table I. The stream gas composition, the thermodynamic, transport and flow properties, used for calculating heat flux and flow parameters, were calculated from a thermochemical computer code (ACE) described in reference 6. There was no particular flight condition simulated although the equivalent earth altitude is listed in Table I for reference. The matrix of test conditions provided a range of variables including heat flux, spin rate, angle of attack, model pressure, and freestream pressure.

DATA ACQUISITION AND SPECIAL COMPUTATIONAL TECHNIQUES

Data Acquisition

The information from model test sensors consists of low frequency data such as the temperature rise of the retaining ring, and very high frequency data, such as the transient surface pressures during the petal removal process. The output of the gages was recorded at 20 samples per second on a low frequency system filtered at 2 Hz, and concurrently on two FM tape recorders. The signal from the gages was input to each system with an isolation amplifier with a gain of 1. The FM recorded signal was flat to within 1 db up to 20 kHz. The FM data were sampled at 50×10^3 samples per second to prevent aliasing (see ref 7) and filtered at 12.5 kHz using a sharp rolloff constant amplitude filter (48 db/octave). Consequently the data should be accurate to at least 10 kHz. Ground loop electrical noise at 60 Hz was present but was of such a low magnitude that the transient data were unaffected and because of the 2 Hz filter the low frequency data were not affected at all.

Flowfield Calibration

The flowfield and the conditions at the surface of the cone in particular were calculated with the use of the gas properties calculated from reference 6 and used as input to the program of reference 8. Figure 4 presents the results of some of those calculations. The ratio of cone surface pressure to free-stream static pressure is given as a function of freestream Mach number for air and various total temperatures of the combustion products. The information from reference 9 was used to verify the computational method of reference 8 for air. It is evident from figure 4 that as the total temperature increases there is a significant difference between the values of the cone to freestream pressure ratio for air and for combustion products over the Mach number range shown.

The tunnel conditions were assumed to be constant for the capture diameter (38 cm.) of the cone. This is a reasonable assumption since the flowfield diameter is 244 cm and previous calibrations, reference 10, have indicated that the flowfield is fairly uniform over a 102 cm diameter of the center of the wind tunnel. Using the sharp nose cone with the bare wind tunnel model and by varying the position of the support strut, the flow Mach number and its radial distribution were determined with the use of the curves of figure 4. The flow

for the test conditions of Table I has a mean Mach number of 6.75 with a standard deviation about the mean of 0.077 (σ) for the central 2 m core of the flow.

PREDICTION TECHNIQUES

In order to predict when the release of the forward split nut would occur, it was necessary to utilize a good heat transfer prediction; measure the actual heat flux; develop a release time prediction; and correlate the parameters. The following sections will elaborate on each topic.

Heat Transfer Prediction and Measurement

The heat transfer coefficient distribution about the face and after body of the forward split nut was calculated using the methods of references 11 and 12 and the gas properties calculated by reference 6. Tests were made using the blunt nose with the Gardon type heat flux gages and yielded the heat transfer coefficient distribution shown in figure 5 to an s/r_b of 0.65. The results shown are for an angle of attack of zero; all other conditions of angle of attack, spin rate, total pressure and temperature were measured but are not reported here. The heat transfer coefficient distribution was calculated and measured in reference 11 for air at a Mach number of 8.0. The agreement between the coefficient distribution for air and that of the present test as shown in figure 5, using combustion products was very good. The continuous increase in heat transfer coefficient can be substantiated by similar distributions found in references 13 and 14. In all these references and in the present tests, the unit Reynolds number of the flow was high (at least 3 million per m) and the flow hypersonic. Since the flat face geometry of both was identical (up to $s/r_b = 0.81$) and the Mach number and Reynolds number were similar, the coefficient distribution up to an s/r_b of 0.81 from reference 11 was plotted and used in figure 5. The distribution about the rest of the forward split nut was calculated using the methods of reference 12 and a modified Newtonian pressure distribution. Other methods of predicting heat transfer are reviewed in reference 15; in general the methods yield values that can vary up to 10 percent from each other. The agreement between the measured values and the curve from reference 11 gives good confidence for the technique used.

Split Nut Release Time Prediction

Using the computer code SINDA of reference 16 and the combined measured and calculated heat input distribution, the temperature of the surface and inner temperatures of the brass split nut and zinc retaining ring were calculated as functions of time and position. A typical result of these calculations is shown in figure 6. Figure 6 shows the calculated internal temperature distribution of the forward split nut and zinc retaining ring at the zinc retaining ring failure time. Based on the results of the calculations, the zinc should melt in about 20 seconds for the conditions shown and the split nut should then come apart.

Release Time-Heat Load Correlation

A simplified method of predicting stagnation heat flux was developed in reference 17. Eckert's reference temperature was used and a Lewis number of one (no dissociation) was assumed. The derived expression was compared

with that of Fay and Riddell (reference 18) and found to agree within about one percent. By using the methods of reference 17, the maximum variation of the measured stagnation heat transfer coefficient from that calculated was about six percent.

A heat input parameter for use in release time correlation may be derived from the expressions of reference 17 for stagnation point heat transfer coefficient. Any variables found to have less than a 2 percent effect on the heat transfer coefficient were dropped to simplify the expression derived. The heat input was normalized such that the resulting parameter was less than 1.0 for this experiment. The resulting parameter, K, is given by:

$$K = \frac{\sqrt{P_{o,2}}\, T_o^{0.18}(T_o - \bar{T}_w)}{50{,}000} \tag{1}$$

where

$$\bar{T}_w = \frac{\int_{t_o}^{t_1} T_w \, dt}{t_1 - t_o} \tag{2}$$

The heat input parameter, K, will be used to correlate the release time of the split nut as a function of time.

RESULTS

Split Nut Release Time

In figure 7, the observed and calculated split nut release times, t_1, are plotted as a function of the parameter K. The calculated release time as shown in the figure agrees reasonably well with the experimental data with the agreement between theory and experiment being better for the longer duration tests (lower heat flux). Near the solidus point of the zinc alloy (645K for AG40A) used, the variations in strength and fabrication translate into variations in the release time of the split nut. The observed split nut release times and the failure temperature, T_{zr}, of the zinc retaining ring are tabulated in Table II. The observed temperature of the retaining ring at failure varied from 617 to 625K with a mean value of 622K. If the mean strength of the zinc was used as the most probable failure stress, then the retaining ring would fail at 625K which was the measured maximum failure temperature. Thus, the prediction techniques used appear to be valid and reasonably accurate.

Protective Shell Removal

The removal process can best be studied by observing the sequence of photographs of figure 8. As seen in the figure, after about 16 to 18 ms, the petals have opened enough so that the load on the aft restraint band causes it to fail. The petals move outward from the model and fracture, the split nut halves, the bolt, the fractured petals, and the broken aft restraint band are all accelerated downstream. In figure 8, the bolt remains on the nose since it was held there by the thermocouple assembly, which was mounted through the bolt and used to measure the zinc retaining ring temperature. When the

thermocouple assembly was not used the bolt left the nose as expected. In all of the observed tests (using eight (8) 1000 fps and four (4) 400 fps cameras on each test) the removal process was essentially the same, requiring about 35 to 60 milliseconds (see Table II). No model impacts by the components of the protective mechanism were observed even at the highest angle of attack ($\alpha = 9°$) and lowest rotational speed. The aft restraining band always broke before the petals fractured. However, at the highest angle of attack ($\alpha = 9°$) an additional 1/4 spin revolution was required before the windward petal flew outward from the model. In addition, the bolt, when not restrained by the thermocouples, left the nose and traveled downstream. Thus the removal process appears to be reliable; however, downstream tunnel components must be rugged to withstand the bolt and nut impacts.

The mechanism is most suitable for open circuit (usually blow down type) wind tunnels but could be employed in closed circuit wind tunnels which use capture nets to screen debris before return to the compressors. If the model does not spin, the mechanism can only be used when the angle of attack is zero or near zero.

Transient Loads

Figure 9 presents a typical low frequency model surface pressure history and figure 10 a typical transient pressure history of the cone surface. As can be seen from figure 9 the seams between the petals are not perfect and allow the pressure between the shell and model to increase above the test section static pressure but substantially lower than the surface pressure on the outer surface of the shell. However, there was no detectable heating of the model surface. As the split nut opens, the interior pressure increases at a faster rate; then the protective shell is removed and the pressure on the model quickly reaches the cone surface pressure. The transient pressure history is shown in detail on figure 10. The figure shows the background line 60 Hz noise; the frequency was determined by auto-correlating the signal before and after the shell removal. The smaller oscillations are caused by broadband turbulent boundary layer noise. The process of the pressurization of the cavity between the shell petals and the model requires about 14 to 18 ms, being faster for the higher stagnation pressure. The interior pressure increases to 1.5 to 3 times the cone surface pressure with the pressure rise being greater toward the aft end of the cavity. When this process has been completed, the load on the aft restraining band causes it to break. Immediately thereafter, the petals move outward with a consequent sharp drop in cone surface pressure. There may be one relatively slow, major amplitude, oblique shock wave, indicated by the sharp spike in pressure, or there may be two or more pressure spikes (fig. 10b). These transient pressures may occasionally reach 70 to 80 percent of the pitot pressure, but the most probable value observed is 50 percent or less of the pitot pressure with the amplitude of the shock wave decreasing towards the forward end of the cone.

The pressure history from each of the 20 pressure gages was integrated with respect to time, then area, and the impulse imposed on the model was calculated from

$$I = \sum_{n=1}^{20} \left(A_n \int_{t_o}^{t_3 - t_1} P \, dt \right) \qquad (3)$$

where A_n are equal surface area segments.

The effective location of the impulse relative to the body was also calculated. These values plus the cavity fill and removal times are tabulated in Table II. The impulse imparted to this model during the petal removal was usually less than 13 N/s at low angles of attack (0 to 3 degrees); however, at larger angles of attack (6 to 9 degrees), the lateral impulse varied from 36 to 53 N/s. These loads are still extremely low and should present no problem to any wind tunnel model or most flight vehicles.

Potential Applications

In addition to wind tunnel use, the mechanism could be used for the protection of axisymmetric high velocity research vehicles from particle or water impact damage or for heat transfer research. Other applications could be a protective shell for a planetary research probe. The mechanism is reliable, passive, and should be functional indefinitely.

CONCLUDING REMARKS

A protective shell mechanism has been developed that will shield a wind tunnel model and then expose the model to the hypersonic flow field. The mechanism is completely passive in that aerodynamic heating of a brass forward split nut, held together by a zinc retaining ring, caused the ring to fail and thus exposed the petals of the protective sehll to aerodynamic loading. As the cavity pressure between the model and shell petals increases, the loading on an aft restraint band causes it to break. Then, all of the components of the protective shell mechanism are accelerated downstream and out the wind tunnel diffuser. The expected removal process was validated by a series of wind tunnel tests that included varying the heat input, the model angle of attack, and spin rate. The time required for the release process to begin could be calculated with reasonable accuracy and the removal process occurred in 60 ms or less. The mechanism worked reliably with no model strikes from shell components, although at the highest angle of attack an additional 1/4 revolution was required to separate the windward petal. Transient surface pressures were measured and the net lateral impulse delivered to the model was usually less than 15 N/s for angles of attack below 3 degrees; however at larger angles of attack (6 to 9 degrees) the impulse varied from 36 to 53 N/s. The protective shell mechanism can be used for wind tunnel models and has potential application to high velocity research vehicles.

REFERENCES

1. Kurtz, A. D.; and Gravel, C. L.: Semiconductor Transducers Using Tranverse and Shear Piezoeresistance. 22nd ISA Conference, Chicago, September, 1967.

2. Kurtz, A. D.; and Kicks, J. S.: Development and Applications of High Temperature Ultra-Miniature Pressure Transducers. ISA Silver Jubilee Conference, October 1970, Philadelphia.

3. Schaefer, William T., Jr.: Characteristics of Major Active Wind Tunnels at the Langley Research Center. NASA TMX-1130, 1965.

4. Howell, R. R.; and Hunt, L. R.: Methane - Air Combustion Gases as an Aerodynamic Test Medium. Journal of Spacecraft and Rockets, Vol. 9 No. 1 January 1972.

5. Hunt, L. Roane: Aerodynamic Heating and Loading Within Large Open Cavities in Cone and Cone-Cylinder-Flare Models at Mach 6.7. NASA TN D-7403.

6. Kendall, Robert M.: An Analysis of the Coupled Chemically Reacting Boundary Layer and Charring Ablator. Part V - A General Approach to the Thermochemical Solution of Mixed Equilibrium - Nonequilibrium, Homogeneous or Heterogeneous Systems. NASA CR-1064, 1968.

7. Bendat, Julius, S.; Piersol, Allan G.: Measurement and Analysis of Random Data. John Wiley, New York, 1966.

8. Prozan, R. J.: Solution of Non-Isoenergetic Supersonic Flows by Method of Characteristics. Volume III. NASA CR-132274, July 1971.

9. Sims, Joseph L.: Tables for Supersonic Flow Around Right Circular Cones at Zero Angle of Attack. NASA SP-3004, 1964.

10. Deveikis, William D.; and Hunt, L. Roane: Loading and Heating of a Large Flat Plate at Mach 7 in the Langley 8-Foot High-Temperature Structures Tunnel, NASA TN D-7275, 1973.

11. Jones, Robert A.: Heat Transfer and Pressure Distributions on a Flat-Face Rounded-Corner Body of Revolution With and Without a Flap at a Mach Number of 8. NASA TMX-703, September, 1962.

12. Beckwith, Ivan E.; and Cohen, Nathaniel: Application of Similar Solutions to Calculations of Laminar Heat Transfer on Bodies with Yaw and Large Pressure Gradient in High-Speed Flow. NASA TN D-625, 1961.

13. Cooper, Morton; and Mayo, Edward E.: Measurements of Local Heat Transfer and Pressure on Six 2-Inch Diameter Blunt Bodies at A Mach Number of 4.95 and At Reynolds Numbers Per Foot Up to 81 x 10^6. NACA Memo 1-3-59L, March, 1959.

14. Stalmach, C. J., Jr.; and Goodrich, W. D.: Aeroheating Model Advancements Featuring Electroless Metallic Plating. AIAA 9th Aerodynamic Testing Conference. Arlington, Texas, June 7-9, 1976.

15. Hoshizaki, H.; Chou, Y. S.; Kulgein, N. G.; and Meyer, J. W.: Critical Review of Stagnation Point Heat Transfer Theory. AFFDL-TR-75-85, July, 1975.

16. Gaski, J. D.; Fink, L. C.; and Ishimoto, T.: Systems Improved Numerical Differencing Analyzer. NASA Contract 9-8289 and 9-10435 Sept. 1970 and April 1971, TRW Systems Inc., Redondo Beach, California.

17. Buckley, Frank T.: Constant-Mach-Number Simulation of Critical Flight Loads on High-Velocity Projectile Fuses. Harry Diamond Lab TR-1466, August 1969.

18. Fay, J. A. and Riddell, F. R.: "Theory of Stagnation Point Heat Transfer in Dissociated Air," JAS, V.25, 73 (1959).

TABLE I. TEST CONDITIONS

TEST	$\bar{P}_{oc}$*	$P_{0,2}$	$\bar{T}_{oc}$		FREE-STREAM DYNAMIC PRESSURE	P_∞	ANGLE OF ATTACK	N_R	ROTATIONAL SPEED OF MODEL	EQUIVALENT EARTH ALTITUDE
	MPa	kPa	K	$\sigma/\bar{T}_{oc}$	kPa	kPa	deg	per m $\times 10^6$	rev per s	km
1	18.27	136.1	1860	0.030	72.0	2.83	0	4.62	1.4†	24.3
2	18.38	136.9	1860	0.030	74.2	2.52	0	5.00	3.6	25.1
3	18.25	136.0	1858	0.025	73.6	2.50	3	4.93	2.0	25.1
4	18.31	137.3	1823	0.033	73.4	2.50	6	4.80	2.5	25.1
5	10.86	74.40	1561	0.030	38.0	1.49	0	3.02	4.4	28.5
6	10.86	81.43	1831	0.036	43.3	1.47	0	2.67	4.2	28.6
7	10.85	80.33	1741	0.037	42.0	1.50	6	2.81	3.3	28.5
8	10.85	80.06	1729	0.030	41.4	1.49	9	2.88	2.6	28.5

* - $\sigma/\bar{P}_{oc}$ WAS USUALLY 0.0025 OR LESS

† - REPEATED AT ZERO ROTATIONAL SPEED

TABLE II. SUMMARY OF TEST RESULTS

TEST	t_1-t_0	t_2-t_1	t_3-t_1	T_{zr}	I	$X_{CI/L}$
	s	ms	ms	K	N/S	
1	19.55	17	55	617	12.9	0.30
2	20.80	16	55	622	11.6	0.99
3	20.05	17	45	622	14.2	0.47
4	20.69	15	60	622	51.2	0.68
5	33.18	17	60	625	9.8	0.94
6	27.67	23	45	*	11.1	0.75
7	27.41	25	65	622	42.7	0.75
8	28.62	23	35 205†	*	35.6	0.74

* - RETAINING RING THERMOCOUPLES NOT USED SO BOLT BEHAVIOR COULD BE EVALUATED

† - TIME OF SECOND PETAL REMOVAL

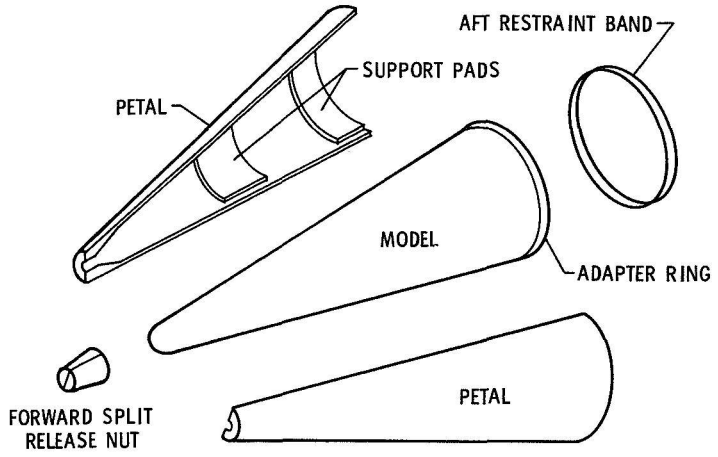

Figure 1.- Protective shell mechanism components.

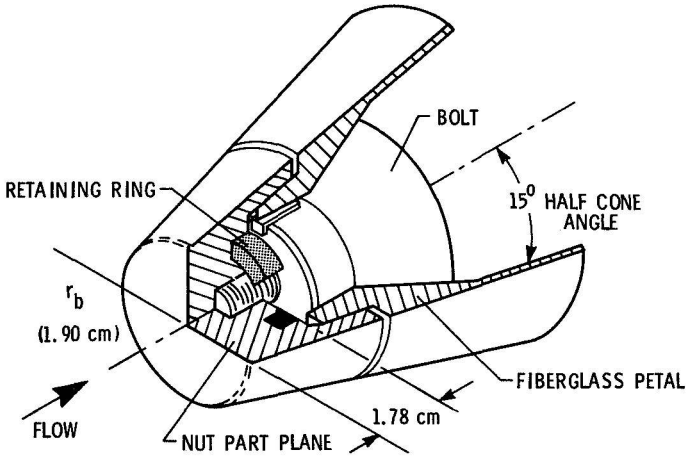

Figure 2.- Details of split release nut.

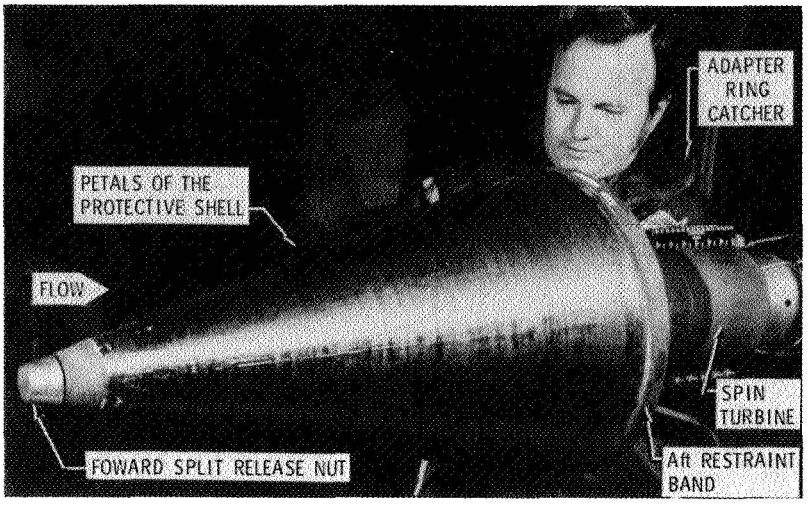

Figure 3.- Assembled model in test section of wind tunnel.

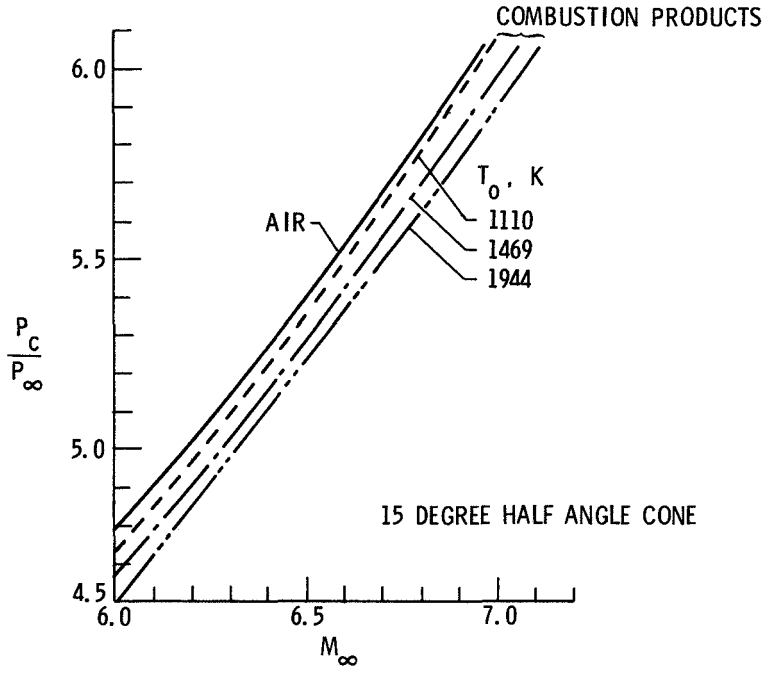

Figure 4.- Variation of cone to freestream pressure ratio with freestream Mach number

	h_o, W/m^2 - K	M_∞	$N_R \times 10^6$	T_o, K	P_o, MPa	TEST GAS
O	509	6.75	4.92	1808	18.2	COMBUSTION PRODUCTS
—	210	8.0	3.05	728	6.31	AIR (REF. 11)
---	CALCULATED FOR THIS TEST FOR $s/r_b > 0.81$					

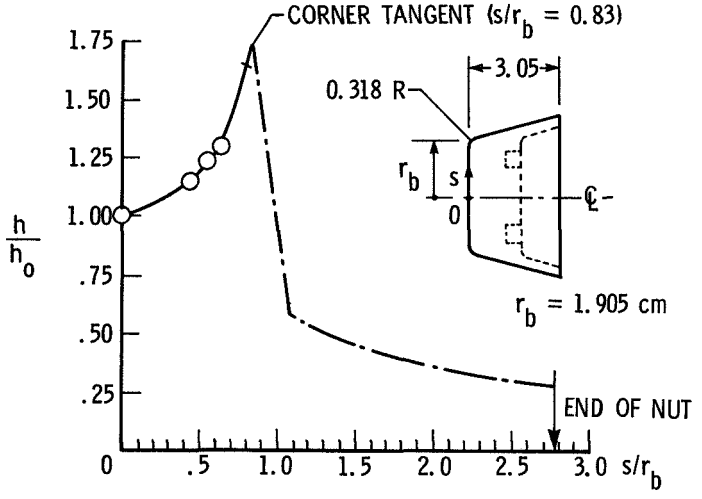

Figure 5.- Variation of heat transfer coefficient over surface of forward split release nut.

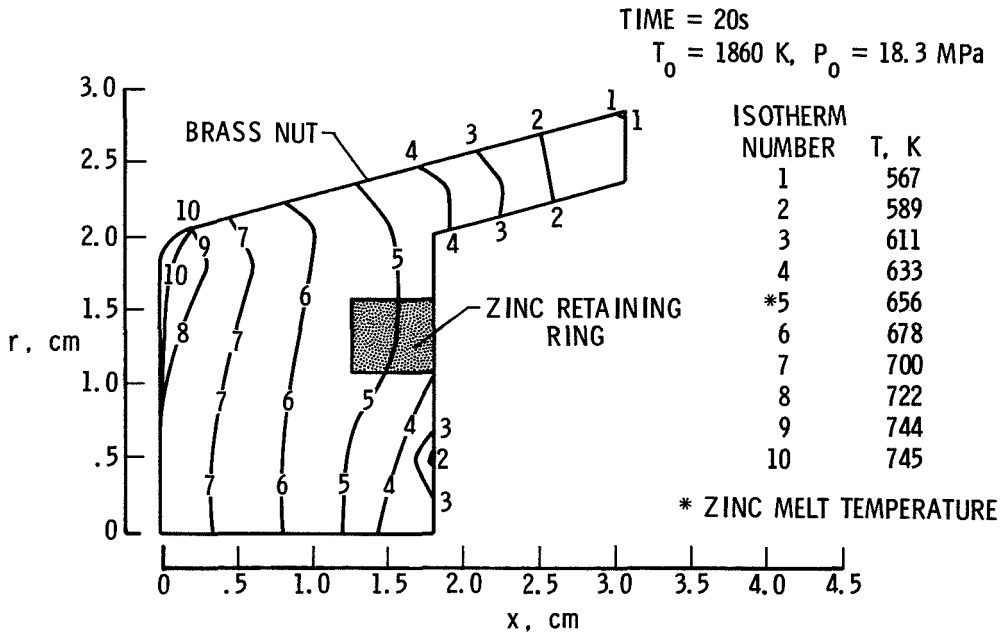

Figure 6.- Contour plot of isotherms through the nut and zinc retaining ring.

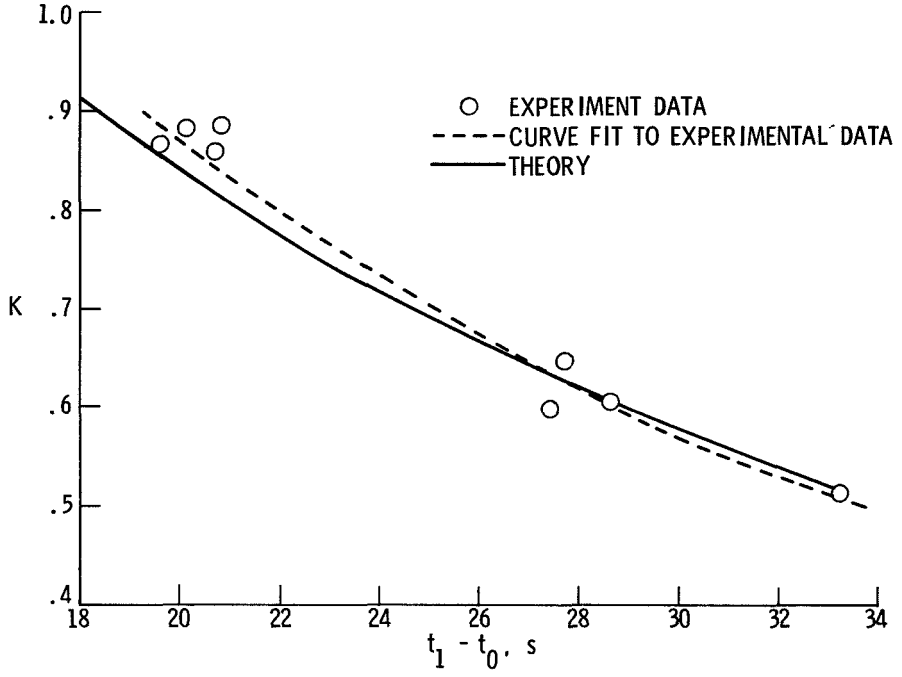

Figure 7.- Comparison of the calculated and experimental split nut release times.

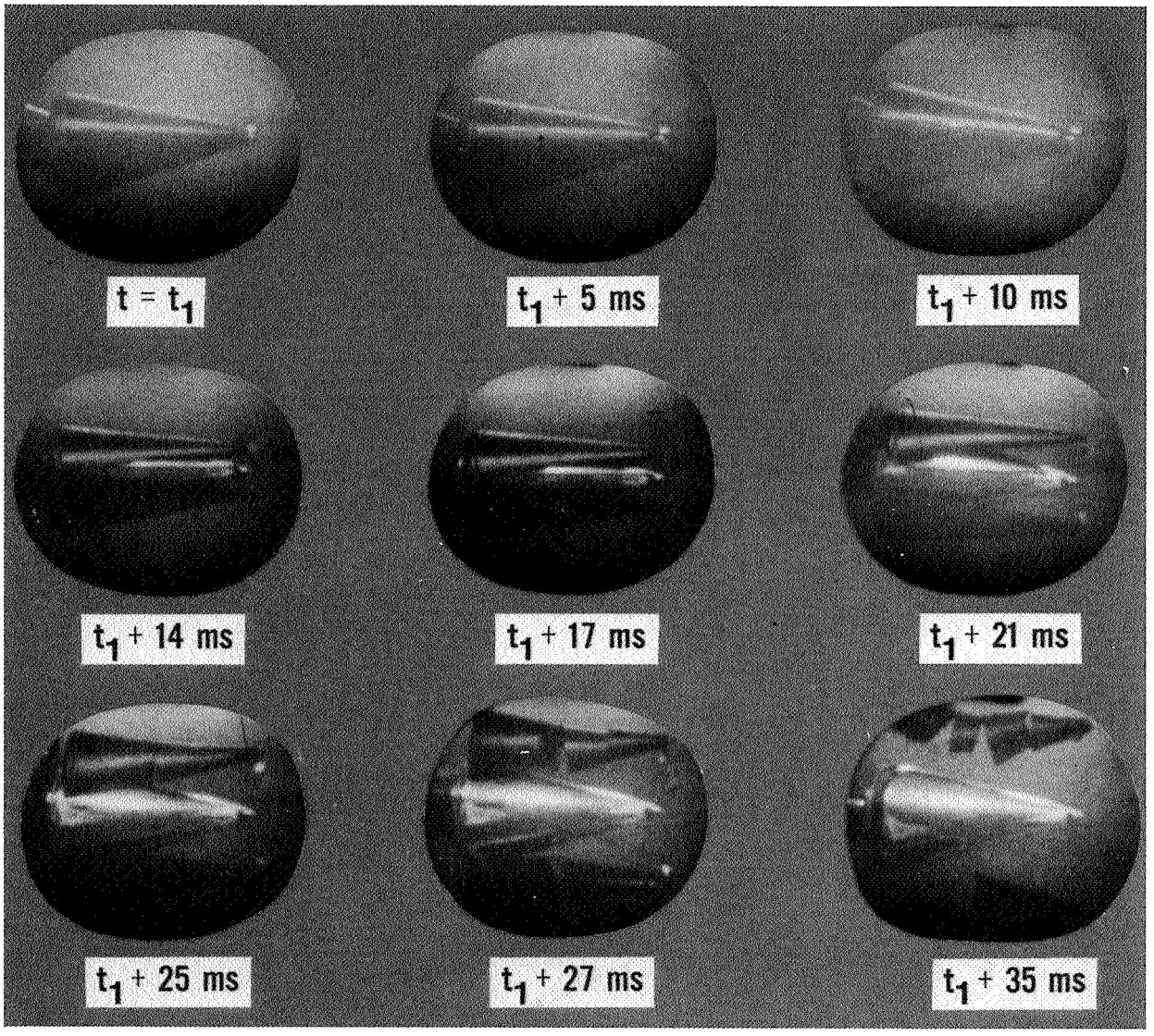

Figure 8.- Removal sequence of protective shell.

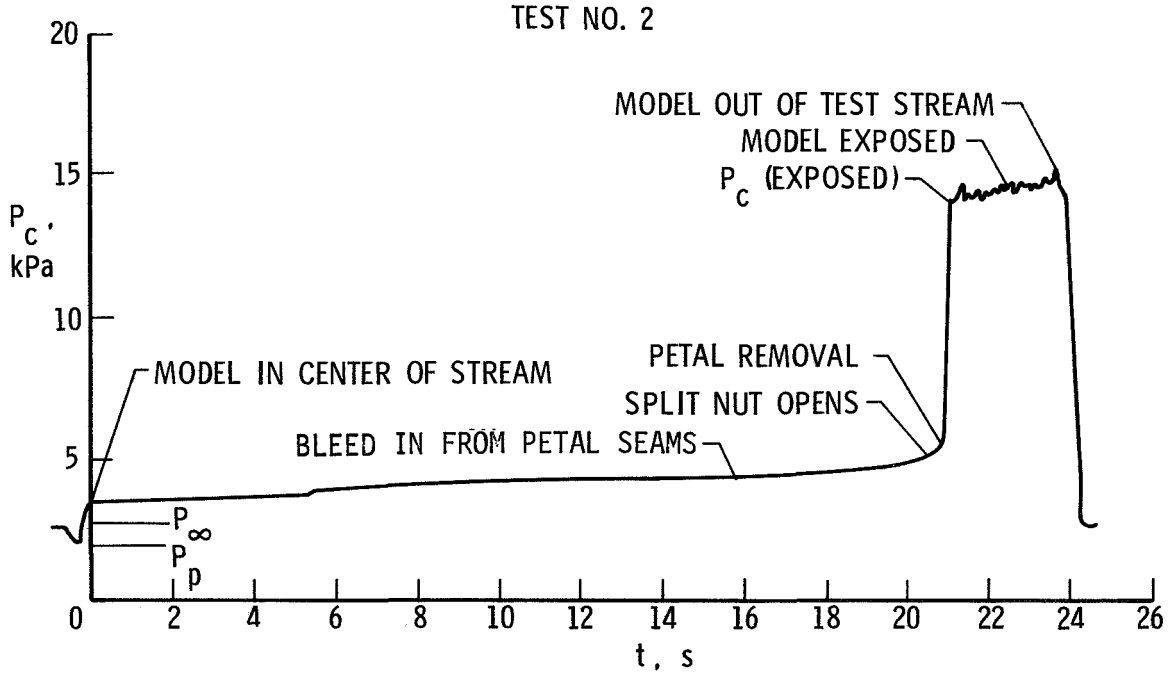

Figure 9.- Cone surface pressure during a typical test.

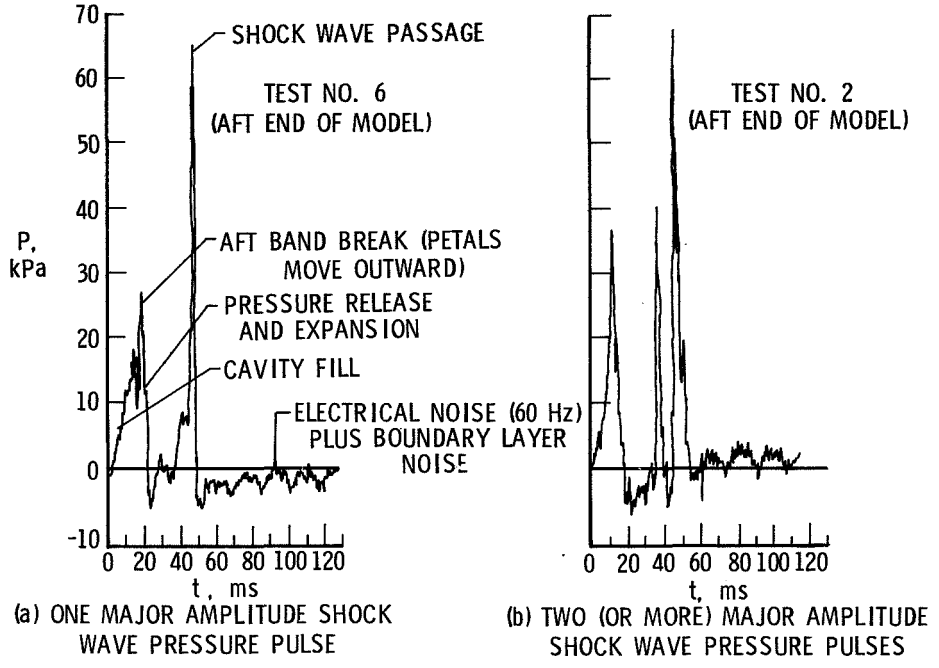

Figure 10.- Dynamic pressure history of cone surface during petal removal.

MAGNETIC SPRING IN OSCILLATING MIRROR LINEAR SCANNER FOR SATELLITE CAMERA

by G. THOMIN
of the Centre National d'Etudes Spatiales (CNES)

and C. FOUCHE
of the Société Européenne de Propulsion (SEP)

SUMMARY

One of the main difficulties encountered in the development of a multispectral scanner is the realisation of an oscillating mechanical device. This paper presents a magnetic device which is characterized by the absence of friction. The main developments concern the analysis of magnetic forces. A preliminary project of a device which could be used in a satellite is presented.

INTRODUCTION

The multispectral pictures of the earth taken by satellite are of great interest for the understanding of natural phenomena. The device presented here has the potential qualities which enable us to envisage in the near future an increase in the performance of scanners.

A mirror placed in the lens's space of a telescope is animated by a linear oscillation, thus means that the diagram of angular movement has a triangular shape.

The characteristics used as a basis for elaboration of the project are the following :

- useful angular amplitude = $\pm$ 4.4. degrees
- oscillation frequency = 8 Hertz
- pupil/beam diameter = 280 mm

The following performances are required :

- Linearity better than $\pm$ 0.5 %
- Scanning efficiency on away movement 0.35
- reproductibility of the movement less than $4 \cdot 10^{-6}$ radian
- pivoting precession less than $4 \cdot 10^{-6}$ radian

This paper is based on work carried out in collaboration between the CNES and the SEP, the magnetic device presented is subject of patent pending.

PRINCIPLES OF THE MAGNETIC SPRING

The linear oscillation of the mirror is obtained by a magnetic thrusting effect on both ends of the useful angular movement. The magnetic thrusts are associated with a pivot without spring torque effect using an active electromagnetic bearing. Consequently, the rotor is guided in its oscillation only by the magnetic forces. The drawing of the principle of a magnetic thrust is presented in figure 1. A highly induced saturation ferro-magnetic strip moves between two armatures so that the magnetic circuit gaps are small and constant. The gaps do not vary when the strip is moved along the whole length of the armature. But, at the end of the run, the magnetic resistance of the gaps increases abruptly. As a result there appears at both ends a reaction force, F_R, which is proportional to the derivative of the magnetic resistance.

$$F_R = \frac{1}{2} \varphi^2 \frac{\partial R}{\partial \theta}$$

φ = magnetic flux of the gaps
R = magnetic resistance of the gaps
θ = rotation angle of the mirror

Figure 2 represents the outlook diagram of Torque and diagram of the angular movement in relation to time.

The distribution of the magnetic field lines goes from a symetric distribution at the center to asymmetric distributions at both ends of the course (see figure 1). The result is a assymmetry in the pressure of forces generated by the magnetic field on both lateral faces of the strip and the appearance of a return-force towards the center. The pressure on the contours of the strip is calculated by the formula :

$$df = \frac{B^2}{2\mu o} \, dS$$

where B = magnetic induction
dS = elementary section
$\mu o = 4 \pi 10^{-7}$

However, as in all magnetic attraction systems, the stiffness of the recentering described above has for result, a strong unstable stiffness in the direction of the magnetic flux circulation.

In the central position, the strip has an unstable balance which means that a shift in its position creates a force which tends to increase this shift. This instability is produced by an increase in magnetic field density lines at the end of the strip closest to the armature and inversely at the other end. The presence of an unstable stiffness is the major difficulty in the setting-up of the magnetic thrust, this difficulty being overcome by using SEP electromagnetic bearing which has a large position stiffness.

Moreover, a ferror-magnetic material used for the armature having a weaker saturation induction than that of the strip contributes to a notable instability reduction.

The magnetic thrust intrinsic instability has been the object of a theoretical survey using a numerical finite elements method to calculate magnetic field distribution.

As an example, the visualisation of the magnetic field lines near the gap is represented in figures 3 and 4. On figure 3, the materials (ferro-cobalts) are identical for the strip and the armature. On figure 4, the strip is of ferro - cobalt (B_S = 2,4 Tesla) and the armature is ferro-nickel (B_S = 1,3 Tesla). It would appear that the use of material with a low induction saturation has the effect of reducing the density of field lines on the end of the strip, and that of creating a saturated zone in the armature near the gap. Depending on the proximity of this strip, this saturable zone increases. In comparison with the figure 3, the case plotted on figure 4 having for effect the instability reduction with a ratio of 120%. This phenomenom has been confirmed by laboratory experiments.

PRELIMINARY SURVEY MODEL

To validate the principle of the magnetic thrust, an experimental oscillating assembly was constructed. The overall view of this is represented in picture 5. The experimental assembly was constructed around a precision pivot by conical air bearing and has two devices for magnetic thrusts situated at both ends of an oscillating arm. The magnetic circuit of the thrusts is represented in figure 9, the armature a_1, a_2 in cylindrical form, are connected to the rotor represented in picture 6, the strips b_1, b_2, b_3, b_4 are mounted on two mechanical gap alignment systems (photo 7), the whole of the pieces making up a magnetic thrust is represented by picture 8. The main parameters of the experimental mount are as follows :

rotor inertia	:	0,15 m2 kg
Useful angular amplitude	:	$\pm$ 5 degrees
Frequency	:	2.2. Hz
Maximum Torque Thrust capacity	:	2 N m

In a dynamic situation of the thrusts reaction, torque is represented in figure 10 (measured by accelerometer). Figure 11 represents the angular rotation in relation to time, the effect of linearisation is obtained with a scanning efficiency nearer 32% for a linearity better than 1%. To simplify this experiment, the armature have been produced in a solid magnetic material and the result is large eddy current losses per cycle in the order of 20% compensated for each cycle by a precise torque impulsion controlled in a servo-loop.

A scanning reproductibility measure was produced by a laser device and photodiodes, the whole measuring apparatus is shown in figures 12 and 13. The histogram of oscillation angular variations of the mirror is shown in figure 14. The reproduction error is at most 3.10^{-6}radian and 78% of these errors are less than 10^{-6} radian.

These results have enabled more important work to be started leading to a preliminary project for a complete scanner model.

REACTION FORCES OF THE MAGNETIC THRUSTS

Two tests assemblies for the magnetic thrusts have been produced to analyse, as precisely as possible, the reaction forces of the magnetic thrusts. Picture 15 shows the test apparatus for measuring reaction torque and picture 16 shows the testing apparatus for the unstable forces. These tests have facilitated the verification fo the influence of the main dimensional paramaters of magnetic circuit :

The increase in the breadth of the strip has for effect not only an increase of the torque capacity but also increase in the unstable force.

The reduction of the gap diminishes the foot curvatum reaction torque diagram and increases the instability.

The use of saturable materials on the armature reduces instability.

The method of flux generation clearly influences the reaction torque capacity ; in the event of powering, the armature with constant magnetic potential, the flux decreases quickly when the strip leaves the armature, which reduces the torque capacity. On the other hand, a constant flux generation realized by placing additionals gaps in series in the magnetic circuit allows to increase notably the capacity of torque without increasing the instability very much.

Parts of experimental results are plotted on the figures 17,18,19,20.

PRELIMINARY SCANNER PROJECT

Figure 21 shows a design of a preliminary project of a mirror oscillating from 280 mm x 320 mm, the magnetic thrusts are formed by two strips of ferro-cobalt 60 mn long, 40 mn wide and 3.5 mn thick, fixed at the end of the long axis of the mirror, the ferro-nickel armatures have been laminated to reduce eddy current losses. The provision of flux is provided for by magnets of samarium-cobalt and is closed to the stator by a piece of soft iron.

The magnetic bearings are placed at the ends of the small axis of the mirror, they are formed by :

- a set of electromagnets acting over the five degrees of freedom

- a detection set of the position of the rotor on the five degrees of freedom . They are inductive detectors supplied at 100 KHz with demodulator.

The degree of precision of this detection set is considerable : the value of rotation noise is less than a hundredth of a micron.

- an electronic set for five degrees servo-loop.

The active electomagnetic bearings offer the advantage of having a long experience at the SEP, both for space applications (Spacelab) as well as industrial applications. The choice of these instruments, to assure the rotation of the mirror, is justified by the following requirements.

- guiding precision of the rotation axis. This axis must be maintained in a conical semi-angle less than 4.10^{-6} radian.

- great stiffness of 5 degrees of freedom in pivoting.
This quality is of prime necessity : the precision of rotation is to be preserved under the influence of unstable forces of thrusts, these forces acting by axial translation and transverse rotation in the mirror.

- elimination of all frictions

- absence of spring rotating torque and low drag torque

An arch of light alloy allows to connect rigidly the bearing and the magnetic thrusts, especially following the strong instability directions of the thrusts.

The reduction in the mirrors inertia around its rotation axis is essential for reducing the torque capacity of the thrusts and their transversal instability.

Considering a linear torque-angle characteristic for the thrusts, formulas for the torque capacity and for the reaction stiffness torque can be established :

$$Cmax = Ir \times \frac{Teta}{2\pi} \cdot \frac{(2\pi F)^2}{Te(0,5-Te)}$$

$$Rm = Ir. \left(\frac{2\pi F}{0,5-Te}\right)^2$$

Ir = rotor inertia

Teta = useful angular scanning

F = Oscillation frequency

Te = Scanning efficiency on away movement

Rm = Magnetic stiffness of the thrusts assumed like constants

Cmax = Capacity of the torque thrusts

In the preliminary project configuration in figure 21, the oscillation characteristics have been extrapolated from the results of the experimental survey of the thrusts. These results are shown in figure 22 . The rotor inertia is 0.04 m2 Kg, and scanning efficiency is 0.36 with ± 0.5% of linearity.

The mirror, in its berylium lightened structure, has been the subject of a numerical analysis of finite elements of vibration methods and the deformations undergone under the influence of the reaction torque of thrusts.

The first vibration mode of the mirror is at 6280 Hz and it appears that in relation to the torque angle characteristics of the thrusts the mirror has no resonance. It simply undergoes deformations at the end of the run which then cancel one another out on the useful part of the scanning.

The maximum values of the deformations at the end of the run can be seen in figure 21, for particular points plotted on a quater mirror (unit : micron).

All the magnetics losses in rotation (hysteresis and eddy current in the thrusts and the pivot) have been calculated and correspond to less than one percent of the maximum rotor kinetic energy.

The compensation of these losses, most of which are reproducible is safeguarded by a torque impulsion that is generated at each cycle by a motor in relation to the gap between the oscillation period and the period of reference.

In this preliminary project, the most serious difficulty is the compensation by the magnetic bearing of the thrusts' instabilities which have been calculated by extrapolating the results of measures taken individually on the test apparatus of figure 16.

Value of axial instability : $K_2 = 1{,}5 \times 10^6$ N/m

Value of the rotation instability in the mirror : 6.10^4 Nm/Rd

Depending on these two degrees of freedom a great mechanical rigidity must be guaranteed by the stator and the rotor to obtain a good margin of stability for the controls loops of the magnetic bearing.

Evaluations for acceleration , velocity and angular rotation are plotted against the time in figure 22.

CONCLUSION

The main oscillating scanning quality by magnetic thrusts is the reproductibility of the oscillation. Values much lower than 10^{-6} radian can be envisaged. This quality has been confirmed by the preliminary tests carried out.

For the future extrapolations for larger mirrors where higher frequencies are possible.

These perspectives can be taken into account in the drawing up of a new range of futur observation instruments satellite.

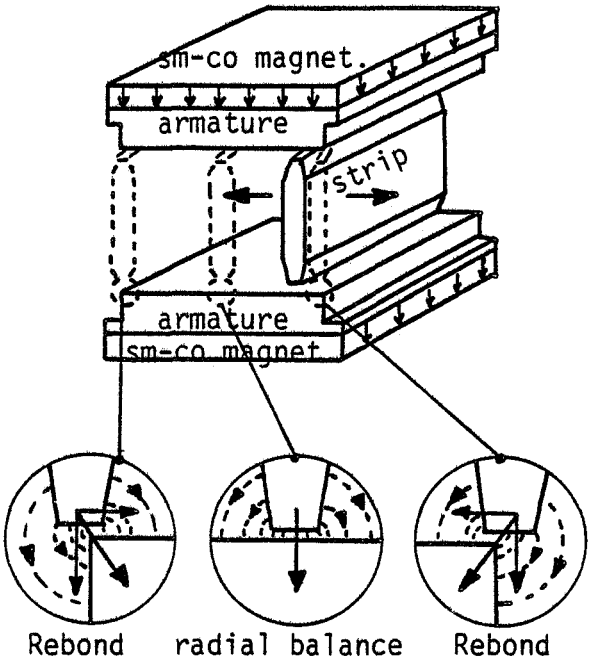

Fig. 1

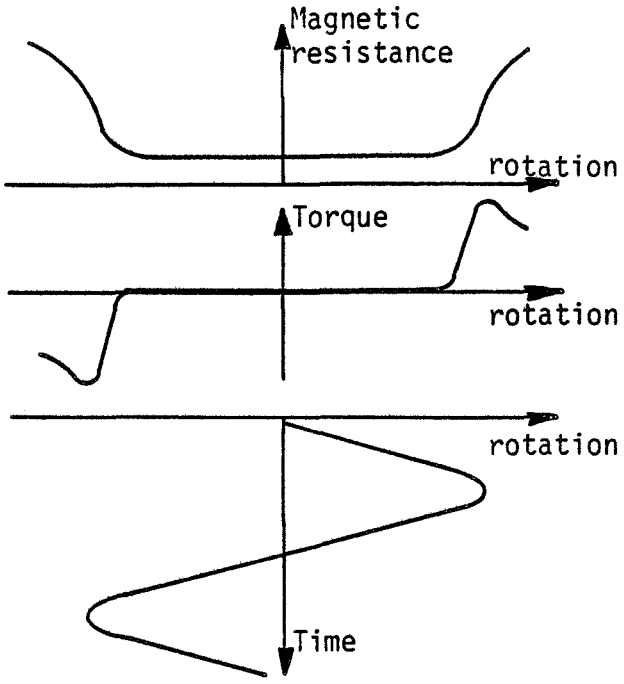

Fig. 2

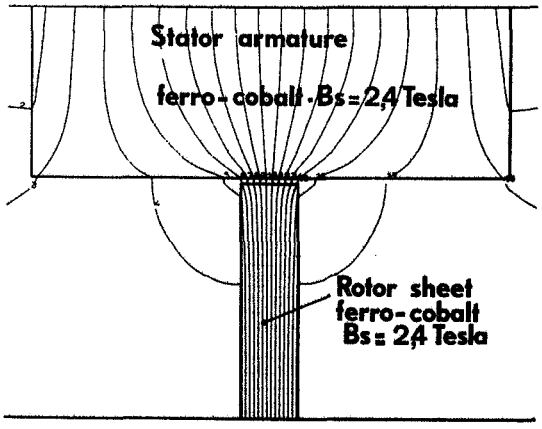

Flux lines distribution

Fig. 3

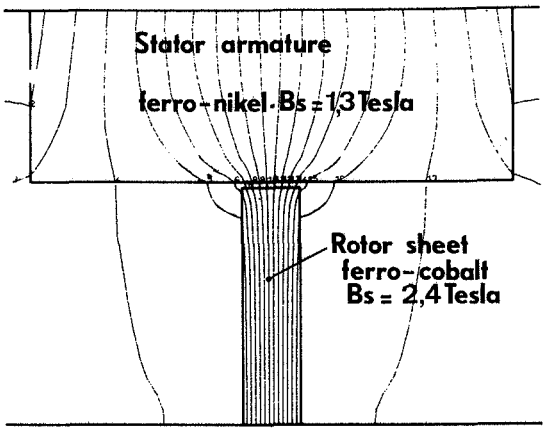

Flux lines distribution

Fig. 4

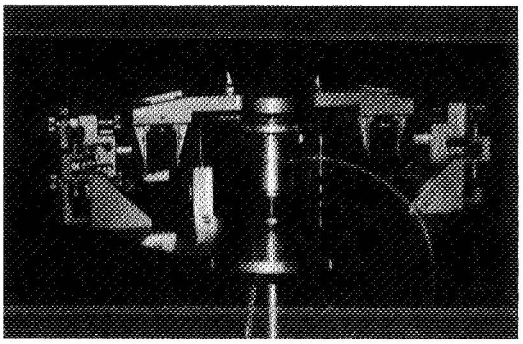

Fig. 5

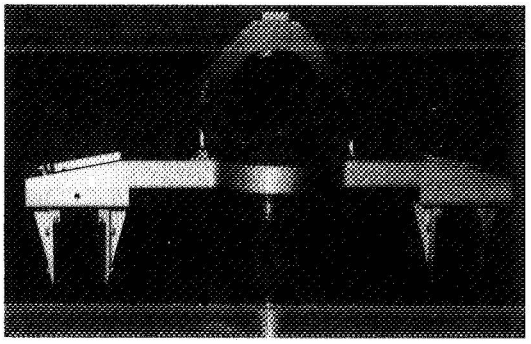

Fig.6

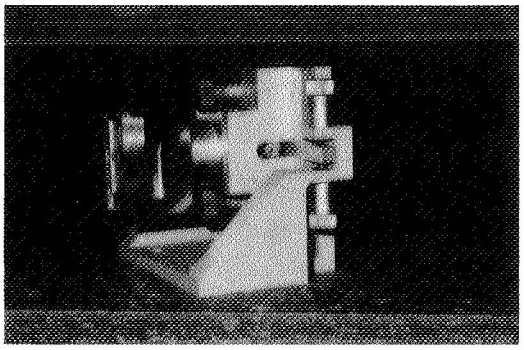

Fig.7

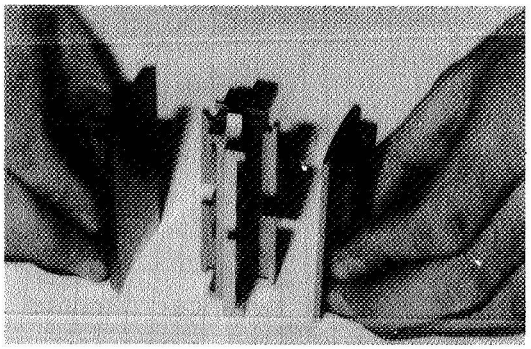

Fig.8

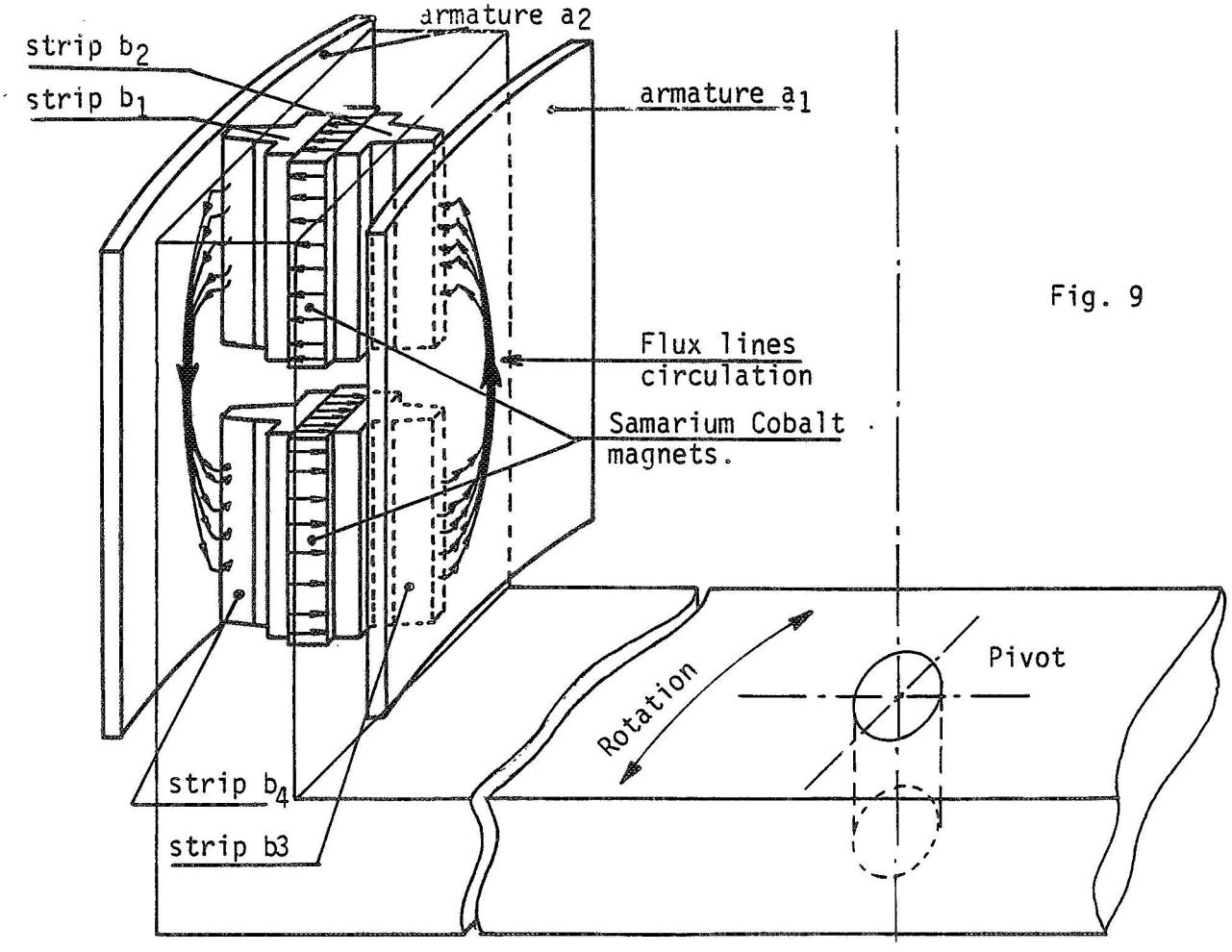

Fig. 9

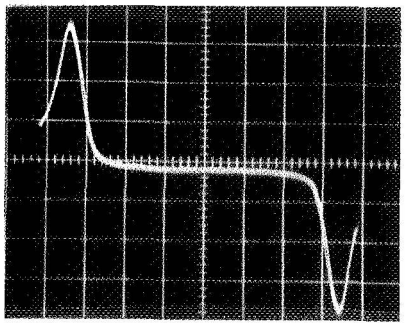

fig. 10

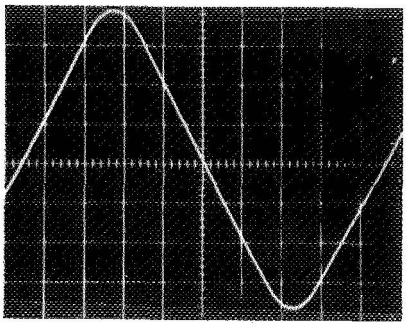

fig. 11

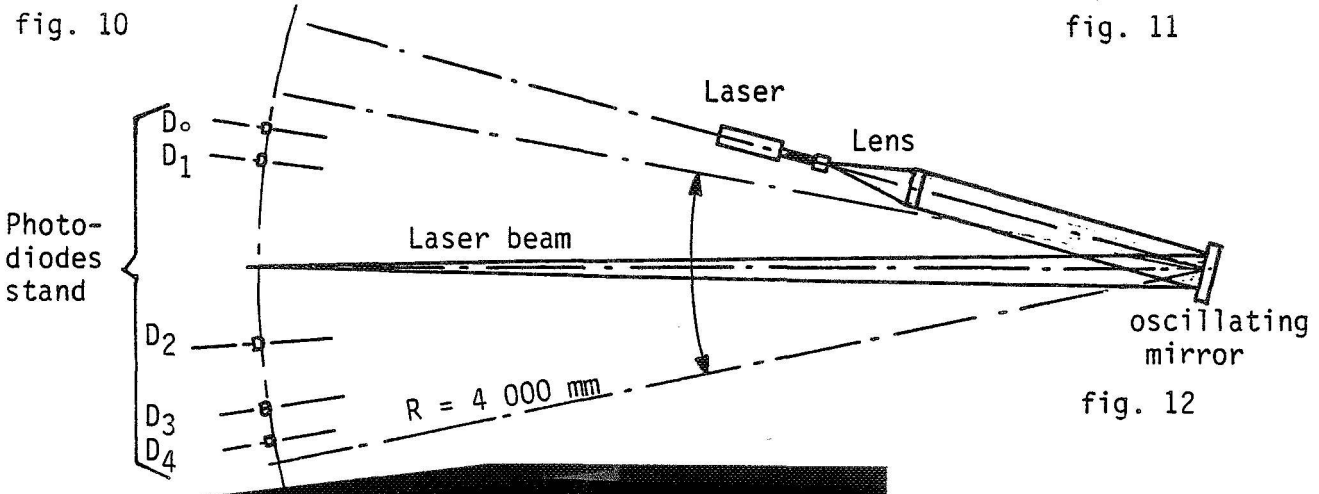

fig. 12

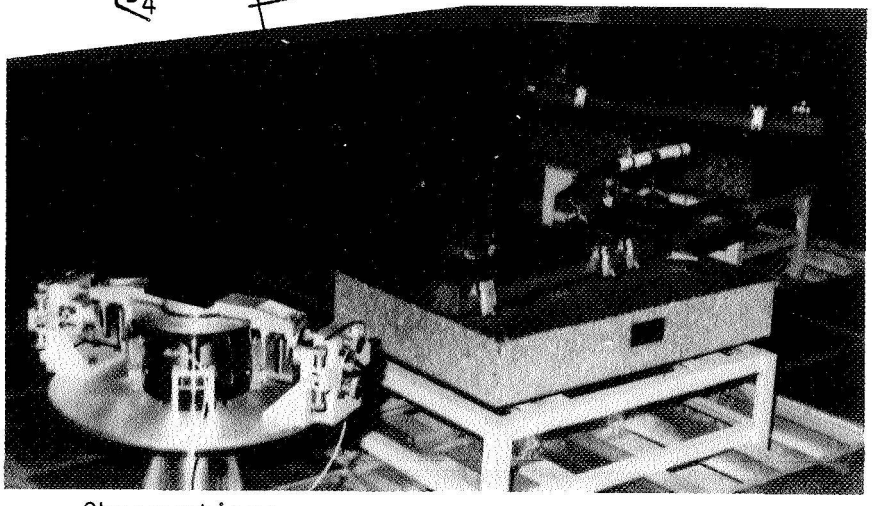

Experimental
laser-control
assembly

fig. 13

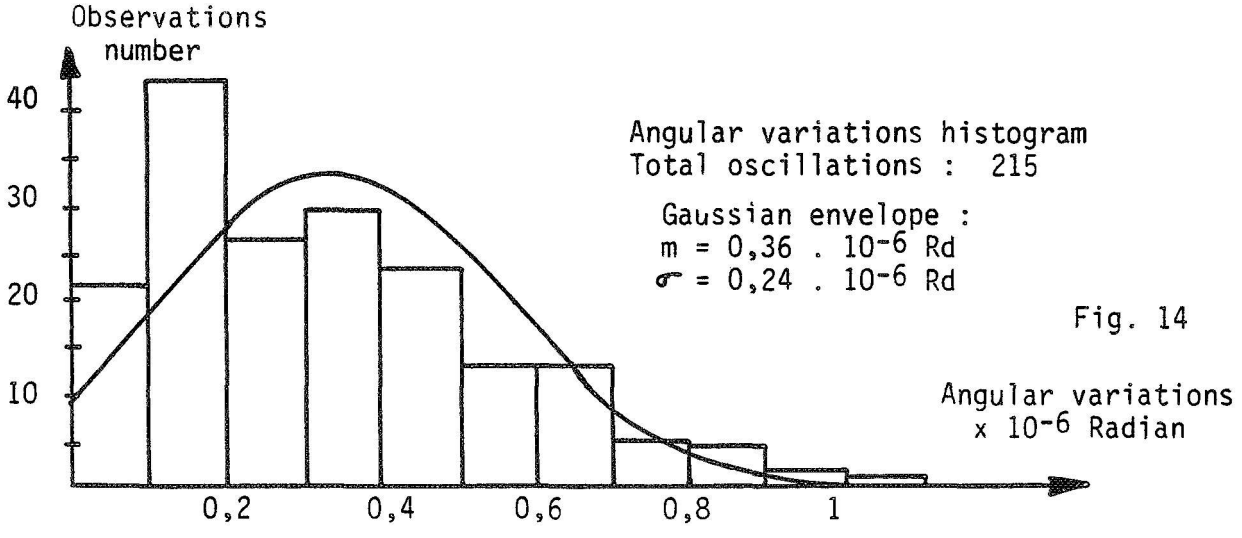

Fig. 14

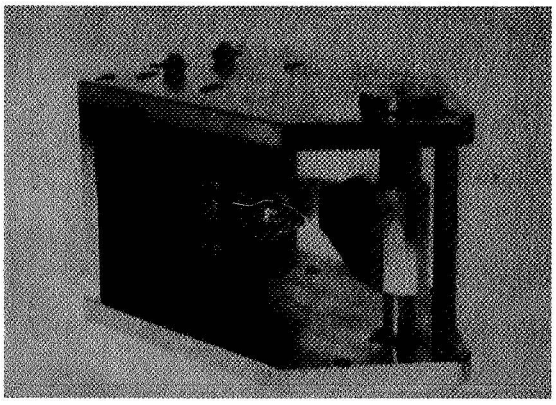

fig:15

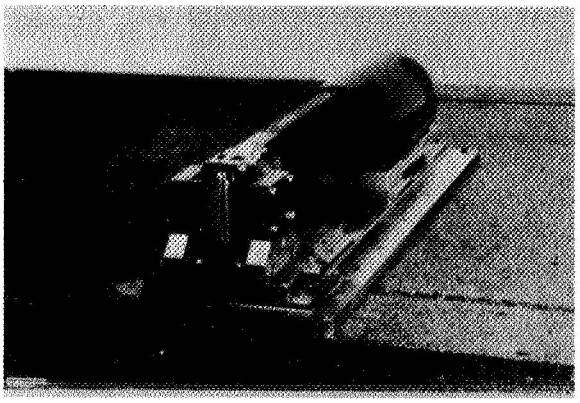

fig:16

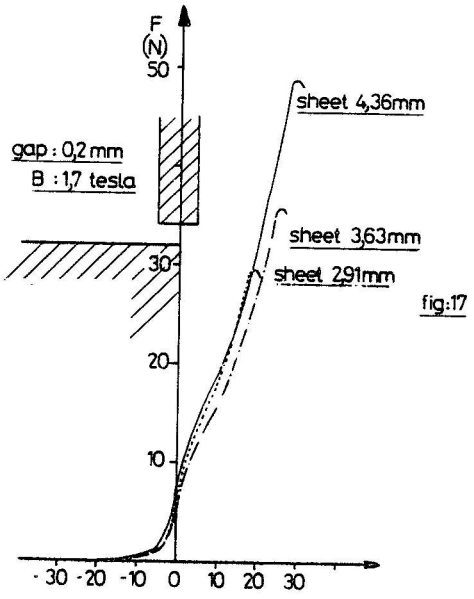

fig:17

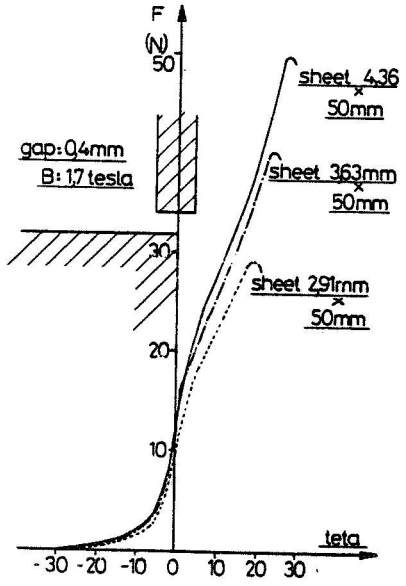

fig:18

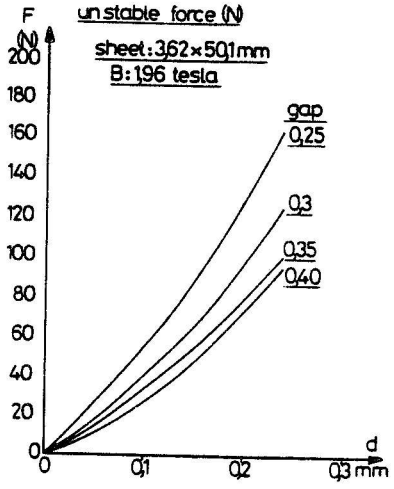

fig:19

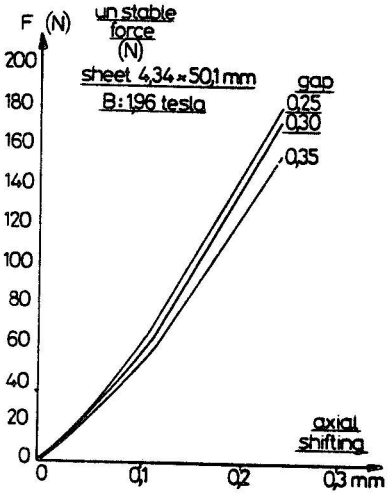

fig:20

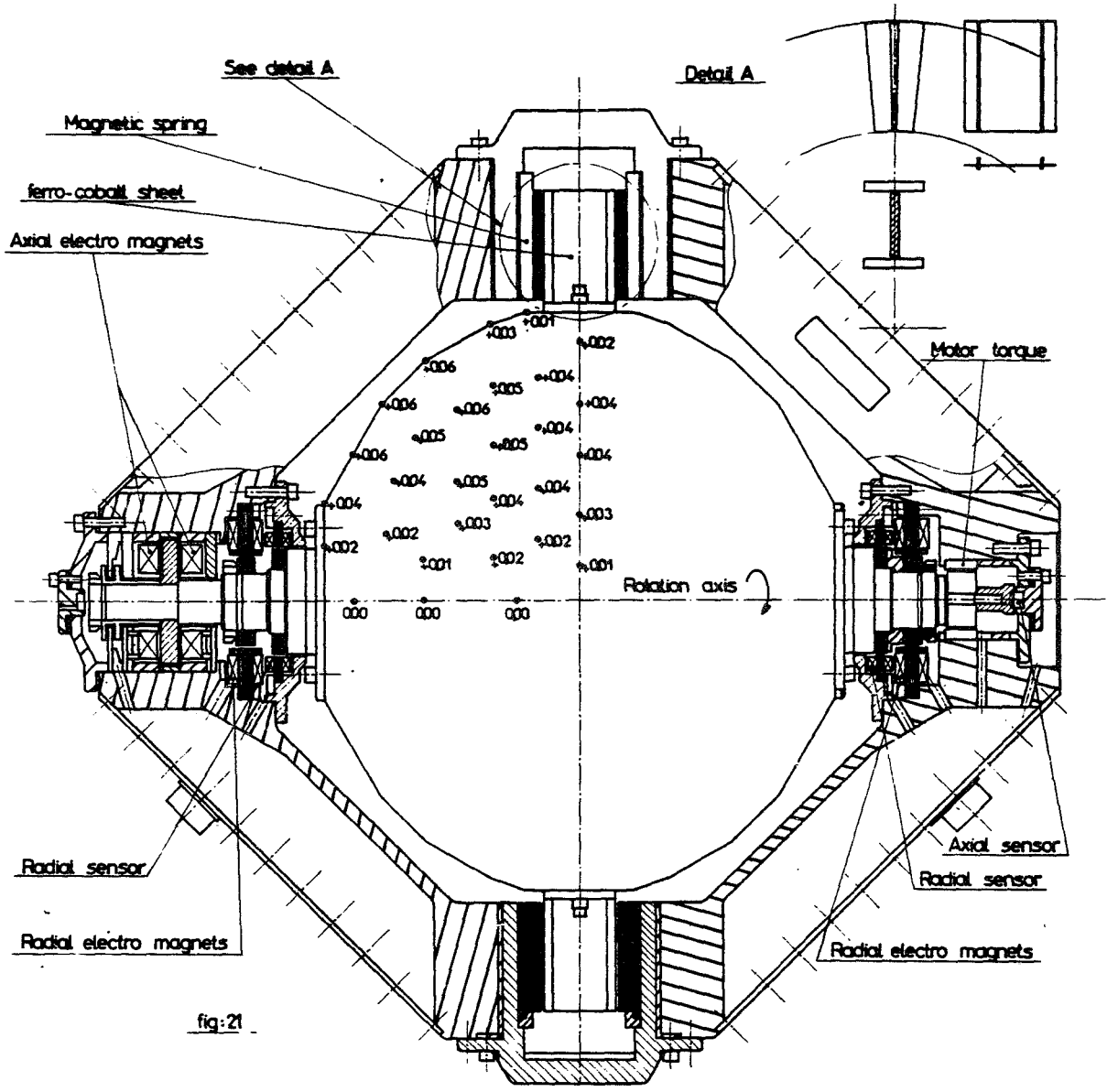
See detail A
Detail A
Magnetic spring
ferro-cobalt sheet
Axial electro magnets
Motor torque
Rotation axis
Radial sensor
Radial electro magnets
Axial sensor
Radial sensor
Radial electro magnets

fig:21

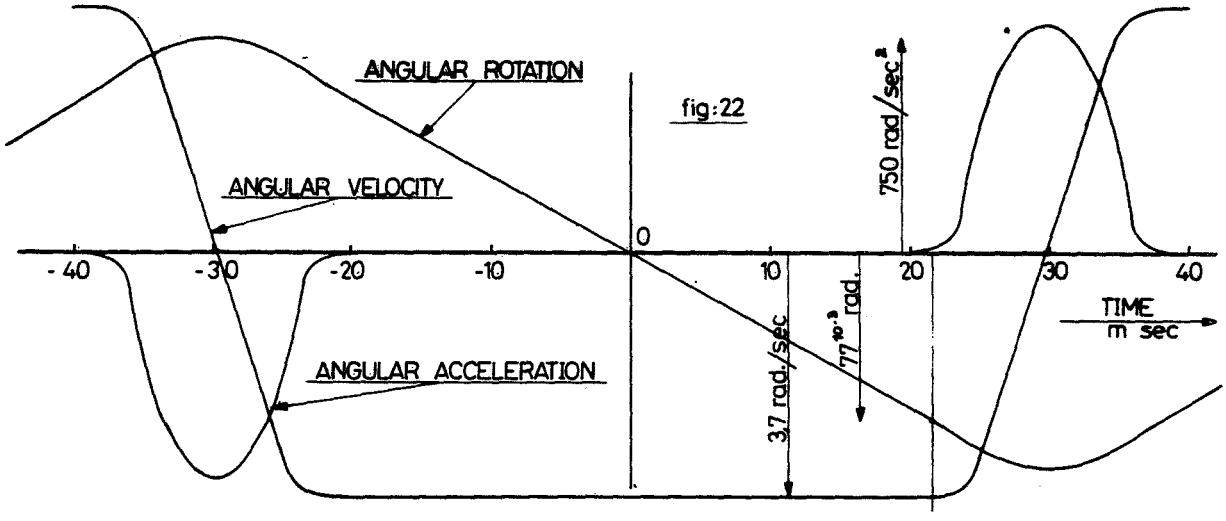
ANGULAR ROTATION
ANGULAR VELOCITY
ANGULAR ACCELERATION
0
-40
-30
-20
-10
10
20
30
40
TIME
m sec
750 rad/sec²
3,7 rad./sec
77 10⁻³ rad.

fig:22

THE IMPACT OF RARE EARTH COBALT PERMANENT MAGNETS ON ELECTROMECHANICAL DEVICE DESIGN

R.L. Fisher, Inland Motor Specialty Products Division
P.A. Studer, Goddard Space Flight Center

ABSTRACT

The discovery of rare earth cobalt magnets has introduced a new class of permanent magnets with energy products several times greater than heretofore available. The prospects for performance improvements and the miniaturization of electromagnetic devices are great.

This paper discusses specific motor designs which employ this revolutionary material with special emphasis on its unique properties and magnetic field geometry. Magnetic field geometry is an important design consideration since the material derives its high energy product from extremely high coercive force whereas flux density is the parameter which affects the motor torque equation directly. New magnetic circuit designs are therefore needed to capitalize on the potential benefits of this material in conventional torque motors. The advantages of this material in the design of ironless armature motors and linear actuators are more obvious. In addition to performance improvements and power savings, higher reliability devices are attainable.

Both the mechanism and systems engineer should be aware of the new performance levels which are currently becoming available as a result of the rare earth cobalt magnets.

INTRODUCTION

The rapid advance of electronics has stolen most of the headlines in recent years with regard to miniaturization. It is less well recognized that an exponential improvement in permanent magnet materials has also been underway. Most large systems are composed of both control electronics and a variety of electromechanical devices. In spite of all the advances in microcircuitry, in the end the desired function generally involves some physical motion or work to be done.

Of the large variety of electromechanical devices which are utilized in spacecraft and instruments, many employ permanent magnets. The design and utilization of these devices are a fertile field for significant performance improvements as well as weight and power savings if early attention is paid to the design and specification of mechanisms making full use of these new materials.

The designer of electromagnetic devices has seen the continued improvements in the energy products of permanent magnet materials available. During the 50's new alnico alloys appeared regularly year after year with an even more rapid rise with the development of directional cooling techniques in the presence of a magnetic field. For a few years this rapid progress seemed to have leveled off until the dramatic discovery of rare earth cobalt alloys and the commercial introduction of $SmCo_5$ and more recently Sm_2Co_{17} (Fig. 1).

ENERGY PRODUCT OF COMMERCIALLY AVAILABLE MAGNET MATERIALS

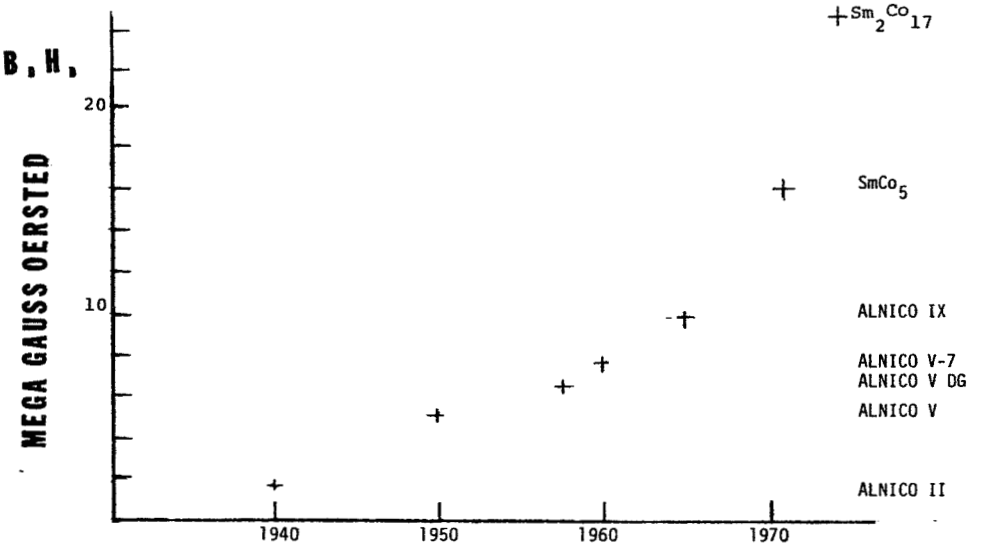

FIGURE 1

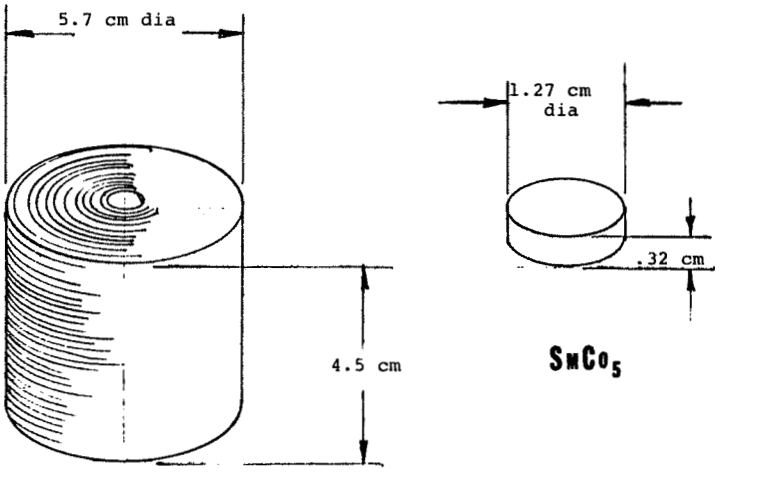

ELECTROMAGNET @ 1000 A/IN² ← **1010 AMPERE TURNS** →

575 gm	**WEIGHT**	3.3 gm
2.68 W	**POWER**	0

FIGURE 2

This exponential increase in permanent magnet characteristics has continued to broaden the range of applications to which electromagnetic devices can be effectively employed. Figure 2 shows the dramatic size and weight savings of modern rare earth magnets compared to an electromagnet.

Rare earth magnets are having a profound impact on the performance of electromechanical devices. Despite the obvious advantage of their higher energy product (β H max) usually expressed in millions of gauss oersteds a considerable amount of engineering is required to make effective use of their potential. The fundamental reason for this is that the improvement is in the coercive force rather than flux density.

Figure 3 shows the magnetic properties of the most commonly used alnico magnet materials and some of the rare earth materials. As can be seen, there is quite a difference in the magnetic characteristics. It is not possible to obtain improved motor performance by merely substituting rare earth magnets in place of alnico magnets. The motor must be designed to exploit the characteristics of the particular magnet material. If you consider the basic equation for the force or torque developed by a motor it is only the air gap flux density rather than the coercive force which has a direct effect on the performance. The challenge to the device designer then is to utilize this high coercive force most effectively to produce a more effective, higher performance, lighter weight, and/or more cost effective mechanism.

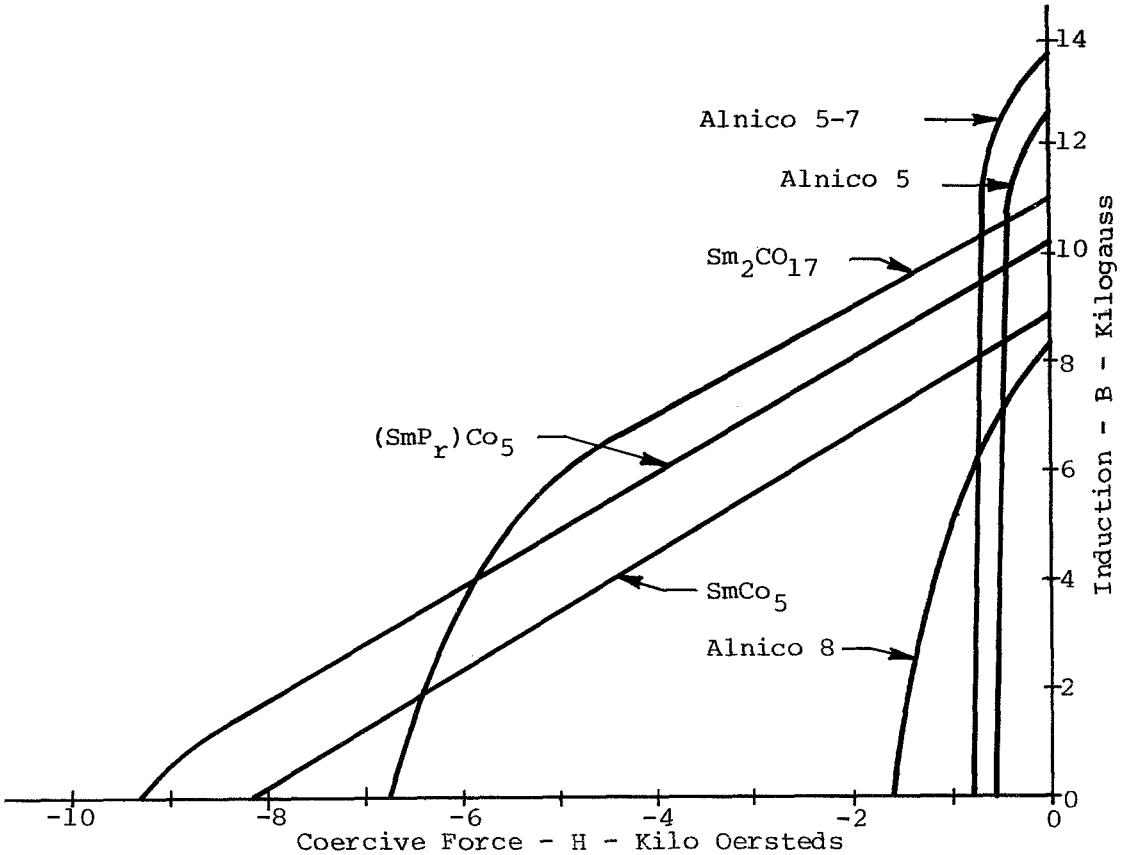

Figure 3 - Typical Magnetic Properties

DEVICES USING RARE EARTH MAGNETS

DC Torque Motors

A DC torque motor is an electromagnetic actuator which can be attached directly to the load. Most torque motors are provided as frameless units consisting of a wound rotor assembly, a permanent magnet stator assembly, and a brush ring assembly. They are usually thin in axial length compared with diameter, and have a relatively large bore through the rotor for direct mounting on the load shaft. A DC torque motor is designed to provide the highest torque practical for the size, weight and power available while providing smooth control in a high response system.

The key to improved DC torque motor performance is improved permanent magnet materials. Figures 4 and 5 depict the construction of motors with alnico magnets and with rare earth magnets. Alnico magnets need a large length-to-area ratio because of the low coercive force. For example, if the operating slope for an alnico 5-7 magnet were to fall below 18 cgsu, the magnetic flux would be reduced due to permanent demagnetization of the magnet. Therefore, much care must be taken in keepering the stator assembly during handling and assembly, and to insure that current spikes are controlled so as not to cause demagnetization.

The alnico torquers are constructed with two magnets feeding one pole piece in order to keep a large length-to-area ratio. Anywhere from one-third to one-half the total magnetic flux is lost as leakage flux. The stator assembly must be mounted in a non-magnetic housing to prevent the housing from shunting the magnetic flux.

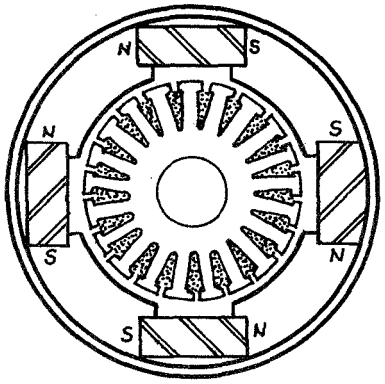

Figure 4

Alnico Magnet Construction

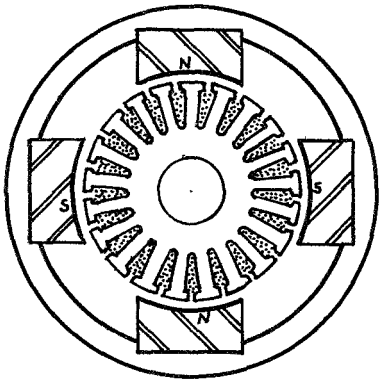

Figure 5

Rare Earth Magnet Construction

The rare earth magnets have less induction but a much larger coercive force than the Alnico magnets. Therefore, a much smaller length-to-area ratio is possible, allowing the construction shown in Figure 5. With this configuration, the housing can be either magnetic or non-magnetic without affecting performance. Only about 10% of the magnetic flux is lost as leakage flux. Since the permeability of the rare earth materials is very close to that of air, the inductance of the motor is reduced, resulting in lower electrical time constant. Because of the large coercive force a rare earth magnet torquer cannot be demagnetized as the result of overcurrent conditions. Keepering is not required for handling.

The advantages of DC torque motors having rare earth magnets are:

1. Greater peak torque capability.
2. In most cases less power required for a given torque.
3. No keepering required.
4. Overcurrent will not demagnetize.
5. Less electrical time constant.
6. Fewer stray magnetic fields.
7. Larger air gaps are possible, making rotor-to-stator concentricity less critical.

Inland torquer QT-1207 with $SmCo_5$ magnets was designed to be a direct replacement for a similar size unit which has Alnico 5-7 magnets. The characteristics of the two motors are compared in Table I. Pulse currents were applied to the new design to avoid overheating at the large values of current, and the output torque measured with a torque transducer. At 0.282 Nm (40 oz.in) peak torque (double the peak torque rating), the torque sensitivity was reduced by only 11%. No demagnetization resulted from the high current pulses.

TABLE I

CHARACTERISTICS	T-1218A	QT-1207A	UNITS
Magnet material	Alnico V-7	$SmCo_5$ ($18\ MGO_e$)	---
Peak torque rating	106	141	mNm
Power input at 106 mNm	63	46	watts
Motor constant	13.4	15.6	$mNm/\sqrt{watts}$
Static friction	3.5	4.9	mNm
Motor weight	65	65	g
Torque sensitivity	84.7	98.9	mNm/A
DC resistance	40.0	40.0	ohms
Inductance	12	7.9	mH

Table II compares the performance of three Inland torque motors; one with alnico 8 magnets, one with $SmCo_5$ magnets (18 MGO_e), and one with $(SmP_r)Co_5$ magnets (26 MGO_e). The $SmCo_5$ unit develops 29% more torque than the alnico unit and the $(SmP_r)Co_5$ unit 48% more.

TABLE II

CHARACTERISTICS	T-2405A	QT-2402A	QT-2403A
Magnet material	Alnico 8	$SmCo_5$ (18 MGO_e)	$(SmP_r)Co_5$ (26 MGO_e)
Peak torque rating Nm	3.39	4.38	5.01
Power input, stalled watts	285	261	261
Motor constant $Nm/\sqrt{watt}$	0.20	0.27	0.31
Static friction Nm	0.07	0.11	0.11
Torque sensitivity Nm/A	0.339	0.438	0.501
DC resistance ohms	2.85	2.61	2.61
Inductance mH	5.0	2.7	2.7

Ironless Armature Torque Motors

One type of motor of particular interest to the aerospace mechanism and instrument designer is the ironless armature motor. The advantage of this type of motor is the complete elimination of breakway friction caused by hysteresis and cogging due to the interaction of discrete poles and slots in the usual motor lamination. For certain applications such as position control servo loops, these non-linear effects can result in a fundamental limitation on achievable precision. Ironless armature motor construction eliminates all hysteresis, cogging, and static forces between rotor and stator. This is accomplished by combining all of the "iron" structure with the permanent magnet assembly and inserting the armature conductors into the air gap. These motors also have an order of magnitude lower armature inductance since the motor windings are essentially an air-core within the air gap. Of necessity, large coercive force is required to produce high flux densities in an air gap large enough to accommodate many conductors of adequate current carrying capability. Prior to the advent of rare earth magnets, the use of this type of motor was generally restricted to high performance servos with stationary magnet assemblies where the weight of the magnet assembly was not critical (Fig. 6).

MAGNET ASSEMBLIES FOR AIR CORE ARMATURES

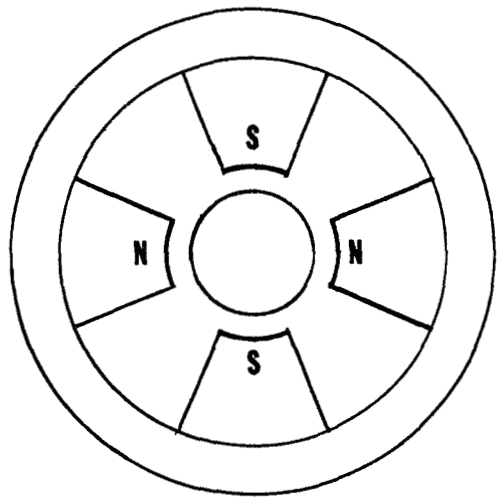

ALNICO

Gap Volume 5 cm^3
Weight 1.25 Kg

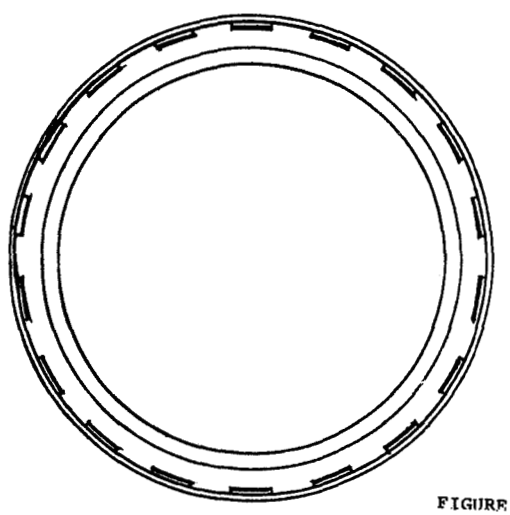

Gap Volume 12.3 cm^3
Weight 0.25 Kg

$SmCo_5$

FIGURE 6

Samarium cobalt magnets however have made it feasible to drastically reduce the weight of the magnet assembly and to rotate the magnet assembly with only the windings stationary. The non-rotating mass of a typical ironless armature motor is only 20% of the total motor weight.

The most effective use of rare earth magnets in this case is to bring the face of the magnet directly to the air gap with the magnet itself forming the pole. These magnets can operate at their peak energy product (minimizing magnet volume) while supplying flux across an air gap nearly equal to their length in the direction of magnetization. This allows a large number of adequately sized conductors to be inserted in the gap achieving good power ratings.

In a reaction wheel the magnet assembly can be built into the wheel near the rim where its mass contributes to the necessary inertia leading to a very substantial weight reduction. In other applications the elimination of motor induced disturbances is even more important. With advances in sensors, especially with the advent of extremely narrow beam widths for communication links, the elimination of hysteresis and preferred position is vital. These motors have been applied successfully to fractional arc second pointing systems and are being applied to the Space Sextant. They have been used in conjunction with an optical encoder to develop a microprocessor based programmable stepper* with an order of magnitude greater resolution than realizable with mechanically defined steps. This machine retains the advantages of fast slew rates and servo damped behavior of a true torque motor. The servo designer at last has a system which behaves exactly as his linear analysis has predicted it should, even around null. A multi-axis and all-digital controller** has more recently been developed which is being integrated with ironless armature motors for the Spacebore Geodetic Ranging System. This will snap a laser beam from target to target on each orbital pass to detect earth fault motions. The ironless armature motor for this system is shown in Figure 7.

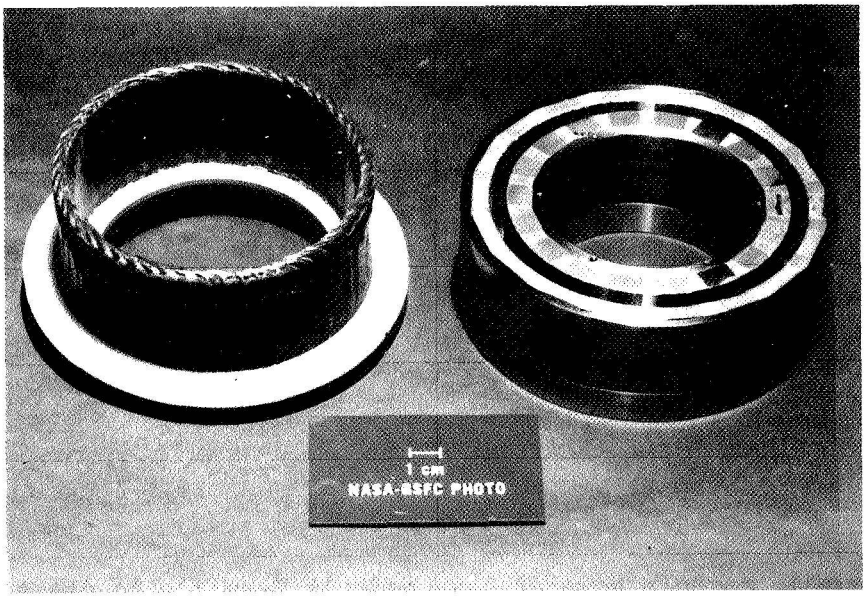

Figure 7 - Ironless Armature Motor

*Programmable Step Scan, NAS5-24048
**All Digital Controller, NAS5-24199

Linear DC Force Motor

A linear DC force motor developed recently at Inland is another example of the use of rare earth magnets. The magnet assembly is the moving member or slider. Therefore the size and weight of the magnets are important. Inland model FM-1901 develops a force of 245 newtons (55 lbs) with a slider weight of only 2.45 Kg (5.4 lbs).

The linear force motor consists of a stationary winding assembly and a slider. The windings are commutated through brushes which are attached to the slider.

The slider contains four $SmCo_5$ magnets, two on either side of the stator assembly. The two sets of magnets are mechanically connected together. The slider also has brushes for commutation and brushes to bring the input power from the stator to the slider.

The stator contains a lamination core, windings, commutator, and two power rails. The windings are arranged so that only the windings under the magnet assembly are energized.

This particular model was designed for a total travel of 429mm (16.9 in). The travel can be modified by changing the length of the stator assembly without affecting the motor performance. The performance parameters are shown in Table III.

TABLE III
LINEAR FORCE MOTOR (FM-1901)

PERFORMANCE CHARACTERISTICS		
Peak Force (Fp)		245 N (55 lbs)
Power Input at Peak Force @ 25°C		570 watts
No Load Speed @ Vp		226 cm/s (89 in/s)
Electrical Time Constant		4.6 ms
Static Friction		5.6 N (1.25 lb)
Ripple Force (average to peak)		4.5%
Theoretical Max. Acceleration		9936 cm/s^2 (326 ft/s^2)
WINDING PARAMETERS		
Voltage @ Fp		29.3 volts (Vp)
Force Sensitivity		12.6 N/A (2.82 lb/A)
DC Resistance @ 25°		1.5 $\pm$ 0.2 ohms
DIMENSIONS	STATOR (Winding Assembly)	SLIDER (Magnet Assembly)
Height	48.3 mm (1.90 in)	94.0 mm (3.70 in)
Width	98.3 mm (3.87 in)	118 mm (4.65 in)
Length	604 mm (23.8 in)	175 mm (6.90 in)
Travel		429 mm (16.9 in)
Weight	14.4 Kg (31.7 lbs)	2.45 Kg (5.40 lbs)

DC Tachometer

Rare earth magnets have also been utilized to good advantage in DC tachometers. Unlike the DC motor, a tachometer does not have to withstand large demagnetizing currents. The tach is normally connected to a high impedance load. The main objectives are to provide a high voltage sensitivity and to have a low ripple voltage.

Since rare earth magnets have very low magnetic leakage, it is possible to reduce the flux in the commutation zone. The high coercive force of the magnets also helps reduce flux changes due to reluctance changes with rotation. This results in reduced ripple voltage.

Recently a tachometer with alnico magnets was redesigned with $SmCo_5$ magnets. As a result, we obtained a 25 percent increase in voltage sensitivity, ripple voltage was reduced by one third. Additionally it does not require keepers for assembly.

MAGNETIC BEARINGS

As early as 1970 GSFC introduced permanent magnets into magnetic bearings in order to minimize power consumption. This early attempt utilized a pair of cylindrical alnico magnets, each 4 cm in diameter and 2 cm in length. The advent of rare earth cobalt magnets has made magnetic bearings vastly more feasible for space applications on both a power and weight basis. For example, a recent magnetic bearing* used a single 3 cm diameter by .65 cm $SmCo_5$ magnet for 3 axis support. The use of permanent magnets in magnetic bearings permits the establishment of high flux densities in the air gap which in turn allows the ampere-turn requirement of the control windings to be greatly reduced. The curve in Fig. 8 shows the force per unit area produced plotted versus flux density. Since the force is a function of the square of the flux density, sizeable forces would require substantial ampere-turns from a pure electromagnet. The tradeoff between number of turns and high currents both lead to undesireable effects. A high number of turns leads to poor speed of response and compromises dynamic response while high currents result in power dissipation and thermal problems. Permanent magnets can be utilized to establish a high flux density which allows a smaller control signal to modulate the net force. A desireable by-product is that the force becomes a linear function of the control current.

A particularly effective way of using samarium cobalt is illustrated by the controllable permanent magnet biased electromagnet in Fig. 9. A set of these magnets at 3 points supported a 1.5 meter diameter momentum wheel jointly developed for the Goddard Space Flight Center and Langley Research Center in 1974. The volume of magnet material was only 2.6 cm^3 in each of these permanent magnet biased electromagnet modules. The angular positioning of the magnets afforded flux focusing and a low reluctance to control flux. With the magnet at a 30 degree angle, the flux density in the iron is twice that of the permanent magnet and its reluctance to control flux is only half of what it would otherwise have been.

*NASA TM78048

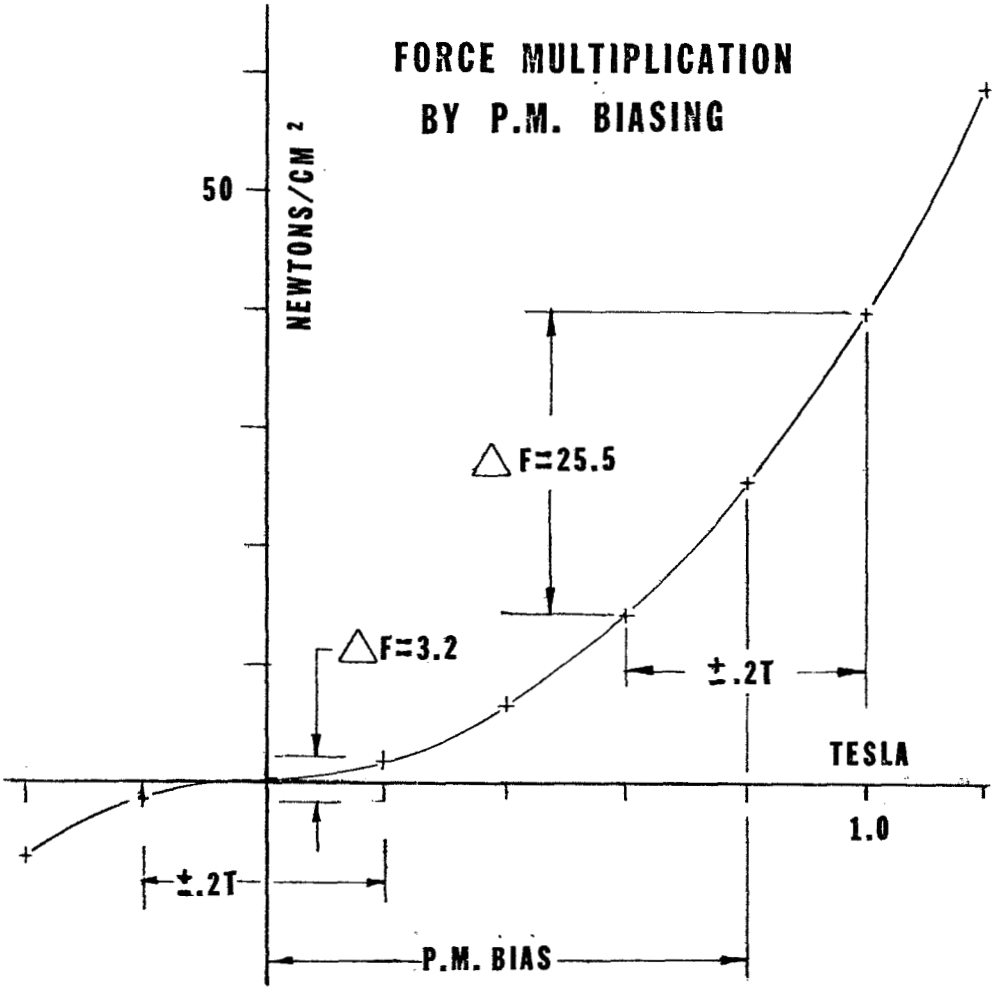

FIGURE 8

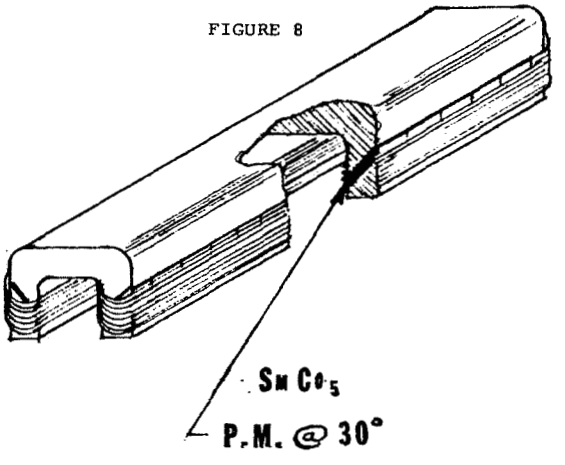

P.M. BIASED

ELECTROMAGNET MODULE

FIGURE 9

Magnetic bearings offer the spacecarft mechanism and instrument designer several new freedoms. Active electromechanical systems can be designed without life-limiting restrictions of lubrication in vacuum and without some of the speed limiting factors which restrict the power density of rotating devices. The suspension dynamics, including damping, can be electronically controlled. Only one magnetically suspended system is known to be operating in space. However, the European Space Agency is planning to introduce magnetically suspended wheels into communications satellites and NASA is developing a vernier pointing platform for Shuttle based instruments.

CONCLUSION

The order of magnitude improvement in permanent magnet energy products has spawned a whole new generation of electromechanical devices. These span the whole field from torque motors which are used routinely for countless applications to special purpose devices and even totally new mechanisms. The improvements are dramatic in terms of power and weight savings but even more significant in performance.

Aerospace instrument and systems engineers are likely to profit most from these new developments. Yet the automobile industry, also currently interested in shaving pounds, was well represented at the last R.E.-Cobalt magnet workshop. General Motors engineers showed that total costs could be reduced with the use of advanced and relatively expensive high energy magnets when the total system cost including power supply, structure, etc. was considered.

It is hoped that this paper will assist the mechanism designer to see some of the possibilities and challenges of designing with this new material by affording some insight into key aspects of some successful designs. As these developments become mature products a wider knowledge of their availability and characteristics is needed by instrument and spacecraft systems designers.

REFERENCES

1. B. R. Patel, "Mischmetal Rare Earth Magnet Tradeoffs in Automotive Accessory Motors," Third International Workshop on Rare Earth-Cobalt Permanent Magnets, 1978

2. David T. Curry, "Rare-Earth Magnets Power New Actuators," Machine Design, September 7, 1978

3. S. Noodleman, "Application of Rare Earth Magnets to D.C. Machines," Second International Workshop on Rare Earth-Cobalt Permanent Magnets, 1976

4. P. A. Studer, "New Type Torque Motor," Second International Workshop on Rare Earth-Cobalt Permanent Magnets, 1976

5. R. J. Parker, "Rare Earth Permanent Magnets - Their Properties and Potential Impact on Magnetoelectric Device Technology," Third European Conference on Hard Magnetic Materials, 1974

UNFOLDING THE AIR VANES ON A SUPERSONIC AIR-LAUNCHED MISSILE

Martin Wohltmann* and Michael D. O'Leary**

ABSTRACT

ASALM (Advanced Strategic Air-Launched Missile) is a supersonic air vehicle designed to be air-launched from a carrier aircraft. The four aft aerodynamic control vanes are folded to maximize the number of missiles carried on-board. The unfolding (erection) system must be small, energetic, fast, and strong. This paper describes the materials selected and problems that arose during development of the unfolding system. An artist's concept of the ASALM in flight is shown in Figure 1.

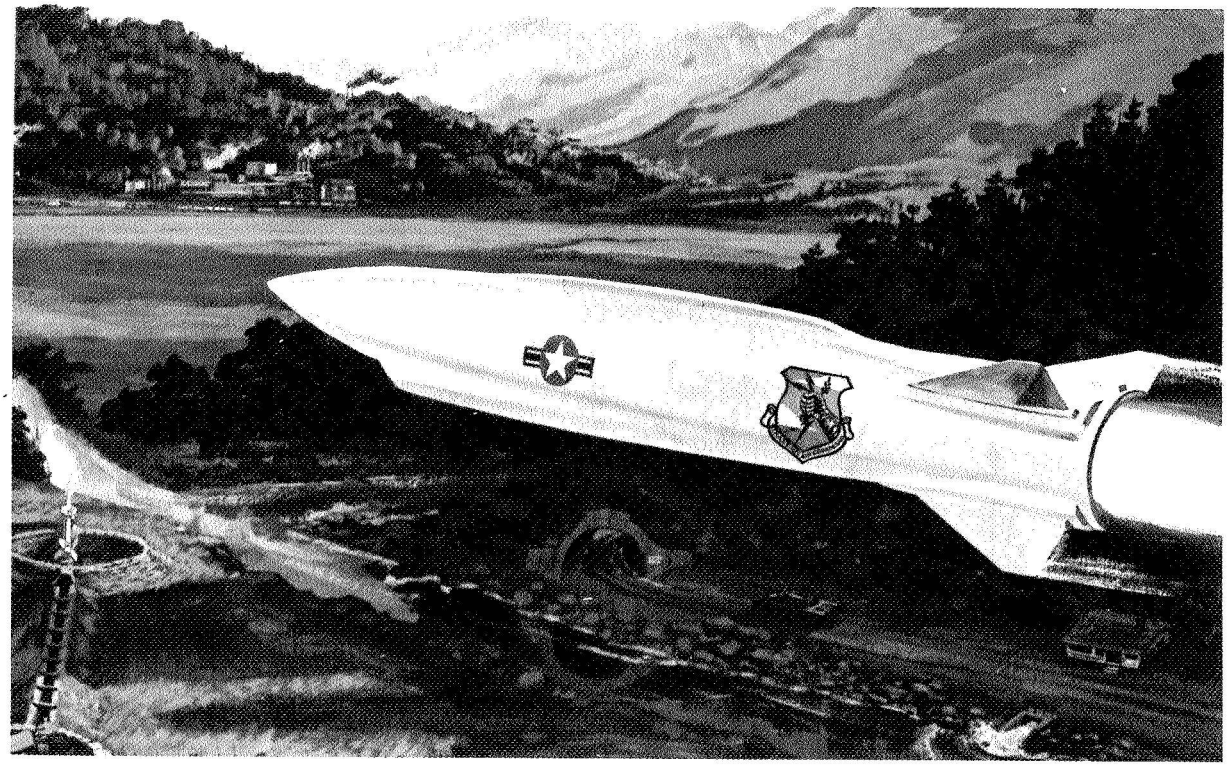

Figure 1. The Advanced Strategic Air-Launched Missile (ASALM)

INTRODUCTION

To maximize internal carry packaging efficiency on one of several carrier aircraft, the four aft aerodynamic control vanes on the ASALM must be folded to fit within a pie-shaped sector around the launcher spindle. Analysis of the launch sequence has shown that 350 ms can be allocated for vane

* Senior Group Engineer, Martin Marietta Aerospace, Orlando Division, Orlando, Florida 32855

** Senior Engineer, Martin Marietta Aerospace, Orlando Division, Orlando, Florida 32855

deployment. However, 250 ms of this allocation are required for the missile to separate from the launcher and clear the weapons bay door, leaving 100 ms for vane opening. Figure 2 shows the ASALM/weapons bay interface.

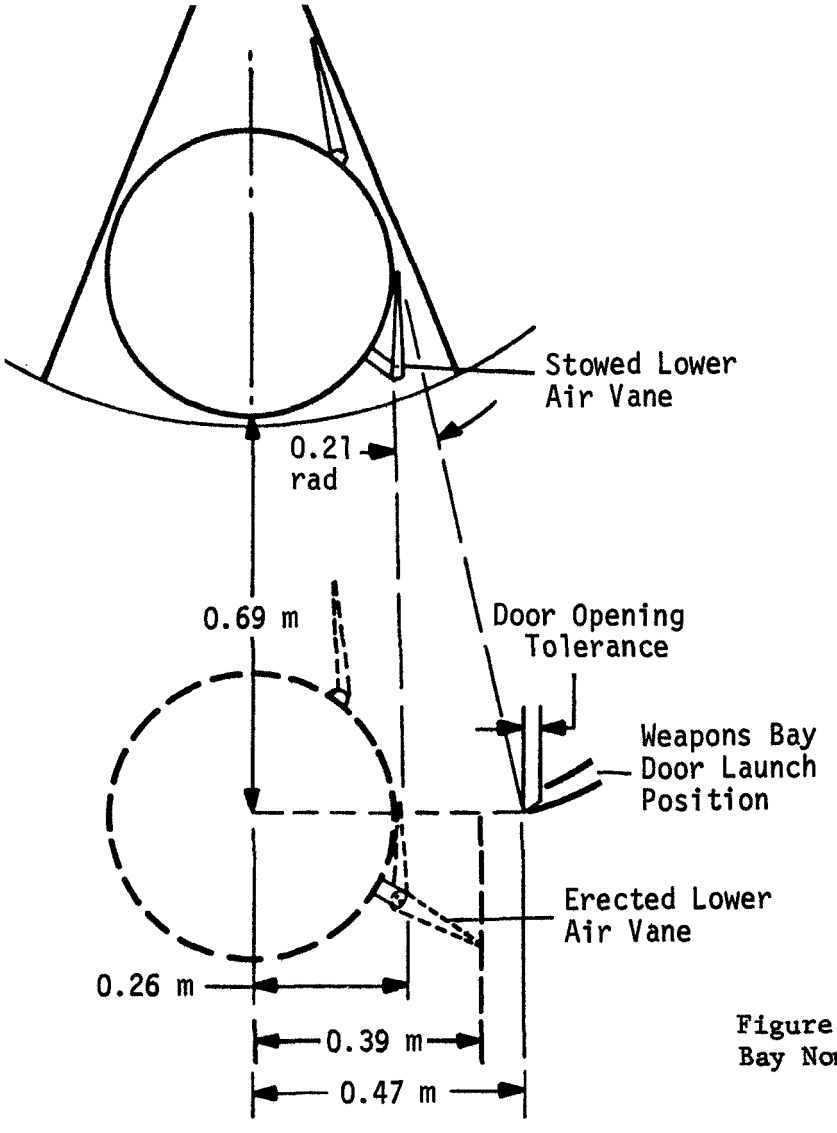

Figure 2. ASALM/Weapons Bay Nominal Clearances

Loads analysis which considered separation velocity, aircraft flow field, missile attitude, and various launch aircraft cruise conditions resulted in two cases of predicted load. The first case, a supersonic launch, shows that the unfolding air vane is opposed by an increasing moment which reaches a maximum of 339 N·m (3000 in-lb) as the air vane approaches its fully erect position. The second case is an aiding air load which peaks at 243 N·m (2150 in-lb) at approximately one-half the fold angle. These requirements necessitate an extremely compact, high-energy air vane erection system (AVES) which must act within the allocated 100 ms.

DESIGN CONCEPT

The concept selected for this mechanism (a type of "yankee" screwdriver) uses a small gas generator (thruster) to pressurize a piston in the

fixed root of the air vane. Two helical tangs located diametrically opposite on the piston ride in helical grooves machined in the piston bore. These grooves impart rotary motion to the piston. The forward end of the piston rod is splined and engages female splines in a sleeve which is rigidly connected to the folding part of the air vane, thus erecting the vane as the piston is forced forward. The end of the piston/splined rod opposite of the gas pressurized end forces hydraulic fluid through a sharp-edged orifice, producing damping forces proportional to the square of the piston translational velocity. Damping is essential to reduce the variation in air vane angular velocity between the two aerodynamic load cases. Both up- and downlock provisions have been incorporated, along with manual erection and folding capability. Air vane dimensions are approximately 63.5 cm (25 in) root chord, 22.9 cm (9 in) span, and 3.8 cm (1.5 in) maximum thickness. Figure 3 presents an exploded view of the AVES.

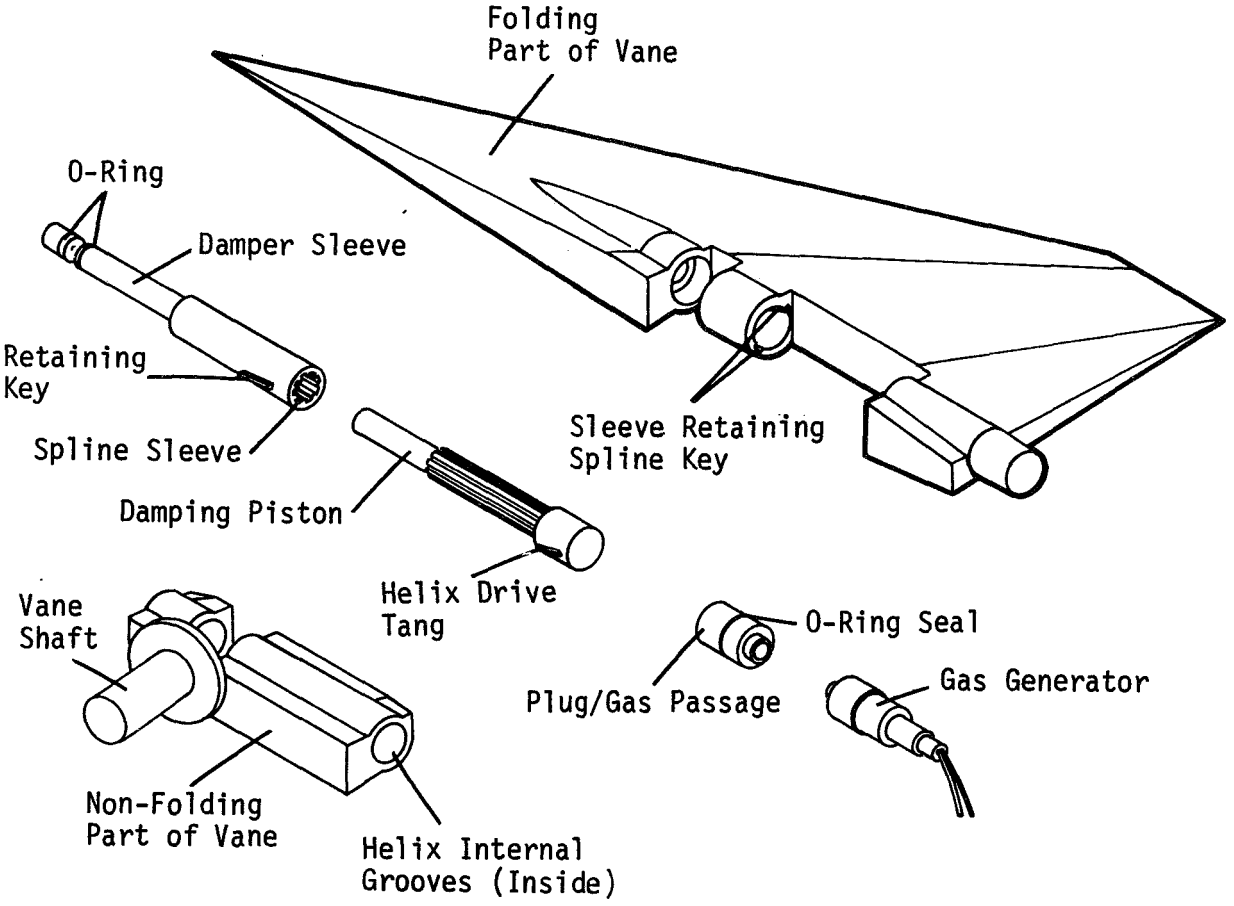

Figure 3. Piston-Helix AVES Concept

MATERIAL SELECTION

Due to high air loads on the vane and the small size requirements for the AVES, stress analysis dictated the use of high strength materials. Candidate steels which could meet the high strength requirements include AISI 4340, 250 and 300 grade maraging, Custom 455, 13-8-PH, 17-4-PH, and 440C CRES. AISI 4340 and 250 grade maraging steels were selected because of

their ready availability. The folding component was fabricated from titanium 6-2-4-2.

To alleviate or minimize galling effects, the piston/spline component was made of 250 grade maraging steel. The helix groove component and female spline sleeve were constructed from 4340 steel heat-treated to a strength of 1790 MPa (260,000 psi). Some concern was initially expressed in the use of 4340 at such a high strength level. Opinion was that ductility was very poor and that problems could be expected during the application of dynamic loads during air vane unfolding. As discussed later, however, no problems with the 4340 material were encountered throughout the entire test program. Damping fluid seals were made of ethylene propylene, which is compatible with the Dow Corning 510 silicone oil damping fluid. These seals were effective against high pressure warm gases.

GALLING FRICTION TEST

A test was devised to determine the galling/friction characteristics of maraging steel sliding against 4340 steel. Torque loads, up to and including ultimate, were applied to a drive piston/spline while a hydraulic ram translated the drive piston/spline in mating parts. The test pieces were geometrically similar to AVES parts, however, all motion was linear. Both male and female parts were coated with Everlube 811 dry film molybdenum disulfide lubricant. The test set-up is shown in Figure 4, and Table I presents the measured results. Inspection of the parts revealed no galling or other detrimental wear, thus indicating satisfactory choice of materials and lubricant.

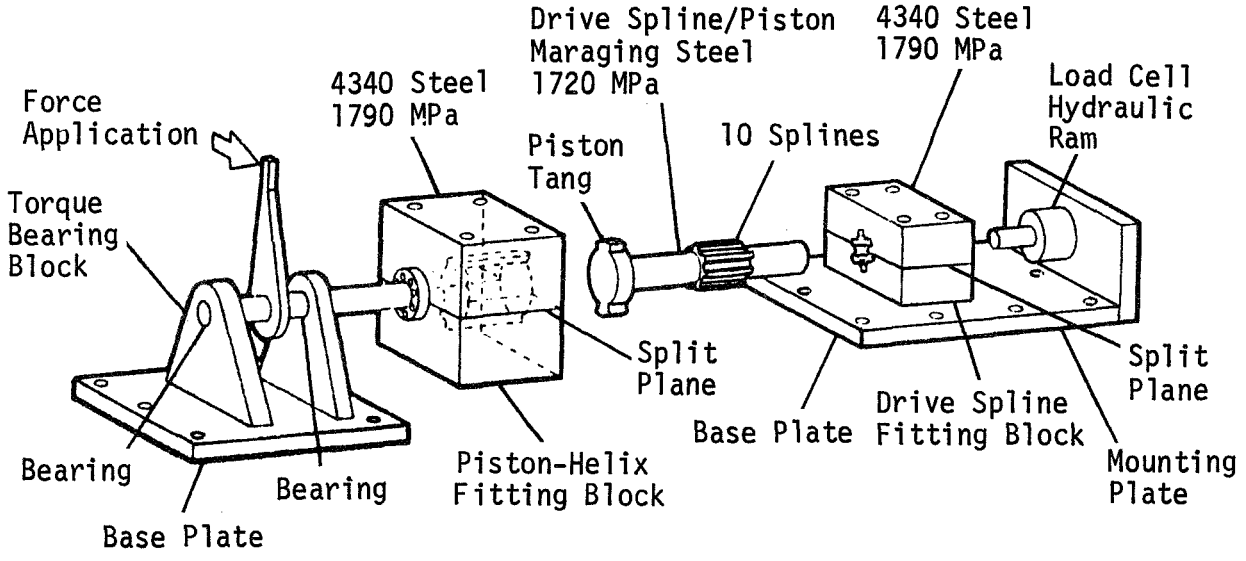

Figure 4. AVES Galling/Friction Test Set-up

TABLE I. FRICTION TEST SUMMARY

Run Number	Applied Torque (N·m)	Axial Load (N)			Friction Coefficient			Velocity (m/s)
		Breakaway	Min	Max	Breakaway	Min	Max	
1	51	~3,114	1,010	-	-	0.23	-	0.831
2	111	3,220	2,440	2,990	0.19	0.14	0.17	0.820
3	226	3,810	3,420	4,480	0.11	0.10	0.13	0.679
4	330*	5,600	5,340	6,940	0.11	0.10	0.14	0.396
5	336*	6,800	5,200	6,610	0.13	0.10	0.13	0.287
6	503**	8,900	7,540	9,270	0.11	0.10	0.12	0.267
7	620***	10,140	9,210	10,880	0.11	0.10	0.10	0.231

* Design limit load (repeat runs)
** Design ultimate load
*** Proof load (2X limit load)

ACTUATOR SIMULATOR

The gas generator which provides the energy for erection of the AVES was being developed concurrently with AVES fabrication. Since this hardware was not available for gas generator development and verification testing, an actuator simulator was designed and fabricated (Figure 5). This device simulated the reaction forces of the damping fluid, mechanical friction, etc., and duplicated the time rate of change of the gas chamber volume. Its construction provided for gas and fluid pressure instrumentation as well as piston position versus time. Prior to using the simulator for gas generator testing, trial runs were made using 34.5 MPa (5000 psi) of gaseous nitrogen. These experiments demonstrated reliable operation of the simulator and provided a check on damper orifice sizing.

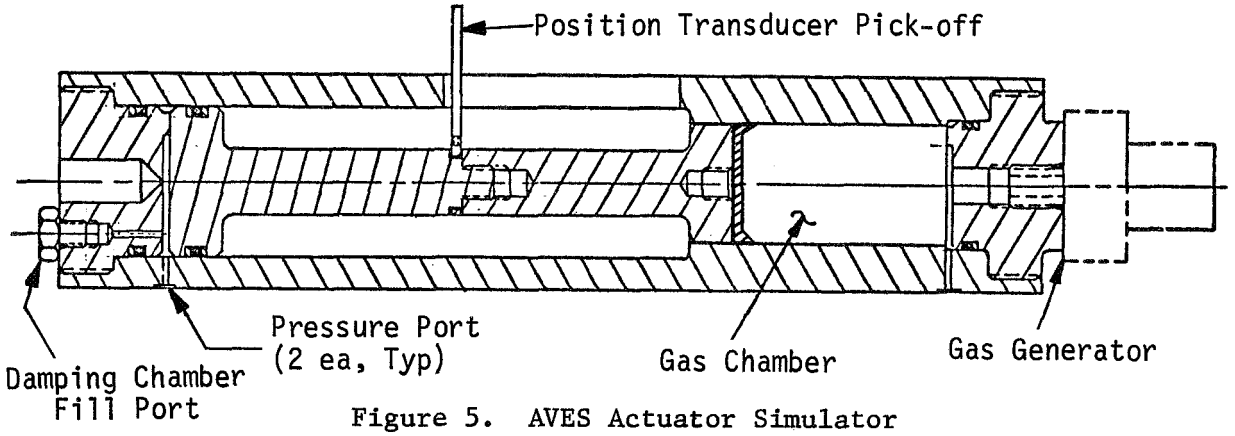

Figure 5. AVES Actuator Simulator

In October 1977, all materials were available to begin testing. The AVES was required to operate against aiding and opposing loads at the minimum and maximum expected temperatures (Table II).

TABLE II. AVES TEST SEQUENCE

Test No.	Gas Source	Pressure (MPa)	Load Condition	Temperature
CG1	Manual Checkout	-	-	Ambient
CG2	Bottled GN_2	3.45	None	Ambient
CG3	Bottled GN_2	13.8	None	Ambient
CG4	Bottled GN_2	34.5	None	Ambient
CG5	Bottled GN_2	34.5	None	Ambient
WG1	Warm Gas	-	None	Ambient
CG6	Bottled GN_2	34.5	Opposing	Ambient
CG7	Bottled GN_2	34.5	Opposing	Ambient
WG2	Warm Gas	-	Opposing	Ambient
CG8	Bottled GN_2	34.5	Aiding	Ambient
WG3	Warm Gas	-	Aiding	344°K
WG4	Warm Gas	-	Opposing	219°K
WG5	Warm Gas	-	Opposing	344°K

All of the cold gas (CG) runs were completed without incident; however, warm gas test (WG1) failed due to gas leakage and erosion of the TFE (Teflon) seal in the "square" corner.

A seal material and configuration test plan was developed in an attempt to curtail gas leakage. The candidate seal materials were required to be effective at 219°K (-65°F) and 344°K (+160°F), and were to provide initial edge preload when installed. They were also required to be resilient so that the gas chamber pressure tending to compress the seal would also create additional edge loads.

Five seal candidates were selected: lead seals 0.32 mm (0.125 in) thick and 0.64 mm (0.25 in) thick; RTV rubber seals 0.32 mm (0.125 in) thick; and copper shim seals composed of stacks of shims 0.008 mm (0.003 in) thick in one concept and 0.013 mm (0.005 in) thick in another. Seventeen layers of shim stock went into the making of one copper seal. Each of the individual shim stocks were made slightly oversize such that the package of shims had to be forced into the test device. With this array of seals, testing began using a modified actuator simulator. Parallel grooves simulating the helical grooves in the AVES were electric-discharge machined in the gas side of the cylinder. The gas piston was modified to include two diametrically opposite tangs. In this manner, the square corner sealing problem would be duplicated. Warm gas was supplied by a handloaded cartridge which used a $BKNO_3$ boosted initiator and IMR 4198 smokeless rifle powder (shotgun shell). Each seal candidate was tested at room temperature; those which did not leak were then tested at 219°K (-65°F) soak temperature. As shown in the summary (Table III), the RTV rubber seal did not leak at either temperature.

The 0.32 mm (0.125 in) RTV seal was then molded to fit the helical grooves in the AVES. A warm gas test was conducted using the AVES hardware and a shotgun shell. Immediate leakage was detected by both thermocouple and pressure instrumentation. The physical characteristics of the actuator

simulator and the AVES were carefully checked and compared to determine what effects (other than the helical twist of the AVES grooves) might have contributed to the seal failure. The dimensional check revealed that the helical groove in the AVES was rougher than that in the simulator (4.75 μm [190 μin] versus 3.25 μm [130 μin]), and that the clearance between the tang and the groove was much greater (0.36 mm [0.014 in] versus 0.05 mm [0.002 in]) on a side. Based on this information, the helical tangs on the AVES gas piston were built-up with flame-spray techniques and remachined to reduce the clearance. The AVES was then assembled with the newly machined piston and RTV seal installed. A warm gas test using the same propellant charge as in the simulator tests was run. Again the seal failed. At this point, it was believed that sealing square corners would involve a high-risk development program. Therefore, an alternate concept was configured wherein the tanged piston was sandwiched between two cylindrical pistons, both of which could readily be sealed against high pressure fluids and gases with the use of O-rings. To verify this concept, the AVES test hardware was modified to accept a cylindrical piston extension and O-rings.

TABLE III. SEAL TEST SUMMARY

Seal Configuration	Ambient Temperature	219°K Temperature
0.32 mm RTV	No leak	No leak
0.32 mm lead	Leak	N/A
0.64 mm lead	No leak	Leak
0.008 mm copper shim	Leak	N/A
0.013 mm copper shim	Leak	N/A

Figure 6 illustrates the redesigned configuration. Minimal changes were required. The new part (A) is an extension of the original piston (part C). The piston head of part A is circular and allows the installation of a standard O-ring seal. Part B, the cylinder containing piston A, replaced the titanium extension in the original configuration. Fastening bolt diameters were the same but the lengths were shortened. Both parts A and B were made of AISI 4340 steel heat-treated to a hardness of 1790 MPa (260,000 psi). Original parts C and D required some machining.

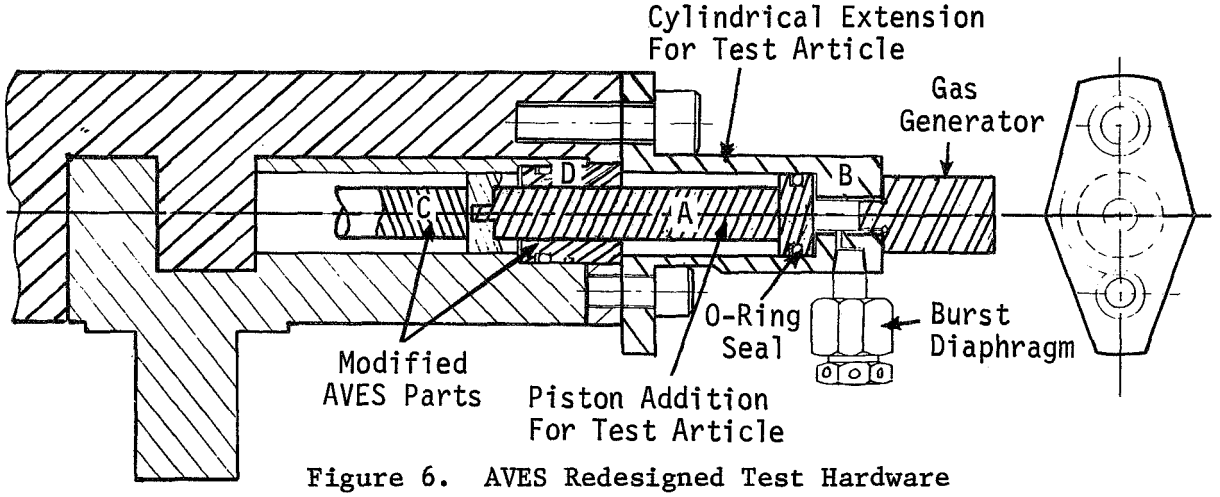

Figure 6. AVES Redesigned Test Hardware

Prior to checking the performance of the redesigned AVES with warm gas generators, two cold gas and three shotgun shell erection tests were conducted. The air vane erected in all cases except the first shotgun shell test. In that test, the burst diaphram ruptured in the first several milliseconds. Reduction of the shotgun shell propellant charge by one-half allowed successful erection of the air vane in the subsequent tests discussed below:

- Test WG1 was conducted at ambient temperatures with no external loads applied to the AVES. The air vane opening time was 78 ms. Maximum warm gas and fluid damping pressures were 40 MPa (5800 psi) and 103 MPa (15,000 psi), respectively. Post-test examination of the AVES revealed no mechanical damage - all seals worked effectively and the locking pin fully engaged.

- Test WG2 was conducted at ambient temperatures with an opposing simulated external aerodynamic torque of 339 N·m (3000 in-lb) applied to the AVES. The air vane erected to within 0.05 rad (3 degrees) of full opening in 96 ms. Partial engagement of the locking pin verified the vane erection angle. Examination of the driving piston following AVES post-test disassembly and inspection revealed galling of the piston surface. This galling action was the result of a skewed alignment between the axes of the cylinder and the driving piston (localized titanium yielding was involved). Failure of the vane to fully erect was believed due to the restraint forces introduced by galling. This effect was eliminated from succeeding tests by machining the drive piston to an approximate spherical shape.

- Test WG3 was conducted at 344°K (160°F) with an aiding simulated aerodynamic torque of 243 N·m (2150 in-lb) applied to the AVES. The vane erected with full locking pin engagement within 66 ms. The angular velocity at full erection was 26.2 rad/s. Peak warm gas and damping pressures of 54.5 MPa (7900 psi) and 142 MPa (20,600 psi), respectively, were recorded. Post-test examination revealed no mechanical damage, other than partial extrusion of the hydraulic damping fluid Teflon sealing backup rings.

- Test WG4 was conducted at 219°K (-65°F) with a simulated opposing load applied to the AVES. The vane erected fully within 114.5 ms and then backed off about 0.05 rad (3 degrees) due to the opposing load. The locking pin did not move - indicating a frozen condition. After warm-up, however, the locking pin engaged. An opening time in excess of 100 ms was partially attributed to opposing torques generated in the test fixture equipment (i.e., bearings). Measurement of this torque ranged from 8.5 to 17 N·m (75 to 150 in-lb). The work involved in erecting the AVES is increased about 6 percent due to this effect.

- Test WG5, conducted at 344°K (160°F) with an opposing load applied to the AVES, was expected to develop the highest pressures of any of the tests. The gas pressure rose to 75.8 MPa (11,000 psi), when the safety burst diaphragm (rated 77.6 to 81.0 MPa [11,250 to 11,750 psi]) ruptured. The erection process terminated in 30 ms, at which point the air vane had erected 1.05 rad (60 degrees). No physical damage was

sustained by the AVES other than Teflon backup ring extrusion on the damping fluid seals (pressure ∿169.6 MPa [24,600 psi]).

For subsequent testing, the damping orifice area was increased by a factor of 2.0 to reduce the erection time for the opposing load, 219°K (-65°F) condition. This selected value was based on results of dynamic analyses which showed that air vane opening time was reduced 9 ms by increasing the damping orifice area to 1.5 times the nominal value. An additional 3 ms was gained by doubling the area. Only 1 additional ms would be gained if the area were to be increased 2.5 times.

FINAL AVES TESTING

In April 1978, additional gas generators were purchased to repeat AVES tests WG2, WG4, and WG5. A brief description of each of these tests follows:

- Test WG2R was conducted at ambient temperatures with an opposing simulated external aerodynamic torque of 339 N·m (3000 in-lb) applied to the AVES. The air vane erected with full locking pin engagement in 99 ms. Expected opening time was approximately 75 ms. Prior to the test, the wiring on one of the two initiators was accidentally broken. Each of the initiators contained 115 mg of propellant. With only one-half the propellant available, the initial chamber pressure was considerably reduced for this test. Despite this deficiency, all test requirements were met.

- Test WG5R was conducted at 344°K (160°F) with an opposing load applied to the AVES. The air vane opened with full locking pin engagement (visual observation) in 51 ms.

- Tests WG4R and WG4R2 were conducted at 219°K (-65°F) with simulated opposing loads applied to the AVES. The air vane failed to fully erect in either test due to failure of the O-rings to seal the warm gas pressures; however, full erection was achieved in test WG4, and no gas leakage past the O-ring seal occurred in that test. Post-test examination of the O-ring in both tests indicated erosion of the O-ring over a sector width of about 1.05 rad (60 degrees). Position of this sector was symmetrical about the piston topside. Failure of the O-rings to seal was attributed to excessive yielding of the titanium folding air vane in the vicinity of the gas generator. This yielding caused misalignment between the axes of the gas cylinder and O-ring sealed gas piston. As a result, a greater amount of O-ring on the piston topside was exposed to the hot gases than on the piston sides and bottom. Yielding of the titanium was first noticed on test WG2. Apparently, the amount of yielding was not enough to cause leakage on test WG4; however, continued testing increased the yielding. In an AVES redesigned for tactical use, this type of structural behavior would not occur. Typical dynamic response characteristics of these tests are shown in Figure 7.

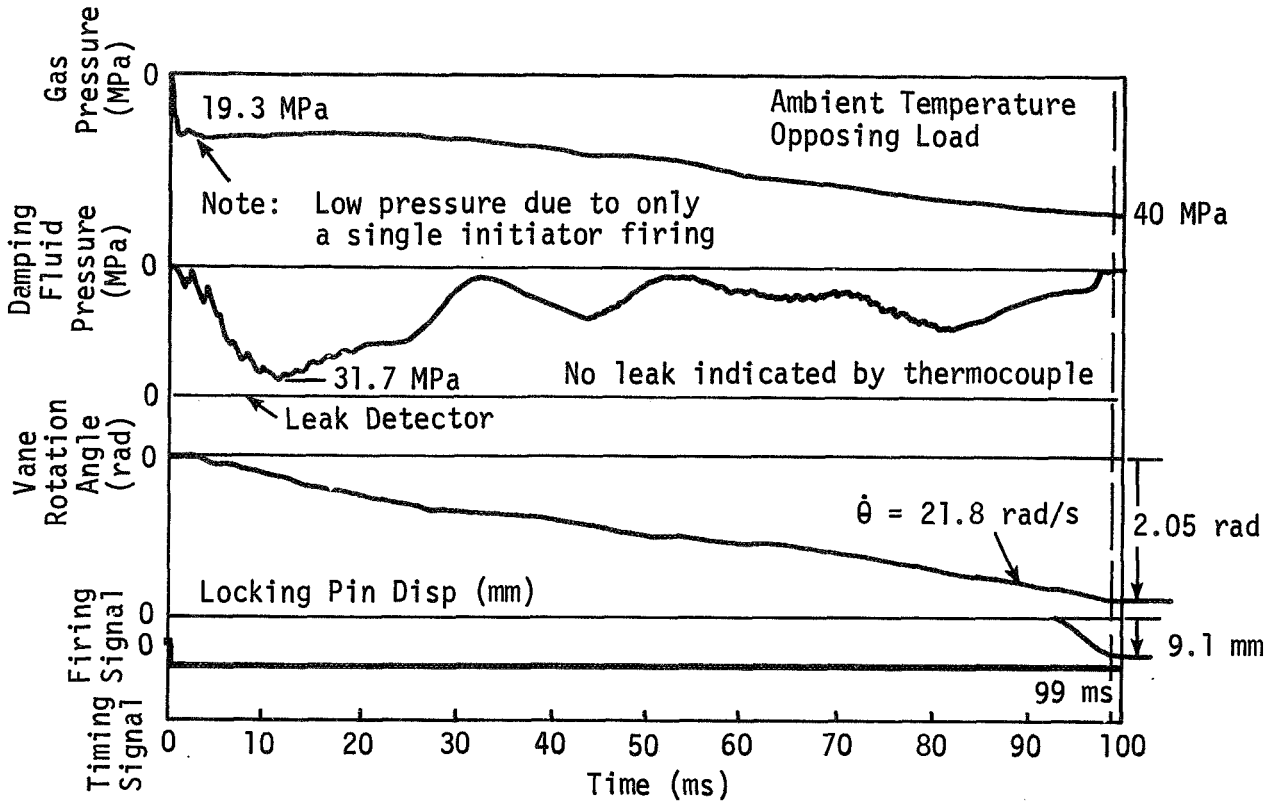

Figure 7. AVES Dynamic Response for Test WG2R (Typical)

Figure 8 summarizes AVES performance with respect to opening time and angular position requirements. For all load and temperature conditions, the AVES erected fully on tests WG1, WG2R, WG3, WG4, and WG5R within 100 ms, and had full engagement of the locking pin except on test WG4. The erection time performance of WG4 (cold temperature opposing load) will meet 100 ms requirement by doubling the damping orifice area. An alternate locking pin design has been implemented which will prevent freeze-up at cold temperatures.

CONCLUSIONS - LESSONS LEARNED

The AVES development program has shown that the piston-helix concept, initially shown feasible through analyses and later demonstrated experimentally, is a sound concept. This design withstood 11 warm gas, 5 shotgun shell gas, and 8 cold gas erection tests with no degradation in performance until the last 2 tests. Future development effort will concentrate on weight reduction, ease of manufacture, good maintainability, and incorporation of lessons learned from the initial development effort (i.e., gas sealing and locking pin mechanism).

Lessons learned from the AVES development test program include:

1. Gaps between the helix drive tang and helix internal grooves could not be effectively sealed against high gas pressures. O-rings proved to be effective seals.

2 The O-ring sealed, spring-loaded locking pin was inoperative at 219°K (-65°F). A concept change to remove O-rings or the use of gas pressure as the locking force is required for a redesigned tactical AVES.

3 Damping bellows should be designed such that repeatable rupture patterns occur during vane erection.

4 A gas generator with a smaller temperature sensitivity coefficient is recommended to reduce variations in AVES performance due to temperature environments.

5 Ethylene propylene O-rings will satisfactorily seal dynamic damping fluid pressures as high as 165 MPa (24,000 psi) and gas pressures as high as 75.8 MPa (11,000 psi).

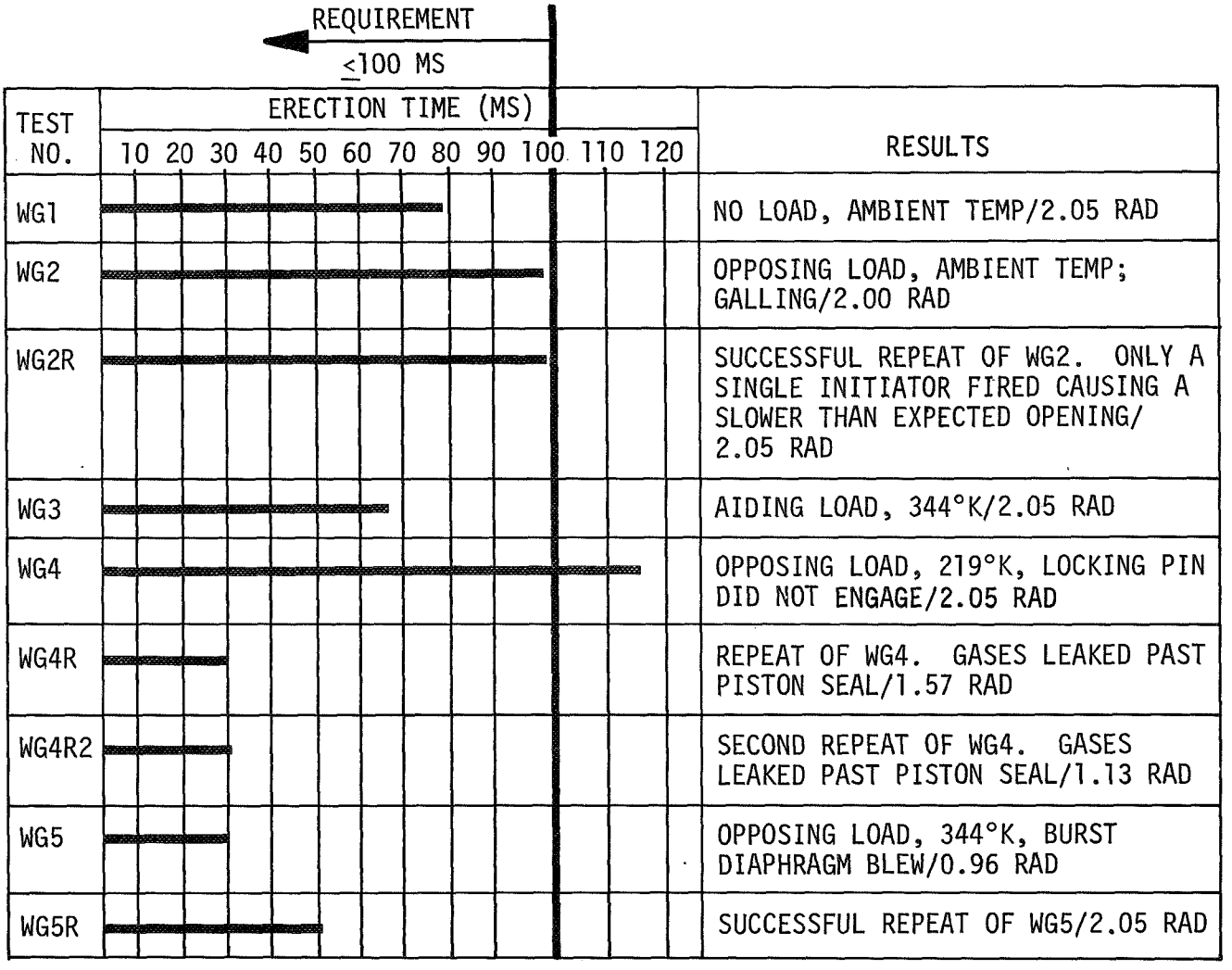

Figure 8. AVES Test Performance

SUMMARY OF THE ORBITER MECHANICAL SYSTEMS

By John Kiker* and Kirby Hinson*

ABSTRACT

Major mechanical systems of the Orbiter space vehicle are summarized with respect to general design details, manner of operation, expected performance, and, where applicable, unique features. A synopsis of data obtained during the five atmospheric flight tests of spacecraft OV-101 and status of the systems for the first orbital spacecraft STS-1 are presented.

INTRODUCTION

The NASA Orbiter manned spacecraft is the next generation of space vehicles being designed for reuse and to reduce the cost and increase the effectiveness of using space for commercial, scientific, and defense needs. The primary design and operations goal for the Orbiter is to provide routine access to space. The general configuration and details of the Orbiter are shown in figure 1. The successful operation and accomplishment of the NASA mission objectives, using this new generation of spacecraft, is dependent on the proper functioning of numerous mechanical systems.

This paper is devoted to a review of Shuttle mechanical systems, including separation systems, the crew escape system, aerothermal seals, pressure seals and thermal barriers, payload bay door mechanisms, and the landing deceleration system. These systems have in common certain mechanical design aspects but obviously involve many other engineering disciplines, both within the system and in interfaces between the mechanical system and other Shuttle systems. Vehicle dynamics and aerodynamics are particularly important to the design of the separation, crew escape, and landing deceleration systems. Each of these systems also includes pyrotechnic components. The aerothermal seals, the pressure seals, and the thermal barriers derive requirements from aerodynamic heating and static pressure environments. The aerothermal seals are unique in that seals must be maintained between moving surfaces during the high aerodynamic heating pulse of atmospheric entry.

Design of all mechanical systems for the Shuttle is based on maximum use of existing aircraft and spacecraft technology. This approach minimizes direct development costs and schedule risk and reduces the need for extensive systems-level tests to establish reliability. For example, the ejection seat used in the crew escape system is one previously qualified for use in another aircraft, and most of the components of the landing deceleration system are of conventional design and materials.

*NASA Lyndon B. Johnson Space Center, Houston, Texas.

New technology is applied only where it results in significant weight savings, as in the use of the carbon/beryllium brake, or where no solid technology base exists, as in the aerothermal seals.

Another unusual factor governing the design and development of Shuttle mechanical systems is the limited life requirement. Each Orbiter vehicle has a planned design life of 100 missions, with appropriate margins. However, for components which are easily changed out between flights, the cost of replacement as frequently as every fifth mission is traded against the cost of developing a component with full 100-mission capability. For example, the Orbiter tires and brakes are designed for 5 to 10 missions, and their routine replacement is scheduled in the normal turnaround procedure. Lifetimes as short as five design missions result in lightweight components but reduce the margin between the design five-use and emergency one-use capability. This reduction dictates a realistic assessment of the design and emergency system requirements; such an assessment is the basis for extensive systems analysis and careful attention to the conditions imposed in limited test programs.

The mechanical systems are described independently. For each system, key design requirements and the impact on systems design of changing requirements are discussed. Early trade-offs and system design options are reviewed with consideration of critical design issues and primary design drivers. Interesting design and development problems are treated primarily to indicate the technical evolution of current Shuttle systems designs. The application of new technology is discussed as appropriate during the presentation of each mechanical system.

AEROTHERMAL SEALS AND REMOTELY OPERATED DOOR THERMAL BARRIERS

The Orbiter is the first manned spacecraft to use aerodynamic control surfaces that are movable during the high heating pulse of entry. Aerothermal seals are required to restrict gas flow into the control surface hinge-cavity areas so as to maintain structural temperatures within acceptable limits. Such seals are used on the elevon, rudder/speed-brake, and body flap control surfaces. Each of the three control surface seals is unique in design and materials because of varying thermal requirements and varying hinge-cavity geometry. The elevon lower cove is closed out with a polyimide seal rubbing against aluminum and Inconel tubes and plates. The elevon upper surface is sealed with formed Inconel springs rubbing against Inconel panels. The body flap seal is composed of Inconel hinged panels. The rudder/speed-brake seal is made of graphite seal blocks rubbing on conic Inconel panels. Only the basic design/materials concept has been mentioned. Each of the aerothermal seals is quite complex in design detail as each includes several unique solutions to specific geometric and thermal problems. For example, the elevons are composed of two independently movable surfaces per side; thus, there are four ends of the elevon hinge cove per side which must be closed out. The hinge locations constitute another sealing challenge. The entire

seal system must accommodate the surface distortion associated with high aerodynamic and thermal loads. It was even more difficult to achieve a design that could be assembled and verified by inspection after assembly.

Thermal barriers are provided to close out doors, hatches, and other penetrations through the vehicle thermal protection system. Because these hatches and doors are generally not cycled during the entry heating pulse, relatively simple, passive thermal barriers can provide aequate thermal sealing. Three basic types of thermal barriers are used in door edge gaps. In the nose gear door, a pad-type barrier is used to fill the gap out to the outer mold line and thereby to ensure a very smooth surface in this very high heating region. A fiber brush barrier is used to accommodate relative deflections at the edges of the extremely large payload bay doors. Most other doors and openings incorporate unique variations of metal springs filled with insulating material and wrapped with ceramic cloth. Figure 2 shows representative aerothermal seal and static thermal barriers. Figure 3 shows the body flap aerothermal seal.

The Orbiter aerothermal seals and thermal barriers will be flown for the first time in the upcoming Orbital Flight Test program. The approach and landing flight tests of 1977 did not include the extreme thermal environment; therefore, the sealing requirements were much less severe. Certification of the Orbiter aerothermal seals is to be accomplished through a program which combines the results of tests and analysis activities to ensure that the subsystem provides adequate protection to the structure when exposed to the mission environment.

Basic materials testing was performed to ensure thermostructural properties of all materials used. Samples of critical seals combined with adjacent reusable surface insulation (RSI) to make a test article of approximately 0.46 meter (1.5 feet) square were tested in arc-jet facilities at three NASA centers. These tests simulated approximate thermal entry environments. One full-size outboard elevon and portion of the trailing edge wing will be tested under entry thermal and structural loads. Various large panels and portions of the aerodynamic surfaces will be acoustic life tested with seals installed.

CREW ESCAPE SYSTEM

The general concept of the Orbiter is to provide a transport- or airliner-type vehicle to routinely shuttle multiple passengers and cargo to and from orbit. Provisions for handling emergency situations are therefore based on maintaining the integrity of the Orbiter to provide safe return of crew and passengers. This "intact abort" concept is the same as that used by commercial airliners. However, for the first few missions, the Orbiter is very much an experimental aircraft. During these missions, the crew will be limited to two; and, early in the program, it was recognized that a reasonable option existed to provide individual emergency escape capability for the critical launch and landing phases. Individual ejection seats have been incorporated for the pilot

and the copilot. These crew escape provisions will be removed following the Orbital Flight Test series, which will provide added confidence in the reliability of Shuttle systems and procedures.

The general philosophy of using developed, tested, and qualified systems resulted in selection of the U.S. Air Force SR-71/F-12 ejection seat. A careful evaluation of the performance of all available qualified seats showed the SR-71 seat to have the greatest range of high- and low-altitude capability. Figure 4 shows the design altitude/velocity capability of the SR-71 seat system, as well as a typical Shuttle trajectory. The seat provides reasonable escape capability from sea level to an altitude of 21 336 meters (70 000 feet) during launch and provides complete coverage during final descent to landing and for the complete Approach and Landing Test (ALT) envelope.

A major effort was made to use the seat as designed; however, the unique Orbiter crew cabin and structure arrangement, plus the vertical launch attitude, indicated the necessity for seat modifications. One change resulted when early reach and vision studies showed the crew would have problems reaching and seeing the necessary controls to fly the Orbiter during ascent. These findings were verified in a centrifuge test. As a result, a two-position back angle was incorporated into the seat. Should ejection be required during ascent, the back would automatically reposition the crew aft before exit. Following launch, the crewmember manually repositions the seat back for entry and landing. Pyrotechnic devices already used in the seat are used also for operating this device. See figure 5 for details of the seat-back modification and the salient features of the system.

The sled test program disclosed two other problems. First, the side-by-side arrangement of the seats in the Orbiter led to very high rotation rates (in yaw direction) as the seats entered the airstream. This problem was alleviated by a slight change in timing of drogue parachute deployment so that the stabilizing forces of the drogue would be effective earlier. Second, during the second dynamic sled test, one of the seats recontacted and damaged the inflated personnel parachute. Another slight timing change, this time to increase the interval between separation of the crewman from the seat and deployment of the personnel parachute, significantly reduced the possibility of recontact. Both of these sequence timing changes were verified in subsequent sled testing.

The Orbiter inner and outer crew cabin and structural hatch required a unique mechanical system design to enable jettisoning of the two hatches before the seats are ejected. The method of accomplishing this is shown in figure 6. This requirement differs from normal aircraft design, in which only a single structural surface must be cut or jettisoned. The U.S. Air Force standard SR-71 ejection seat, with the modifications described previously, was flown on all ALT flights. The same system is being installed on the first orbital flight spacecraft.

LANDING DECELERATION SYSTEM

The Orbiter landing deceleration system consists of a conventional tricycle landing gear including struts, wheels, tires, brakes, brake skid control, and nosewheel steering (fig. 7). The general design philosophy is to use conventional components and materials, yet to provide the lightest system capable of meeting predicted requirements. The Orbiter system is unconventional in three major areas, all based on achieving a lightweight system: (1) the landing gear is deployed by gravity rather than using hydraulic actuators - possible because there is no in-flight gear retraction requirement; (2) the brakes are composed of beryllium heat sinks with carbon linings - a combination with very high energy capacity; and (3) brakes and tires are designed for 5 uses rather than the usual 100 or more uses. This limited use requirement narrows the gap between the planned operating condition and the emergency ultimate operating capability of the hardware. As a result, a much more detailed and accurate analysis of Orbiter landing performance than that typically given commercial and military aircraft systems was required. This analysis is based on a limited number of very carefully planned tests.

Except for the brakes, the Orbiter landing deceleration system is designed of materials similar to those on other aircraft. The struts are machined from 300M alloy forgings - the same material used on 727, 737, 747, DC-10, etc., aircraft (fig. 8). The tires are manufactured of nylon cord and natural rubber - the same as commercial and military aircraft. The wheels are conventional aluminum forgings. The brake/skid-control system is the same brand used on nearly all large commercial and military transport aircraft, and the steering package is the same brand used on the B-1 bomber.

The brakes are of a multidisk design similar to that of other current large aircraft. One brake is included in each of the four main wheels. The brakes are commanded electrically through foot-pedal-operated transducers, which control hydraulic actuators. The unique feature of the brakes is the use of carbon linings attached to beryllium heat sinks. Other aircraft use brakes with beryllium heat sinks - the C-5A and the F-14, for example - and several use all-carbon brakes. The unique Orbiter carbon/beryllium combination was developed from that technology. The Orbiter brakes weigh about half as much as conventional sintered-iron-lined brakes for the same energy absorption capacity. (See fig. 9.)

The Orbiter size and landing weight are comparable to a medium size commercial airliner, but the landing speed is almost twice that of the typical airliner or military aircraft. Landings at a speed of 102.9 m/sec (200 knots) will be routine. Emergency landings with the full 29 484-kilogram (65 000 pound) payload can result in speeds as high as 115.7 m/sec (225 knots). Fortunately, for this case, all landings will occur at the launch site, where a 4572-meter (15 000 foot) runway is available. The brakes are capable of bringing the Orbiter to a safe stop under these conditions but are expended in the process. The four brakes must absorb as much as 301 megajoules (222 million foot-pounds) of energy at a peak

rate of nearly 22 371 kilowatts (30 000 horsepower). Some brake elements reach temperatures of 1255 K (1800° F). Several tests of the brake at these conditions have been executed on a dynamometer. The carbon/beryllium combination has proved to be an excellent emergency brake. Of course, the normal operating conditions are much less severe; and, whereas the design requirement is for five uses, many uses per brake are expected to be obtained with routine landings.

An interesting characteristic of the Orbiter brake is that it does not "fade" as it heats during a hard stop. Rather, it produces more and more torque for a given hydraulic pressure as the Orbiter velocity decreases, with low-speed torque about 50 percent higher than that available at braking initiation. This characteristic contributes significantly to the brakes' good emergency performance, but it requires that the pilot "ease off" the brakes at low speed during a normal stop to reduce the possibility of brake damage.

SEPARATION SYSTEM

The major components for separation of the Orbiter from the Shuttle external tank (ET) are illustrated in figure 10. At the forward attachment, release is accomplished by a pyrotechnic-actuated shear-type separation bolt. This type device is used at the forward attachment to satisfy a stringent requirement for a smooth outer mold line after separation and to withstand high structural loading before separation. The purpose of the smoothness criteria shown in figure 10 is to control the aerothermal heating on the spacecraft in order to prevent excessive structural temperatures during entry. The unique feature of this device is the internal fracture surface. After a piston shears the fracture plane, it closes out the bolt cavity to provide the required smooth surface.

At the two aft structural attachments, a 6.35-centimeter (2.5 inch) frangible nut is used as the release device. These frangible nuts are also fractured by pyrotechnic charges. They have recently been increased in diameter from 5.08 centimeters (2 inches) to 6.35 centimeters (2.5 inches) to provide additional structural margin at these attachments. Once the Orbiter is separated from the external tank, doors close out the cavities at the aft structural and umbilical attachments to protect the Orbiter structure during entry.

These structural attachments were used to release the Orbiter from a Boeing 747 aircraft during a series of Orbiter atmospheric test flights completed in 1977. The release devices for these tests were pyrotechnic-actuated separation bolts which fractured in tension, rather than shear as in the present bolt configuration. The shear bolts and frangible nuts are qualified to the flight environments as components, then the forward and aft structural assemblies are flight certified in a series of functional separation and structural loads tests. These tests are scheduled for completion by late August 1979.

ORBITER/ET UMBILICAL SEPARATION SYSTEM

The Orbiter/ET umbilical separation system provides the separation interface between the Orbiter vehicle and the external tank for fluid lines and electrical connections. There are two separate umbilical disconnect clusters between the Orbiter and the ET; both are located in the bottom aft fuselage of the Orbiter. The left-hand umbilical contains an electrical disconnect assembly and the liquid hydrogen (LH_2) system fluid disconnects, which include a 43.18-centimeter (17 inch) diameter propellant feed line, a 5.08-centimeter (2 inch) diameter tank repressurization line, and a 10.16-centimeter (4 inch) diameter prestart and tank replenishing line. The right-hand umbilical is similar, with an electrical disconnect assembly and two liquid oxygen (LO_2) fluid disconnects: one 43.18-centimeter (17 inch) diameter propellant feed line and a 5.08-centimeter (2 inch) diameter tank pressurization line. The umbilical separation system is designed to provide complete separation of the fluid and electrical interfaces between the Orbiter and the ET before initiation of structural separation. Figure 11 contains details of the system.

Two seconds after main engine cutoff (MECO), the LH_2 and LO_2 43.18-centimeter (17 inch) disconnect valves are closed pneumatically. Two seconds later, the LH_2 and LO_2 umbilical carrier plate separation command is issued, detonating the pyrotechnics which fracture three frangible nuts in each umbilical plate. A simultaneous command is issued to activate three hydraulic retractors attached to each of the umbilical plates. Both umbilicals then retract 6.35 centimeters (2.5 inches) into the Orbiter in approximately 4.5 seconds. The ET structural separation is commanded approximately 11 seconds after MECO.

Verification and qualification testing is being conducted on flight configuration LH_2 and LO_2 umbilical assemblies mounted in specially designed support fixtures. All LH_2 separation tests are conducted with liquid hydrogen in the system. During LO_2 separation tests, liquid nitrogen is substituted for LO_2 for safety considerations. During this series of tests, each hydraulic retractor will be individually disabled to simulate failed retractors to demonstrate a design requirement that any two of the three retractors shall provide adequate separation of the umbilical assemblies. Backup propellant valve closure modes are also being tested whereby valve closure is actuated mechanically during separation of the umbilical plates.

The umbilical separation system will be flown for the first time on spacecraft STS-1 since it was not required during the ALT program.

PAYLOAD BAY DOORS

The purpose of the Shuttle spacecraft, as the name implies, is to deliver a cargo to and/or return a cargo from Earth orbit. Since the deliverable item can be as large as 4.57 meters (15 feet) in diameter and

18.29 meters (60 feet) long, the Shuttle Orbiter is a unique spacecraft that requires two payload bay doors that are more than 18.29 meters (60 feet) in length - the largest to ever be operated in space. The graphite epoxy doors, which serve as the base for radiator retention and deployment, must react vehicle loads and protect the payloads during boost and entry and, yet, open and close as required once in orbit. The specific details of the payload bay doors are as presented in reference 1. The general configuration of the payload bay door and radiator system is shown in figure 12.

PAYLOAD RETENTION SYSTEM

The payload retention concept was selected shortly after the Space Shuttle Program was initiated, primarily because the selected approach would have a significant effect on the design of the Orbiter structure and, hence, on vehicle weight. The basic approach is a statically determinate load reaction system as shown in figure 13. This approach would use two retention fittings on the longeron to react X- and Z-axis loads, one additional longeron to react Z-axis loads, and a single reel fitting for Y-axis loads. Each fitting is designed to slide with minimum friction in those axes not designated as primary load carrying. Based on data available, the coefficient of friction achievable was selected as a maximum of 0.1 for the expected temperature range. To date, this value has not been achievable for temperatures to 200 K (-100° F), apparently because sliding surfaces are also geometrically sensitive.

To further complicate the problem, many of the payload suppliers desire to use a nondeterminate, four-point, longeron attach scheme. This design requires that the retention latch reach and "latching" pulldown force be sufficient to accommodate the out-of-plane condition that will exist during payload retrieval. Retrieval also required that some sort of integral guides be added to the retention fitting to aid in the installation of payloads in orbit.

In summary, what appeared at the outset to be a simple actuator design has evolved into a complex system when considering present Orbiter/payload restrictions. The design and function of the payload retention system is being evaluated in various ground test efforts involving a mockup of the payload bay, dummy payloads, and the remote manipulator system.

CONCLUDING REMARKS

In this paper, only a brief introduction to some of the more important Orbiter mechanical systems has been presented. Each of these systems involves interesting design features and unique performance requirements. Several papers could be written on special testing efforts, such as tire and wheel-bearing tests to actual load, yaw angle, and velocity histories, and arc-jet testing of aerothermal seal components and sections. Obviously, in a general paper of reasonable length, only the highlights of each system

can be presented. Those having special interest in a particular system or technology field covered herein are encouraged to contact the authors for more detailed discussion or information exchange.

REFERENCE

1. McAnally, Bill M.: Space Shuttle Orbiter Payload Bay Door Mechanisms. Paper prepared for presentation at the 13th Aerospace Mechanisms Symposium (Johnson Space Center, Tex.), Apr. 26-27, 1979. Rockwell International rep. SOD 79-0072.

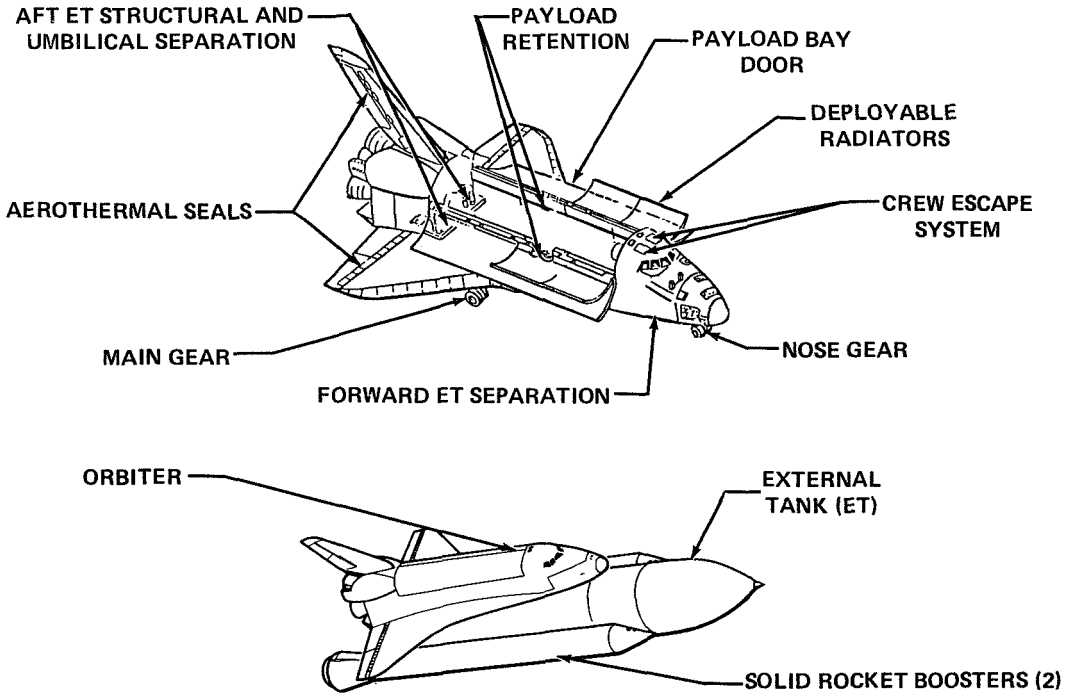

Figure 1.- Orbiter mechanical systems.

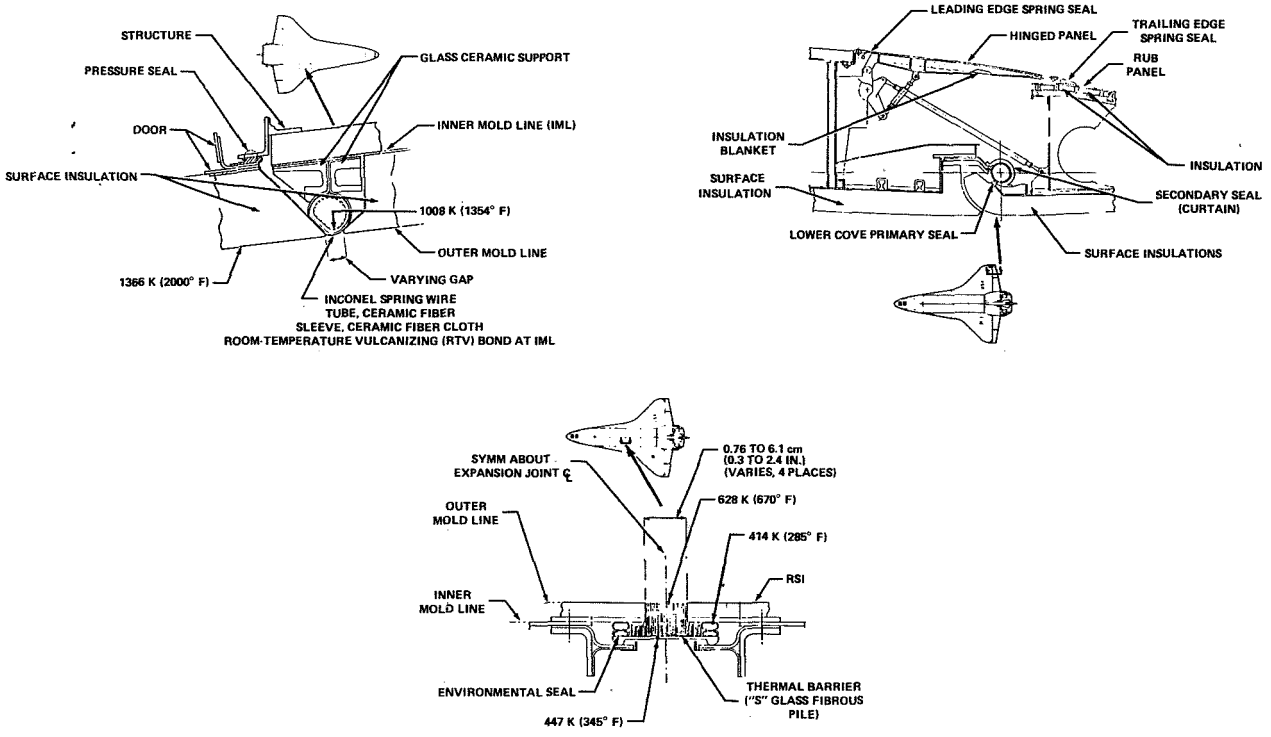

Figure 2.- Composite aerothermal seals and static thermal barriers.

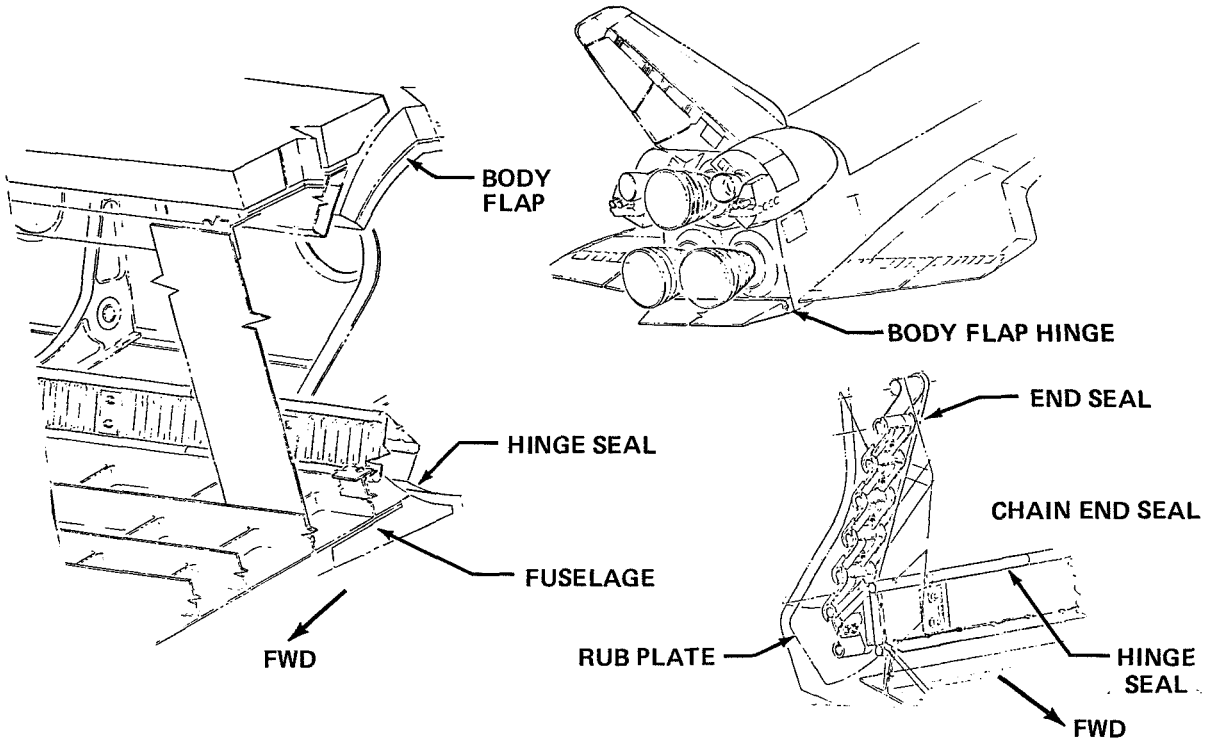

Figure 3.- Body flap aerothermal seal.

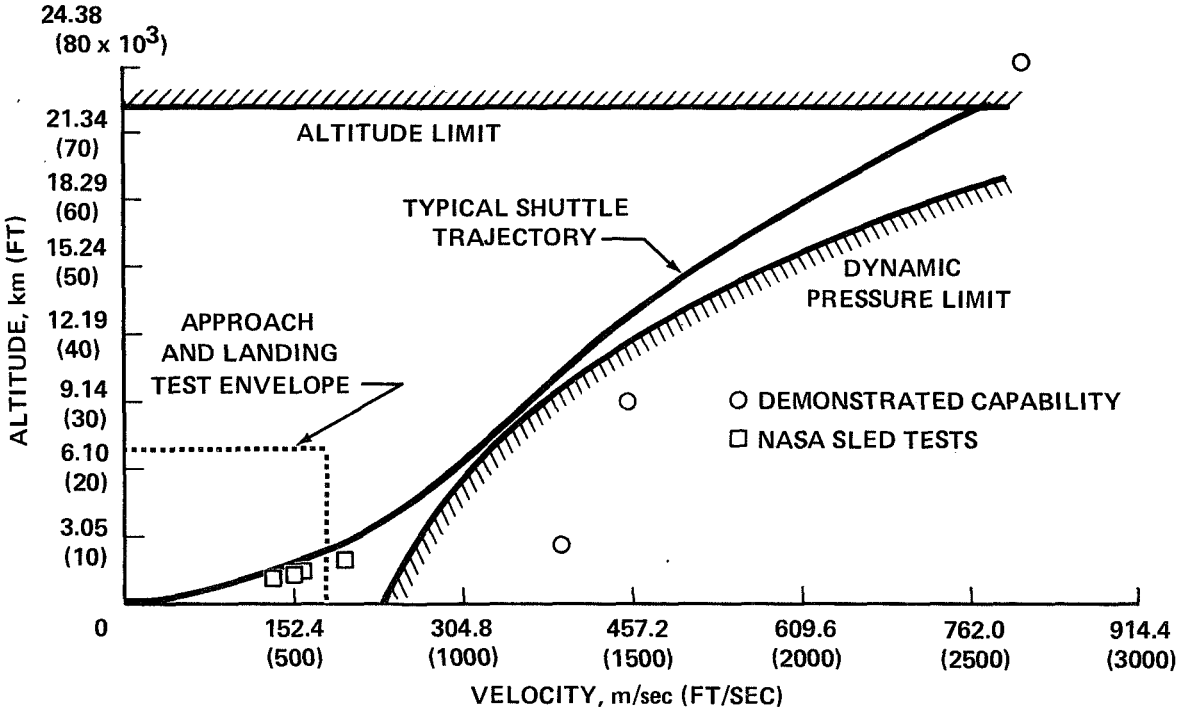

Figure 4.- Ejection seat capability.

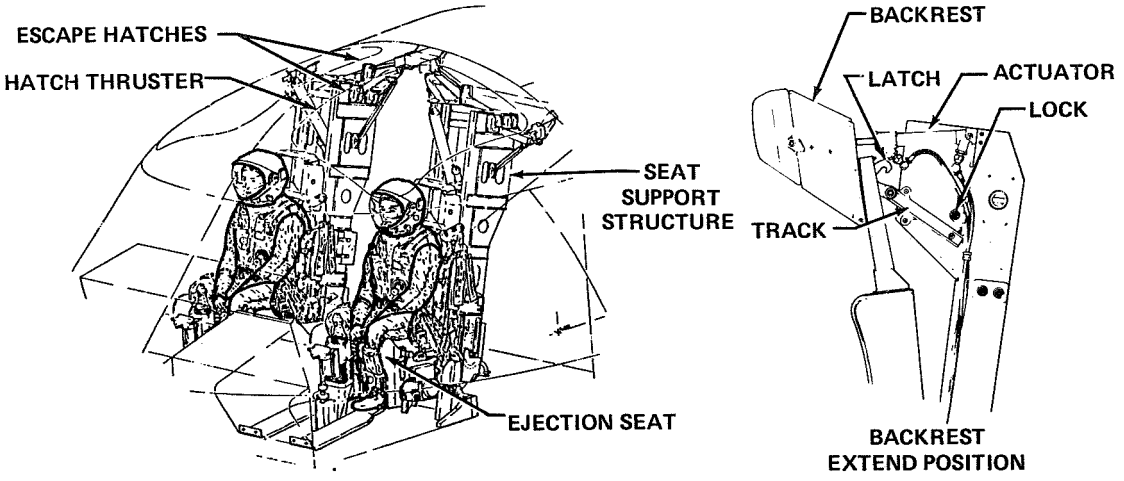

Figure 5.- Crew escape system installation.

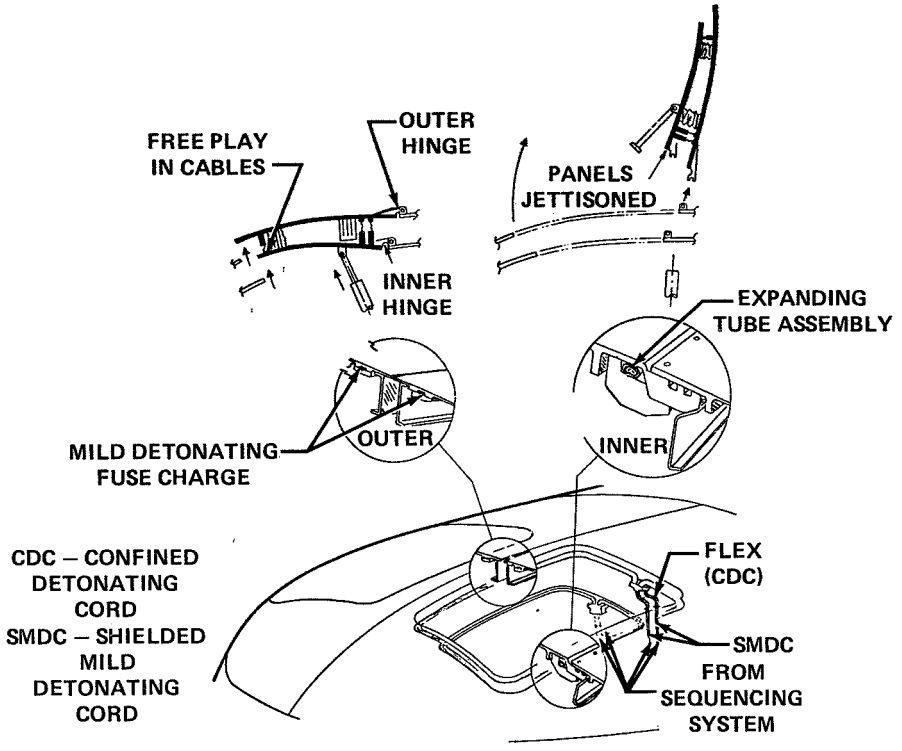

Figure 6.- Crew escape hatches.

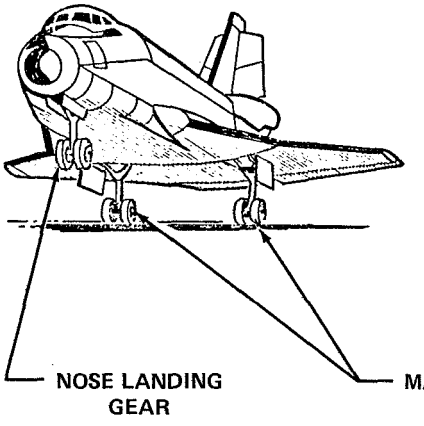

- NOSE AND MAIN LANDING GEAR
- GEAR UPLOCK, EXTENSION, AND RETRACTION MECHANISMS
- MAIN WHEEL BRAKES
- SKID-CONTROL SYSTEM
- NOSEWHEEL STEERING

Figure 7.- Landing deceleration system.

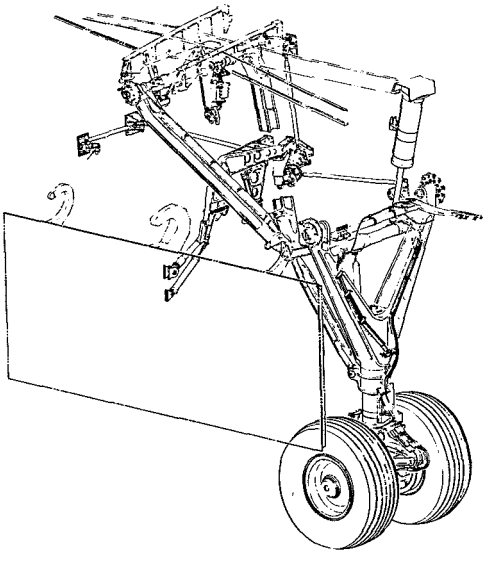

		MAIN		NOSE
DIMENSION, cm (IN.)				
COMPRESSED LENGTH		233.7 (92)		137.2 (54)
STROKE		40.6 (16)		55.9 (22)
TIRE RADIUS		55.9 (22)		40.6 (16)
DRAG BRACE LENGTH		307.3 (121)		182.9 (72)
WEIGHT, kg (LB)				
STRUTS	2 EA	1080.5 (2382)	1 EA	215.0 (474)
WHEELS	4 EA	213.2 (470)	2 EA	35.4 (78)
TIRES	4 EA	272.2 (600)	2 EA	43.5 (96)
BRAKES	4 EA	257.6 (568)		–

Figure 8.- Main landing gear.

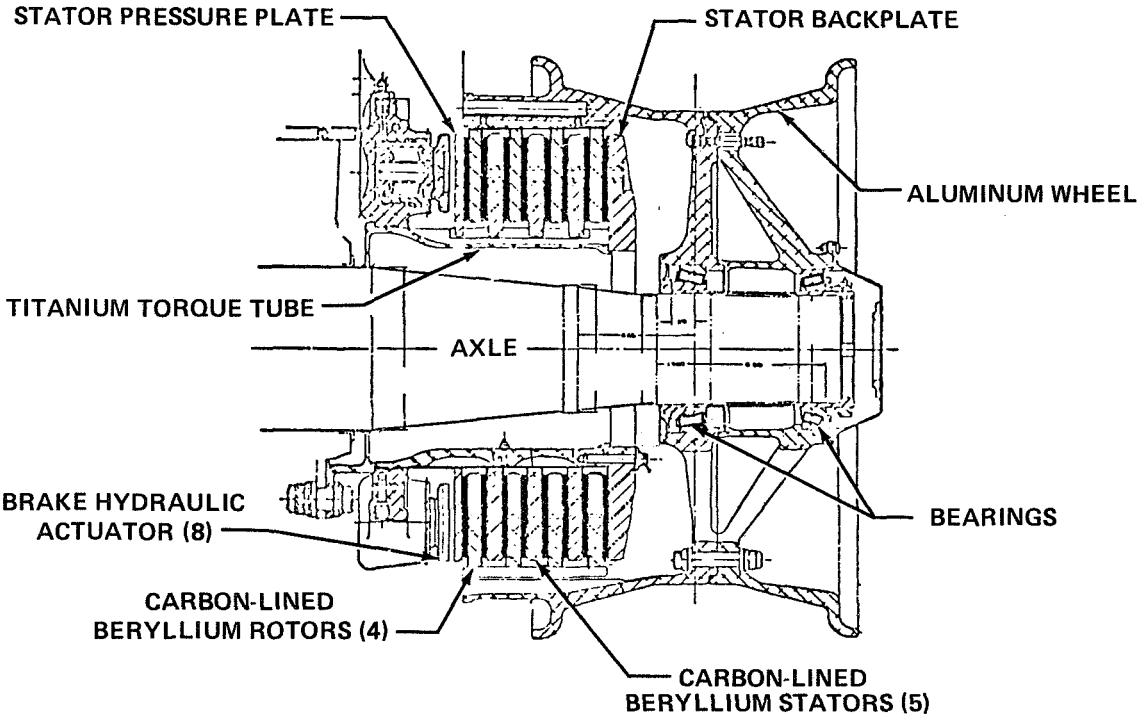

Figure 9.- Wheel brake assembly.

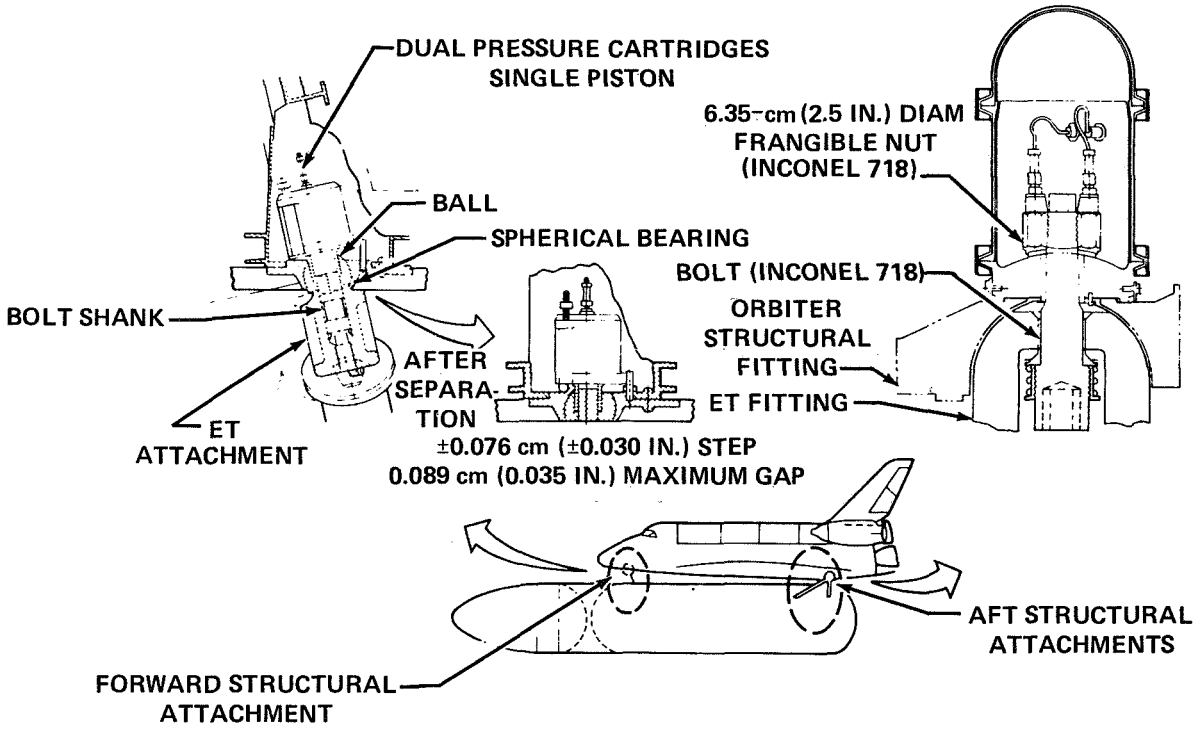

Figure 10.- Orbiter/external tank structural separation system.

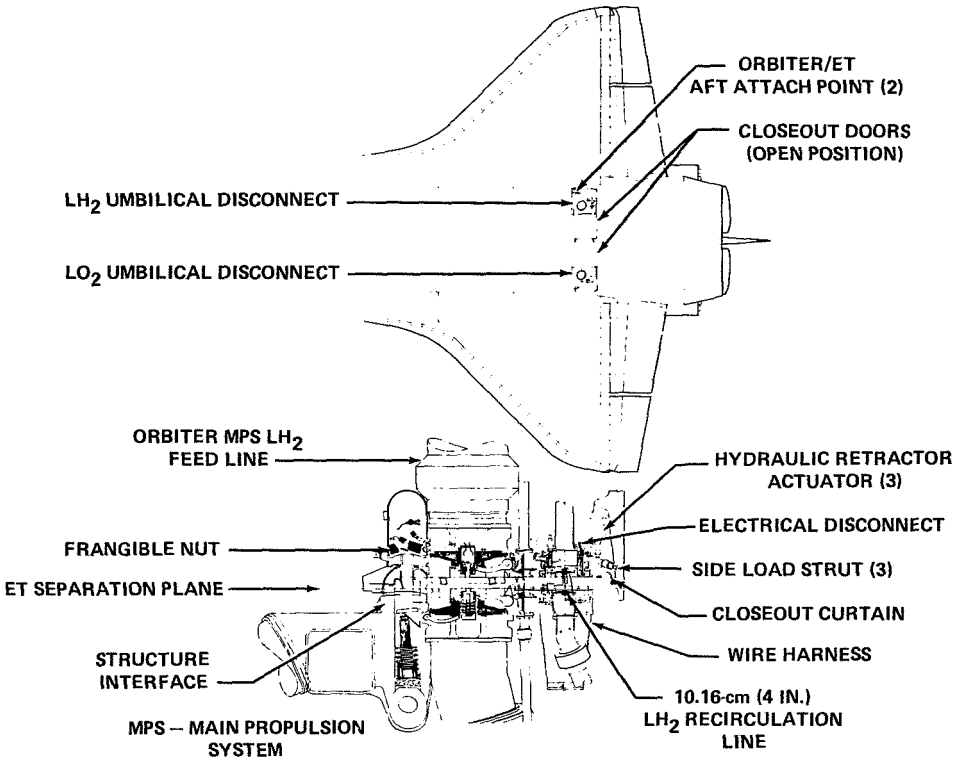

Figure 11.- Orbiter/external tank umbilical separation system.

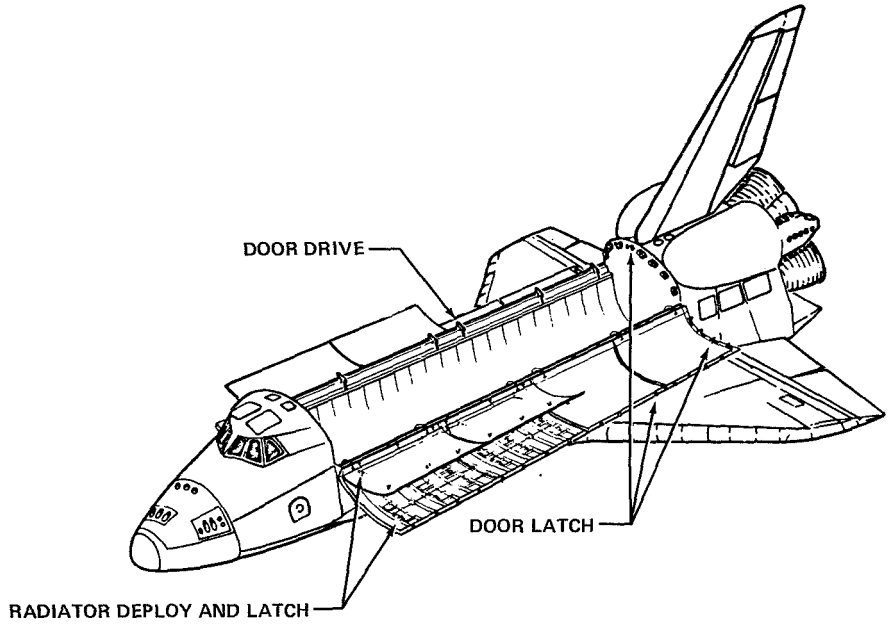

Figure 12.- Payload bay door/radiator system.

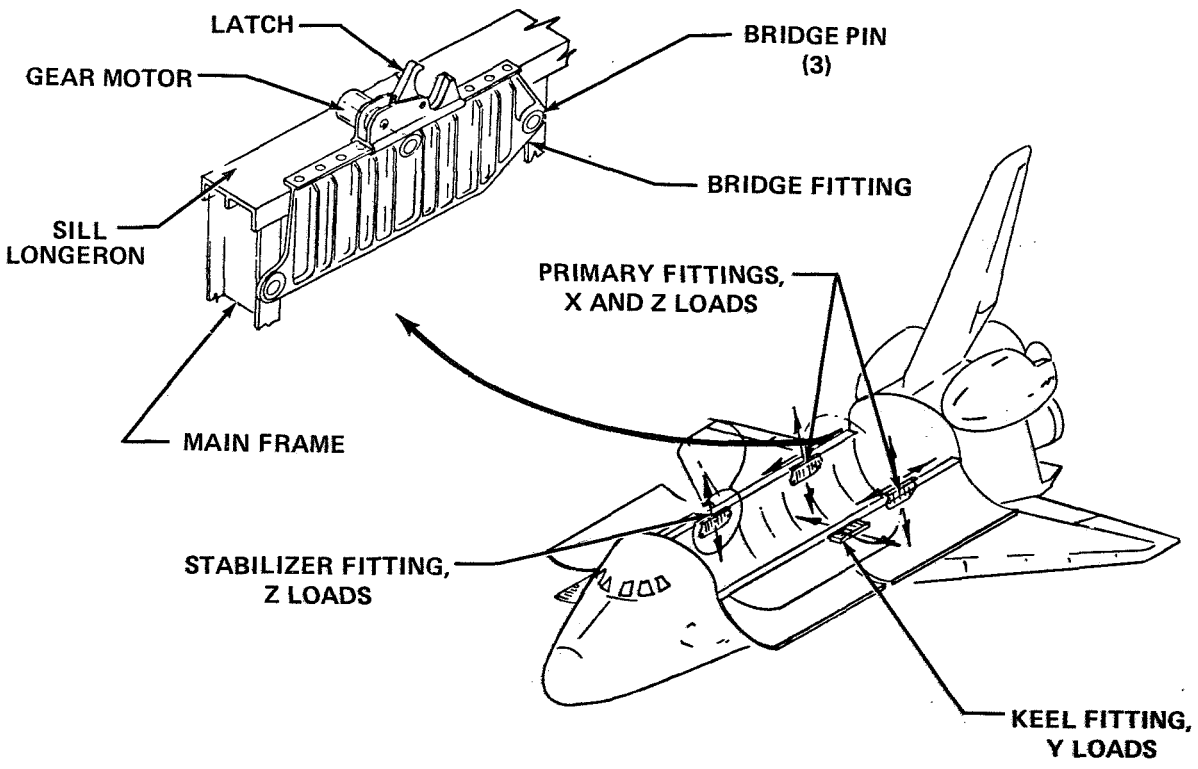

Figure 13.- Payload retention system.

PAYLOAD INSTALLATION AND DEPLOYMENT AID FOR SPACE SHUTTLE ORBITER SPACECRAFT REMOTE MANIPULATOR SYSTEM

Thomas O. Ross

Lyndon B. Johnson Space Center
Houston, Texas

ABSTRACT

Early developmental testing of the Remote Manipulator System (RMS) revealed that on-orbit handling of various payloads on the Space Shuttle Orbiter Spacecraft may prove to be beyond the capability of the system without the assistance of a handling aid.

An aid concept known as the PIDA (Payload Installation and Deployment Aid) is presented as a way to assist the RMS by relaxing the accuracy required during payload handling in the payload bay. The aid concept was designed and developed to move payloads through a prescribed path between the confined quarters of the payload bay and a position outside the critical maneuvering area of the Orbiter.

An androgynous docking mechanism is used at the payload/PIDA interfaces for normal docking functions that also serves as the structural connection between the payload and the Orbiter, that is capable of being loosened to prevent transfer of loads between a stowed payload and the PIDA structure. A gearmotor driven drum/cable system is used in the docking mechanism in a unique manner to center the attenuator assembly, align the ring and guide assembly (docking interface) in roll, pitch, and yaw, and rigidize the mechanism at a nominal position. A description of the design requirements and the modes of operation of the various functions of the deployment and the docking mechanisms are covered.

INTRODUCTION

The conceptual design study and operational simulations of the Remote Manipulator System (RMS) in the JSC Manipulator Development Facility (MDF) identified a need for an aid in the handling of large payloads into and out of the cargo bay by the manipulator.

In response to this need, a payload handling aid concept was designed and developed for use with the RMS.

The initial design concept was turned into prototype hardware for test and evaluation and this developed into a second set of prototype hardware that helped to define the concept as it is presently known and described in the following sections.

The initial concept of the deployment mechanism contained one rotating arm assembly to be used in conjunction with the RMS/operator for payload handling.

After building and testing prototype hardware of the Aid with a prototype of the manipulator, it was discovered that the RMS operator was unable to follow the arc path required to keep the payload aligned. It was concluded that the handling aid should be capable of moving the payload between the stowed and deployed positions automatically without the assistance of the RMS in the control loop but that the RMS would be in complete control of the payload during docking or undocking with the payload/orbiter interfaces on the handling aid mechanism.

The resulting aid concept, depicted in Figure 1, known as the PIDA (Payload Installation and Deployment Aid), is presently being fabricated as flight-like hardware for engineering development test and evaluation in the JSC Manipulator Development Facility. This effort is intended to develop the aid concept to a state of readiness for a minimum lead time for flight hardware and at the same time developing the electromechanical actuator and the docking mechanism for potential use in other applications.

REQUIREMENTS

The basic requirements that were imposed on the Payload Installation and Deployment Aid concept are:

- Provide line of sight docking points outside of critical maneuvering area.
- Utilize single point capture steps as opposed to multi-points requiring simultaneous capture.
- Use mechanism to move the payload from deployed to stowed position without exceeding a 75mm (3.0 inch) payload clearance envelope.
- Accommodate payloads ranging up to 4.57 meters (15 ft) dia by 18.3 meters (60 ft) long and 289 kN (65,000 lbs) weight.
- Accommodate payload contact velocities up to 30mm/sec (.10 ft/sec) and .011 rad/sec with a lateral mismatch of 150mm (6.0 inches) maximum and angular mismatches of $\pm 15°$ in pitch and yaw and $\pm 10°$ in roll.
- Design to stow in a confined space under the closed doors with a large payload in the cargo bay.
- Utilize existing longeron bridge fitting attachments for structural connection.

PIDA ASSY DESCRIPTION

The PIDA assembly shown in Figure 6 is made up of a deploy/stow mechanism, an interface mechanism, an electromechanical rotary actuator with its respective electronic controls, and a base, with a jettison interface, that connects the assembly to the Orbiter longeron bridge fitting on installation.

The operation of the assembly between the stowed and deployed positions, shown in Figure 7, is done remotely from the RMS operator's station. The operator can select the degree of deployment desired and monitor its position from a display of the optical encoder data that is used to control the drive motors and keep them synchronized to within one-tenth of a degree. Preprogramming for a specific payload provides the control of the master drive to accelerate and then decelerate the payload to stop at the desired point without overrun or excessive structural loads on the PIDA structure or the Orbiter longeron attach points. The accuracy provided by the control system offers precise pointing of payloads and opens the possibility of limited tracking using the PIDA drive system with added tracking sensors.

DEPLOY/STOW MECHANISM

The basic purpose of the deploy/stow mechanism is to control the movement of the payload positively and accurately between the stowed and deployed positions and to locate the payload in a deploy position that is away from the Orbiter, outside of the critical maneuvering area but with the docking interfaces in the line of sight of the RMS operator. Design guidelines required that the movement between the stowed and deployed positions be provided without exceeding a 75mm (3.0 inches) payload clearance envelope and that the deployed position be located for a minimum clearance of 50cm (19.5 inches) between the payload and the Orbiter. The configuration had to permit the mechanism to be stowed in a confined space under the closed door and radiator with a large payload 4.57 meters (15 feet) diameter by 18.3 meters (60 feet) long in the payload bay.

The original version of the present deployment mechanism employed a two-stage actuation as shown in Figure 3. The first stage used a pivot point close to the tangency of the payload on one side for an upward z-z axis path of withdrawal and the second stage utilized a pivot point at the docking mechanism interface to swing the payload outboard to a noncritical maneuvering area for payload/PIDA docking. The two stages were driven from a single actuator on each arm assembly that required a clutching operation for the change over from one stage to the other.

Due to the complexity of the two-stage actuation, a single actuator drive mechanism, shown in Figure 4, with a continuous integrated motion was conceived to replace it while at the same time closely approximating the motion desired. A trial and error graphical approach was used to define the mechanism necessary to provide the desired motion. At the onset, the graphical layout was intended to identify the constraints for an analytical approach but it was concluded that the graphical approach would be quicker to complete the geometry definition.

The four bar mechanism shown in Figure 5 has a tubular drive arm member that is connected at one end to the base and the other end to the crank arm on the interface mechanism. A drag link that serves as a tension/compression tie between the base and the end of the crank arm provides the linkage to turn the crank arm as the main arm is driven from one position to another by an Electromechanical Rotary Actuator. As the main arm rotates through an angle of 56°, the crank arm rotates the interface mechanism 102°37' for an angular displacement ratio of 1.83:1. The total rotation of the payload axis relative to the Orbiter axis is the sum of these two angles or 158°37'.

Note in Figure 4 how the initial part of the C.G. path approximates an upward (z-z axis) linear withdrawal by a low amplitude sinusoidal movement. The movement of the longeron trunnion next to the mechanism, shown in detail "Z", provided an upward and outboard movement that although unplanned was found to be acceptable in the mating envelope of the retention fitting halves.

INTERFACE MECHANISM

The payload/PIDA interface mechanism, shown in Figures 8 and 9, includes a docking mechanism for the RMS operator to connect or disconnect the payload from the deploy/stow mechanism and a structural connection to positively hold the payload during deploy or stow actuation to aid accurate positioning of the payload in the payload bay. After the payload has been placed in the fully stowed position, the structural connection through the PIDA is loosened to provide compliance in order to force the retention fittings to be the primary load paths. The mechanism provides the basic functional modes of docking, such as, compliance, capture, energy absorption, alignment and rigidization in addition to the stowed position compliance.

Docking Compliance

The purpose of docking compliance is to allow the two mating sides of the interface to align in order that the capture latches can operate. The mechanism on the active side of the docking interface moves as required for alignment except for lateral compliance.

The lateral compliance and attenuation is not an active part of the mechanism, but is accommodated by the dynamics of the Orbiter and payload interreactions.

The axial compliance and attenuation, both compression and extension, is furnished by a hydraulic-type attenuator that has internal spring action to return it to a nominal position that is preloaded in both directions.

The roll alignment movement is permitted by the outer part of the ring and guide assembly being free to rotate relative to the center part of the assembly. The two parts are connected through two ball bearings and are spring loaded to a nominal position by the spring preload.

The pitch and yaw compliance is provided by a "U" joint located between the center of the interface ring and the attenuator assembly.

Docking Capture

The guides on the interface ring are sized for 152mm (6.0 inches) lateral misalignment (which includes the mismatch due to $\pm 15°$ pitch or yaw) in combination with a roll misalignment of $\pm 10°$. The guide configuration provides lateral forces to act on the Orbiter and payload for dynamic lateral compliance to permit the capture latches to engage. The capture latches are designed such that, if insufficient latches are engaged to react capture loads, none will remain engaged. Any two latches are able to react the capture loads. If only

one latch is engaged, the force vectors act in a direction upon the latch during a separation motion such that the toggle linkage of the latch will collapse to allow the two docking surfaces to separate freely. The capture latches serve a dual role in as much as they are also used as the structural latches to secure the payload to the Orbiter after the docking phase is complete.

Energy Absorption

A payload with kinetic energy relative to the Orbiter, contacts the docking interface causing the attenuator assembly to be compressed. During this compression stroke, hydraulic fluid is metered from the head end to the rod end of the attenuator. Part of the kinetic energy is dissipated by the fluid metering and the remainder is stored in the attenuator spring as potential energy. At the end of the compression stroke, the spring forces the attenuator to extend toward the nominal position transferring the potential energy back into the payload as kinetic energy. During this extension stroke, the fluid is metered from the rod end to the head end of the attenuator, further dissipating energy. As the attenuator reaches its nominal position the attenuator spring reverses its force direction to once again store the undissipated energy as potential energy. The residual energy is dissipated by the subsequent extension and compression strokes with rapidly decaying amplitude so that ultimately all motion is arrested and the interface returned to the nominal position.

Alignment and Rigidization

Roll, pitch and yaw alignment across the interface is provided by the ring and guide assembly on each side mating with the one on the other side of the interface. This allows a payload to be positioned accurately even in installations employing only one PIDA assembly.

Realignment of the ring and guide assembly on the active half of the docking interface, with its mechanism is accomplished by the use of three pusher rods and a cable drive system. The action of taking up cable slack in three cable assemblies forces the three pusher rods to extend to a nominal position and retracts the active ring and guide assembly in contact with the ends of these pusher rods for alignment and rigidization. The ends of these rods are hemispherical and contact a conical seat on the surface of the other part of the interface ring to provide the camming action necessary to realign the ring in roll, pitch, and yaw. Actuation is provided by an electromechanical actuator driving a cable drum through a gear train. The electric motor has a brake that is energized to hold the mechanism rigid after the drive motor has stalled out, to preload the cable assemblies, and is then turned off.

The holding requirement of the mechanism is based on an interface moment of 678 N-m (500 lb-ft) as determined from dynamic analysis of the payload/Orbiter system using math modeling.

The inside of the cable drum has two cam surfaces located symmetrically opposite each other to actuate two cam followers, one on each side of the attenuator, to force it to a centered position or free it to allow the attenuator to pivot during the stowed position compliance movement. In the upper

half of Figure 9 the attenuator is held centered and the lower half of the view shows the cam surface away from the cam follower to allow the attenuator to pivot.

STOWED POSITION COMPLIANCE

The payload retention system requires that the payload be permitted to have a three axis movement to accommodate thermal deflections. This necessitated that the PIDA have the same freedom if it is not to act as a primary structural connection for a stowed payload. The x-x axis freedom is provided by floating one of the passive docking interfaces on the payload with it being spring loaded to a center or nominal contact position. The y-y axis and z-z axis movement is provided by retracting the three pusher rods to allow the attenuator to stroke and backing off the two cam followers to permit the attenuator to pivot in the y-z plane.

ELECTROMECHANICAL ROTARY ACTUATOR

The electromechanical rotary actuator designed and fabricated to drive the deploy/stow mechanism was sized to provide a maximum torque of 1356 N-m (1000 lb-ft) at a rate of one degree per second. This is accomplished through the use of a gear box with two high ratio planetary drives, a 24/1 input stage and a 32/1 output stage, resulting in an overall ratio of 768/1 for the actuator in conjunction with a 5.4 N-m (4.0 lb-ft) 28 volt direct current electric motor.

CONCLUSIONS

The Orbiter baseline configuration does not include the PIDA handling aid concept. Further test and evaluation both on-earth and on-orbit will be required to resolve the need for a handling aid to assist the Remote Manipulator System (RMS) on the Orbiter.

Tests results on prototype hardware indicate that the PIDA payload handling aid concept can be of significant help to the RMS operator by relaxing the control requirements and promises to enhance payload bay packaging density and payload maintenance access.

Initiation of the development of the PIDA concept has been effective in reducing the long-lead time required for flight hardware. A continuation of this development will provide hardware that with minimal changes could be flown as an on-orbit experiment with a RMS and a test payload to evaluate the overall payload handling capability of the Orbiter.

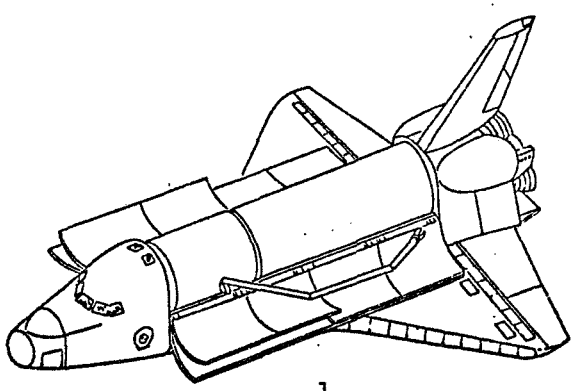

1

RETENTION FITTINGS UNLOCKED TO RELEASE PAYLOAD & PAYLOAD/PIDA INTERFACES RIGIDIZED (MANIPULATOR MOVED CLEAR OF PAYLOAD)

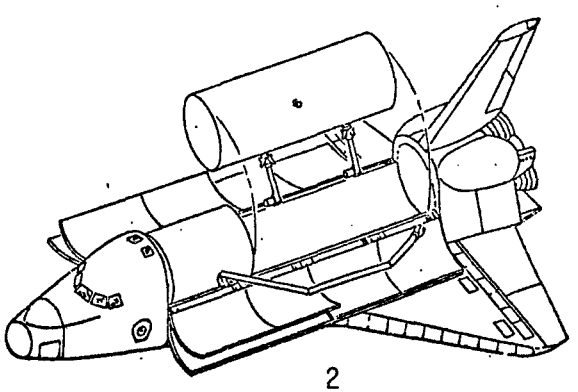

2

SYNCHRONIZED DRIVE ARMS ROLL PAYLOAD OUT OF BAY TO FULLY DEPLOYED POSITION

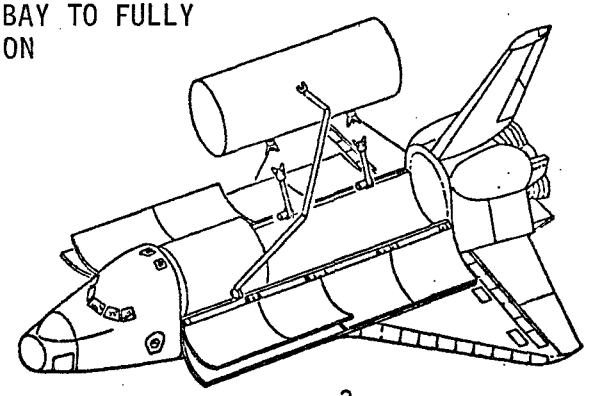

3

PAYLOAD GRAPPLED BY MANIPULATOR, PAYLOAD/PIDA INTERFACES UNDOCKED & PAYLOAD POSITIONED FOR RELEASE

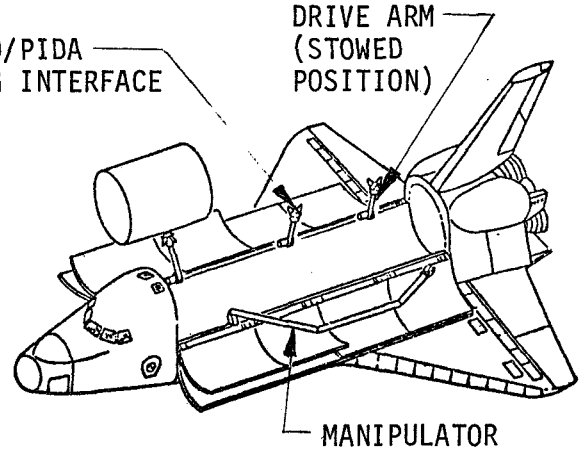

4

REPEAT STEPS 1 & 2 TO HOLD PAYLOAD FOR POINTING, INFLIGHT MAINTENANCE ACCESS OR ORBITAL ASSEMBLY

FIGURE 1
DEPLOYMENT SEQUENCE

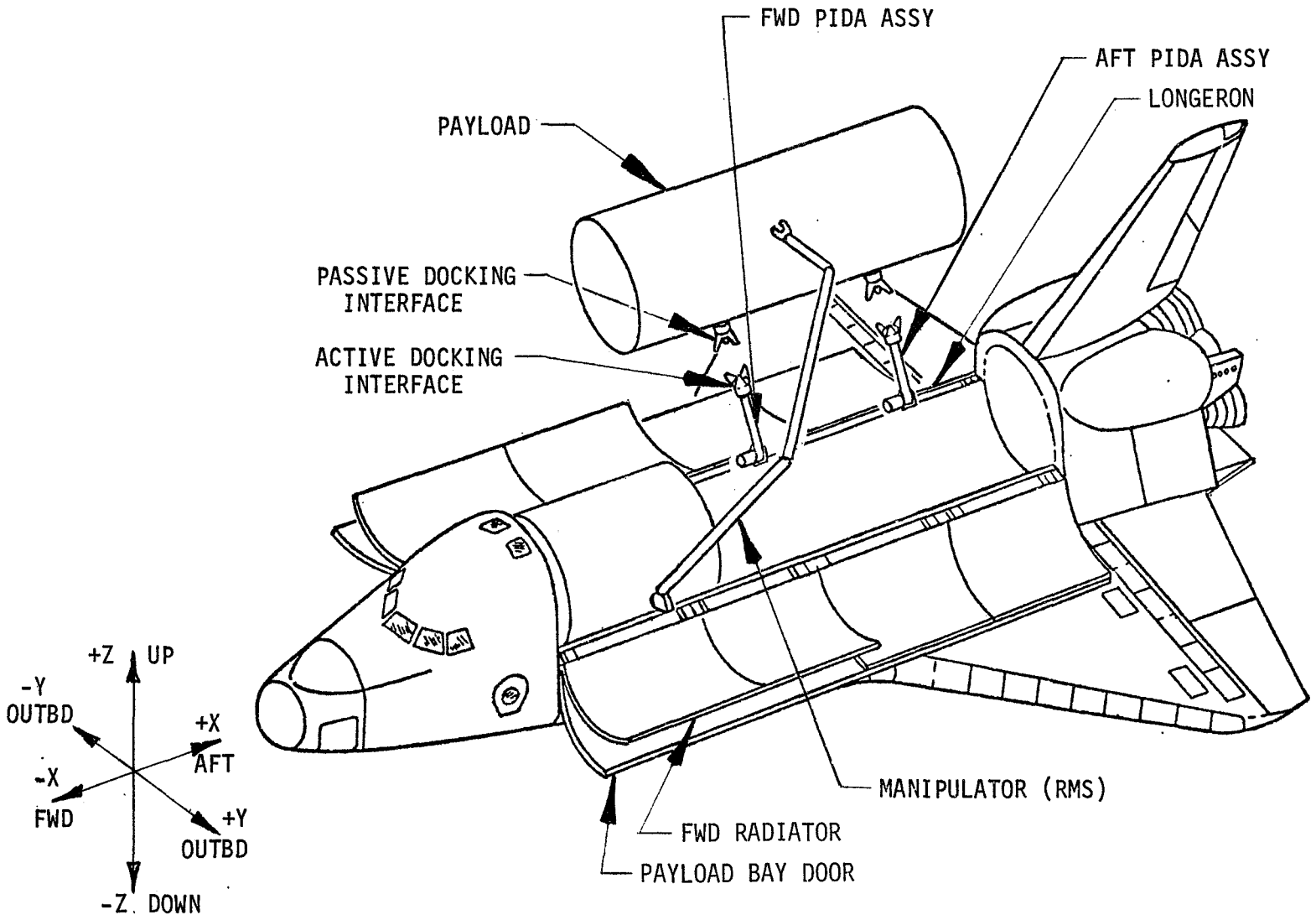

FIGURE 2
NOMENCLATURE

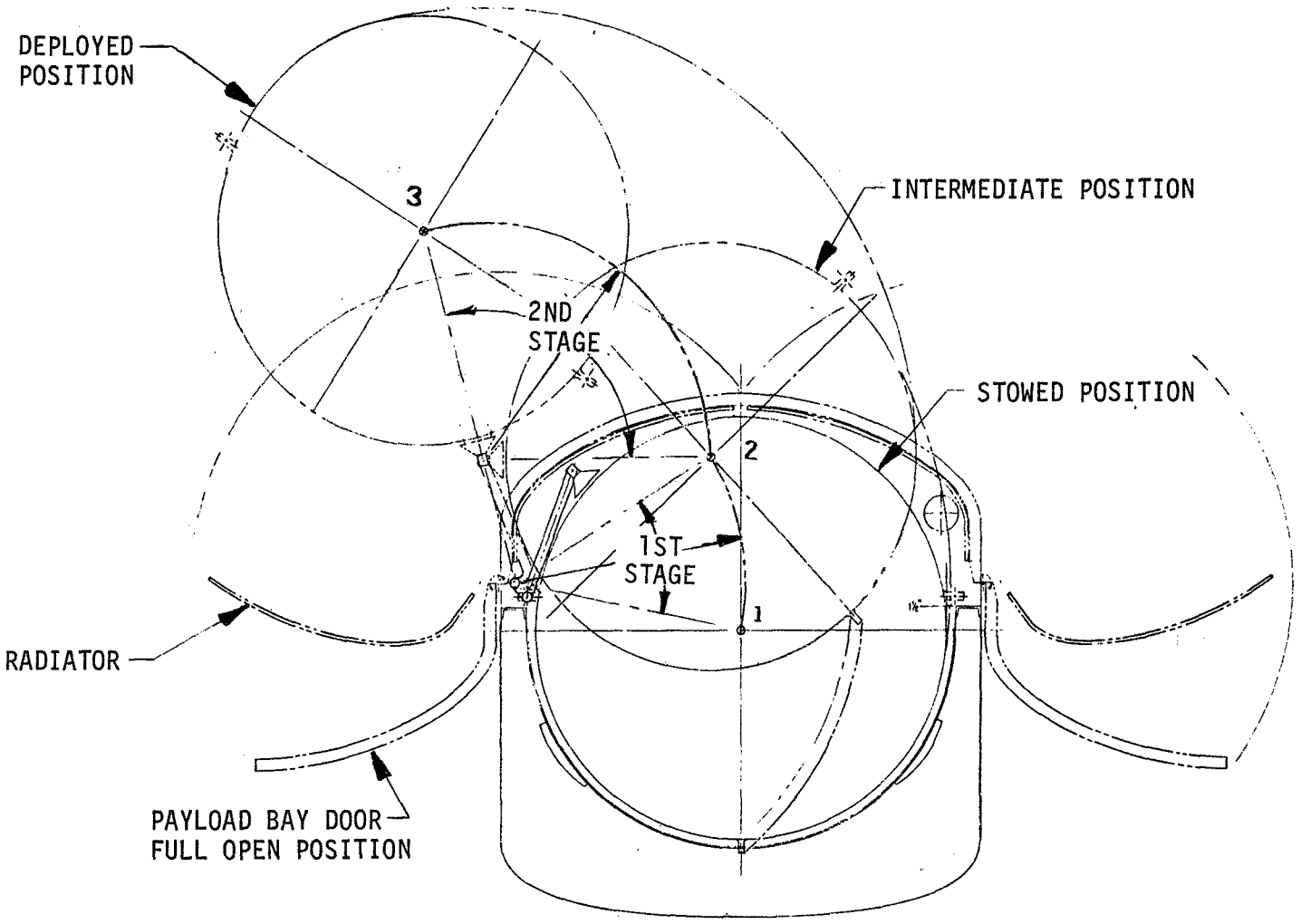

VIEW LOOKING AFT

FIGURE 3
2 STAGE DEPLOY/STOW ACTUATION

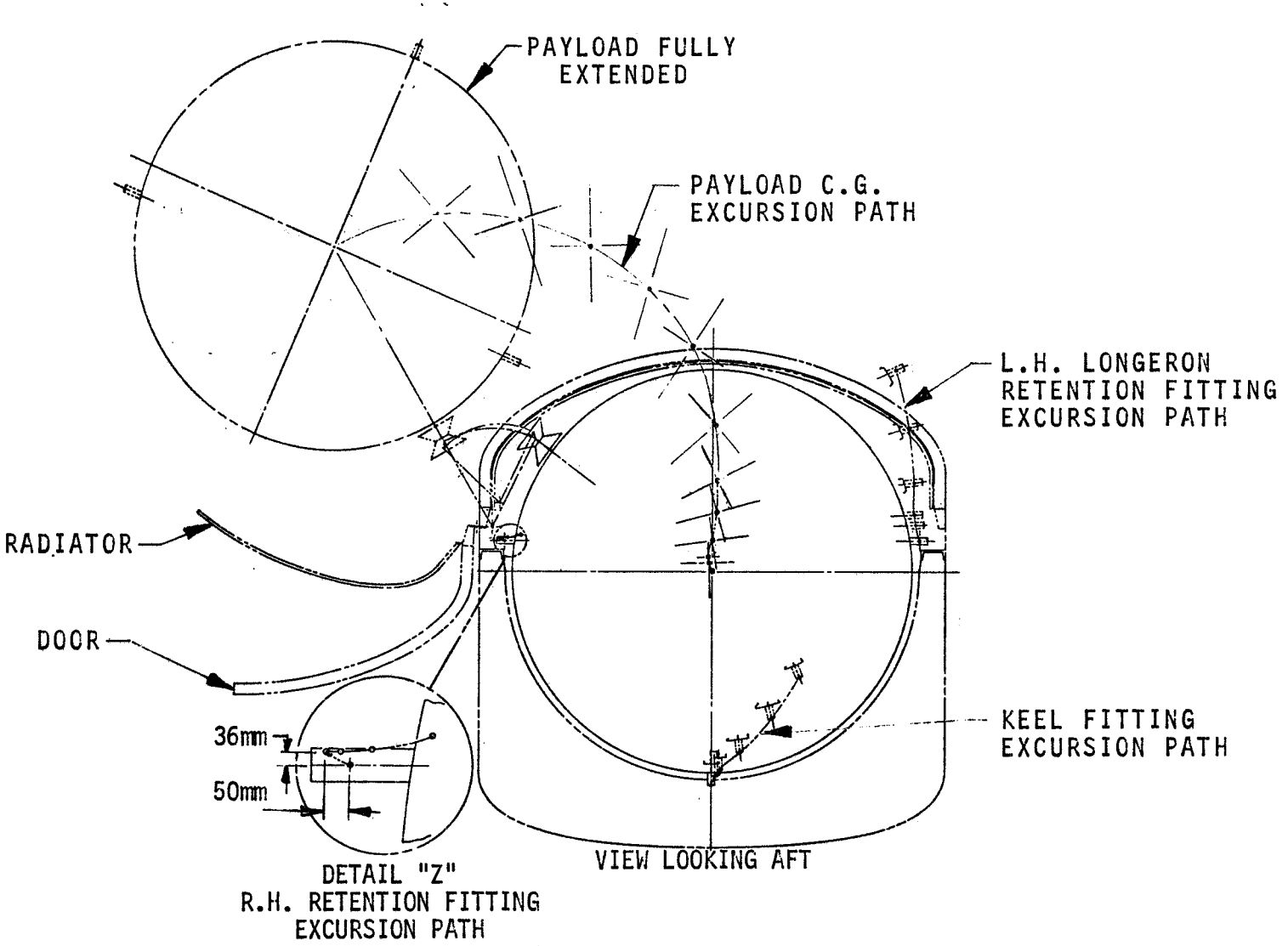

FIGURE 4

SINGLE STAGE DEPLOY/STOW ACTUATION

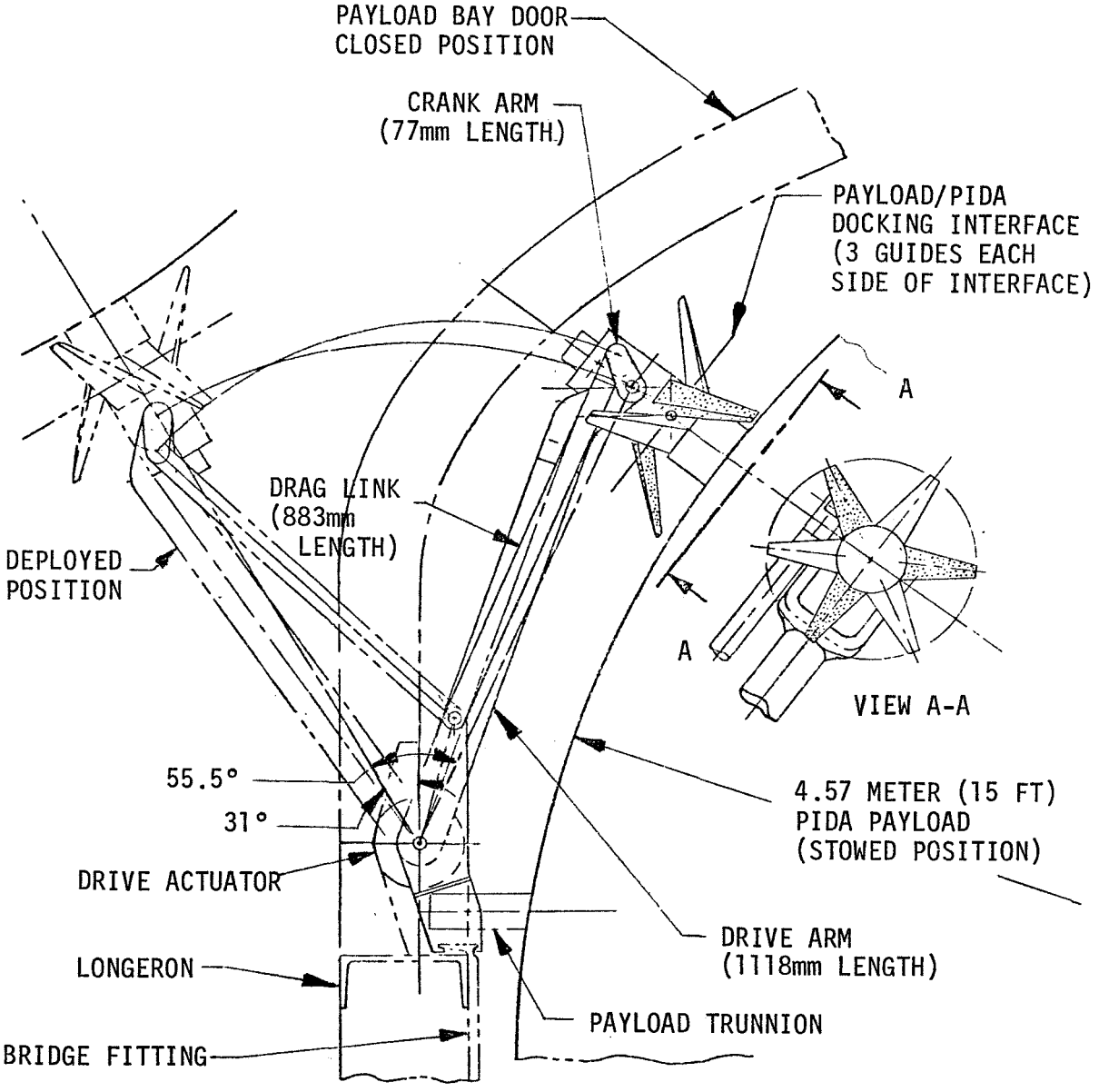

FIGURE 5
DEPLOY/STOW MECHANISM

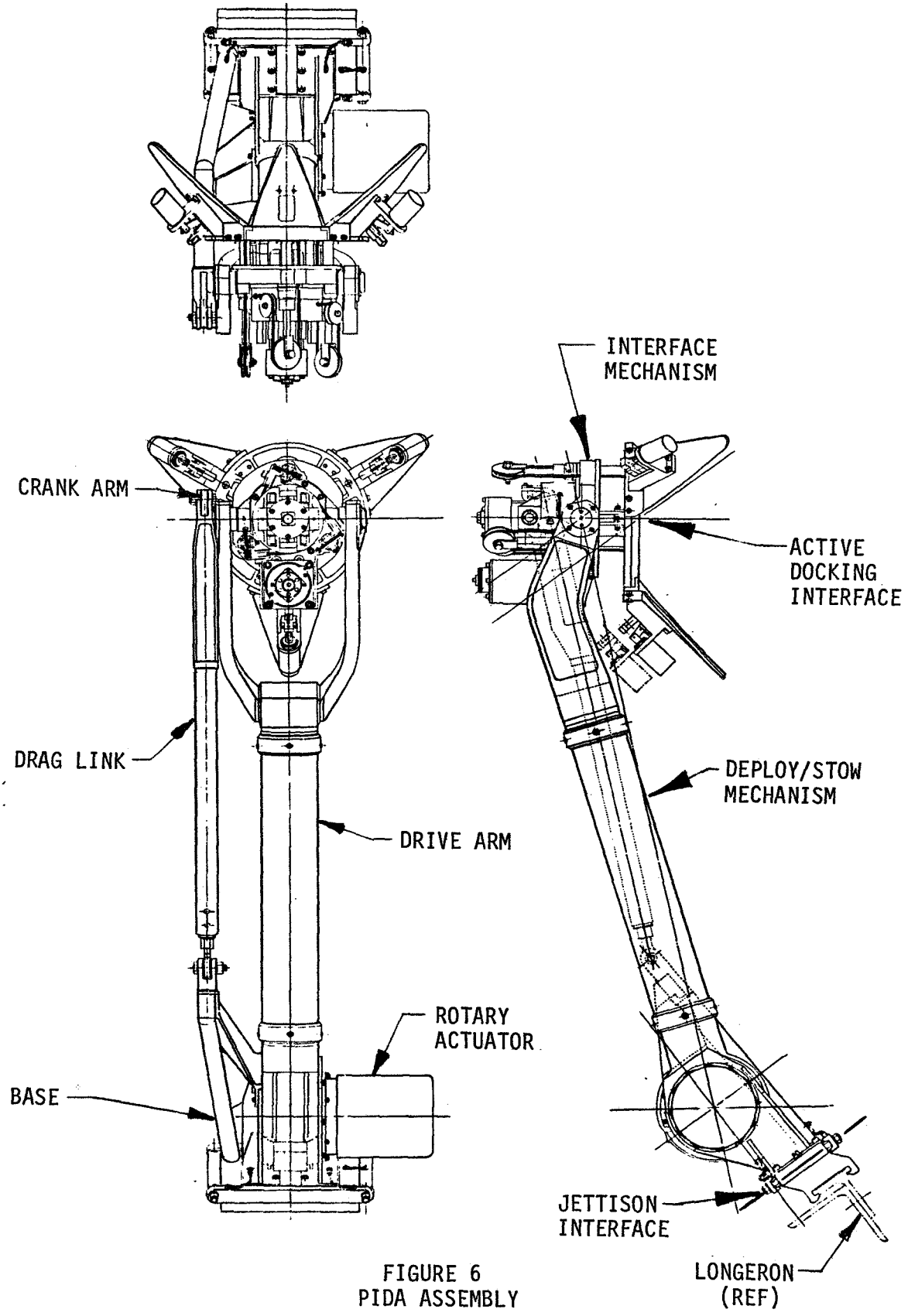

FIGURE 6
PIDA ASSEMBLY

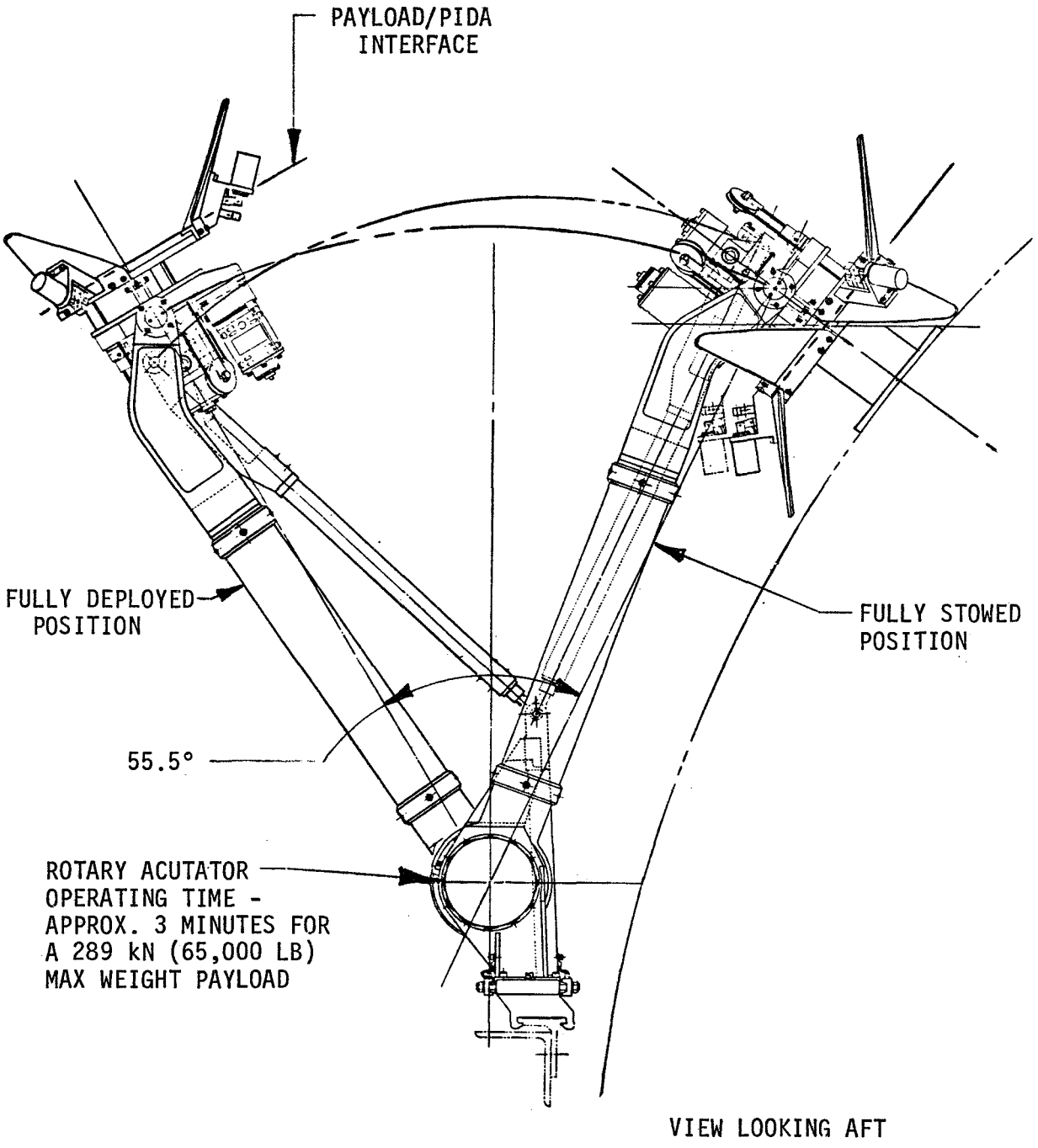

FIGURE 7
PIDA ASSY
OPERATING POSITIONS

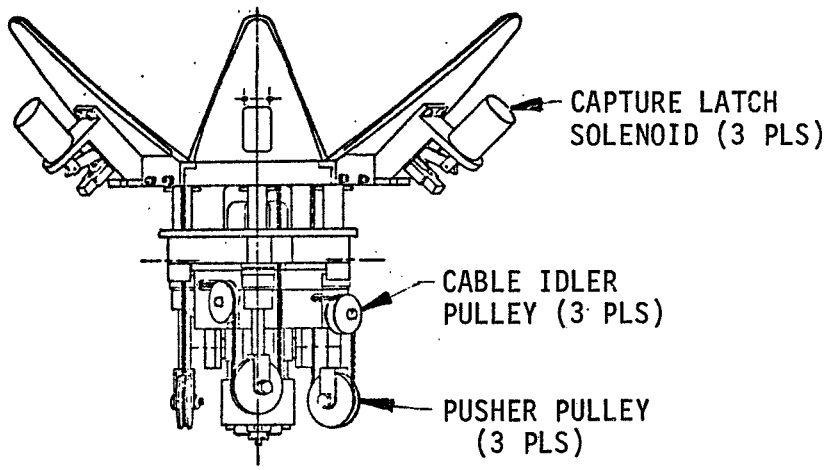

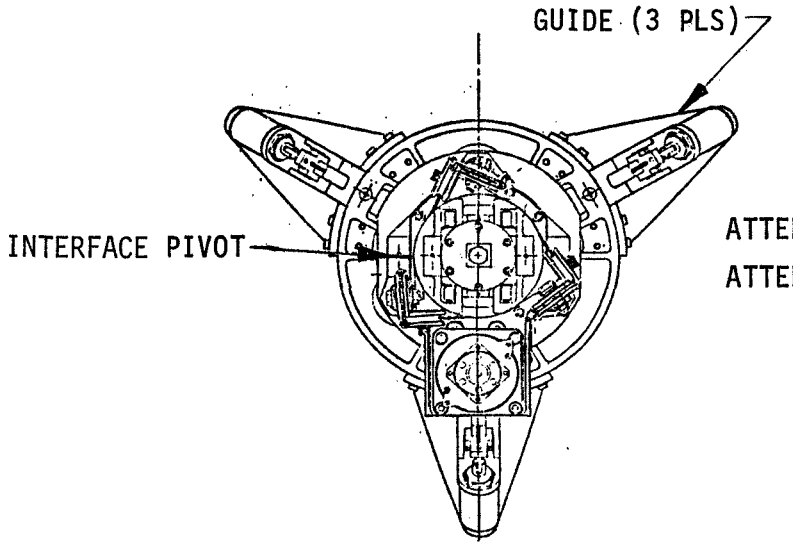

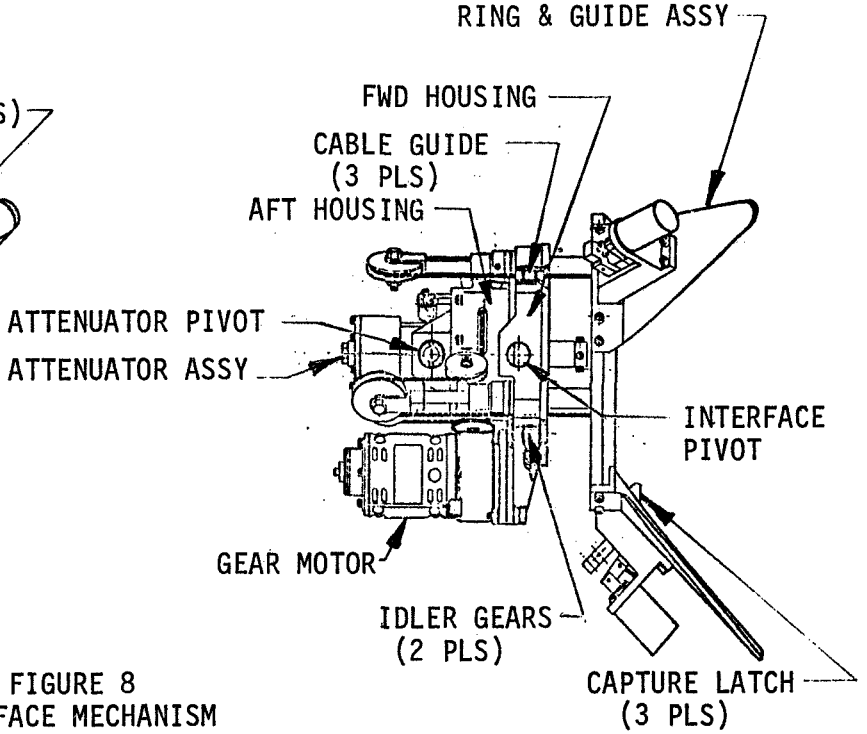

FIGURE 8
INTERFACE MECHANISM

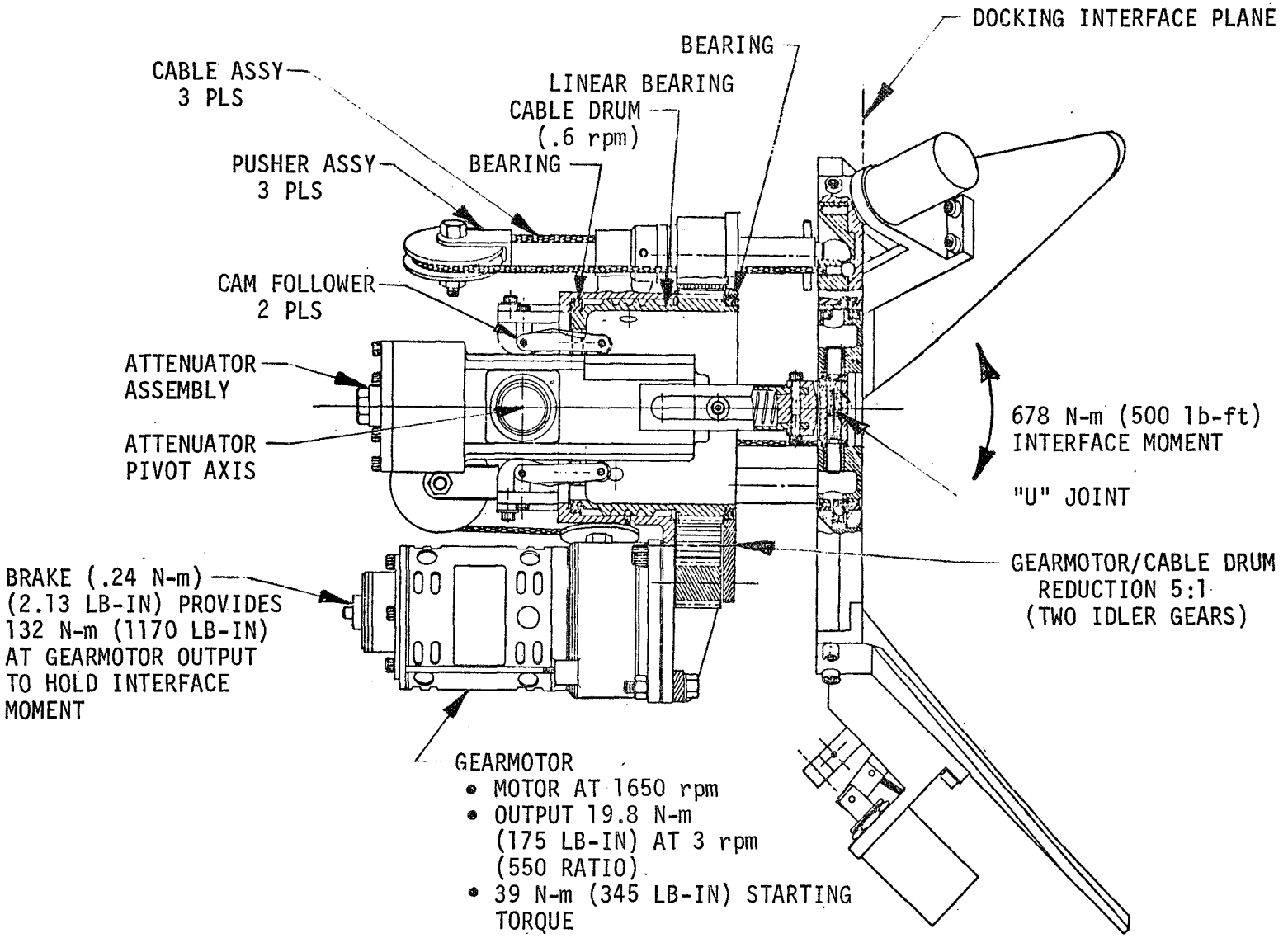

FIGURE 9
INTERFACE MECHANISM

SPACE SHUTTLE ORBITER AFT HEAT SHIELD SEAL

L.J. Walkover*

ABSTRACT

An intriguing assignment in the design of the orbiter has been the development of the aft heat shield seal (AHSS). It is a structure and mechanism at the three main propulsion system (MPS) engine interfaces to the aft compartment structure. Access to each MPS engine requires disassembly and removal of the AHSS. Each AHSS accommodates the engine movement, is exposed to an extremely high temperature environment, and is part of the venting control for the aft compartment. This paper discusses the baseline design, various improvements for engine access, and technical problem solutions.

INTRODUCTION

The Space Shuttle system orbiter vehicle is being developed as a "space truck" to deliver large and heavy payloads to space. This paper discusses the evolution of the orbiter AHSS design, which involved advancing mechanical seal technology in a severe thermal environment.

The orbiter structure is divided into separate compartments. The three MPS engines are located at the orbiter aft end; they are installed partly in and form part of the aft compartment enclosure. The three AHSS's are a major factor in the structural integrity of the aft compartment. Compartmentation is used to minimize compartment pressures and loads generated during ascent venting and descent repressurization. Excessive seal leakage or failure could cause increased pressures and possible failure of other aft fuselage structures, i.e., the X_o 1307 bulkhead.

Each AHSS is both a structure and mechanism at the three MPS engines interfaces to the aft compartment structure (Figure 1). Each AHSS consists of a stationary conical dome heat shield fastened to the base structure, a hemispherical engine heat shield mounted on and moving with the engine, and a seal mounted to the dome heat shield. The seal bears against the engine heat shield and accommodates the relative movement between the two heat shields (Figure 2). The seal mechanism, whose mean diameter is 210 centimeters (7 feet), is basically two assemblies—the sliding and flexible seals. The sliding seal accommodates the engine gimbaling, and the flexible seal accommodates the forward motion between the engine and compartment structure. For the baseline design, access to an MPS engine for maintenance or line replaceable unit (LRU) removal requires the disassembly and removal of the seal components, removal of the dome heat shield halves, and removal of the engine heat shield halves. The remaining base structure opening, 265 centimeters (106 inches) in diameter, is adequate for engine installation clearance.

As the AHSS baseline design was developed, the MPS maintainability requests matured and became more definitive. In addition, the thermal environments and the dynamic loads were

*L. J. Walkover is Manager of Structure Design for the Space Shuttle Program at the Rockwell International Space Systems Group in Downey, California.

increased. Concern was expressed with respect to engine turnaround time. The thermal, structural, and turnaround time concerns became the basis for AHSS improvement studies, which were to include baseline redesigns as well as new design concepts. This paper discusses the baseline design, the various improvement studies, and the technical problems that were overcome.

BASELINE REQUIREMENTS

The AHSS was designed according to the requirements listed below. Orbiter control requires the large engine gimbal angles. The thrust structure reacts the engine thrust and compresses under loading. The engine, therefore, moves forward relative to the base structure. Structure fabrication tolerances, structure deflection, engine and dome heat shields installation tolerances—all require additional seal design compensation. The reversible pressures limit design solutions. The seal venting area must be controlled to the limits shown. The upper and lower temperature limits decree the use of high-temperature materials for the engine heat shield and the seal. The engine access is to be as readily accessible as possible. A multiuse request of 100 flights is the goal.

- MPS engine gimbal angles
  $\pm 11^{o}$ pitch, $\pm 9^{o}$ yaw } $\pm 14^{o}$ corner
- Movement, deflection, and tolerances
  Engine forward movement = 5.5 cm (2.2 in.)
  Structural deflection, Installation tolerances } As defined
- Delta pressure
  +7.75 kg/cm^2 (+2.65 psi) burst
  -3.86 kg/cm^2 (-1.32 psi) crush
- Allowable venting area
  58.5 cm^2 (9 in.^{2}) per engine
  175.5 cm^2 (27 in.^{2}) total (per orbiter)
- Temperature
  871^{o}C (1600^{o}F) design—external
  177^{o}C (350^{o}F) design—internal
- Acoustics
  164 dB
- MPS engine access
  As readily as possible
- Multiuse
  100 flights (goal)
- Minimum weight/cost

BASELINE DESIGN

The AHSS baseline design (Figure 3) was developed in accordance with the baseline requirements. The seal design was limited by the space that could be made available between the dome and engine heat shields as defined by the engine movements. The baseline design was utilized only on the main propulsion test article (MPTA) vehicle.

As noted, the seal is the mechanism between the two heat shields. It consists of the sliding and flexible seals. The sliding seal is a series of graphite blocks held in a retainer ring with 48 spring cans that are uniformly spaced about the periphery and exert pressure on the graphite blocks to slide and seal against the engine heat shield spherical surface. The dome heat shield provides support and reaction to the spring cans. The sliding seal/retainer ring is held in posittion by three articulated links anchored to the dome heat shield. The links allow the sliding seal to follow the engine heat shield's forward translation as the engine thrust builds up. The ring stiffness is tailored so that it can distort momentarily to a noncircular, nonplanar shape as the links pass over center at the midpoint of the forward motion.

The flexible seal materials must be capable of operating in a high-temperature environment. The materials, especially the silica fabric, cannot tolerate excessive wrinkles. The silica fabric encloses the thermal insulation, the glass fabric pressure seal/structure, the polyimide film for the pressure seal backup, and Inconel mesh for lightning protection. The entire assembly is sewn together by quartz thread (Figure 4).

The flexible seal has a unique design to cope with the reversible pressures (Figure 5). Under positive or burst pressure, the flexible seal cross section is radial to provide hoop tension forces between the load reaction pivot attachments at the dome and engine heat shields. Under negative or crush pressure, flexible seal circumferential elements are circular and provide complete hoop tension forces. The design has a controlled shape, is properly supported at the edges, and requires only slight flexures–which results in minimum wrinkling and no shape reversals.

Seal disassembly requires a lacing disengagement at the flexible seal vertical meridian splices, structural disconnection of the retainer ring, and a folding back of the flexible seal to unbolt it from the dome heat shield's circumferential joint. The individual spring cans are then removed as opposite pairs to balance out the spring forces. After all the spring cans are removed, and the stabilizing links are disengaged, the flexible seal and the retainer ring/graphite blocks are removed as two individual assemblies.

The dome heat shield is bonded aluminum honeycomb with reusable surface insulation (RSI) tiles on the outside and thermal insulation blankets on the inside. It consists of two half-cones structurally joined by bolts at the vertical meridian splices. A row of outer peripheral bolts attaches the dome heat shield to the base structure. Additional bolts are used to attach the RSI tiles at both the meridian and peripheral joints.

The engine heat shield is a spot-welded, Rene 41 honeycomb assembly protected by a thermal coating (Pyromark) on the outside and thermal insulation blankets on the inside. It consists of two spherical segments that are structurally joined by dual rows of bolts at the vertical meridian and by a row of bolts at the heat-shield-to-engine-nozzle inner peripheral joint.

IMPROVEMENT STUDIES

Various studies were undertaken to improve both the structural and maintenance aspects of the AHSS design. The studies included new concepts as well as revisions of the baseline design.

Design

A "roman tunic" design with overlapping steel plates or sheaves was attached to a dome heat shield and slid on the hemispherical engine heat shield, but the large positive and negative differential pressures and the engine's forward movement during firing made the design impossible. Utilizing a "quarter segments" design instead of half segments to remove specific LRU's did not improve maintenance and added weight.

The "flexible curtain" concept consisted of a high-temperature flexible material (similar to the baseline flexible seal) attached to both the base structure and the engine nozzle. Its conical length allowed engine gimbal action, and the design was extremely appealing because it was visualized as

two half panels fastened together at the meridian splices and at the base structure and engine nozzle peripheral joints. However, it was dropped because the shape could not be controlled and the excess material required in the conical length created wrinkles and folds that the material could not tolerate.

The "conical bellows" was another appealing design that did not work. It was a steel, cone-shaped bellows attached to both the base structure and the engine nozzle. The design was visualized as either a two-part or a single assembly. It did not work because the cone configuration was too short for the bellows' angular motion. Also, there was no known way to design a meridian split in the bellows to allow installation on the engine. Preassembling the bellows on the engine nozzle before the nozzle was attached to the engine was impractical.

Several designs of "cylindrical bellows" were investigated but the size required—inner diameter of 265 centimeters (106 inches)—to slip over the engine nozzle and the length required to allow angular motion made them too heavy.

The "external engine-mounted heat shield" reversed the baseline engine heat shield and dome heat shield locations. The engine heat shield was aft of the dome heat shield for easier removal—especially advantageous for specific LRU removal. But it would not work because there was not enough room for the engine heat shield gimbal action relative to the back end of the orbiter.

A ground support equipment (GSE) "restraint device" for locking each baseline spring can to the dome heat shield was designed but not used. The advantage was that the spring cans did not have to be dismantled from the seal. The disadvantage was that the flexible seal still had to be folded over and disconnected from the dome heat shield to allow insertion of the restraint device on the spring can.

The "lock-out device" is a design improvement that was incorporated (Figure 6). The lock-out device is a GSE tool that is inserted through the RSI tile and the spring can to lock the spring can to the dome heat shield. Its advantage is that the seal does not have to be dismantled. The disadvantages were minor. The revised access procedure is to lock the seal to the dome heat shield, disengage the lacing and disconnect the retainer ring at the seal meridian splices, disconnect and remove the dome heat shield (plus seal) in two major assemblies, and disconnect and remove the engine heat shield in two halves.

Engine Accessibility

Access requirements for each engine were incrementally defined by Rocketdyne and Kennedy Spacecraft Center (KSC) throughout the later portion of the design phase. The engine power head is to be inspected and the turbopumps are to be internally inspected and torqued after each MPTA firing and after each research and development (R&D) flight. The sequence thereafter occurs after every 12th operational flight. There are planned replacements for the major engine components (fuel and oxidizer pumps, nozzle, and total engine replacement) during the MPTA firings, but none is planned through R&D and operational flights. An exception is the replacement of the total engine after every 55th operational flight.

Further maintenance studies disclosed that the engine power head could be inspected from within the aft compartment without removing the AHSS. However, the KSC maintenance studies

for pump access indicated advantages for a local hole with a removable cover (access port) in the engine heat shield for pump internal inspection and torquing. KSC could also accept the planned (every 12th operational flight per engine) pump torquing and inspection by removal of the AHSS, since it would not impact the turnaround time line. Unplanned contingency pump torquing and inspection could be a time line problem.

The access port design improvement was not initially utilized because there was no strong KSC requirement. Also, the access ports could not be designed into the baseline engine heat shield, which was made of Rene 41 material. The access port design required an edge member whose heat sink problem, when combined with the other engine heat shield thermal problems, could not be solved for the thermal gradients in and across the structure.

Joint Attachments

Joint attachment improvement studies were done on joints whose disassembly was required for removal of the AHSS. The improvements were to decrease the number of bolts, combine structural and thermal protection system (TPS) bolts, and utilize quick-action Milson fasteners. These fasteners were dropped in favor of power-driven tools for bolts. There were 14 studies in all whose joint improvements, if utilized, would decrease maintenance time (Figure 7).

The use of lock-outs halted the single improvement study for the flexible seal attachment to the dome heat shield. Two dome-heat-shield-to-base-structure studies were stopped when the base structure was installed on Orbiter 102 because changes to the base structure or RSI tiles on the base structure would severely impact tooling, manufacturing, and the tile subcontractor. Four dome heat shield meridian splices were studied. One concept was incorporated into the dome heat shield being redesigned for the improved spring-can angular offset problem. Three engine-heat-shield-to-engine peripheral joints were studied. No improvement could be made because of a thermal problem in this area. Four engine heat shield meridian joints were studied. The design improvement was a fallout of the solution to a thermal problem. These three problems and others are discussed below.

PROBLEMS AND SOLUTIONS

The engine heat shield, the seal designs, and the maintenance improvement studies were repeatedly interrupted by the need to solve various design problems (Figure 7).

Seal Loading

Thermal distortions, structural deflections, and manufacturing tolerances (outer shell, thrust structure, dome heat shield, engine heat shield, and engine installation) were greater than originally anticipated and resulted in inadequate seal loading. The angular offset of the seal cans (Figure 3) could not provide adequate sealing forces, nor could the major assembly tooling control the problem.

Figure 8 is the spring geometry and force diagram for the spring can installation. It indicates the problem that arises if the engine heat shield is located too far aft relative to the dome heat shield. Dimension (B) must always be reasonably positive to guarantee that the spring cans impose a positive sealing force (C) by never being on or near center.

Table I summarizes all tolerances and deflections for the baseline design and the design fix. The nominal spring offset (A) (Figure 8 and Table I) was increased from 2.11 to 4.000 centimeters (0.833 to 1.600 inches). All manufacturing tolerances for the aft fuselage assembly and dome heat shield were literally tooled out at the seal detail installation. Nothing could be done about the engine heat shield and engine installation tolerances and the various deflections. The result was that dimension (B) minimum (Figure 8 and Table I) was increased from +0.273 to +2.998 centimeters (+0.109 to +1.199 inches).

The increased spring-can angular offset required revision of the dome heat shield aft end to allow the spring can's outer pivot point to be relocated further aft without being moved inboard (Figure 6). The redesign of the dome heat shield and spring cans was combined with two improvements previously described: lock-out device and dome heat shield meridian splice. The manufacturing tolerances were minimized by a special tool that duplicated the engine centerline at null position. It also defined the location of the dome heat shield structure trim lines and seal components—all in the correct position relative to the engine. In effect, the seal installation was customized for each actual engine location. This tool is used by both manufacturing and field operations to define the null position of the engine centerline for rigging purposes, and by manufacturing for seal component assembly.

Thermal Considerations

MPS engine plume heating is the largest heating source of the adverse thermal environment. The latest thermal data update indicated increased heating rates (Figure 9) with the maximum heat load at 420 seconds. The temperatures are as high as 882°C (1620°F) in local areas between the engines. The problem is now the high temperature, the temperature gradients both in plane, through the thickness gradient, and in the circumferential gradient. In addition, engine dynamic loads on the engine heat shield became a problem at the engine-heat-shield-to-engine peripheral joint.

Design fixes were required for the engine heat shield meridian joints to increase joint capability for thermal stresses. A joint improvement fall-out was the reduction in the number of bolts. A design fix of the engine-heat-shield-to-engine peripheral joint was required by the increased thermal stresses and dynamic loads. This problem nullified any joint attachment improvement.

The incompatibility (high temperature, gradients too severe across the seal area) of the graphite sliding seal with the Rene 41 honeycomb engine heat shield was solved by changing the engine heat shield material and the sliding seal design to decrease the graphite seal thermal mass (Figure 10).

The engine heat shield was redesigned to be made of Inco 625, which does not exhibit the brittle failure characteristics of Rene 41. Instead, it yields at relatively low stress levels with good elongation, so that the thermal stresses that are above yield and in the plastic range are self-relieving. Since there is no known thermoplastic analysis method for spherical shapes like the engine heat shield, certification must be accomplished by test. Inco 625 at the 882°C (1620°F) maximum operating temperature yields and retains some permanent strain. Repeated exposures result in accumulated strain, which appears as intracell wrinkling of the heat shield face sheets during each flight and a gradually increasing wrinkle amplitude as the flights are repeated. To obtain the maximum wrinkle/life capability, the gauge of the face sheets was increased from 0.043 to 0.063 centimeter (0.017- to 0.025-inch) skins. The final face-sheet thickness will be determined by thermal data obtained from the first orbital flights. The final thickness is estimated to be 0.040 centimeter (0.016 inch) for acceptable wrinkle/life capability. The use of Inco 625 also allowed the porthole improvement when the requirement for turbopump torque/inspection was changed to after every operational flight.

The sliding seal was redesigned (Figure 6) to reduce seal thermal mass by using a wiper and slider blocks. The thermal mass reduction also reduced the gradient to approach the desired value shown in Figure 10, which in turn decreased the wrinkling tendency in the Inco 625 engine heat shield. The wiper is Teflon-coated silicone rubber. The slider blocks are individual electro-deposited nickel units. The wiper and slider block seal are also more compatible with the engine heat shield wrinkled face sheet for pressure sealing. The wiper will deteriorate under high-temperature repeated usage. Thermal coatings were added to the inside of the sliding seal. The three articulated links were increased to four. The engine heat shield surface coating was changed to Linde L103 to increase its life. The flexible seal outer material was changed from Irish Refrasil silica fabric to AB312 for improved handling characteristics.

Small, spherical, gore-component thermal cyclic tests were conducted to provide data and confidence that the full-up AHSS design and the forthcoming certification test will be successful. The tests are designed to produce representative flight thermal strains to check the behavior of the honeycomb face sheets and the seal wiper. The Inco 625 engine heat shield and the seal wiper should have a repeated usage of at least 20 flights. The maximum usage will be determined by later test data. All efforts will be made to improve the engine heat shield and wiper life to reduce orbiter maintenance operation. Replacement of the wiper requires removal of the dome heat shield and seal. Replacement of the engine heat shield requires removal of the total AHSS.

SUMMARY

In summary, the structural deflections, the assembly and installation tolerances, and high-temperature, high-gradient requirements were the drivers that led to the present design. The lock-out device and portholes were the major maintenance improvements. The dome and heat shield meridian joints were structural and maintenance improvements.

TABLE I – TOLERANCE/DEFLECTION SUMMATION (INCHES)

	Item	Baseline Design			Design Fix		
(A)	Nominal Spring Offset	0.833 √			1.600 √		
	Mfg Tolerances		√			√	
	Dome and seal details	±0.211	±0.488		Tooled	±0.030	
	Engine mount/dome	±0.277					
	SSME	±0.050	±0.250		±0.050	±0.250	
	SSME heat shield	±0.200			±0.200		
	Deflections						
	Structural defl	+1.487 -0.170	+1.744 -0.290		+1.487 -0.170	+1.744 -0.290	
	Thermal distortions	+0.157 -0.020			+0.157 -0.020		
	Vibration (acoustic)	±0.100		Rms Values	±0.100		Rms Values
	Subtotal			⬇			⬇
	Tolerances and deflections		+2.482 -1.028	+1.752 -0.724		+2.024 -0.570	+1.429 -0.401
(B)	NET OFFSET (nom + Σ tol and defl)	Max	+3.315	+2.585	Max	+3.624	+3.029
		Min	-0.195	+0.109 √	Min	+1.030	+1.199 √

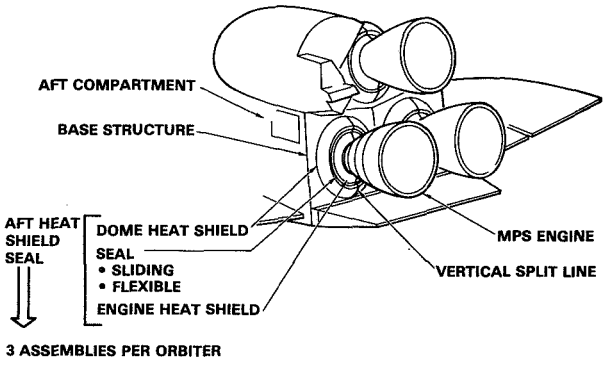

Figure 1 – Aft Heat Shield Seal

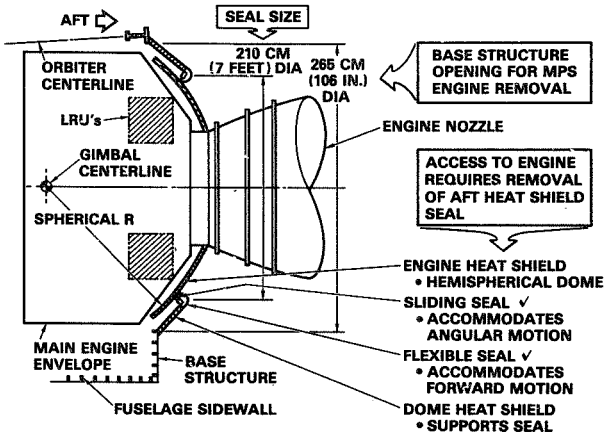

Figure 2 – Operation and Access

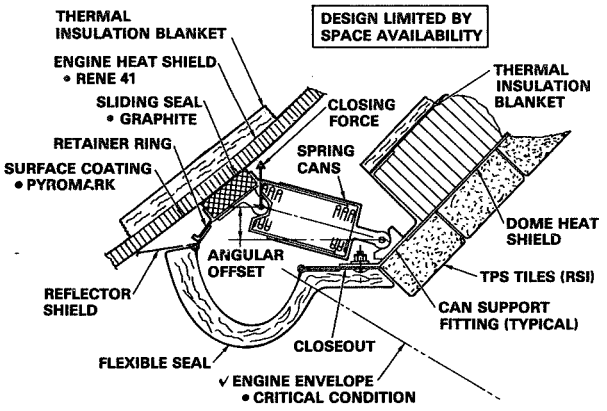

Figure 3 – Seal Installation Baseline Design

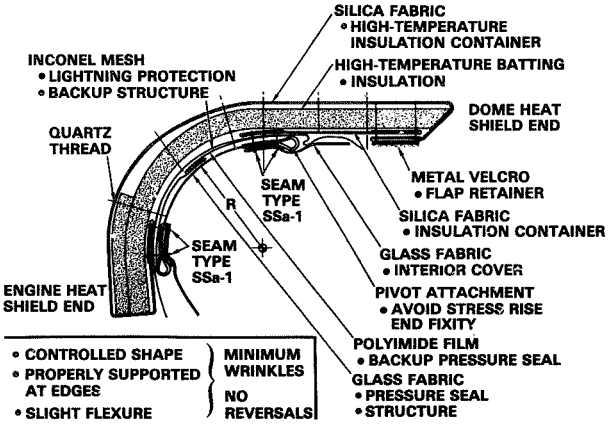

Figure 4 – Flexible Seal Baseline Design

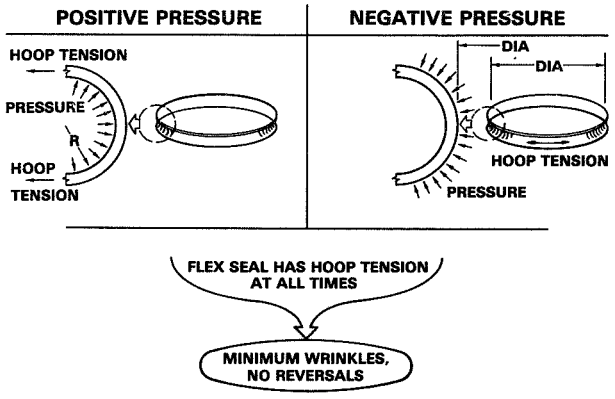

Figure 5 – Flexible Seal Pressure Capability

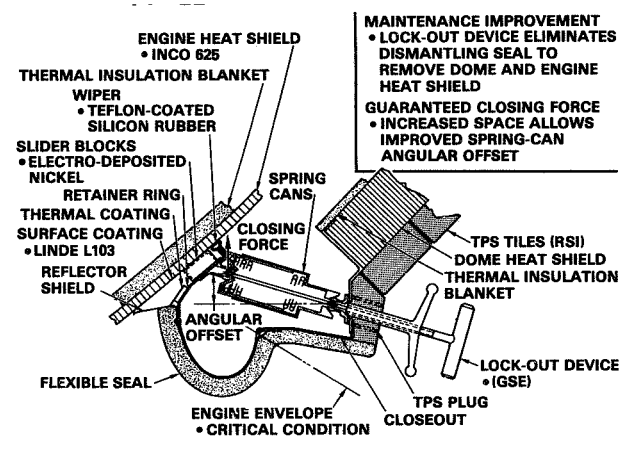

Figure 6 – Seal Installation With Lock-out Device

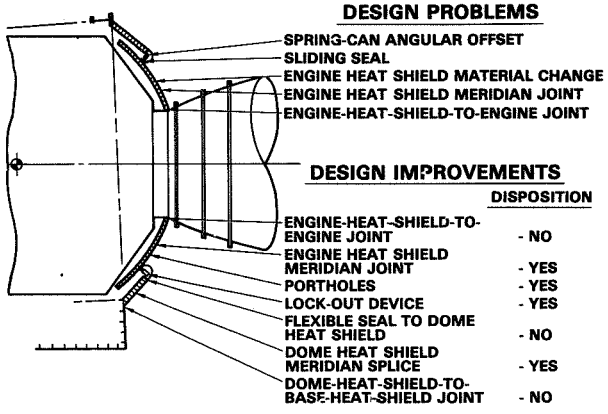

Figure 7 – Problems and Improvements

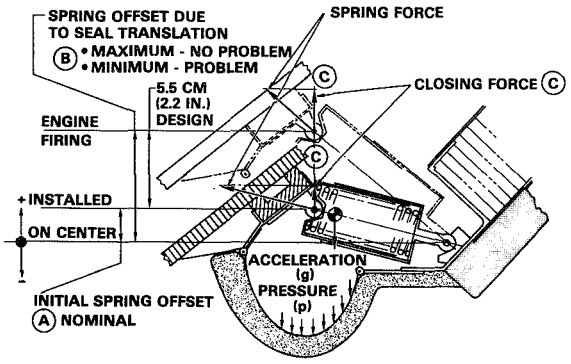

Figure 8 – Spring Geometry/Force Diagram

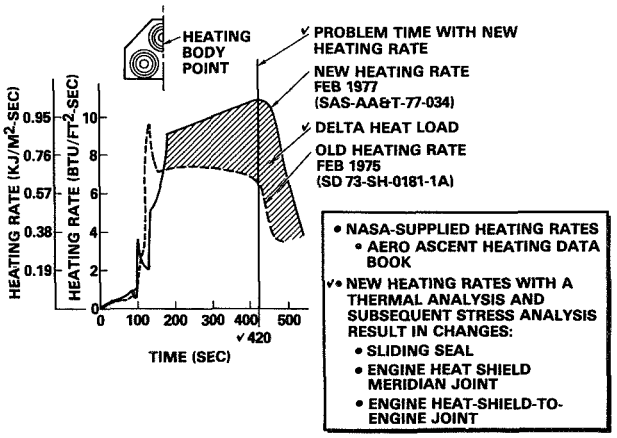

Figure 9 – Aft Heat Shield Seal Heating Rates

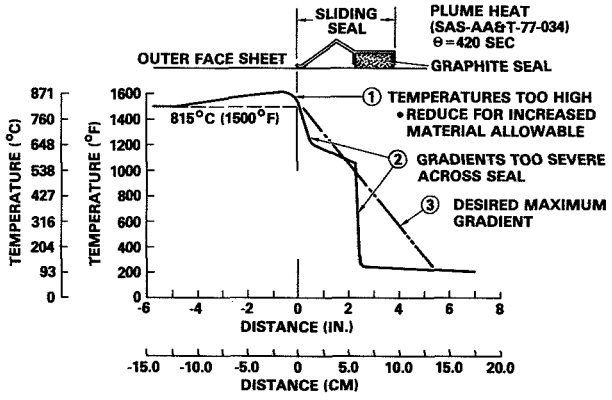

Figure 10 – Engine Heat Shield Baseline Temperature Gradient

SPACE SHUTTLE ORBITER PAYLOAD BAY DOOR MECHANISMS

Bill M. McAnally*

ABSTRACT

The opening, closing, and latching of the first large clamshell door to operate in space presents some unusual challenges for the mechanism designer of the Space Shuttle Program. This paper describes the requirements, hardware configuration, design trade-offs, and qualification testing in process to meet the challenge and to make the system operational for the Shuttle orbiter's approaching first orbital flight. This work was conducted under NASA Contract NAS9-14000.

INTRODUCTION

The unique, reusable, cargo-carrying "space airplane," called the Space Shuttle orbiter, can also be described as a contemporary delta-wing aircraft launched into orbit as a spacecraft, then returned from orbit to a conventional landing. The orbiter's cavernous cargo or payload bay will enable it to transport various sizes, shapes, and weights of payloads to and from earth orbit.

The payload bay doors are designed around the payload requirements that call for an envelope 4.6 meters (15 feet) in diameter and 18.3 meters (60 feet) long. The doors provide the aerodynamic fairing required for the mid fuselage and the complete environmental envelope for the payload bay. They react fuselage torsional loads in addition to supporting their own flight and purge pressure loadings. They also provide structural support for the fixed and deployable environmental control system radiators that are attached to the inner surface of the doors. The payload bay doors are hinged along the side and split at the top centerline–i.e., one door per side 18.3 meters (60 feet) long. Each side consists of four 4.6-meter (15-foot) segments that are interconnected through expansion joints that allow the door to act as one 18.3-meter (60-foot) door. The doors have the structural integrity and capability of being opened and closed in zero gravity; but in 1 g, they require ground support equipment assistance in both the vertical (launch) position and the horizontal position.

The payload bay door mechanisms include the elements associated with remote operation and latching of the payload bay doors and deployable radiators. The functions of these mechanisms include (1) closing and opening the doors and retaining the doors in an open position; (2) unlatching and structurally securing (latching) the closed doors to the orbiter structure; (3) stowing, deploying, and retaining the radiators in the deployed position; (4) unlatching and structurally securing (latching) the deployable radiators to the payload bay doors; and (5) providing controls and measurements to indicate door, radiator, and latch mechanism status. Table I summarizes the number of components to perform these functions.

*B. M. McAnally is Engineering Manager of Mechanical/Actuation Systems for the Space Shuttle Program at the Rockwell International Space Systems Group at Downey, California.

DESIGN REQUIREMENTS

The mechanisms have been designed to satisfy a wide variety of structural, mechanical, and mission-unique requirements. Among these are the following:

- Last for 100 orbital missions and 10 years.
- Operate in 1-g and 0-g conditions.
- Maintain orbiter structural integrity.
- Provide load paths for torsional door capability.
- Maintain orbiter door outer mold-line smoothness.
- Accommodate thermal/structural deflections and maintain pressure/thermal sealing.
- Latch to overcome deformation, deflections, misalignment, friction, pressure seals, and thermal barriers.
- Maintain payload clearance.
- Withstand nonoperating temperature range of -110.6°C (-167°F) to +171.1°C (+340°F).
- Operate within temperature range of -73.3°C (-100°F) to +121.1°C (+250°F).
- Tolerate a single electrical power, motor, or switch failure.

CONFIGURATION DESCRIPTION

Door Mechanisms Overview

The doors are opened soon after orbit insertion and remain open until just prior to reentry, as shown in Figure 1. The two 18.3-meter (60-foot) doors require structural latching of approximately 33.5 lineal meters (110 lineal feet) of door edge—18.3 meters (60 feet) at the upper centerline and 7.6 meters (25 feet) each at both the forward and aft end—as depicted in Figure 2. The doors are opened/closed and latched sequentially, either manually from the on-board control panel or automatically from the on-board computer, by electromechanical actuators. Figure 3 depicts the door opening/closing and latching sequence, revealing the use of ganged latches (four latches in each gang). The door mechanisms are broken into four basic subelements: door drive actuation, forward bulkhead latches, aft bulkhead latches, and centerline latches.

Door Drive Actuation

The actuation system drives the door to the required positions, as illustrated in Figure 4. There are two actuation systems, one on each side of the orbiter, driving an 18.3-meter (60-foot) "half door" at six points along the hinge line. The six gear boxes are connected by torque tubes to each other and to an electromechanical power drive unit. The output of the six gear boxes is transmitted through the drive linkage to the door, as noted in Section A-A of Figure 4. The door actuation system is sized for operating the doors in 1-g conditions with ground support equipment assist when the orbiter is either horizontal or vertical.

Forward Bulkhead Latches

The forward bulkhead latches connect the doors to the forward structural bulkhead, as depicted in Figure 5. The forward latches consist of a right-hand gang (four latches) and a left-hand gang

(four latches), each latch operating in a sequential manner controlled by the kinematics of the ganged mechanism. The latch mechanism is mounted on the door, and the mating hook rollers are mounted on the bulkhead. The latches also help to maintain door sealing to the fuselage structure, as shown in Figure 6. Note that the sliding seal, which requires the engaged latch hooks to slide fore and aft on the rollers, allows for relative movement between the door and forward bulkhead. Each ganged mechanism is driven by a single electromechanical rotary actuator (two motors).

Aft Bulkhead Latches

The aft bulkhead latches connect the doors to the aft structural bulkhead in much the same manner as the forward bulkhead latches (Figure 7), the only difference being the added fore/aft shear tie at each latch on the aft bulkhead (identified as a "passive roller" in Figure 7). The tie is required to effect an adequate door-to-structure seal with the given aft bulkhead seal configuration of Figure 6.

Upper Centerline Latches

The upper centerline latches connect the right-hand and left-hand doors along the upper centerline, as shown in Figure 8. There are four gangs of latches (four latches each), the active latches on the right-hand door and the mating rollers on the left-hand door. Within each gang, the four latches are connected by torque tubes to each other and to a single electromechanical rotary actuator. Each latch gang also contains one passive shear fitting to carry fore and aft shear loads. Again, the latches also help to maintain door-to-door sealing, as shown in Figure 6. Alignment rollers are used at each latch to ensure proper engagement of the opposite door under any warpage condition (Figure 9).

Radiator Mechanisms Overview

The environmental control deployable radiators are hinge-mounted to the forward 9.1-meter (30-foot) sections of the payload bay door, as shown in Figure 10. Each 9.1-meter (30-foot) radiator consists of two 4.6-meter (15-foot) panels interconnected to operate as one. After the payload bay doors are opened, the radiators are deployed to a predetermined position to provide dual-sided radiative surfaces to dissipate heat accumulated from orbiter systems. The radiators are opened/closed and latched manually from the on-board control panel by electromechanical actuators. The radiator mechanisms are broken into two basic subelements: radiator drive actuation and radiator latches.

Radiator Drive Actuation

The actuation system drives the radiator to a position 0.62 radians (35.5 degrees) away from the payload bay door, as shown in Figure 10. The drive system is very similar to the payload bay door drive system, one on each door driving a 9.1-meter (30-foot) deployable radiator at four points along the hinge line. The four gear boxes are connected by torque tubes to each other and to the electromechanical power drive unit. The output of the four gear boxes is transmitted through the drive linkage to the radiator.

Radiator Latches

The radiator latches provide the mechanisms to attach the deployable radiators structurally to the doors during boost to orbit and reentry. Each 9.1-meter (30-foot) radiator has 12 latches, in two groups of six each, each group being driven by one electromechanical power drive unit and three rotary gear boxes, as depicted in Figure 10.

DESIGN DETAILS

The structural integrity required to ensure a safe deorbit of the orbiter vehicle reflects the criticality of the payload bay door mechanisms. Remotely unlatching, opening, then closing and latching 18.3 meters (60 feet) of the orbiter mid body on orbit and prior to reentry are the primary challenges. In addition, the deployable radiators must first be remotely opened, closed, and latched in order to close the payload bay doors for reentry. The on-orbit conditions, along with the boost and reentry to earth landing conditions, are presented in a design load matrix in Table II.

Latched conditions during boost to orbit and reentry to landing are generally basic requirements. However, the latching conditions on orbit present the challenge, primarily because of the size of the doors and the thermal distortions resulting from long-duration orientations of the orbiter to the sun and deep space. Figure 11 presents fore and aft design deflections at the door centerline. Only the door mechanisms are discussed here, since the radiator mechanisms are so similar in design and operation.

The electrical commands to open and close the doors are initiated as a function of mission elapsed time, mission event, or manual switch operation. Only the door closing sequence is discussed here, since the opening sequence is basically the reverse of closing. Before the payload bay door can be closed, the right- and left-hand deployable radiators must be stowed and latched strictly by manual switch operations.

Receipt of the door CLOSE command initiates the following steps:

1. Initiate CLOSE command for left door.
   a. When door reaches READY TO LATCH position, a signal is generated to initiate the next step.
   b. If after 126 seconds READY TO LATCH signals are not received, a malfunction signal is generated in the cockpit CRT display, requiring the crew to take corrective action.
2. Initiate CLOSE command for forward and aft left bulkhead four-latch gangs.
   a. When latches are closed, a signal is generated to initiate the next step and turn off applicable drive motors.
   b. If after 60 seconds latches are not closed, a malfunction signal is generated in the cockpit CRT display, requiring the crew to take corrective action.
3. Initiate CLOSE command for right-hand door.
   a. Same as Step 1a
   b. Same as Step 1b
4. Initiate CLOSE command for forward and aft right bulkhead four-latch gangs.
   a. Same as Step 2a
   b. Same as Step 2b

5. Initiate CLOSE command for forward and aft centerline four-latch gangs.
   a. When latches are closed, a signal is generated to initiate the next step.
   b. If after 40 seconds latches are not closed, a malfunction signal is generated in the cockpit CRT display, requiring the crew to take corrective action.
6. Initiate CLOSE command for the mid centerline four-latch gangs.
   a. Same as Step 5a
   b. Same as Step 5b
7. Generate signals for crew display: PAYLOAD BAY DOORS CLOSED.

The above sequence can be stopped and/or reversed at any point.

As noted earlier, the door mechanisms consist of 32 latches: 8 at the forward door edge, 8 at the aft door edge, and 16 along the door centerline. The latches are all approximately 0.91 meters (3 feet) apart. Once the doors are unlatched on orbit and each door is opened 3.11 radians (178 degrees), the huge doors and the "opened" fuselage structure are exposed to varying thermal conditions: the open payload bay (and inner surface of the doors) may be exposed to deep space, while the lower side of the orbiter (and outer surface of the doors) may be exposed to the sun; or sun may be on one side of the orbiter with deep space exposure on the other. These are just two examples of many orientations that create a wide excursion of thermal deformations to be overcome during closing and latching of the doors. In addition, the door structure is graphite-epoxy construction while the fuselage structure is aluminum. Again, the on-orbit thermal deflections are more significant in the design because of the large size of the doors.

Because of these deflections, the actuation system required to drive the door to the fully closed position and to ensure that the forward and aft edge of the door is in total contact with the bulkhead structure for "simple latching" would be prohibitive from a power, space, and weight standpoint. Therefore, of all the means considered, the mechanically sequenced ganged latching concept was chosen.

To close the door, the actuation system drives the left-hand door to an approximate 0.03-radian (1.75-degree) open position, overcoming a 1.8-kilogram-per-running-centimeter (10-pound-per-running-inch) seal and thermal barrier load along the hinge line and bulkheads near the hinge line. The door drive must also overcome sliding friction (μ = 0.3) on the bulkhead seals and thermal barriers, hinge line warpage, "oil canning" of the doors, mechanical linkage friction (μ = 0.3), and various fluid and electrical lines crossing over the hinge line from the fuselage to the door and radiator. Therefore, the power drive unit has an output of 7.32×10^8 dyne-centimeters (648 inch-pounds) of torque transmitted through the aluminum torque shafts to the six geared rotary actuators, each with an output of approximately 90.38×10^8 dyne-centimeters (8000 inch-pounds) of torque. The output of the six actuators is transmitted to the door structure through the interconnecting door drive linkage, placing the door, not fully closed, within the reach of the first bulkhead latch. Then the latches must pull the door completely closed.

As the door moves through the 0.07-radian (4-degree) open position, READY TO LATCH switches on the forward and aft bulkheads are "picked up," initiating the bulkhead latch actuators. The door is then within the 5.1-centimeter (2-inch) reach capability of the No. 1 bulkhead latch closest to the door hinge line (Figure 12). Continued door movement to the 0.03-radian (1.75-degree) open position "picks up" the forward and aft bulkhead DOOR CLOSED switch, shutting off power to the door drive system.

The forward and aft bulkhead latch rotary actuators, with output torques of 16.04×10^8 dyne-centimeters (14,200 inch-pounds) each, transmit power to each of the four latches in the gang

through the mechanical linkage. The kinematics of the ganged linkage is such that the No. 1 latch first engages the door, pulling it to a position within reach of the No. 2 latch. As the No. 2 latch continues to pull the door further closed, the door comes within reach of the No. 3 latch, and so on until the No. 4 latch finally pulls the door into total contact with the bulkhead structure.

The ganged latches, mechanically sequenced, thus provide a unique "zippering effect" to close the door. The bulkhead latch actuator must overcome a 1.8-kilogram-per-running-centimeter (10-pound-per-running-inch) seal and thermal barrier load along the bulkhead, sliding friction ($\mu = 0.3$) on the seals and barriers, mechanism friction ($\mu = 0.18$), door stiffness, and the previously discussed thermal distortions. The latch mechanisms are structurally designed to take full actuator stall output (jamming) to within 0.17 radian (10 degrees) of the mechanism on-center position. As the bulkhead latch actuators drive the four-latch gang to the on-center or door-closed position, a switch within the actuator shuts off the actuator and triggers the right-hand door closing sequence.

Some on-orbit thermal distortion conditions result in the tendency of the doors to overlap at the upper centerline—as much as 5.1 centimeters (2 inches) under the worst conditions. Thus, alignment rollers are used along the centerline to force the doors into position (Figure 9) and provide a safe centerline latch engagement envelope.

The right door is closed and latched in the same manner and to the same design requirements as the left-hand door, leaving the upper 18.3-meter (60-foot) centerline of the two door halves to be latched. The full travel of the forward and aft bulkhead latch actuators latching the right-hand door trips a switch inside the actuator, thus initiating the upper centerline door-to-door latches. But the 18.3 meters (60 feet) of centerline latches consist of 16 latches in 4 groups, each group ganging four latches together (as noted in Figure 8). This design results from the varying distorted relationship between the two door halves at the centerline. Only the most forward and most aft four-latch gangs are actuated first. The doors are relatively close together at these points because the door ends are latched to the forward and aft bulkheads. Once the most forward and most aft centerline four-latch gangs are latched, they pull the central 9.1 meters (30 feet) of the centerline door halves closer together, thus making it easier and more positive for the remaining two latch gangs to complete the centerline latching.

Each four-latch gang is identical—a rotary actuator transmitting 45.19×10^8 dyne-centimeters (4000 inch-pounds) of output torque through connecting aluminum torque tubes to the four-latch hooks. The actuator is designed to overcome seal and thermal barrier loads and friction, mechanical friction, door stiffness, and thermal distortions of similar values found in the bulkhead and door drive actuation systems. In addition, each four-latch gang has a passive shear fitting engagement requirement, as shown in Figure 8. The fore and aft shear load capability of 7491 kilograms (16,500 pounds) per fitting provides the load path for the torsional door requirement.

Somewhat different from the bulkhead latch gang, the centerline four-latch hooks within a gang move together to latch simultaneously. However, a similar "zippering" effect occurs in that the full travel of the latch actuators in the forward and aft four-latch gangs trips a switch in each actuator, shutting off its own power and causing power to be applied to the two centermost four-latch gangs. Full travel of these centermost two actuators, and thus completion of the payload bay door closure, trips a switch in each actuator to stop the actuator and provide a DOOR CLOSED display in the cockpit. Thus, the orbiter structure returns to the appropriate, smooth, aerodynamic contour required for a safe reentry into the earth's atmosphere; and structural continuity enables the orbiter vehicle to maneuver to a safe landing at the designated landing site.

TEST PROGRAM

At this writing, a significant amount of testing and analysis remains to be done before the payload bay door mechanisms are certified for the first manned orbital flight of the orbiter vehicle, now scheduled for 1979. The two basic segments of the test program are component testing and major payload bay door test article (PBDTA) tests. Components will be qualified by the individual component suppliers through analysis and testing. These tests are presently in process.

The PBDTA will integrate the payload bay door subsystems and must functionally verify, under simulated on-orbit environmental conditions (zero gravity and thermal deformation), the latching and door drive actuation systems. Other significant tests will involve 1-g operation in both the horizontal and vertical positions.

The test article will consist of a partial set of door assemblies, a simulated mid fuselage, environmental seals and thermal barriers, radiator panels, and latching/actuation mechanisms. The test article is presently being fabricated, the test start date scheduled in early 1979.

CONCLUDING REMARKS

While the payload bay door mechanisms generally reflect conventional aircraft design, the unusual Shuttle applications and critical functions require remote "zipper latching" of a large clamshell door on a "space airplane" that operates in both 1-g and 0-g conditions. The challenge is to ensure that all critical conditions are thoroughly considered in design, development, testing, and implementation.

TABLE I – ELECTROMECHANICAL COMPONENT COUNT

Component	Doors	Radiator	Total
Power drive units	10	6	16
Rotary actuators	12	20	32
Latches	32	24	56
Hinges	26	12	38
Passive fittings	40	4	44
Shafts	52	20	72
Couplings	72	52	124
Switches	68	24	92
Push-pull rods	36	24	60
Shaft support bearings	84	22	106

TABLE II – DESIGN LOADS

Loading Considered	Mechanism			
	Fwd, Aft, & Centerline Door Latch	Door Drive	Radiator Latch	Radiator Drive
Flight Phase				
Ascent	X		X	
Boost	X		X	
On orbit	X	X	X	X
Opening/Closing on Orbit				
Stall/jam*	X	X	X	X
Seal stiffness/friction**	X	X		
Thermal deflection**	X	X	X	X

*Critical condition with regard to strength
**Critical condition with regard to closure

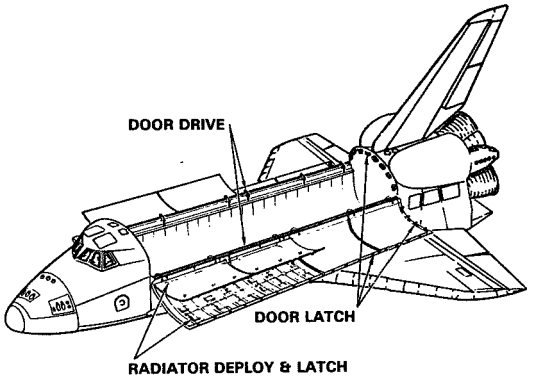

Figure 1 – Payload Bay Door/Radiator System

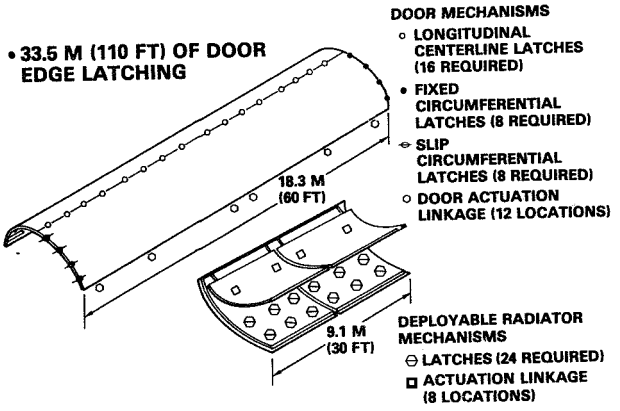

Figure 2 – Configuration of Payload Bay Door Mechanisms

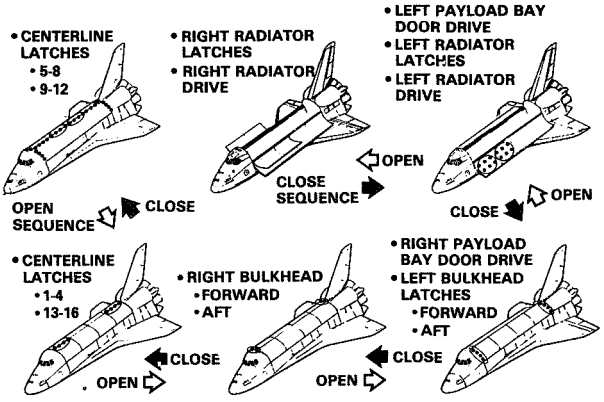

Figure 3 – On-Orbit Payload Bay Door and Radiator Open/Close Sequence

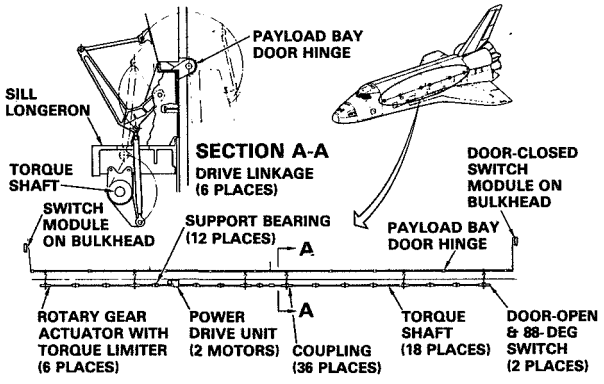

Figure 4 – Payload Bay Door Drive System

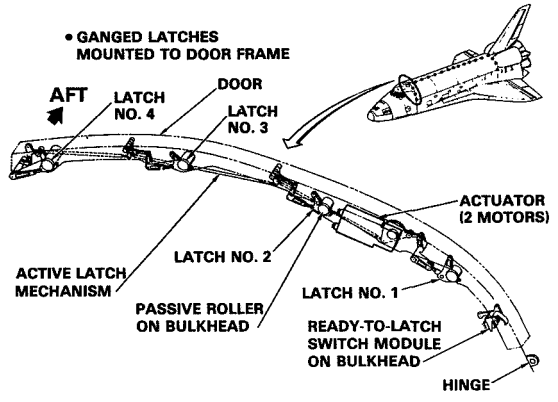

Figure 5 – Forward Bulkhead Circular Latch System

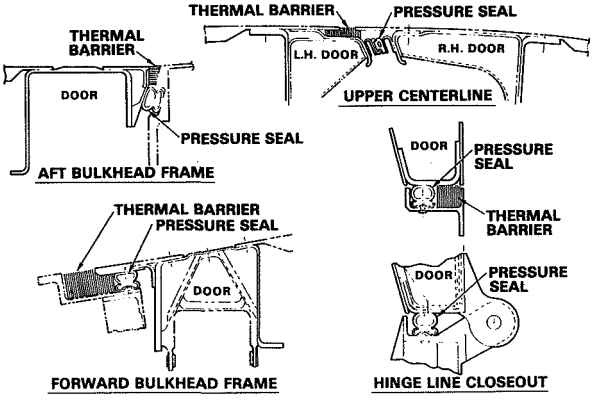

Figure 6 – Payload Bay Door Environmental Seals

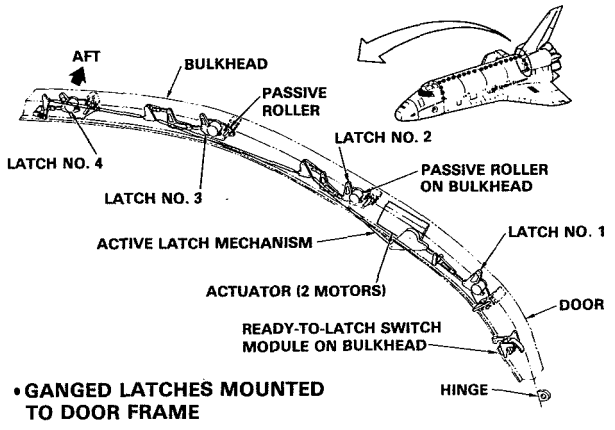

Figure 7 – Aft Bulkhead Circular Latch System

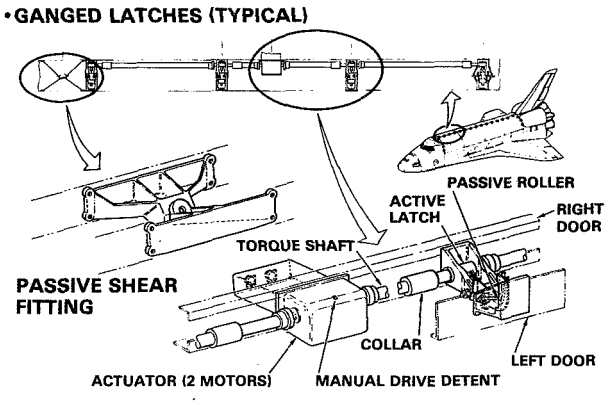

Figure 8 – Payload Bay Door Centerline Latch System

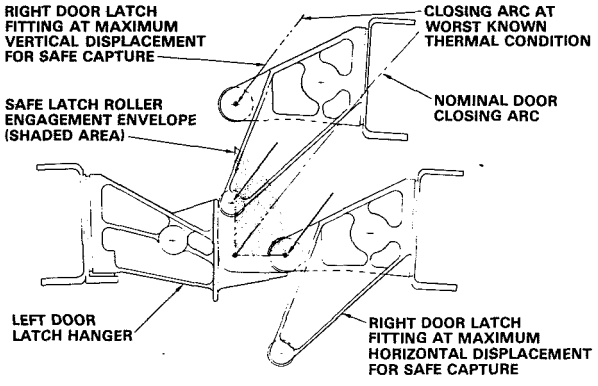

Figure 9 – Payload Bay Door Centerline Engagement and Latching

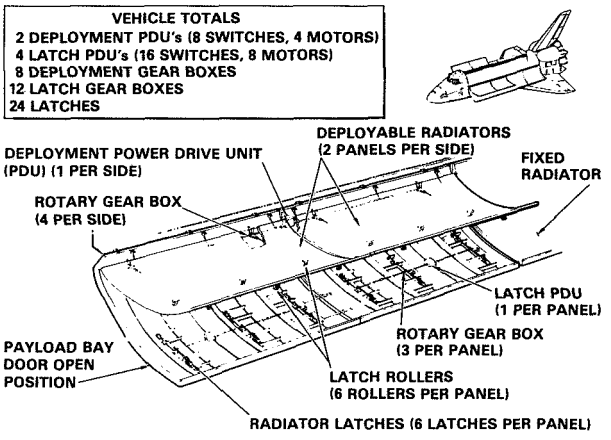

Figure 10 – Deployable Radiator Mechanisms

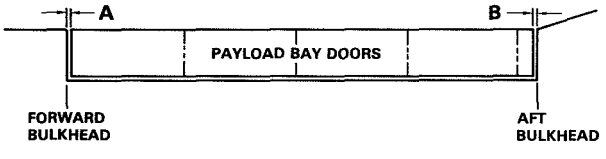

RELATIVE GAP CENTIMETERS (INCHES)	ASCENT (MECHANICAL)		DESCENT (MECHANICAL AND THERMAL)		ON ORBIT (THERMAL)	
	OPEN	CLOSE	OPEN	CLOSE	OPEN	CLOSE
A	1.04 (0.41)	0.74 (0.29)	1.30 (0.51)	1.63 (0.64)	0.23 (0.09)	1.09 (0.43)
B	0.91 (0.36)	1.70 (0.67)	2.29 (0.90)	1.12 (0.44)	1.04 (0.41)	0.97 (0.38)

Figure 11 – Centerline Maximum Deflections

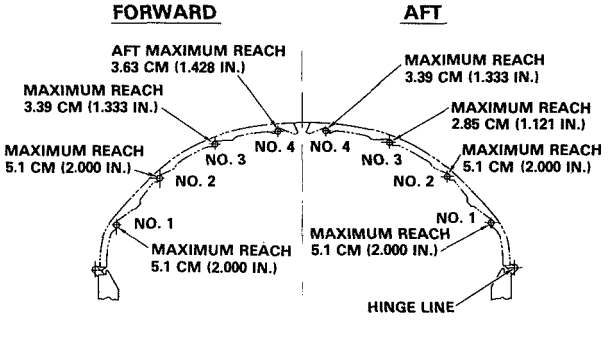

Figure 12 – Bulkhead Latch Reach Capability

IUS THRUST VECTOR CONTROL (TVC) SERVO SYSTEM

G. E. Conner
Chemical Systems Division, United Technologies

ABSTRACT

The IUS TVC SERVO SYSTEM, currently in full-scale development, consists of four electrically redundant electromechanical actuators, four potentiometer assemblies, and two controllers to provide movable nozzle control on both IUS solid rocket motors. The system contains two unique design areas: the use of "mirror-image" potentiometers opposite the actuators on the nozzle to increase system accuracy under varying conditions and the use of a pair of solenoid-operated gears normally meshed with the rotor gear to provide a redundant position lock. Test data obtained to date show excellent performance of both items.

INTRODUCTION

This paper presents an overview of the more severe IUS TVC servo system design requirements, the system and component designs, and test data acquired on a preliminary development unit. Attention will be focused on the unique methods of sensing movable nozzle position and providing for redundant position locks.

DESIGN CRITERIA

The design criteria for the system are shown in Table I. Of particular interest is the requirement to meet all performance parameters under the two significantly different sets of mounting geometries and loads of both stages of IUS solid rocket motors. In addition, the system was to be configured in a standby redundant manner such that a maximum number of failures in the primary contoller or actuator could be detected and corrected by switching to the backup controller/actuator. The entire system is built to the reliability requirements of SAMSO-LVGS-77-005 and SAMSO-STD-73-2C.

DESIGN DESCRIPTION

System Description

The servo system was configured as shown in Figure 1. The controllers are located in the forward compartment of the second stage of the two-stage vehicle; two actuators and two potentiometer assemblies are mounted between

TABLE I

Parameter	Requirement
Input Power	31 amps/axis max at 24-32 Vdc
Stroke	10.2 cm (4.014 in.)
Stall Force	2.8 kN (630 lbf)
Accuracy	±1.6 mm (±.063 in.)
Frequency Response	>6 Hz at 100° phase lag
Weight, Actuator	5.58 kg (12.3 Lbm)
Reliability	>0.99988 redundant drive trail >0.999972 single thread element
Operating Temperature	-34°C to +71°C

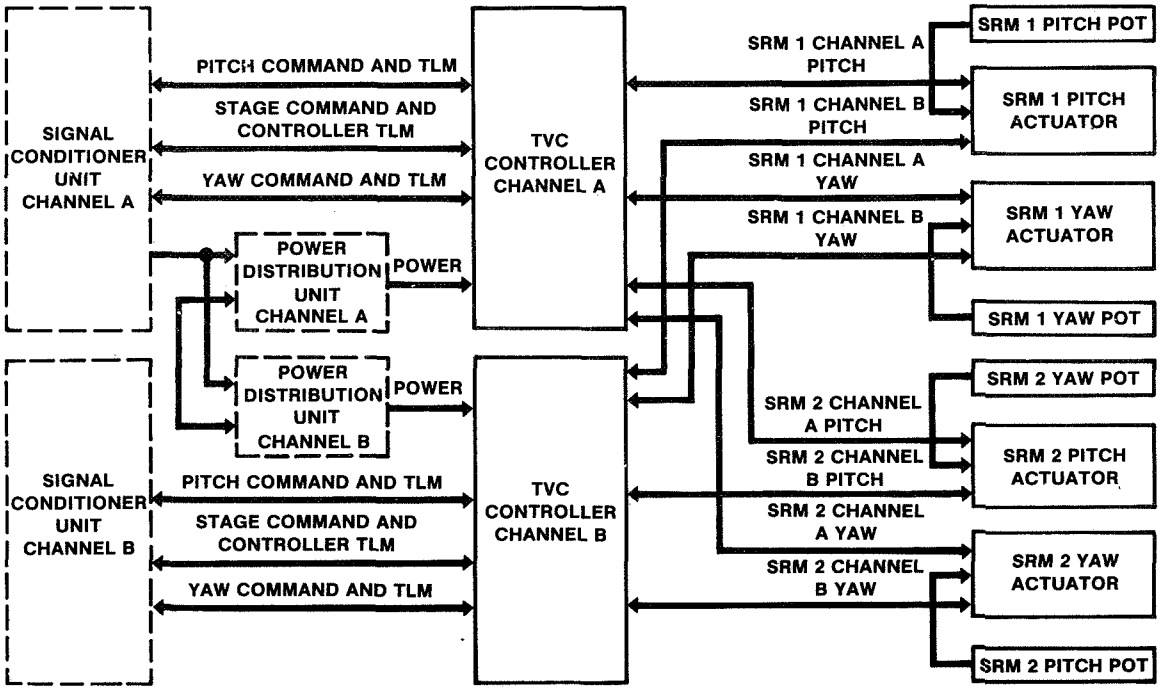

Figure 1. IUS TVC Servo System
Block Diagram

the structure and movable nozzle of each rocket motor. Each controller contains drive and control circuitry for the four actuators. Each actuator contains redundant drive motors, redundant potentiometer feedback elements, and the redundant position lock mechanism.

As shown in Figure 2, the mounting of the actuators and potentiometers is unusual in that the bracket and actuator are configured to form a ball-and-socket connection at the output shaft end, as opposed to a rod end bearing at the rear. This arrangement greatly reduces the bracket weight but tends to increase nozzle cross-coupling errors. Due to these errors and those induced by nozzle axial motion and thermal growth, the potentiometer assemblies were added to the nozzle opposed from the actuators. These potentiometers are identical to those in the actuators and contain two electrically independent feedback elements.

The output of the primary element is electronically summed within the controller with the primary output from the actuator as a measure of nozzle deflection angle. As shown in Figure 3, this arrangement yields very low (0.5%) kinematic errors, and when combined with all other errors results in a maximum error of 1.7%. For comparison, an actuator mounted normally to the nozzle centerline, and without the "mirror-image" potentiometer would have kinematic errors of approximately 5% alone. In addition, environmental temperature changes, nozzle thermal growth, and cross-axis coupling would all introduce errors which are essentially nonexistent with the "mirror-image" approach.

Actuator Description

The actuator shown in Figure 4 contains two rare-earth dc torque motors mounted directly on a ball nut. Both ends of the screw are supported by guide bushings; the nut is supported by a spherical roller bearing. The spherical roller bearing is used, as opposed to ball or roller types, to provide for any possible misalignments between the ball screw and ball nut. The dual-element potentiometer is radially supported on its shaft end by a bushing that slides on the bore of the ball screw and on its aft end by the rear housing of the actuator. The rear housing also provides a bearing surface for the rear guide of the ball screw and the mounting surface for the position lock. All bushings are machined from Delrin AF 113, several of which contain radial slots for thermal growth considerations. The ball screw, bearing, locking gears and solenoid poppets are lubricated with Lubeco M390. All assemblies are vented via stainless-steel mesh cloth to satisfy the program's qualification test requirements.

Position Lock

The position lock shown in Figure 5 consists of two solenoid-retracted gears in mesh with each other and a gear integral with the ball nut. With the solenoids unactivated, return springs inside the solenoids hold the gears in mesh with the ball nut gear. Upon energization of the system avionics power, the primary and backup controllers apply full voltage to both the primary and

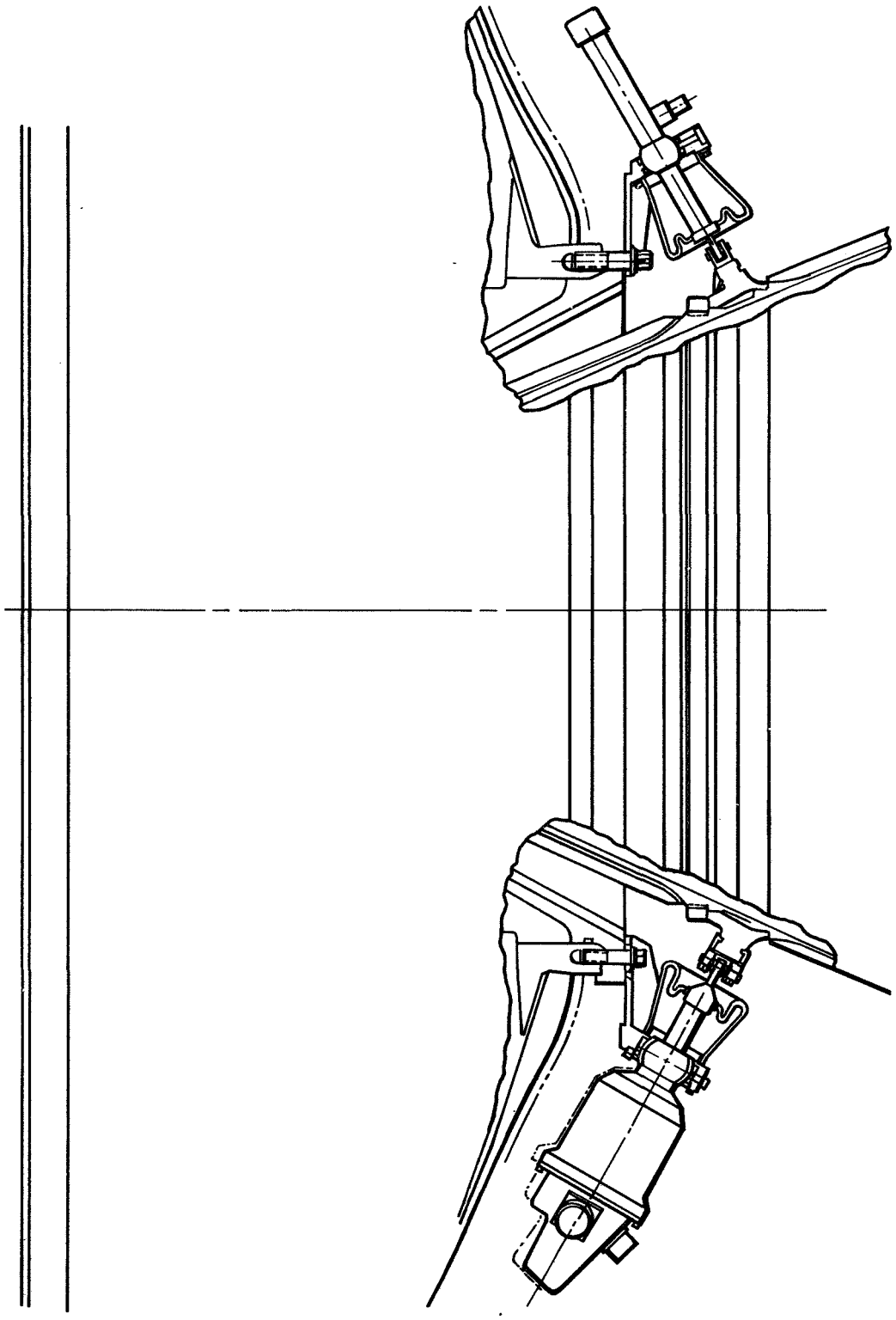

Figure 2. Actuator and Potentiometer Mounting

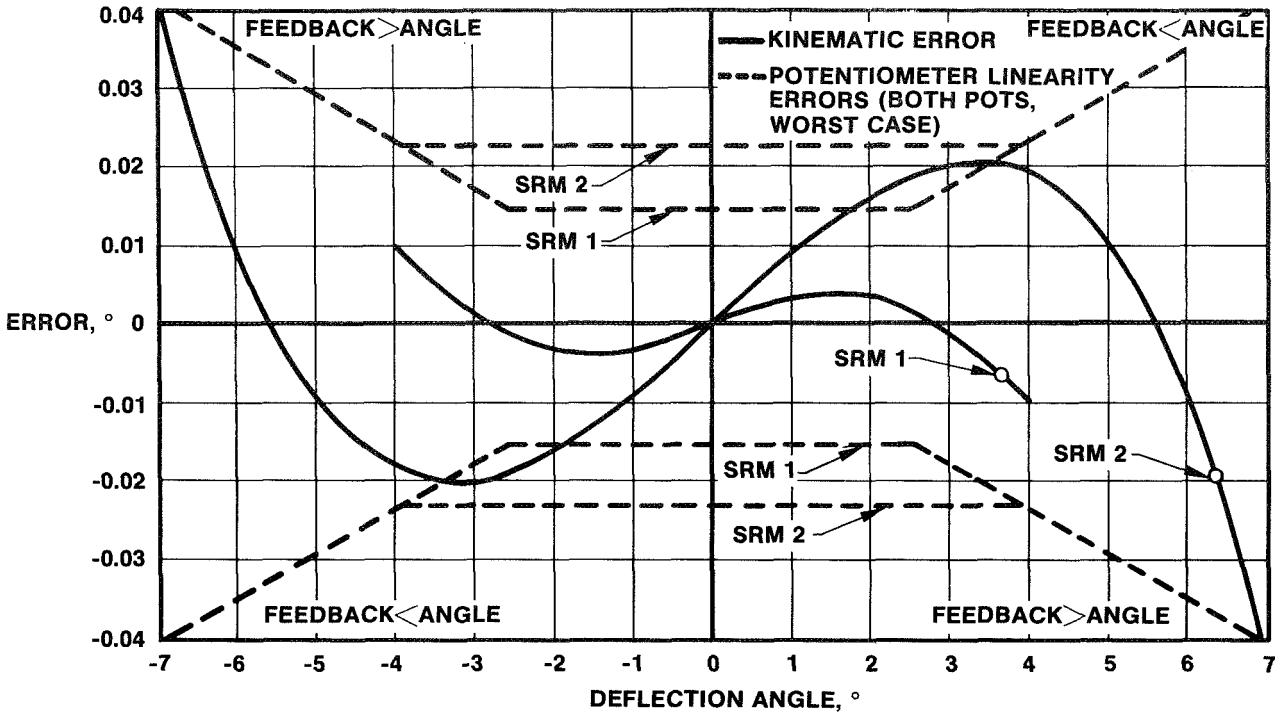

Figure 3. System Kinematic Errors

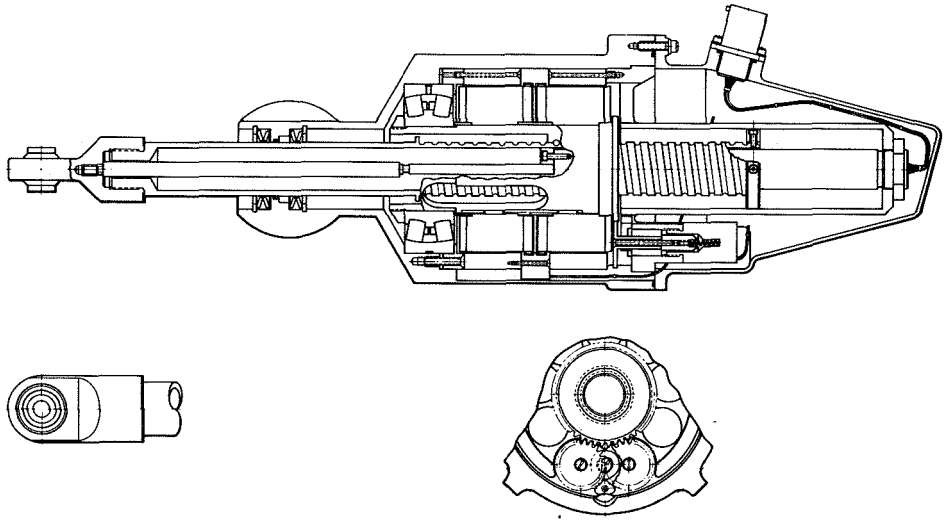

Figure 4. Actuator Assembly

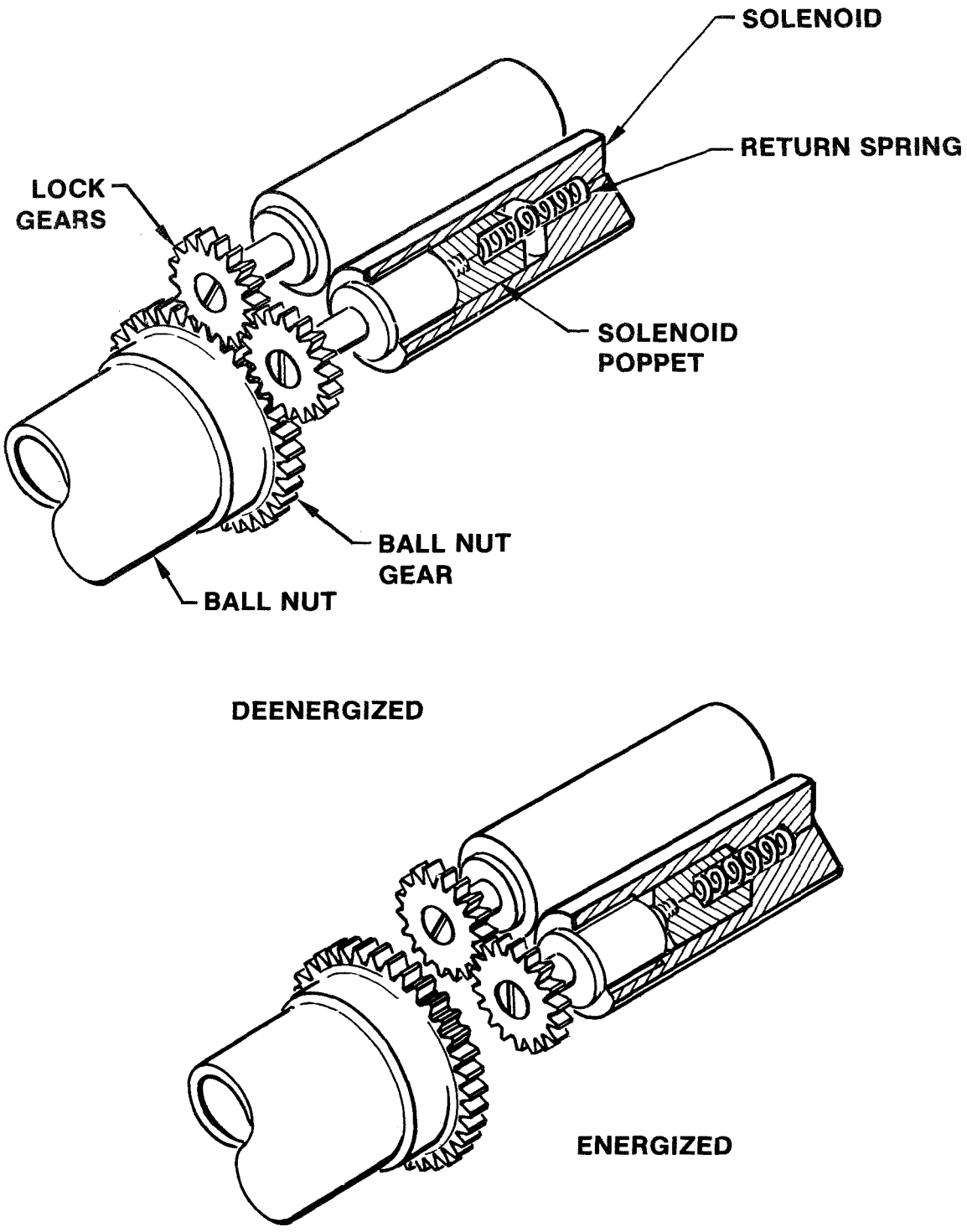

Figure 5. Position Lock Mechanism

backup solenoids for approximately 25 ms, and then switch back to a holding voltage level of 4.0 Vdc to reduce solenoid internal heating. During the 25-ms full-power time period, the solenoids retract the gears against the sum of reflected nozzle loads and the return springs. Both lock gears are supported by bushings in the rear housing.

Since both gears are independently activated and independently spring-loaded, this method is redundant in terms of unlocking and inadvertent relocking. During energization, the failure of one gear to retract has no effect on the other, resulting in the failed gear remaining in mesh with the ball nut gear, and the operative gear being retracted out of mesh. Since the gears are free to rotate, the unretracted gear is merely rotated as the actuator operates. Protection against inadvertent relocking is provided by the independent solenoids. A failure of either solenoid to maintain holding force allows the return spring to remesh the gear, resulting in one meshed and one unmeshed gear.

DEVELOPMENT DATA

Figure 6 shows the assembled and exploded views of the preliminary development unit. This unit was performance-tested on a load test fixture that simulated the kinematics and all load constituents of the stage 2 movable nozzle.

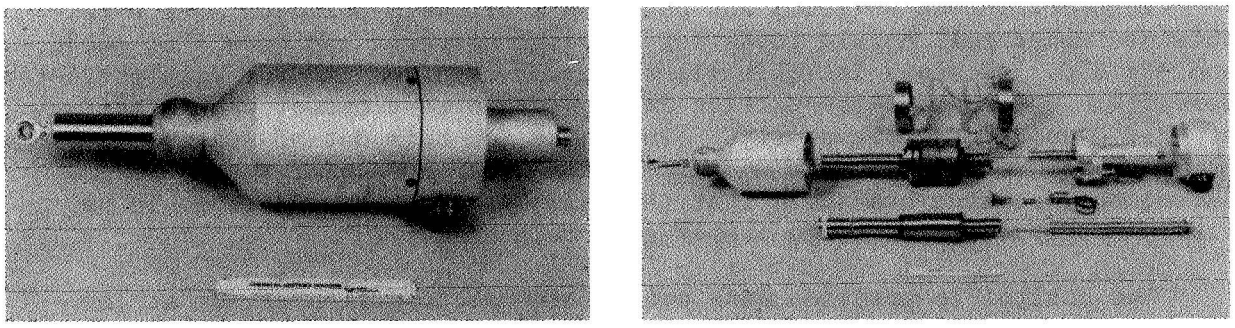

Figure 6. Preliminary Development Unit

Dynamic Performance Data

Figures 7 and 8 present the small- and large-amplitude frequency response data obtained at nominal input voltage and at the maximum expected nozzle loads. Data obtained at miminum input voltage result in a slightly higher break point on the small amplitude command and no significant change for the large amplitude.

Figure 9 presents step response data taken at -23°C with minimal nozzle load. The linear velocity profile is governed by a slew rate limiting circuit within the controller, which was set to 26.4 cm/s for this testing. As shown, the system overshoot is minimal.

STEADY-STATE PERFORMANCE DATA

Table II presents a comparison between the requirements and test results for several steady-state parameters. The stiffness and backlash data were obtained with the locking gears in their normal deenergized position. The stiffness data was taken over the load range of 0 to 2.22 kN (500/Lbf), although the locking gears are structurally sized for loads of up to 6.2 kN (1400) Lbf). Also shown in Table II are the worst observed results taken for the lost motion prior to actuator relocking and actuator unlocking time. The lost motion prior to relocking is very small, equal to the allowable backlash of the system. The unlocking time is also very small, well below the 25 ms full power application time of the controller.

Accuracy Data

Both command-to position and position monitor-to-position data were obtained under full nozzle loads for actuator temperatures of -23°C, +21°C, and +48.8°C. As shown in Table II, the error requirements for both parameters were ±1%. The command-to-position data obtained were out of specification at 48.8°C and nearly out at 21°C. The cause for this out-of-specification performance was traced to an open loop gain which was lower than modeled. Subsequent modeling has shown that the command-to-position data would be within specification had the proper gain been used.

The monitor-to-position data was within specification except at low temperature. The cause for this was not pursued.

All of the accuracy testing included the effects of loads, kinematics, frictions, etc., and were obtained from dial indicator readings taken on the nozzle simulator. This data was then used to calculate the actuator position.

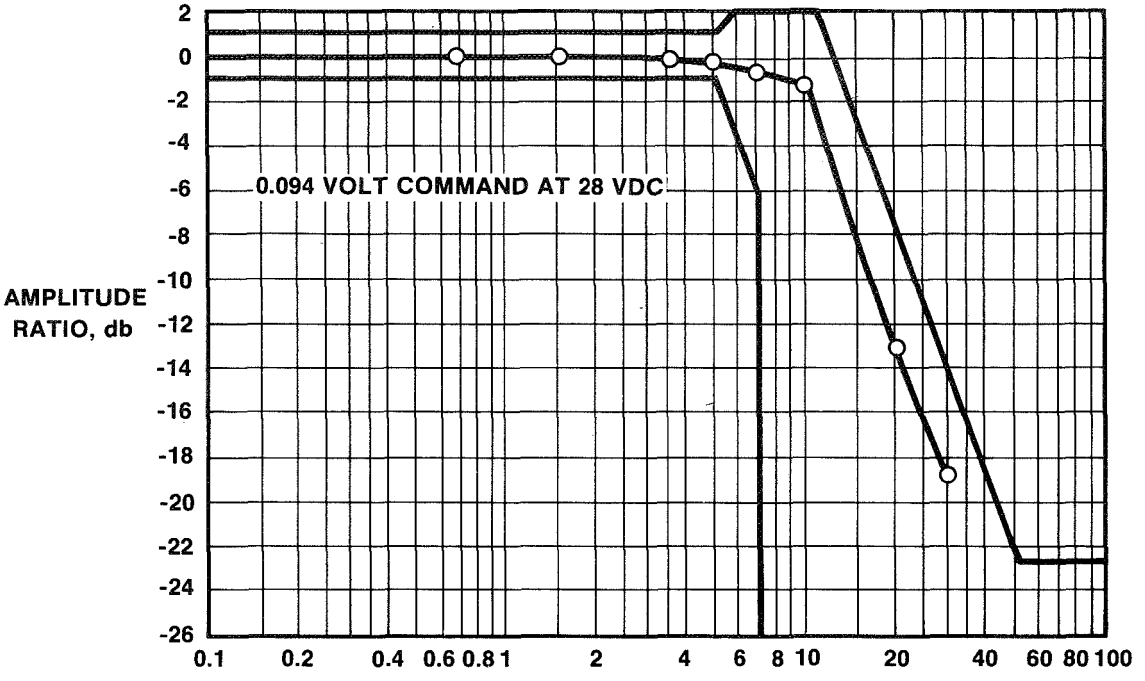

Figure 7. Small Amplitude Frequency Response (±2.4% Stroke)

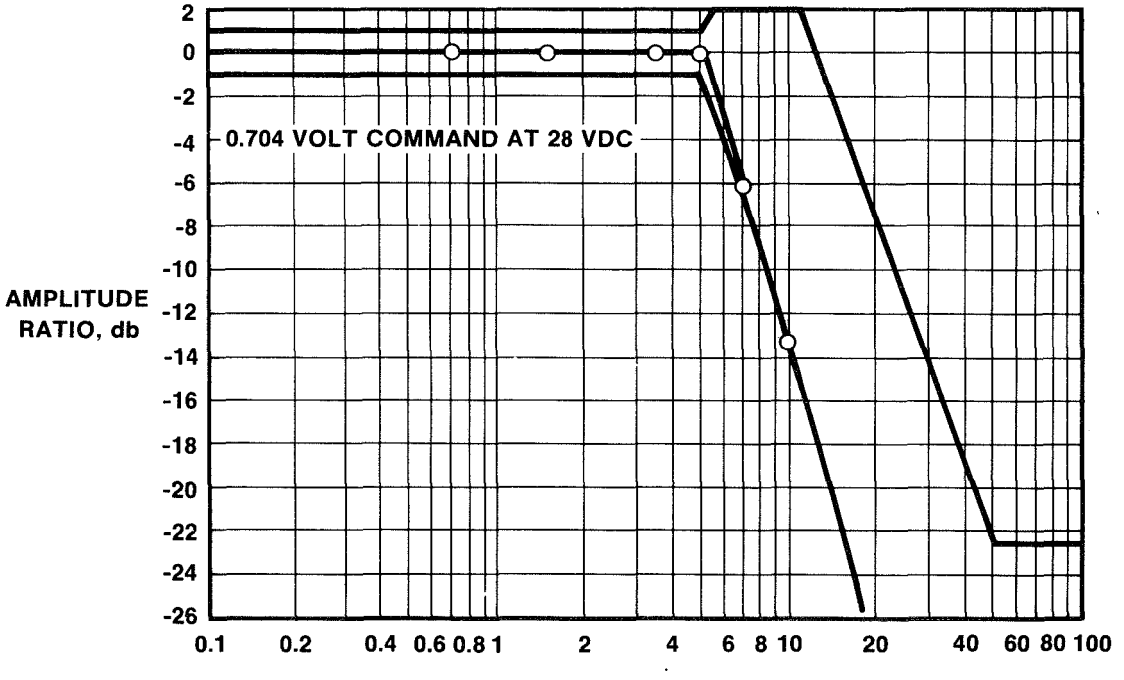

Figure 8. Large Amplitude Frequency Response (±18% Stroke)

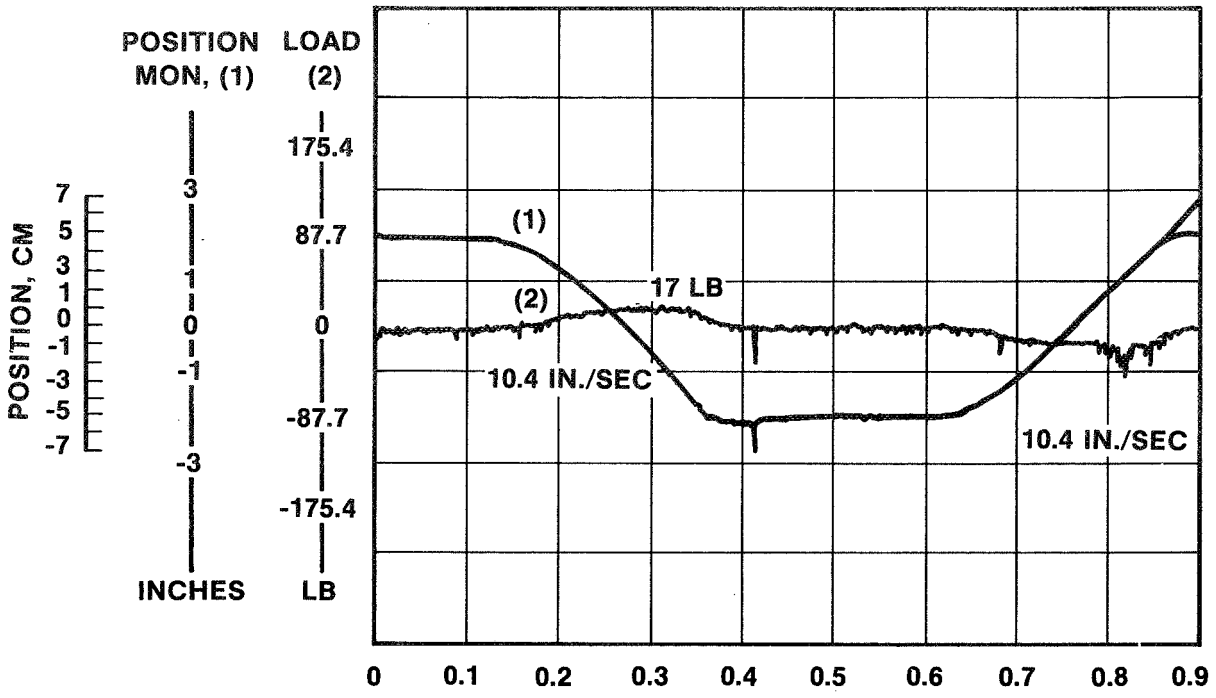

Figure 9. -23°C Step Response Data

TABLE II

Parameter	Requirement	Test Results
Stiffness	4377 kN/m (25,000 Lb/in.) minimum	7581 kN/m (43,300 Lb/in.)
Backlash	(0.254 mm) (0.010 in.) maximum	0.208 mm (0.0082 in.)
Relock lost motion	-	0.251 mm (0.0099 in.)
Unlock time	-	0.006 s
Command-to-Position Error	±1%	1.0% 21°C 1.5% 48.8°C 0.05% -23.3°C
Monitor-to-Error Position Error	±1%	0.1% 21°C 0.25% 48.8°C 1.2% -23.3°C

CONCLUSIONS

In conclusion, both the use of "mirror-image" potentiometers to increase system accuracy and the use of duplex gears to affect a position lock have been successfully developed and demonstrated.

AUTOMATIC IN-ORBIT ASSEMBLY OF LARGE SPACE STRUCTURES

BY

GEORGES G. JACQUEMIN

LOCKHEED MISSILES & SPACE COMPANY

INTRODUCTION

Large space platforms employing nested tapered graphite-epoxy columns reference 1 have been proposed for a number of applications such as communication satellites, multi-kilowatt power modules, large modularized antennas and geostationary platforms. Erection of these platforms which may be up to several square kilometers in size will require several Space Shuttle flights (about 10 per square kilometer) and will necessarily take place at space shuttle orbital altitude. Installation of platform payloads will also take place at this altitude and the completed unit will then be transferred to its final station by towing or under its own power.

The structural concept of these platforms is based on the triangulated tetrahedral space frame described in reference 2. Although this concept is relatively simple, its assembly presents a number of unusual problems because of the large size (20 m columns) and the great number of components which must be connected in a vacuum, zero gravity environment. This operation could be performed manually by astronauts in the course of an extra vehicular activity (EVA). However, the very large number of columns to be assembled (a full Space Shuttle load consists of about 3000 columns and 670 node joints) would require many hours of strenuous astronaut work in the restricted mobility of space suits. Therefore, it appears logical to consider mechanizing this process in order to lighten the astronauts work load. The automatic features of the assembly procedure should be such that only monitoring functions are required from the astronauts, with EVA's being required only in case of difficulties and to assist in loading and unloading supply cannisters.

More complete details of the concepts discussed herein are presented in reference 3.

SPACEFRAME CONFIGURATION

General Geometry

The space platform under consideration is based on the tetrahedral principle which makes use of tri-dimensional triangulation to achieve rigidity. The structure consisting of graphite epoxy columns connected by node joints is shown on Fig. 1. Each node has connections for 6 columns in one plane and 3 interplane columns. The planview configuration presents the appearance of two sets of hexagons offset with respect to each other (Fig. 1). Each column is 20 m (66 ft) long and a full Space Shuttle load corresponds to the assembly of a platform having approximate dimensions 1000 x 100 m (1/10 square kilometer). Since each node joint connects 9 columns and each column is connected to two node joints, the number of columns equals 4.5 times the number of node joints. For a given area, A, the required number of node joints is: $N_j = \frac{4}{\sqrt{3}} \frac{A}{\ell^2}$ where ℓ is the column length. Therefore one square kilometer requires 5774 node joints and 25981 columns, i.e. approximately 9 Space Shuttle loads.

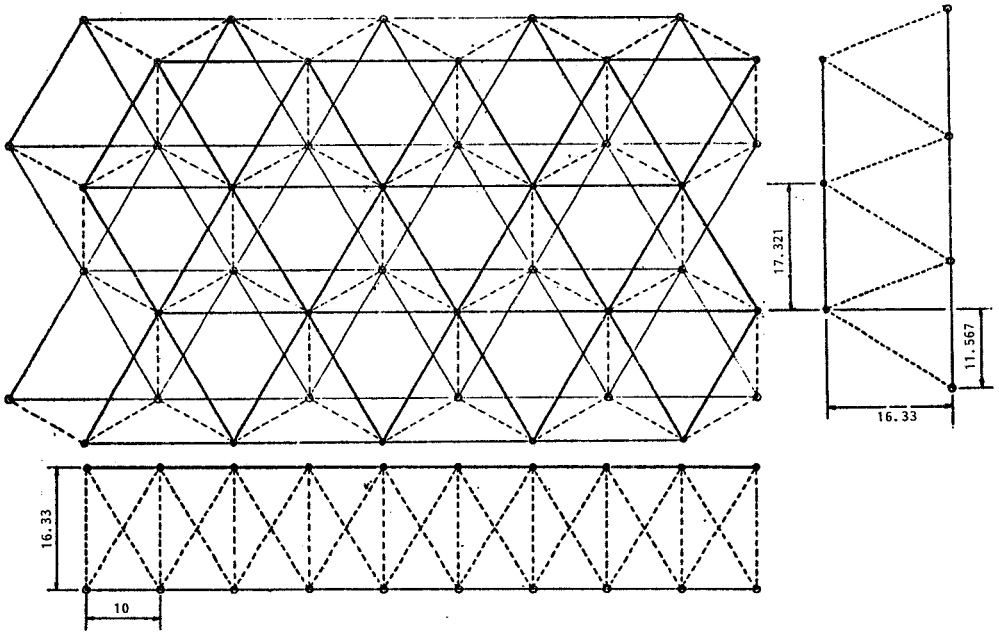

Fig. 1

Columns

The design of the columns is conditioned by the Space Shuttle Stowage requirements. In order to attain the desired loading density, column stacking is a necessity; therefore, each column is made of two narrow conical halves with a connector in the middle. The cones are thin graphite epoxy shells, which allows nesting, or stacking in the fashion of plastic

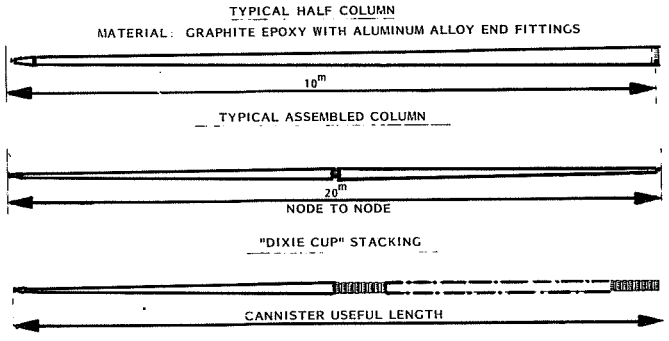

Fig. 2

cups. The number of half columns which may be nested in one stack within the length of the Space Shuttle cargo bay is of the order of 50. Figure 2 presents some details of the columns and the stacking mode. An alternate concept makes use of full columns hinged at the center thus allowing column erection by simple deployment about the spring loaded hinge line without altering the stacking capabilities of the system. This type of column is equipped with a locking mechanism which is a part of its deployment system.

NODE JOINTS

The node joints must provide adequate rigidity to the assembly as well as ease of column insertion. One such design which meets these requirements is shown on Fig. 3. This node connector is self-locking and provides good rigidity about all axes. It can be disconnected manually without effort, even by an astronauts wearing gloves, a feature which allows easy repairs and modifications to the space structure in EVA.

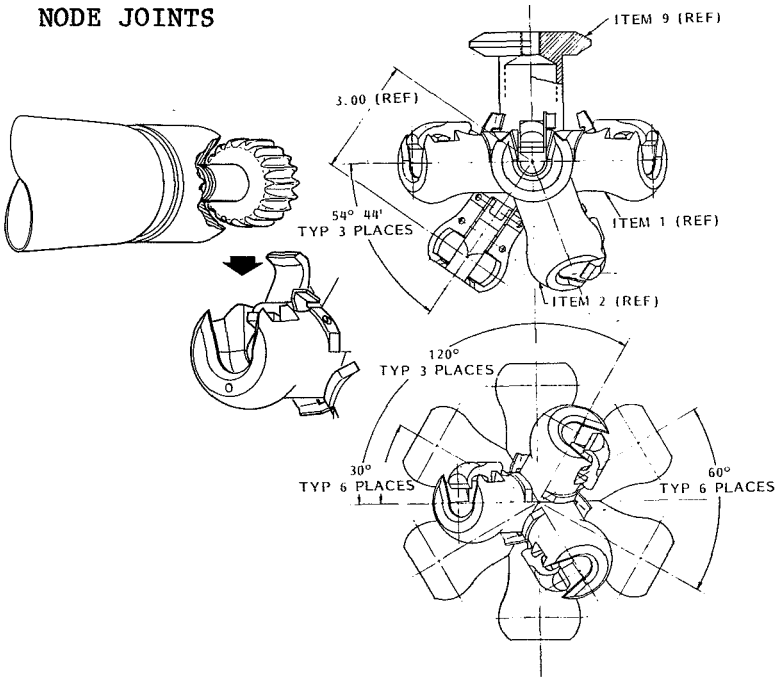

Fig. 3

ASSEMBLERS

General Criteria

In view of the complexity and repetitive nature of the task involved in the assembly of these large space structures, it is desirable to mechanize the process as much as possible and control it through a computer by means of appropriate software. The major criteria which must be satisfied by these machines are as follows:

- Provide adequate jigging of the node joints for accurate column insertion
- Column insertion performed by specialized robotic devices using appropriate end effectors.
- Automatic capture of node joints from supply cannisters, automatic release after installation.
- Automatic capture of columns from supply cannisters, controlled release after insertion is secured.
- Capability to operate during "day" and "night" periods.
- EVA backup mode for emergency operation.

o Compact stowage of the machine in the Space Shuttle Cargo Bay and simple on-orbit assembly without need for special tooling.

Based on these criteria, two assembler designs have been conceptually developed. They are presented below.

Assembler No. 1

The general configuration of Assembler No. 1 is shown on Fig 4. It consists of a main frame which supports a crew and computer compartment on one side and six movable arms on the other side. These arms carry cannisters containing the supply of node joints and columns. Typical concepts of supply

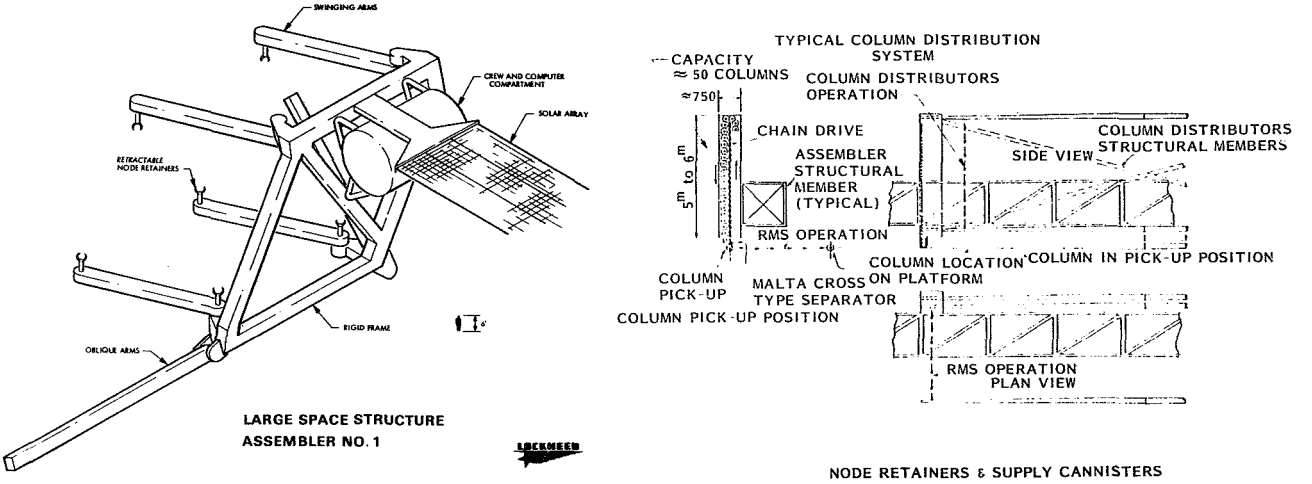

Fig. 4

mechanisms are presented on Fig. 5. Column insertion is performed by means of special mechanisms or robotic manipulator devices as shown on Fig. 6. These devices will be designed for each column insertion point and will perform simple tasks in a rapid repetive manner.

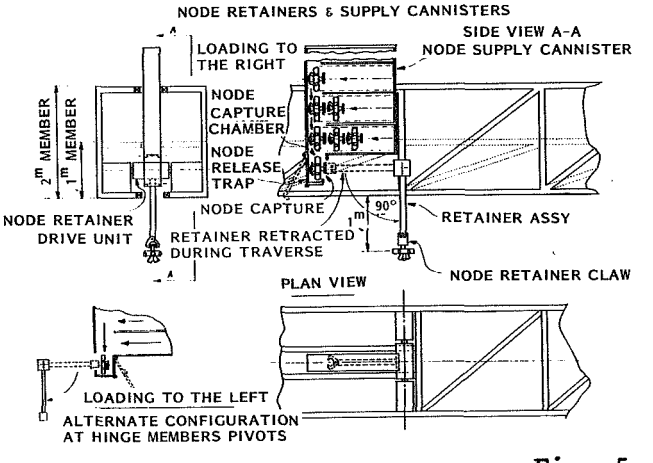

Fig. 5

Traverse Motion

In operation, this assembler progresses along the edge of the space platform, building it as it goes. Its sideways motion (traverse) is somewhat similar to that of a crab as the swinging arms are rotated to walk from node to node on the platform. New nodes are captured from the

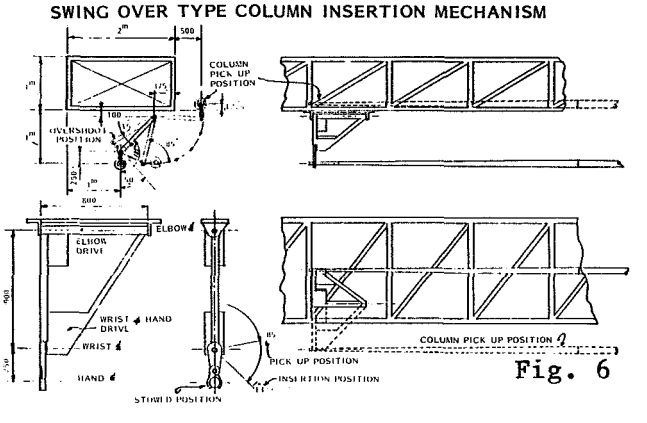

Fig. 6

cannisters, set in place and interconnected with columns. The design can be operated to traverse either to the right or to the left. Also it can be controlled to perform a change of row at the end of a traverse or to go around the corner of a triangle. All these maneuvers can be made computer software dependent, needing only astronaut supervision either by direct observation through the windows of the crew compartment or via spotlights and TV cameras during the night periods.

Specialized Remote Manipulator System (RMS) - Column Insertion

On this assembler, the column cannisters are mounted on the sides of the machine structural members, in close proximity to the final position of the columns. Column insertion is performed over generally short distances and along simple paths. Multi-degree of freedom robotic devices (similar to the Space Shuttle Payload RMS) have been considered to perform this operation because the same system can be used at all column insertion points, thereby simplifying the maintenance and spare parts problem. Such an approach is not very efficient from an operational standpoint since some degrees of freedom will be redundant at some locations. As an alternate, simplified assembly devices have been considered. In this case, the appropriate mechanism differs for each insertion since it must be adapted to meet local requirements. One such typical device is shown on Fig. 7. It consists only of the forearm and wrist with each hinge having only one degree of freedom. This mechanism follows a simple trajectory from the column cannister to the node joint and the wrist motion could be controlled by purely mechanical means (e.g. a cam system). The end effector, however would still have to be powered and controlled separately.

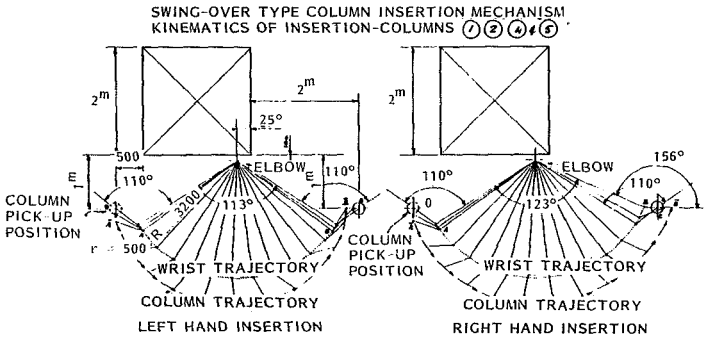

Fig. 7

Column Cannisters

In this application, it is assumed that the half columns would be assembled by a separate machine parked in the vicinity. This machine would receive the Space Shuttle load of cannisters, connect the half-columns together and insert them into the assembly machine cannisters. The astronauts, would then transport these cannisters to install them on the platform assembly machine. The design concept of these cannisters has not been detailed at this time but it is thought of as a mechanically driven system consisting of electrically or mechanically operated holding devices to move the columns and release them one by one upon demand. Each cannister must be approximately 21 m long (70 ft) and requires drive mechanisms at each end. Figure 5 presents the general configuration of these cannisters.

Node Joint Cannisters

The general principle of a node joint cannister is shown on Fig. 8. The node joints are held in position in appropriate compartments and moved forward by a mechanism somewhat similar to that of the column cannisters. Upon reaching the front wall, the node joints are caught by another mechanical transport mechanism which directs them one by one to the capture chamber where the assembly machine node joint retainer can grasp and swing them into place for column insertion.

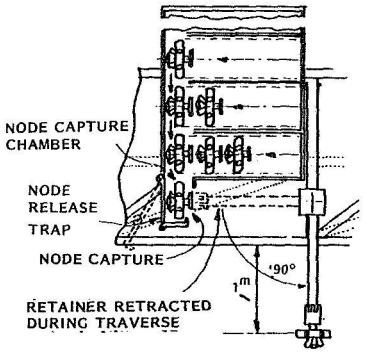

Fig. 8

ASSEMBLER NO. 2

General Principle and Configuration

An alternate concept for assembly of tetrahedral structures is presented on Fig. 9. In this system, the frame work is rigid and serves as the jigging reference. A set of four tracks simultaneously provides the traverse translational facilities and the node joint supply mechanism. The column cannisters are installed at only two locations on the main frame and the transport and insertion of the columns is performed by four identical robotic arms similar in concept to the Space Shuttle RMS, but scaled down and designed to meet these specialized requirements. Here again, it is anticipated that the half column assembly would be performed separately. However, in the case where folded self-deploying columns would be used, it is possible to perform this operation on the machine itself thereby greatly simplifying the whole assembly procedure.

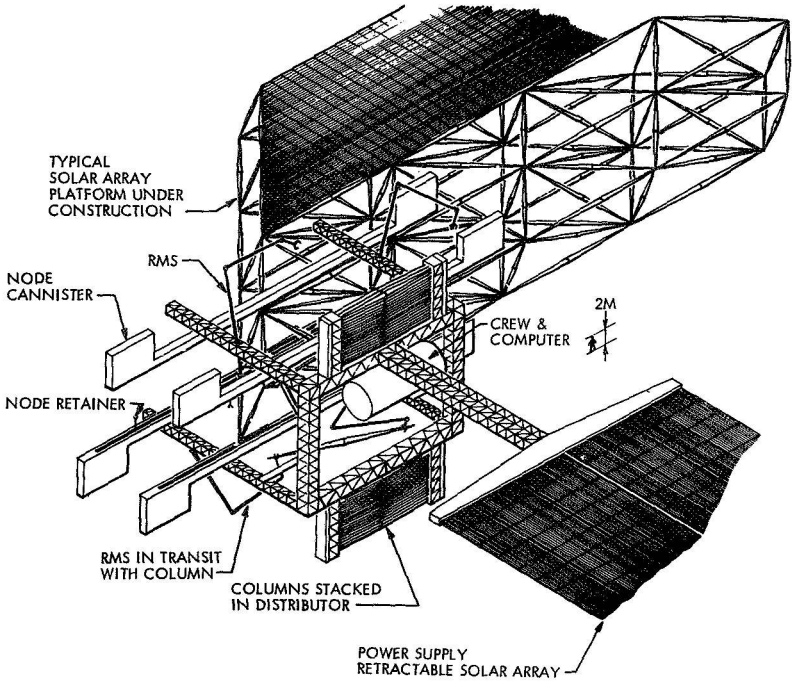

Fig. 9

Traverse Mechanism - Row Change

The traverse mechanism is based on a track system which carries a set of carriages driven by an endless chain, Fig. 10. The node joint retainers are retractable and may be given precision positioning capabilities. The carriages can be located with precision by a track notch locking system capable of providing repeatable positions within specified tolerances.

The traverse motion is obtained similarly to that of a tracked vehicle with the node joint retainers getting hold of the node joint heads in a hand-over-hand fashion, under computer control.

In order to change row, the machine must disconnect itself from the platform under construction and reposition it with respect to the track system. This is accomplished by using the four robotic arms to perform the required manipulations.

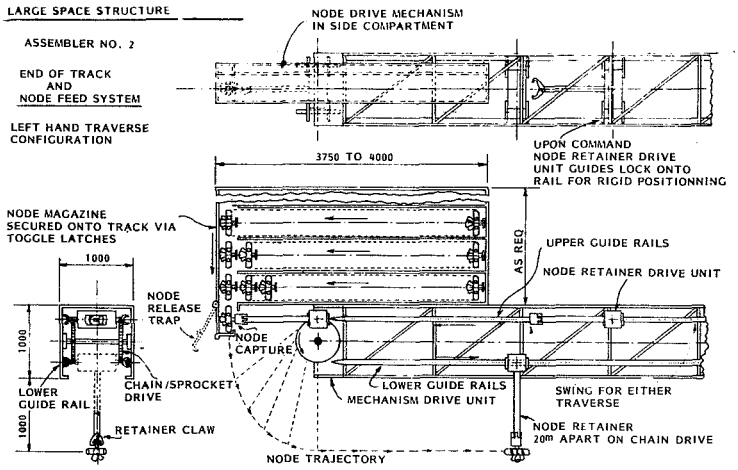

Fig. 10

Specialized Robotic Assembly Devices - Column Insertion

In this system, the columns must be picked up from the cannisters and maneuvered past a number of obstructions to be inserted into the node joints. This manipulation can be performed by robotic arms designed for this purpose. The robotic manipulations required for this application can be designed to move small masses (a few kilograms) but must have the capability to operate at relatively high speeds. The procedure by which this can be achieved consists of defining the coordinates of the trajectories of each end of the columns. A computer program directs the manipulator to follow these trajectories at specified velocities varying with position. Thus accelerations can be controlled throughout the motion and allowances can be made for minimizing the effect of structural flexibility.

Since for this assembler there are only four identical robotic manipulators located in very accessible positions, the problems of interchangeability and replacement are minimized.

Column Cannisters

Except for larger capacity, the design and mechanisms of the column cannisters would follow the principles outlined for those of Assembler No 1. The larger capacity is desirable to reduce the number of loadings and unloadings and to minimize the number of assembly interruptions. The location of these cannisters was selected for its ease of access and the freedom it affords in setting the maximum practical capacity. It is shown on Fig. 11.

Node Joint Cannisters

The storage method and mode of transit of the node joints in their cannisters is similar to that described for Assembler No 1. The size and shape of the cannisters is somewhat different to accommodate the particular conditions at the end of the tracks. Eight cannisters are required in each Space Shuttle load to carry the complement of node joint corresponding to the number of columns.

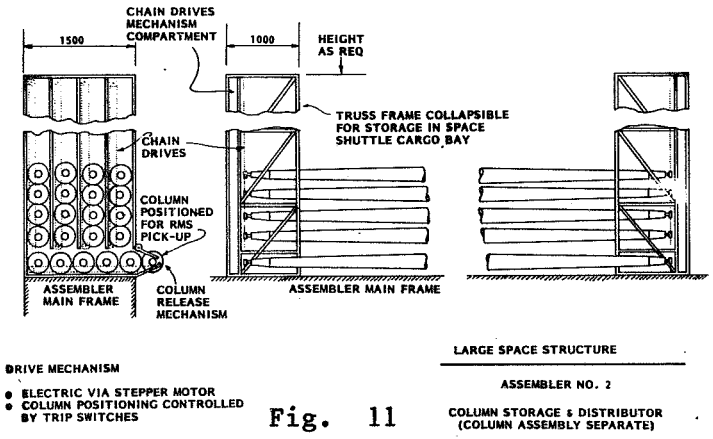

Fig. 11

STRUCTURAL DETAILS OF ASSEMBLERS FRAMES

The structural concept considered for the basic frame of either assemblers is the Warren Truss made from graphite epoxy or aluminum members. These structures are of collapsible type which is self-erectable under the power of spring loaded four-bar linkages. Thus, structural components can be built up on the the ground, deployed in orbit and connected together to form the basic frame. The collapsed elements can be stowed under minimum volume into the cargo bay of the Space Shuttle. Erection of the assembler is therefore considered as an EVA operation.

CONCLUSION

In view of the very large number of components required for the on-orbit erection of large tetrahedral space platforms, their automated assembly is a necessity if the work is to be carried out in a reasonably short time and without undue strain for the astronauts.

The assembly machine is a huge jig in which a multitude of mechanisms must operate continuously in the thermo vacuum environment of space and under the control of computers programmed to command every step of each motion.

The concepts presented in this paper must be refined to determine the most reliable solution. Continuous operation of mechanisms in space presents many unresolved problems, particularly with regard to lubrication of unprotected devices, such as chain drives, which must maintain reasonable positioning tolerances.

ACKNOWLEDGEMENT

This study was sponsored by the NASA Langley Research Center under contract NAS 1-15240, "Development of Assembly and Joint Concepts for Erectable Space Structures".

REFERENCES:

1. Bush, Harold G.; and Mikulas, Martin M., Jr., "A Nestable Tapered Column Concept for Large Space Structures," NASA TM X-73927, 1976.

2. Mikulas, Martin M., Jr.; Bush, Harold G.; and Card, Michael F., "Structural Stiffness, Strength and Dynamic Characteristics of Large Tretrachedral Space Truss Structures", NASA TM X-74001-1977

3. NASA CR-3131, "Development of Assembly and Joint Concepts for Electable Space Structures", Contract NAS 1-15240.

DEVELOPMENT OF A BEAM BUILDER FOR AUTOMATIC FABRICATION OF LARGE COMPOSITE SPACE STRUCTURES

John G. Bodle

General Dynamics Convair Division

ABSTRACT

This paper describes the composite material beam builder concept currently being designed and developed for NASA Lyndon B. Johnson Space Center. * The machine will produce triangular beams from pre-consolidated graphite/glass/thermoplastic composite material through automated mechanical processes for forming; side member storage, feed and positioning; ultrasonic welding; and beam cutoff. Each process lends itself to modular subsystem development. Initial development has been concentrated on the key processes for roll forming and ultrasonic welding composite-thermoplastic materials. The construction and test of an experimental roll forming machine and ultrasonic welding process control techniques are described.

INTRODUCTION

In the ensuing years with the advent of the Shuttle Transportation System, the use of robots will play an indispensible role in the on-orbit construction of large space systems. It will be neither practical nor feasible to use men to perform highly repetitive precision assembly operations that can be accomplished quickly and efficiently by automated machines. Advances in microelectronics coupled with the technology developed for spacecraft mechanisms has paved the way for a new and challenginig field of space fabrication and assembly equipment.

Current studies of advanced space systems generally indicate that a basic piece of equipment required for on-orbit fabrication of large space structures is an automated beam fabrication machine. This beam builder must produce numerous structural beams from materials stored in small volumes within the machine. The beams are then joined together by automatic assemblers into large structures.

*This work was performed on Contract NAS9-15310 and in-house structures and Materials Technology R&D.

The beam builder concept described herein fabricates beams from graphite/glass/thermoplastic composite material. This machine has two key processes which have been evaluated experimentally to prove viability of the concept. The first is the forming process for beam cap members. Some of the problems encountered during prototype cap forming machine development are discussed. The second key process is ultrasonic welding. The advantages of ultrasonic welding are discussed along with its unique process control capabilities.

BEAM BUILDER CONCEPT

The design of a beam builder is primarily determined by the configuration of the beam it must build. The beam design must also be adaptable to automatic manufacturing processes. The beam builder concept of Figure 1 resulted from numerous trade studies of beams and beam fabrication and assembly processes as described in Reference 1. The size and arrangement of this beam builder were established to permit fabrication of a 200m x 11m planar ladder platform in a seven day mission using the Space Shuttle Orbiter as a construction base. The overall machine concept was selected to permit scale-up to a wide variety of beam sizes. This machine has an estimated weight of 3600 kg, including 1000 kg of material, and has a 2 kw average power requirement.

The beam is manufactured from three basic elements, i.e., caps, cords and crossmembers. Open section caps are formed in continuous lengths from long coiled flat strips of pre-consolidated single-ply graphite/glass fabric in polysulfone resin with a special outer coating for radiation protection. Pre-fabricated crossmembers of the same material are stored in clips. Six diagonal fiberglass cords impregnated with polysulfone resin are stored on spools. The beam is manufactured in a cyclic feed operation whereby the cap is driven for 40 seconds to advance the beam one bay length, then stopped for 40 seconds during assembly as illustrated in Figure 2. To build beams continuously would greatly increase the size and complexity of the machine because all assembly operations would have to be placed on a reciprocating carriage to move with the caps. Another advantage of cyclic feed is that faults detected during the assembly period can be corrected without elaborate backout sequences.

The beam builder system is designed with modular subsystems for cap forming, joining, cord positioning and tensioning, crossmember feed and positioning, beam cutoff, and control. A welded aluminum structure provides a chassis on which to mount these modular elements. This approach allows each subsystem to be independently developed, manufactured and checked out before being integrated into the beam builder system. It also simplifies the task of scaling the machine up to produce larger beams.

CAP FORMING MACHINE CONCEPT

The preliminary design concept of the cap forming machine is shown in Figure 3. This machine is sized to manufacture a 1.434m bay length of cap per cycle with a storage capacity for up to 1000m of continuous cap length. Greater length and storage capacity are possible where required. Peak power required to operate this machine is calculated to be 474 watts.

The cap drive unit provides the pull force to move the material from the storage roll through the heating, forming and cooling sections. It also acts to advance the beam through the assembly sections and deploy it from the beam builder. Material is heated to the plastic state (218°C) along the bend zones as the material passes through the heating section. The material goes through a transition from flat to formed in the forming section. Strip heaters are provided in the forming section for start-up and for maintaining material forming temperature when the machine is operated in air. In vacuum where convective cooling is not present, these heaters are turned off during forming operations. Temperature is monitored for control through non-contacting infrared sensors. The cooling section contains retractable fluid cooled platens which are engaged during the 40 second pause cycle and retracted during the 40 second run cycle. The rational for the selected design approach for each of the cap forming machine functions is summarized in Table I.

PROTOTYPE CAP FORMING MACHINE DEVELOPMENT

Initial Design

Although roll forming graphite/thermoplastic composite material had been demonstrated by earlier experiments, it was clear that a fully automated prototype would be required to evaluate and refine the cap forming machine design. The prototype machine shown in Figure 4 was designed as an experimental breadboard with individual assemblies for heating, forming, cooling, drive and control. This provided total flexibility in alteration and adjustment of the configuration.

Cost considerations dictated that heating and cooling sections be scaled down to produce 60 cm of cap per cycle. The heating section shown in Figure 5 used ordinary tubular electric heaters. Temperature control was accomplished with surface contacting thermocouple sensors and commercial temperature controllers. Quartz lamp heaters were used throughout the forming section to maintain material forming temperature during operation in air.

One of the objectives was to minimize the length of the forming section and the number of forming stages required. The initial forming section design shown in Figure 6 used two forming stages. The pre-forming stage would partially form the bend radii

and the final stage would complete the section. Smooth transition from flat to formed section is essential to prevent buckling and wrinkling in the heated bend zones.

The initial material to be evaluated was a laminate as shown in Figure 4. This combination provided the desired structural characteristics and low coefficient of thermal expansion. The glass fabric acted to impede transverse heat transfer while the longitudinal strands of graphite fibers promote heat transfer in the warp direction. These thermal characteristics minimize heating energy and maintain material forming temperature in the bend zones throughout the forming process.

Design Problems and Solutions

The first series of forming tests revealed two major problems in the design which produced very unsatisfactory results. The initial material configuration was not well suited for the process and the forming section configuration was incorrect. The outer glass laminae were compressed and delaminated by the bending along the inside radii of the cap. This caused high drag loads to be created as the material passed through the forming rollers which distorted the formed section. The fine weave glass layers also acted to impede heating making it difficult to control heat rates without scorching the surface of the material.

The pre-forming rollers could not react the twisting moment induced by the unheated strip of material along the side of the cap. This caused the material to eventually be lifted out of the side rollers. As seen on the left in Figure 7, the side radii did not form and the material became bunched-up at the apex.

The breadboard design proved its worth by allowing the roller styles and arrangements to be altered conveniently. Each variation produced a better understanding of how to control the behavior of the material in the forming section. Through trial and error a smooth and stable transition from flat to formed was produced as seen in Figure 8 and a satisfactory cap member could now be formed.

The prototype cap forming machine is a useful tool for revealing very subtle problems associated with various weaves and laminates. One example is that of a single ply weave which had good heating and forming characteristics but poor cooling characteristics. The finished cap showed the result of what could be termed "spring-in" when cooled. The apex angle of the cap formed from this interim material would cool to a shape such that the apex angle was less than 60^{o} as shown on the right of Figure 7. Efforts to refine and evaluate detail material characteristics are continuing.

ULTRASONIC WELDING

Ultrasonic welding of thermoplastic materials has been used in the manufacture of commercial products for years. It is ideally suited for the assembly of composite/thermoplastic space structures because it produces solid joints, uses little energy, produces no debris or outgassing, and has fully automated process control for high reliability.

The beam builder concept employs six ultrasonic welders for joining the beam members together. Welder process controls are shown in the Figure 9 schematic. The weld head consists of a transducer which converts a 20 KHz power signal into ultrasonic vibrations which are transmitted to a metal horn at the half wave resonant frequency of the horn. The horn vibrates axially at both ends at an amplitude fixed by the amplitude output from the transducer. The crossmember and cap are firmly clamped between the horn and a backup anvil by a force applied by the welder drive mechanism. In this case the horn is equipped with three weld tips which impart vibration in the spots to be joined. The vibration quickly heats the thermoplastic resin in the mating surfaces of the parts to be joined to the plastic state. The power to the transducer is turned off and the parts are held clamped together until the thermoplastic solidifies creating a fused bond in the weld zones. A typical weld requires approximately 1 second of excitation and 0.5 second for cooling.

Manufacturers of ultrasonic welders indicate that the process can be controlled by three feedback signals. A load cell measures applied force. The resonant frequency of the horn is monitored directly for slight changes which occur due to temperature change. The amplifier will vary the frequency input to the transducer to maintain resonance of the horn. Finally, the power output of the horn is measured and compared with the amplifier power output. Weld time is automatically varied to allow the proper amount of energy to be input to the weld. Verification and control of these three critical parameters ensures the quality of the finished weld is within acceptable limits. Experiments with candidate hybrid composite/thermoplastic materials have produced excellent results with samples welded in both air and vacuum.

CONCLUSIONS

1. One of the most critical design factors to consider for space construction equipment such as the beam builder will be to provide the software and sensors necessary to ensure positive process control, fault analysis and fail safe operation.
2. The viability of the composite material beam builder concept is firmly supported by the demonstrations performed with its two key processes, the cap forming machine and the ultrasonic welding process.
3. Roll forming of composite/thermoplastic material requires careful selection and verification of material characteristics in order to be compatible with the machine processes. Similarly the machine processes must be tailored for the material to achieve satisfactory operating results.

REFERENCES

1. Browning, D. L., et al, "Space Construction Automated Fabrication Experiment Definition Study (SCAFEDS)," General Dynamics Convair Division, Final Report CASD-ASP77-017, NAS9-15310, May 1978, pp 2-36 thru 2-82.

Table I. CAP FORMING MACHINE CONCEPT SELECTION

FUNCTION	SELECTED APPROACH	RATIONALE

STORAGE	ROLL IN A CAN	• POSITIVE CONTAINMENT
		• NO REEL TO DISPOSE OF
		• HEATERS INTEGRATED
		  • MINIMIZES MACHINE LENGTH
		  • WASTE HEAT RADIATES TO ROLL
		• EASE OF REPLENISHMENT

HEATING	• STRIP HEAT BEND ZONES ONLY • ELECTRIC RESISTANCE WIRE HEATERS • MATERIAL CONFIGURED FOR HIGH LONGITUDINAL AND LOW TRANSVERSE HEAT TRANSFER	GREATEST EFFICIENCY OF ENERGY UTILIZATION
FORMING	PASSIVE ROLLERS (ROLLTRUSION)	• LOW DRAG MINIMIZES FORMING ENERGY • SHORT FORMING TRANSITION LENGTH FOR MINIMUM MACHINE LENGTH
COOLING	FLUID COOLED PLATENS	• MATERIAL COOLS TOO SLOWLY IN VACUUM • ENSURES UNIFORMITY AND STRAIGHTNESS OF FINISHED CAP
DRIVE	FRICTION ROLLERS	• DOES NOT DAMAGE MATERIAL OR COATING • COMPACT DRIVE UNIT MINIMIZES MACHINE LENGTH

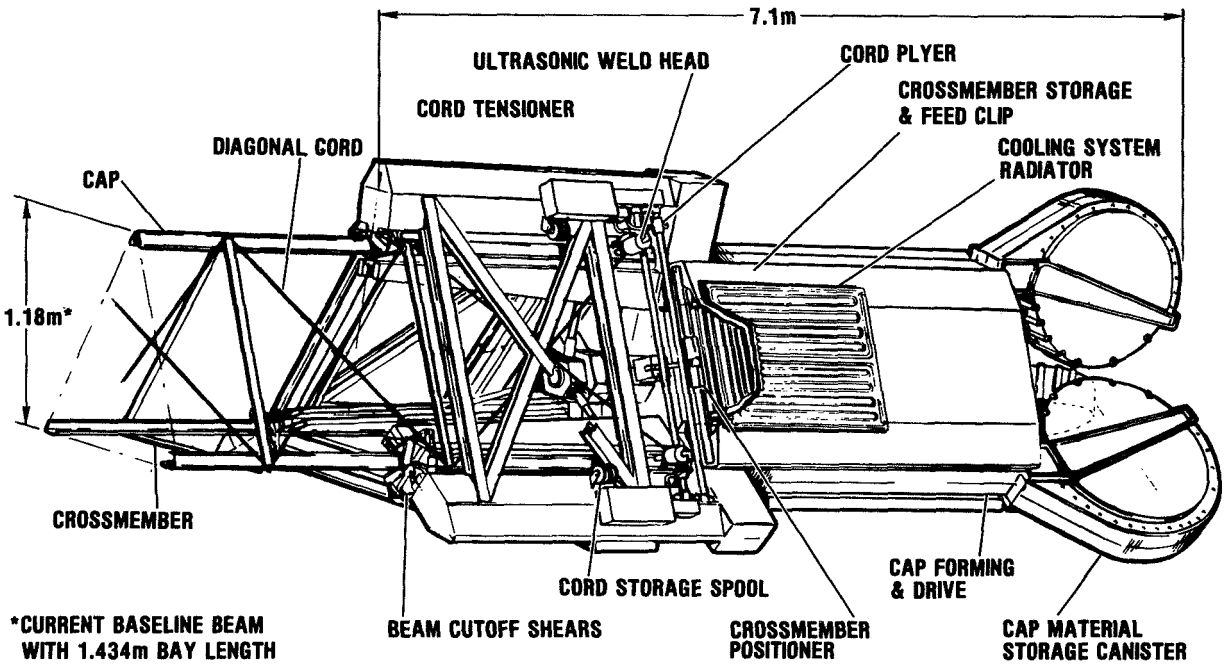

Figure 1. Beam builder concept.

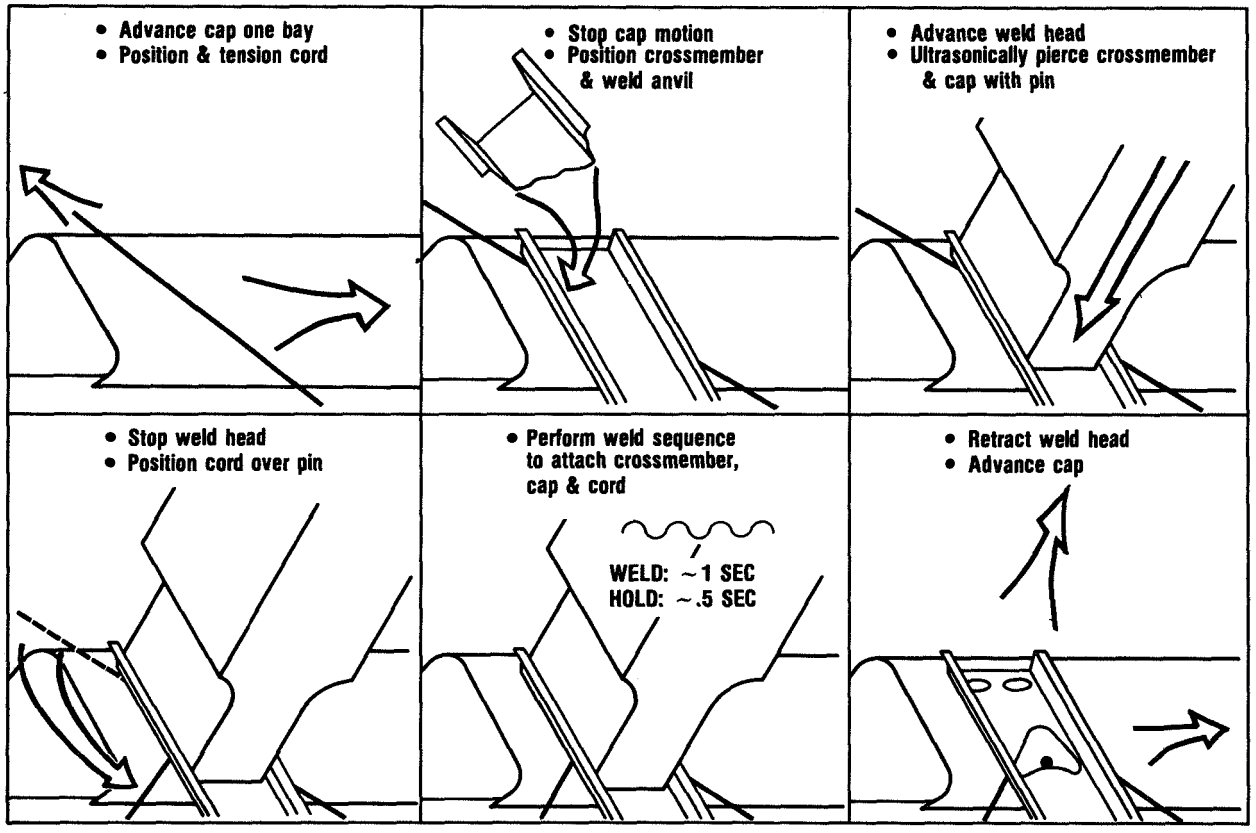

Figure 2. Beam assembly processes.

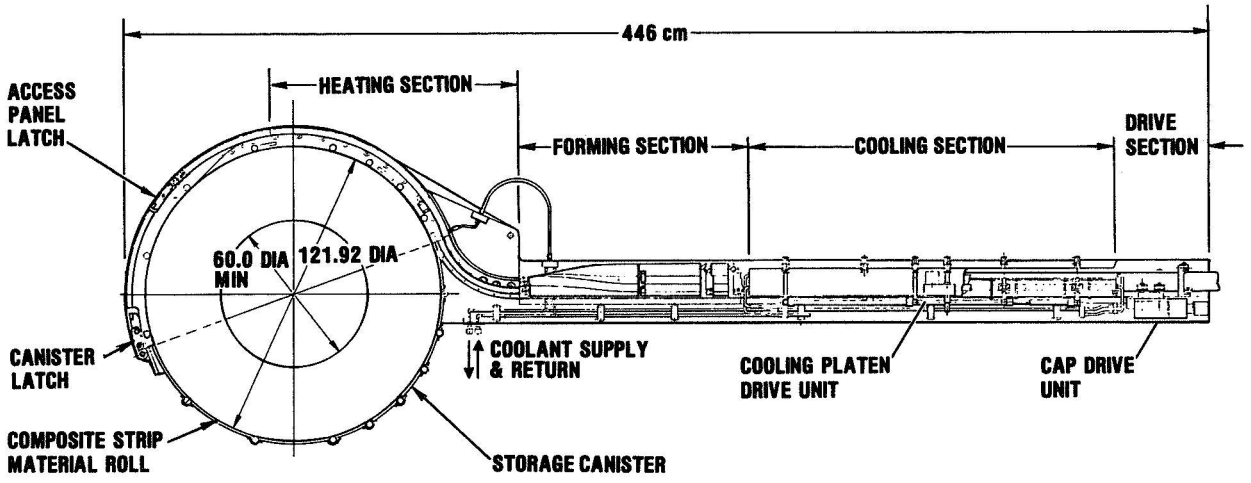

Figure 3. Beam builder cap forming machine design concept.

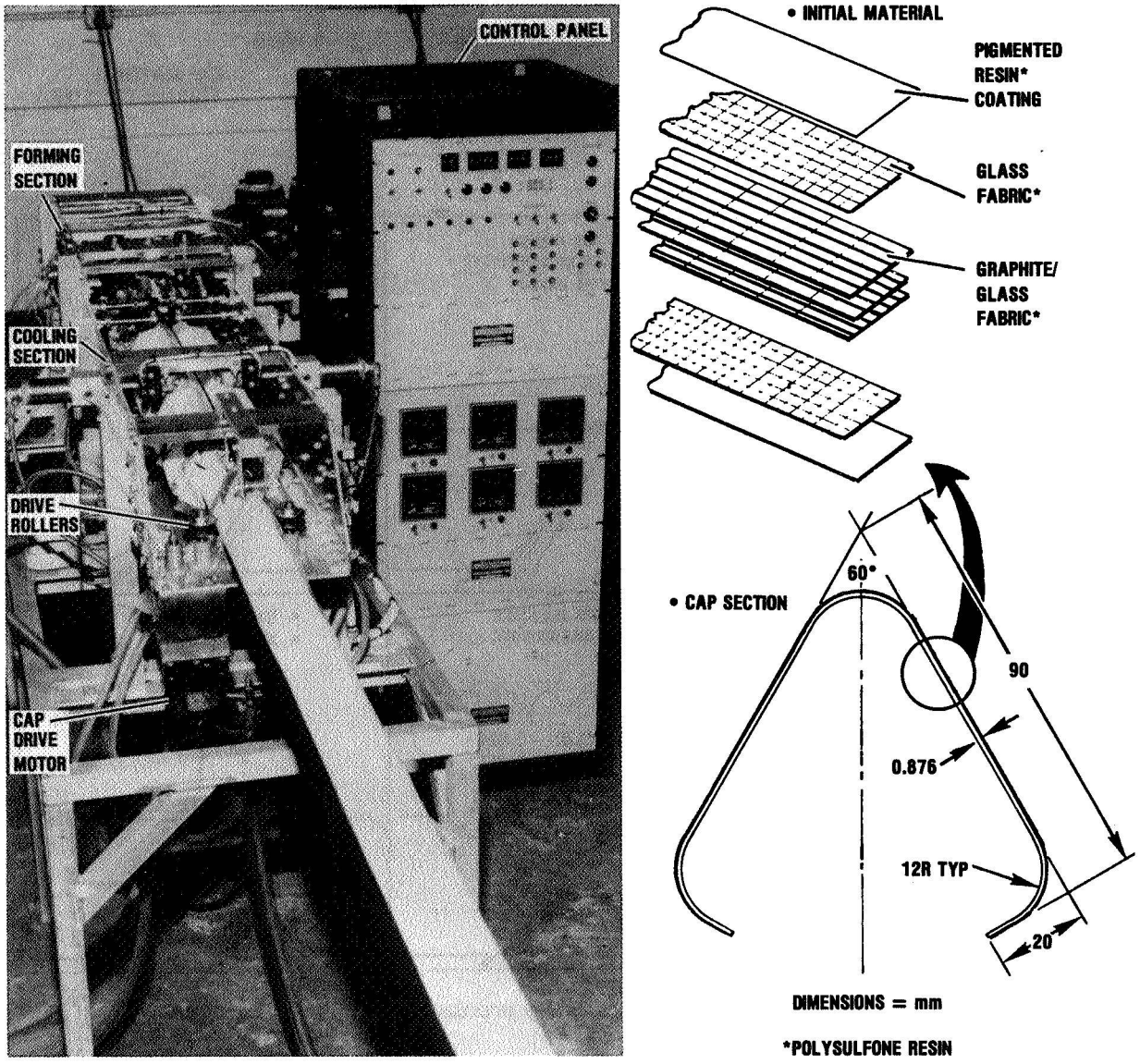

Figure 4. Prototype cap forming machine.

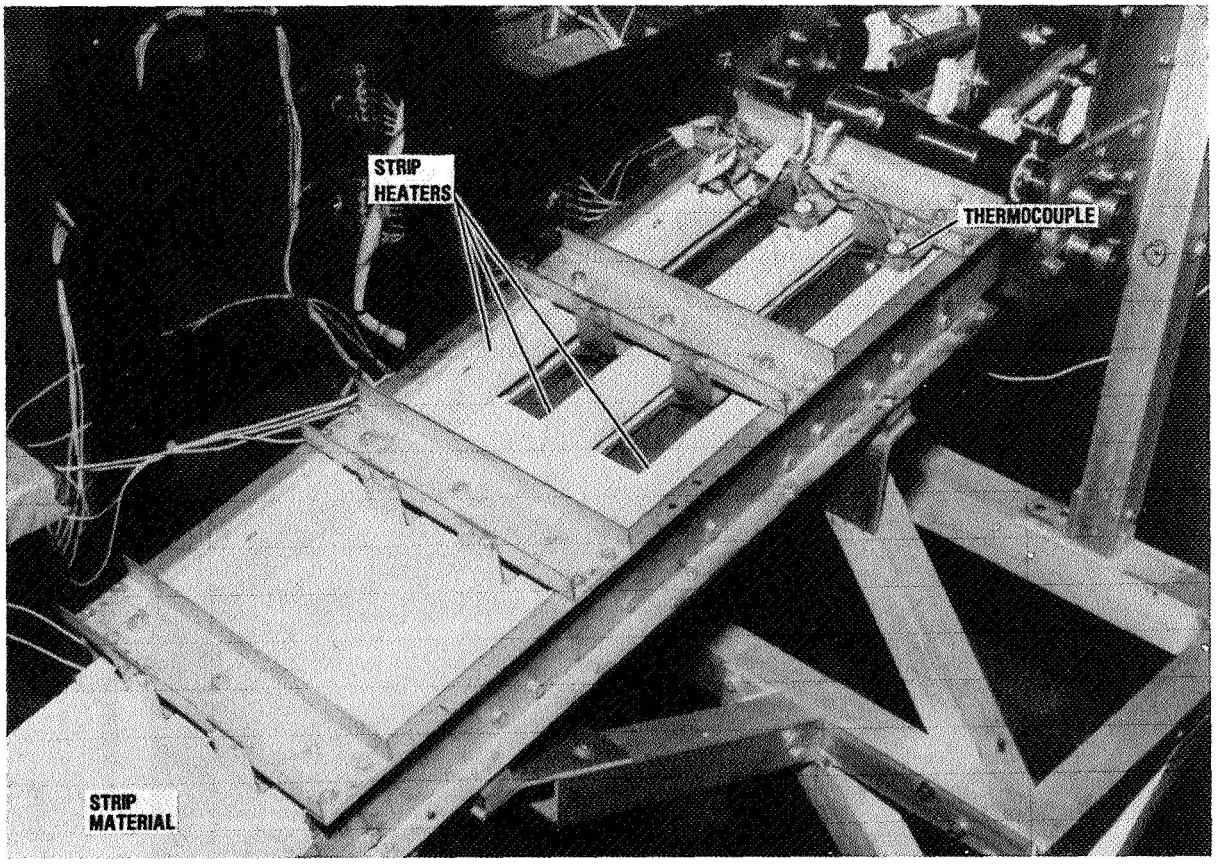

Figure 5. Cap forming machine heating section.

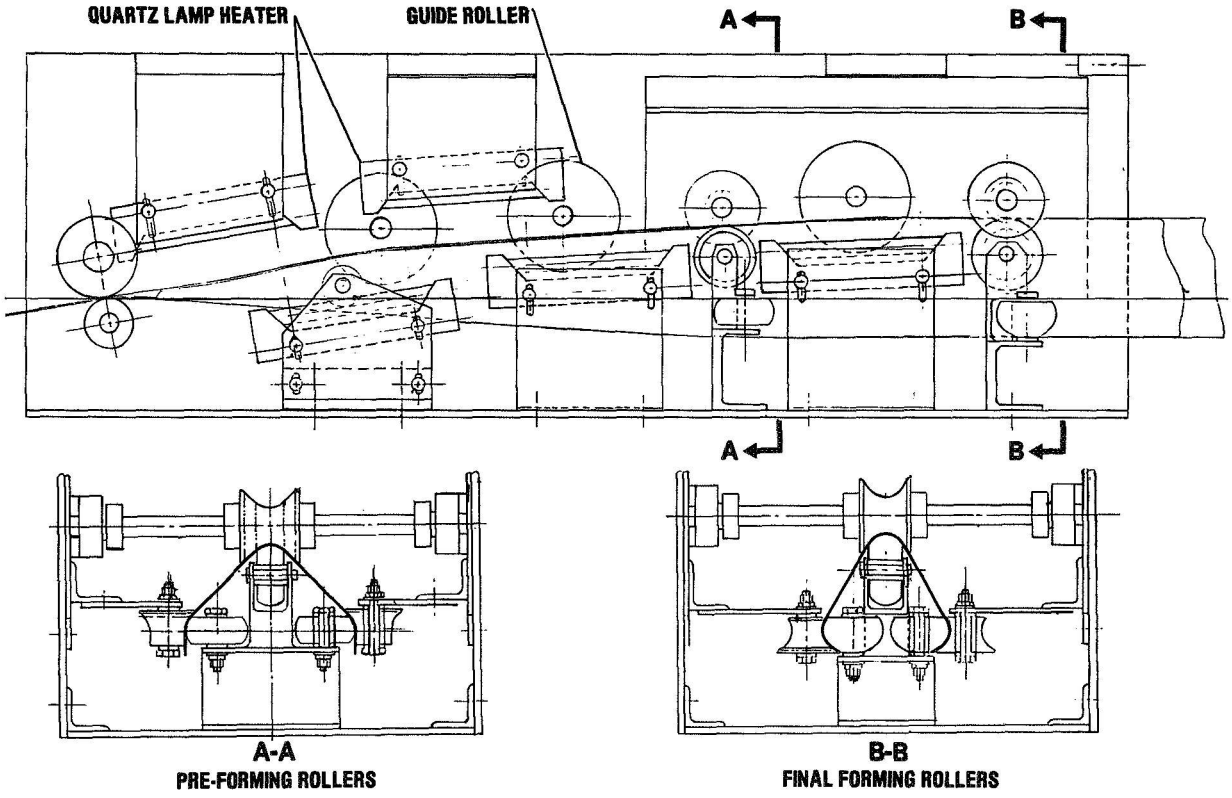

Figure 6. Initial forming section design.

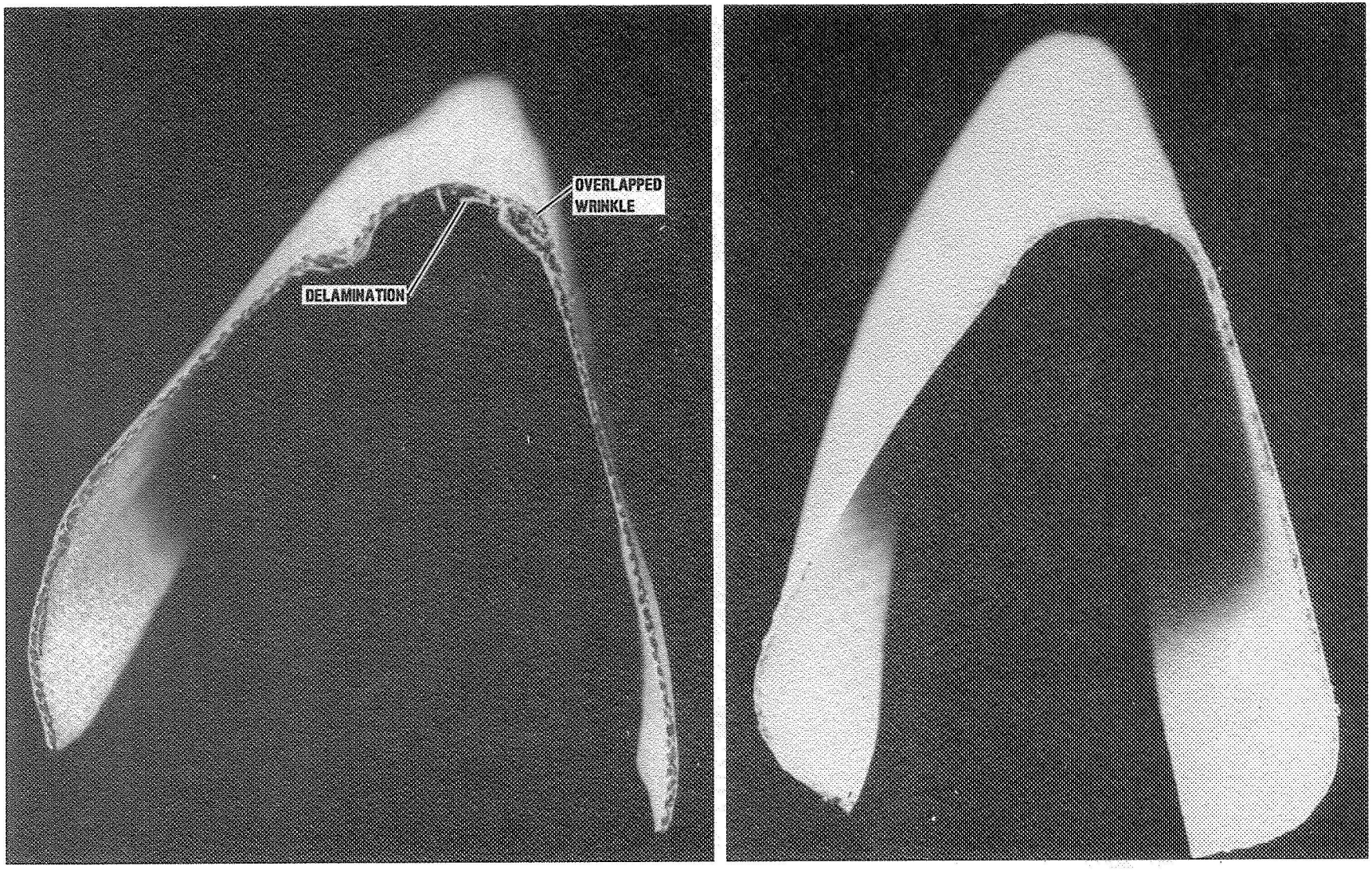

Figure 7. Forming test specimens.

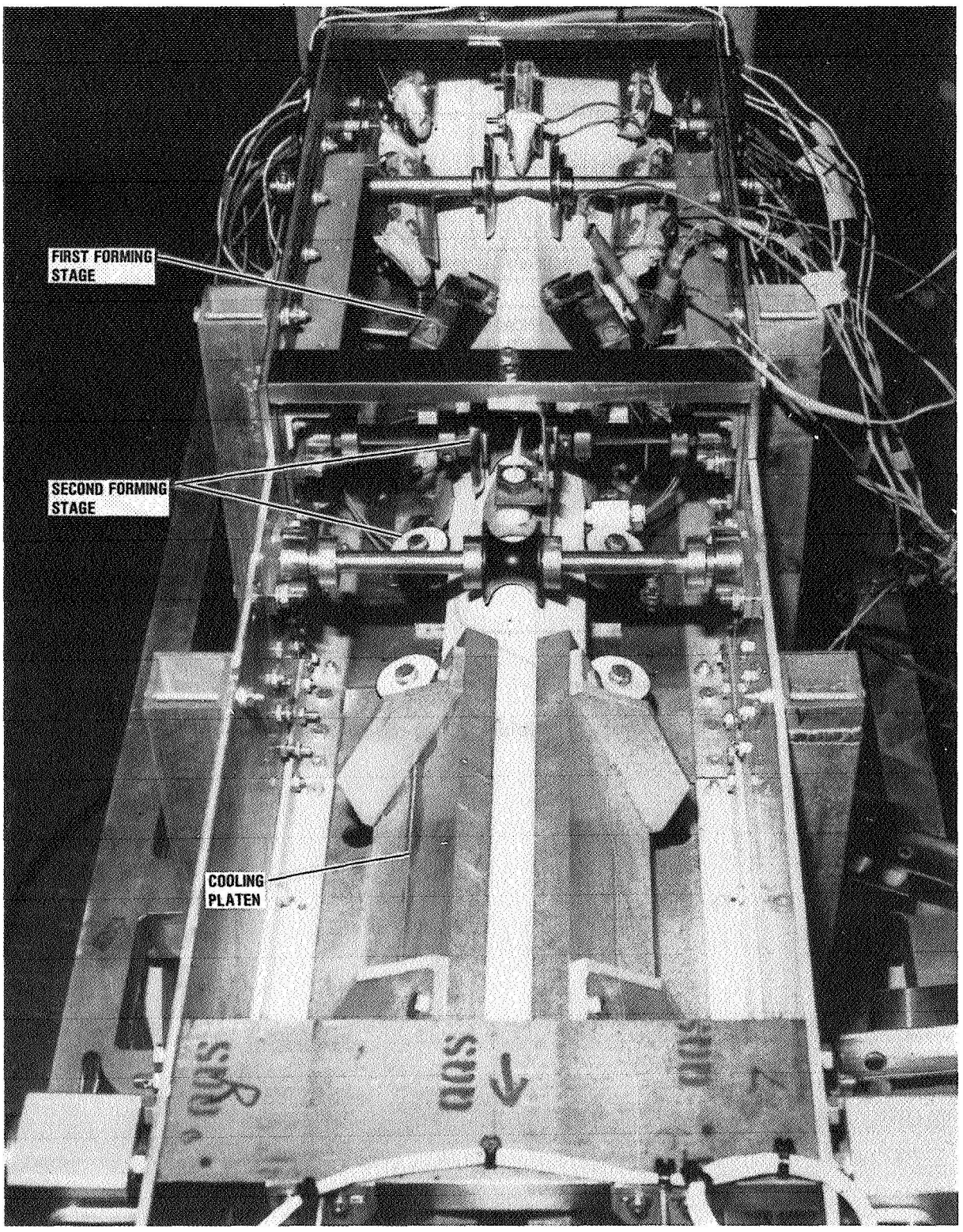

Figure 8. Improved forming section.

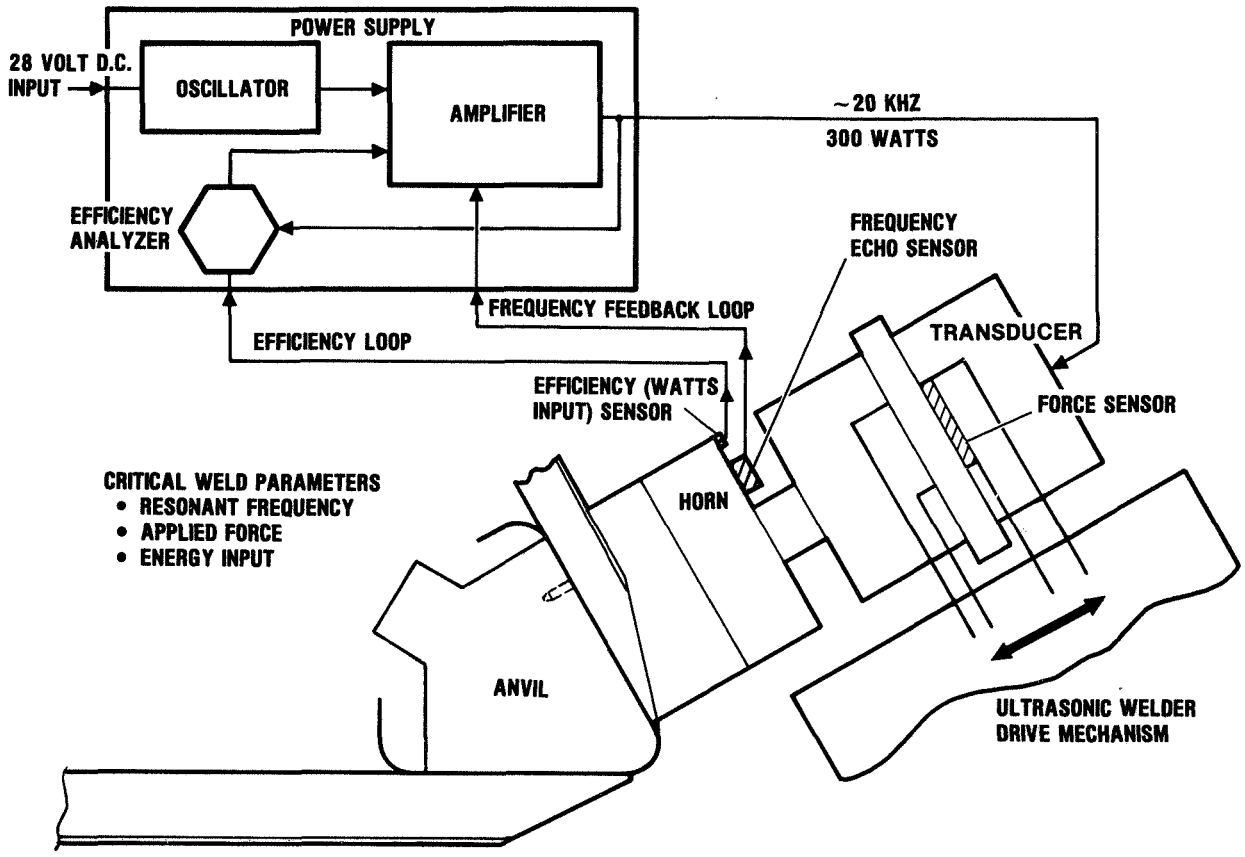

Figure 9. Ultrasonic welding process control techniques.

1. Report No.	2. Government Accession No.	3. Recipient's Catalog No.
NASA CP-2081		

4. Title and Subtitle	5. Report Date
13TH AEROSPACE MECHANISMS SYMPOSIUM	April 1979
	6. Performing Organization Code

7. Author(s)	8. Performing Organization Report No.
Aleck C. Bond, Chairman	S-496
	10. Work Unit No.
9. Performing Organization Name and Address	953-36-00-00-72
Lyndon B. Johnson Space Center Houston, Texas 77058	11. Contract or Grant No.
	13. Type of Report and Period Covered
12. Sponsoring Agency Name and Address	Conference Publication
National Aeronautics and Space Administration Washington, D.C. 20546	14. Sponsoring Agency Code

15. Supplementary Notes

16. Abstract

Papers presented at the 13th Aerospace Mechanisms Symposium are contained. Technological areas covered include propulsion, motion compensation, instrument pointing and adjustment, centrifuge testing, bearing design, vehicle braking, and cargo handling. Devices for satellite, missile, and hypersonic-wind-tunnel applications; Space Shuttle mechanical and thermal protection systems; and techniques for building large space structures are described. In addition, a fluid drop injector device for a Spacelab experiment, a helical grip for cable cars, and applications of rare earth permanent magnets are discussed.

17. Key Words (Suggested by Author(s))	18. Distribution Statement
Product development Electromechanical devices Mechanical devices Experimental design Dynamic characteristics Stress analysis	STAR Subject Category: 39 (Structural Mechanics)

19. Security Classif. (of this report)	20. Security Classif. (of this page)	21. No. of Pages	22. Price*
Unclassified	Unclassified	302	$9.75

*For sale by the National Technical Information Service, Springfield, Virginia 22161

National Aeronautics and
Space Administration

Washington, D.C.
20546

Official Business
Penalty for Private Use, $300

THIRD-CLASS BULK RATE

Postage and Fees Paid
National Aeronautics and
Space Administration
NASA-451

POSTMASTER: If Undeliverable (Section 158
Postal Manual) Do Not Return